Springer Theses
Recognizing Outstanding Ph.D. Research

Claudia Backes

Noncovalent Functionalization of Carbon Nanotubes

Fundamental Aspects of Dispersion and Separation in Water

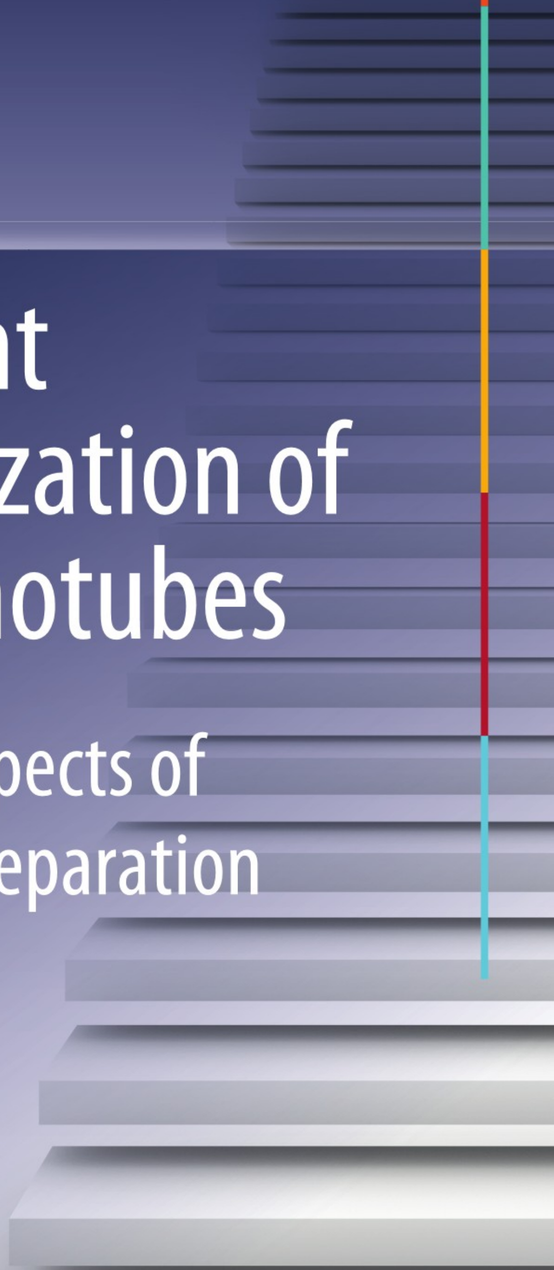

Springer

Springer Theses

Recognizing Outstanding Ph.D. Research

For further volumes:
http://www.springer.com/series/8790

Aims and Scope

The series “Springer Theses” brings together a selection of the very best Ph.D. theses from around the world and across the physical sciences. Nominated and endorsed by two recognized specialists, each published volume has been selected for its scientific excellence and the high impact of its contents for the pertinent field of research. For greater accessibility to non-specialists, the published versions include an extended introduction, as well as a foreword by the student’s supervisor explaining the special relevance of the work for the field. As a whole, the series will provide a valuable resource both for newcomers to the research fields described, and for other scientists seeking detailed background information on special questions. Finally, it provides an accredited documentation of the valuable contributions made by today’s younger generation of scientists.

Theses are accepted into the series by invited nomination only and must fulfill all of the following criteria

- They must be written in good English.
- The topic should fall within the confines of Chemistry, Physics, Earth Sciences and related interdisciplinary fields such as Materials, Nanoscience, Chemical Engineering, Complex Systems and Biophysics.
- The work reported in the thesis must represent a significant scientific advance.
- If the thesis includes previously published material, permission to reproduce this must be gained from the respective copyright holder.
- They must have been examined and passed during the 12 months prior to nomination.
- Each thesis should include a foreword by the supervisor outlining the significance of its content.
- The theses should have a clearly defined structure including an introduction accessible to scientists not expert in that particular field.

Claudia Backes

Noncovalent Functionalization of Carbon Nanotubes

Fundamental Aspects of Dispersion and Separation in Water

Doctoral Thesis accepted by
University Erlangen-Nürnberg, Germany

Springer

Author
Dr. Claudia Backes
ZMP-Institute of Advanced
Materials and Processes
Universität Erlangen-Nürnberg
Dr. Mack Str 81
90762 Fürth
Germany

Supervisor
Prof. Dr. Andreas Hirsch
Chair of Organic Chemistry
Universität Erlangen-Nürnberg
Henkestr. 42
91054 Erlangen
Germany

ISSN 2190-5053
e-ISSN 2190-5061
ISBN 978-3-642-27581-4
e-ISBN 978-3-642-27582-1
DOI 10.1007/978-3-642-27582-1
Springer Heidelberg New York Dordrecht London

Library of Congress Control Number: 2011946220

© Springer-Verlag Berlin Heidelberg 2012
This work is subject to copyright. All rights are reserved by the Publisher, whether the whole or part of the material is concerned, specifically the rights of translation, reprinting, reuse of illustrations, recitation, broadcasting, reproduction on microfilms or in any other physical way, and transmission or information storage and retrieval, electronic adaptation, computer software, or by similar or dissimilar methodology now known or hereafter developed. Exempted from this legal reservation are brief excerpts in connection with reviews or scholarly analysis or material supplied specifically for the purpose of being entered and executed on a computer system, for exclusive use by the purchaser of the work. Duplication of this publication or parts thereof is permitted only under the provisions of the Copyright Law of the Publisher's location, in its current version, and permission for use must always be obtained from Springer. Permissions for use may be obtained through RightsLink at the Copyright Clearance Center. Violations are liable to prosecution under the respective Copyright Law.
The use of general descriptive names, registered names, trademarks, service marks, etc. in this publication does not imply, even in the absence of a specific statement, that such names are exempt from the relevant protective laws and regulations and therefore free for general use.
While the advice and information in this book are believed to be true and accurate at the date of publication, neither the authors nor the editors nor the publisher can accept any legal responsibility for any errors or omissions that may be made. The publisher makes no warranty, express or implied, with respect to the material contained herein.

Printed on acid-free paper

Springer is part of Springer Science+Business Media (www.springer.com)

Parts of this thesis have been published in the following journal articles/books

Articles

Gebhardt, G., Hof F., Backes C., Müller, M., Plocke, T., Thomsen. C., Hauke, F., Hirsch, A. Selective Reductive Sidewall Carboxylation of Semiconducting Single-Walled Carbon Nanotubes. *Journal of the American Chemical Society* **133**, 19459–19473 (2011).

Backes, C., Hauke, F. & Hirsch, A. The Potential of Perylene Bisimide Derivatives for the Solubilization of Carbon Nanotubes and Graphene. *Advanced Materials* **23**, 2588–2601 (2011). (feature article, review)

Backes, C., Schunk, T., Hauke, F. & Hirsch, A. Counterion effect on the aggregation of anionic perylene dyes and the influence on carbon nanotube dispersion efficiencies. *Journal of Materials Chemistry* **21**, 3554 (2011).

Backes, C., Schmidt, C. D., Hauke, F. & Hirsch, A. Perylene-Based Nanotweezers: Enrichment of Larger-Diameter Single-Walled Carbon Nanotubes. *Chemistry—An Asian Journal* **6**, 438–444 (2011).

Backes, C., Englert, J. M., Bernhard, N., Hauke, F. & Hirsch, A. Optical Visualization of Carbon Nanotubes-a Unifying Linkage between Microscopic and Spectroscopic Characterization Techniques. *Small* **6**, 1968–1973 (2010). (feature article, highlighted by Nanowerk Platform)

Karabudak, E., Backes, C., Hauke, F., Schmidt, C. D., Cölfen, H., Hirsch, A. & Wohlleben, W. A Universal Ultracentrifuge Spectrometer Visualizes CNT-Intercalant-Surfactant Complexes. *ChemPhysChem* **11**, 3224–3227 (2010).

Backes, C., Mundloch, U., Schmidt, C. D., Coleman, J. N., Wohlleben, W., Hauke, F. & Hirsch, A. Enhanced Adsorption Affinity of Anionic Perylene-Based Surfactants towards Smaller-Diameter SWCNTs. *Chemistry—A European Journal* **16**, 13185–13192 (2010).

Backes, C., Karabudak, E., Schmidt, C. D., Hauke, F., Hirsch, A. & Wohlleben, W. Determination of the Surfactant Density on SWCNTs by Analytical Ultracentrifugation. *Chemistry —A European Journal* **16**, 13176–13184 (2010).

Backes, C., Mundloch, U., Ebel, A., Hauke, F. & Hirsch, A. Dispersion of HiPco® and CoMoCAT® Single-Walled Nanotubes (SWNTs) by Water Soluble Pyrene Derivatives-Depletion of Small Diameter SWNTs. *Chemistry—A European Journal* **16**, 3314–3317 (2010). (feature article)

Backes, C., Schmidt, C. D., Rosenlehner, K., Hauke, F., Coleman, J. N. & Hirsch, A. Nanotube Surfactant Design: The Versatility of Water-Soluble Perylene Bisimides. *Advanced Materials* **22**, 788–802 (2010).

Backes, C., Hauke, F., Schmidt, C. D. & Hirsch, A. Fractioning HiPco and CoMoCAT SWCNTs via density gradient ultracentrifugation by the aid of a novel perylene bisimide derivative surfactant. *Chemical Communications*, 2643 (2009). (feature article)

Backes, C., Schmidt, C. D., Hauke, F., Böttcher, C. & Hirsch, A. High Population of Individualized SWCNTs through the Adsorption of Water-Soluble Perylenes. *Journal of the American Chemical Society* **131**, 2172–2184 (2009).

Book Chapter

Backes, C., Hirsch, A., "Noncovalent Functionalization of Carbon Nanotubes" in *Chemistry of Nanocarbons* (Eds.: T. Akasaka, F. Wudl, S. Nagase), John Wiley & Sons, **2010**, p. 528ff. (book chapter)

Supervisor's Foreword

Carbon nanotubes represent a family of new synthetic carbon allotropes. They are characterized by unprecedented physical, electronic and mechanical properties. For this reason, an enormous interest arises in developing a number of applications, for example, in molecular electronics or in high performance composite materials. This requires, however, to overcome a number of hurdles. For example, dispersion of carbon nanotubes in solvents is a crucial issue in order to make them available for subsequent processing procedures. One concept to approach this goal is the chemical functionalization of carbon nanotubes. Especially the noncovalent functionalization promoted by the interaction of surfaces active molecules or polymers with the sidewalls of the carbon nanotubes represents an appealing concept, as the π-system and the electronic structure of the tubes remains basically unaffected in this approach.

This scenario represented the background for the goals of the doctoral work of Claudia Backes, namely to develop ground breaking and systematic studies in the field of noncovalent functionalization of single walled carbon nanotubes (SWCNTs). It was intended that she should use, for example, amphiphilic perylenes for the dispersion, but also for the modification and the doping of SWCNTs. Moreover, systematic studies concerning carbon nanotube characterization, separation and visualization, involving modern methods like ultracentrifugation, scanning probe microscopy, fluorescence spectroscopy and Raman spectroscopy should be applied.

Claudia Backes has accomplished a masterpiece of fundamental carbon nanotube research which can be ranked as world class. With her PhD-thesis she has pushed this field a significant step forward. The very nice and groundbreaking results have been published already in 15 articles in outstanding scientific journals such as *Nature Chemistry* and the *Journal of the American Chemical Society*. Claudia Backes was not only enormously creative, she was also able to analyze her scientific results very thoroughly. She structured her insightful results in a very elegant and cogent manner, both in preparation of publications in journals, as well as in her PhD-thesis.

Erlangen, October 2011

Prof. Dr. Andreas Hirsch
Chair of Organic Chemistry II
Friedrich-Alexander University
Erlangen-Nürrnberg

Acknowledgments

I would like to express my gratitude to my supervisor Professor Andreas Hirsch, not only for giving me the opportunity to work in this fascinating area of research in the perfect environment, but also for trusting in my research and its results. With his outstanding expertise and intuition he left me the freedom to approach the numerous questions open-mindedely and thus allowed the content of this thesis to develop almost by itself.

Many thanks should also be dedicated to Frank Hauke for his continual interest and assistance, for encouraging me whenever necessary, for teaching me his systematic way of thinking to tackle scientific problems, for taking me serious as scientist and person, for always having a sympathetic ear and finally for becoming a close friend.

Certainly, this work would not have been possible without the synthetic chemists Cordula Schmidt, Alex Ebel, Torsten Schunk and Karin Rosenlehner who provided me with the foundation, i.e. the beautiful molecules they never got tired of synthesizing. Cordu's name surely has to be placed first in the list, as she synthesized almost all of the perylene bisimide derivatives that became the corner stone of my investigations.

Special thanks are also credited to my collaborators from outside the FAU who greatly contributed with their expertise. In the first place, I would like to thank Wendel Wohlleben from BASF SE for inviting me twice to his laboratory to breathe the fascinating air of (analytical) ultracentrifugation and for the extraordinary fruitful collaboration. This certainly was (and still is) a great experience. I would also like to thank Jonathan N. Coleman from Trinity College Dublin who also gave me the opportunity to visit his facility and who has always been on hand with help and advice.

Furthermore, I would like to acknowledge the former students (Udo Mundloch, Sebastian Etschel, Daniel Malko, Philipp Vecera, and my cousin Cess) who were elaborating some aspects of this thesis within the framework of their Bachelor Theses or practical courses. I also highly appreciate the contribution of Ralf Graupner as XPS expert and his physicist's advice at the early stages of this work.

While working in the ZMP, it was a great pleasure to have many colleagues and friends around who created an enjoyable working atmosphere inside and outside the lab with numerous truly interdisciplinary discussions. Certainly, many persons were responsible for a really great time sometimes with a glass of wine (or two). Thanks to all of you!

On the personal note, I would like to thank my family (especially my parents and brothers), my best friend Jana and my partner in life, Andy, who had to soft-pedal at times, but nonetheless always supported and encouraged me with all the patience that was necessary.

Contents

Abbreviations

a.c.	Alternating current
AFM	Atomic force microscopy
AP	As-received purified
a.u.	Arbitrary units
AUC	Analytical ultracentrifugation
ar	Aryl
BSU	Band sedimentation ultracentrifugation
Cc	Concentrated
cmc	Critical micelle concentration
CNT	Carbon nanotube
CoMoCAT	Cobalt molybdenum catalysis
1D	1-Dimensional
2D	2-Dimensional
DMA	*N*, *N*-dimethylacetamide
DMF	*N*, *N*-dimethylformamide
DGU	Density gradient ultracentrifugation
DOS	Density of states
DTAB	Dodecyl trimethylammonium bromide
F	Fraction
HF	High functionalization degree
HiPco	High pressure carbon monoxide decomposition
HTAB	Hexadecyl trimethylammonium bromide
IR	Infrared
krpm	Kilo rotations per minute
LA	Laser ablation
LDS	Lithium dodecyl sulfate
MF	Medium functionalization degree
MS	Mass spectrometry
MWCNT	Multiwalled carbon nanotube
NMP	*N*-methyl-2-pyrrolidone
nIR	Near infrared

ODCB	*o*-dichlorobenzene
P	Precipitate
PBI	Perylene bisimide
Per	Perylene derivative
PTC	3, 4, 9, 10-perylene tetracarboxylic acid
PTCDA	3, 4, 9, 10-perylene tetracarboxylic acid dianhydride
pyr	Pyrene derivative
PZC	Point of zero charge
RBM	Radial breathing mode
RT	Room temperature
S	Supernatant
SC	Sodium cholate
SDBS	Sodium dodecyl benzene sulfonate
SDC	Sodium deocxycholate
SDS	Sodium dodecyl sulfate
st	Stretching mode (IR spectroscopy)
STDC	Sodium taurodeoxycholate
STM	Scanning tunneling microscopy
SWCNT	Singlewalled carbon nanotube
TM	Tangential modes
TTAB	Tetradecyl trimethylammonium bromide
UV	Ultraviolet
vHs	Van-Hove singularities
vis	Visible
XPS	X-ray photoelectron spectroscopy
δ	Deformation mode (IR spectroscopy)

Chapter 1
Introduction

1.1 The 1D Carbon Allotrope: Structure and Properties

Carbon nanotubes (CNTs) belong to the family of synthetic carbon allotropes and are characterized by a network of sp^2 hybridized carbon atoms. The one dimensional (1D) carbon nanotubes [1, 2] can thus be queued between their zero dimensional relatives fullerenes [3, 4] and the two dimensional (2D) relative graphene [5, 6]. The structure of nanotubes has first been described as helical microtubules of graphitic carbon in 1991 by Iijima who generated the novel material by an arc discharge evaporation process originally designed for the production of fullerenes [1]. Since then, extensive research has shed light into the structure and properties of this highly remarkable carbon allotrope [7–13]. CNTs are theoretically constructed by rolling up a graphene sheet into a cylinder with the hexagonal rings joining seamlessly (Fig. 1.1a) [14]. Commonly, nanotubes are classified as single-walled carbon nanotubes (SWCNTs) consisting of one cylinder and multi-walled carbon nanotubes (MWCNTs) being comprised of an array of cylinders concentrically nested (Fig. 1.1b).

Depending on the way the graphene sheet is rolled up, a huge diversity of SWCNT structures can be constructed differing in length, diameter and roll-up angle which defines the orientation of the hexagonal carbon rings in the honeycomb lattice relative to the axis of the nanotube. The shape of a SWCNT is always a cylinder so that this carbon allotrope can be considered as one dimensional nanostructure due to the long periodical unit.

The structure of a SWCNT is specified by the so-called chiral vector $\underline{C}_h$ which corresponds to a cross section of the nanotube perpendicular to the axis as schematically presented in the unrolled honeycomb lattice in Fig. 1.2. The chiral vector $\underline{C}_h$ can be expressed by the real space unit vectors of the graphene lattice $\underline{a}_1$ and $\underline{a}_2$ and the integer parameters n and m (1.1).

$$\underline{C}_h = n\underline{a}_1 + m\underline{a}_2 \qquad (1.1)$$

C. Backes, *Noncovalent Functionalization of Carbon Nanotubes*, Springer Theses,
DOI: 10.1007/978-3-642-27582-1_1,

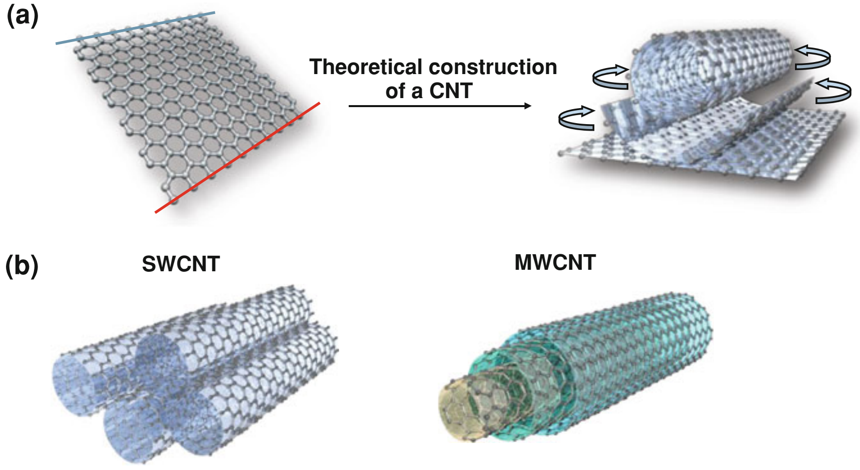

Fig. 1.1 **a** Schematic representation of the theoretical construction of a carbon nanotube by rolling up a graphene sheet. **b** Representation of a single-walled carbon nanotube (SWCNT–*left*) and a multi-walled carbon nanotube (MWCNT–*right*) [15]

Accordingly, the structure of a carbon nanotube is classified by the integer parameters n and m denoted as chiral indices. Figure 1.2 thus exemplarily depicts the construction of a (4,4)-SWCNT with the unit cell represented as blue rectangle. The length of the cylindrical structure is a multiple of the modulus of the translational vector $\underline{T}$, the circumference is defined by the modulus of the chiral vector $\underline{C}_h$. The chiral angle θ is defined as the angle between the chiral vector $\underline{C}_h$ and the unit cell vector $\underline{a}_1$ with values of θ spanning from 0° to 30° due to the hexagonal symmetry of the graphene layer.

The (n, m)-chirality defines the structure of the SWCNT, but contains no information about the so-called helicity of the nanotube. The symmetry of a SWCNT is primarily classified as being chiral or achiral. The mirror image of an achiral SWCNT is super imposable to the original structure, while left- and right-handed species can be distinguished in chiral nanotubes. The majority of SWCNTs is chiral meaning that two enantiomers of a specific (n, m)-SWCNT exist (not considering differences in length). The achiral SWCNTs are limited to chiral angles of 0° (zigzag nanotubes with $\mathrm{m} = 0$) and 30° (armchair SWCNTs with $\mathrm{n} = \mathrm{m}$).

Details on the theoretical calculation of the electronic structure of SWCNTs shall not be discussed within this thesis, as a number of textbooks are concerned with that subject [7, 9–12]. The outcome however, is of tremendous impact and significance, as the density of states of the different (n, m)-SWCNTs can be calculated. This results in the electronic classification of SWCNTs as exhibiting either semiconducting, or metallic character. In other words, the electronic properties of SWCNTs depend on the chiral vector and therefore the way the graphene sheet is rolled up into the cylinder.

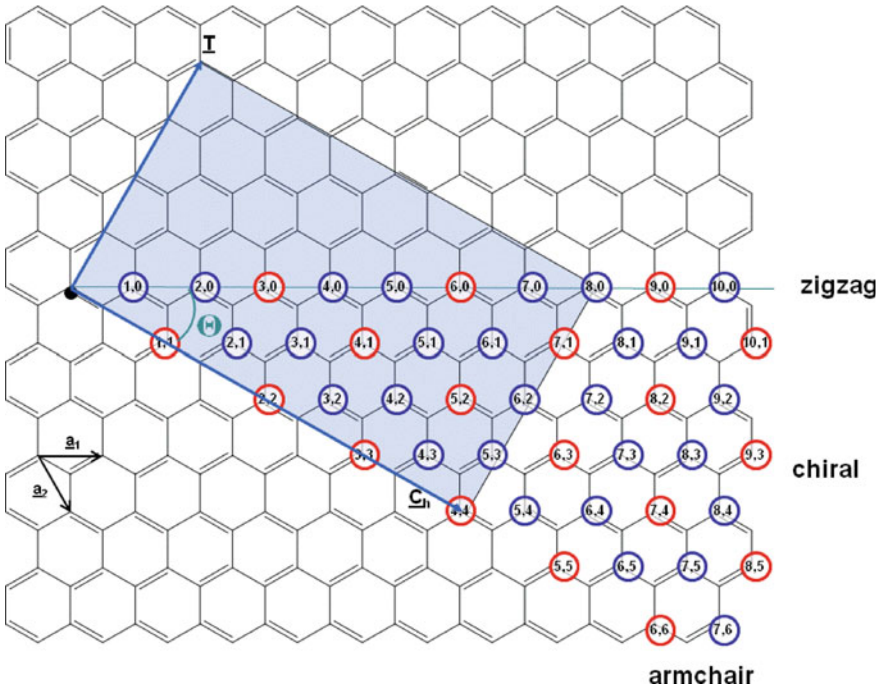

Fig. 1.2 Schematic representation of the unrolled graphene layer of a carbon nanotube with the unit cell vectors $\underline{a}_1$ and $\underline{a}_2$ which define the chiral vector $\underline{C}_h$. The colored rectangle displays the unit cell of the (4,4)-SWCNT. Metallic or quasi-metallic (n, m)-SWCNTs are indicated by the *red* circles, semiconducting species by the *blue* circles, respectively

The electronic structure of a SWCNT can be derived from that of 2D graphene by using periodic boundary conditions: [16] the wave vectors associated with the direction normal to the tube axis become quantized while the wave vectors along the tube axis remain continuous assuming an infinite tube length. Hence, the energy dispersion relations are cross sections of those of 2D graphene. Graphene can be regarded as a zero-energy gap semiconductor with the π and π^*-states being degenerate by symmetry in the K-points. If for a particular (n, m)-nanotube the cutting line passes through a K point, the 1D energy bands have a zero energy gap and therefore are considered as being metallic in first approximation. All metallic CNTs fulfil the equation

$$(\mathrm{n} - \mathrm{m}) = 3\mathrm{q} \tag{1.2}$$

with q being an integer. Thus, all armchair (n, n)-CNTs are metallic and zigzag (n, 0)-CNTs are metallic when n is a multiple of three. This equation also implies that one-third of SWCNTs exhibit metallic character, while two-thirds exhibit semiconducting character, as indicated by the red and blue circles in Fig. 1.2. In addition, the finite curvature of the SWCNT results in the mixing of π/σ bonding

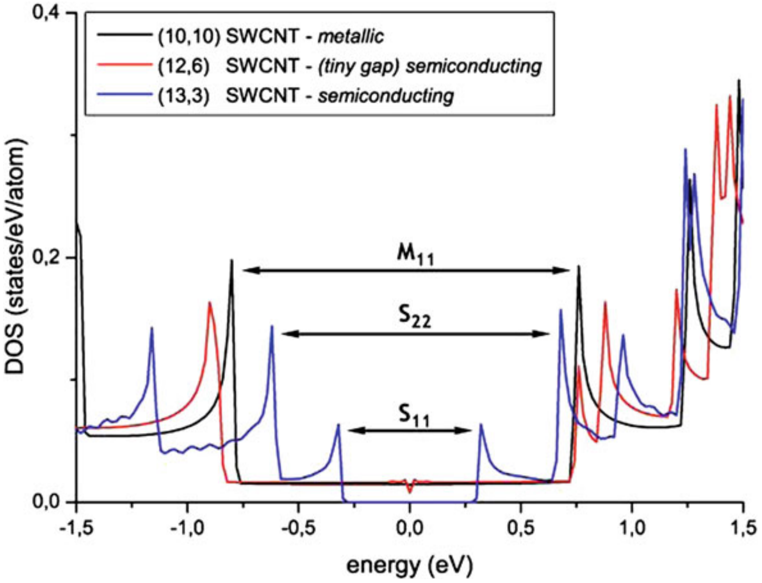

Fig. 1.3 Electronic 1D density of states for a metallic, armchair (10,10)-SWCNT, a quasi-metallic (12,6) SWCNT and a semiconducting (13,3)-SWCNT

and π^*/σ^* anti-bonding states leading to a movement of the graphene band crossing away from the K-point. Thus, small energy gaps in the order of meV are introduced in metallic SWCNTs except for the symmetrical achiral (n, n)- armchair SWCNTs. Therefore, SWCNTs fulfilling Eq. 1.2 are regarded as quasi metallic or tiny-gap semiconductor if n ≠ m.

The characteristic 1D electronic density of states (DOS) of three (n, m)-SWCNTs are displayed in Fig. 1.3 as representatives of metallic armchair (10, 10), quasi metallic (12, 6) and semiconducting SWCNTs (13, 3). The DOS of semiconducting SWCNTs is zero at the Fermi level E_F located at $E = 0$, but non-zero for metallic SWCNTs. Owing to the 1D nature of the nanotubes, the DOS becomes singular by folding the 2D energy bands of the graphene layer into the 1D bands of the SWCNT with an increasing energy separation at decreasing number of energy bands. As a consequence, spikes in the DOS of 1D objects arise (van Hove singularities, vHS) which dominate the optical properties of SWCNTs and are thus of importance for their characterization as will be outlined in Sect. 1.4.

Of equal importance pertaining to semiconducting SWCNTs is the result that their energy gap depends on the reciprocal nanotube diameter, e.g. the band gap increases from larger to smaller diameter SWCNTs, while being independent on the chiral angle.

Apart from their outstanding electronic properties providing the foundation for multiple applications as nanowires, field-effect transistors and electronic devices [8, 17, 18], carbon nanotubes surmount any other compound class in their mechanical properties [11, 13]. The exceptionally high tensile modulus (640 GPa) and tensile strength (≈100 GPa) together with the high aspect ratio (300–1000) make nanotubes an ideal candidate for reinforcing fibers and polymers [19, 20].

However, in order to tap the full potential of nanotubes in electronics, photonics, as sensors or in composite materials, two major obstacles have to be overcome, e.g. separation according to diameter and/or chirality on the one hand and uniform dispersability in a solvent or matrix on the other hand. Responding to a growing interest, progress in the diameter control during carbon nanotube production has been achieved [21]. However, up to now, the as-produced material contains nanotubes of differing lengths, diameters and chiralities, therefore including semiconducting and metallic nanotubes, as well as a varying amount of impurities. This inhomogeneity still forms the bottleneck for nanotube-based technological progress. Furthermore, the strong intertube *van der Waals* interactions of 0.5 eV/μm, which render nanotubes virtually insoluble in common organic solvents and water also constrict any application [22, 23].

Among the efforts to increase processability of this unique material, chemical and especially noncovalent functionalization represents a corner stone, as it is nondestructive meaning it does not alter the intrinsic properties of CNTs. Furthermore, tailoring of the surface properties of carbon nanotubes is accessible, boosting solubility in a variety of solvents and providing the foundation for nanotube sorting, as will be summarized in Sects. 1.2 and 1.3, respectively.

1.2 Solubilization of Single-Walled Carbon Nanotube

Solubilization and dispersion of SWCNTs is addressed by noncovalent functionalization (among others), e.g. modification of the nanotube surface properties by adsorption of either commercially available detergents or designed molecules. In the following, the term dispersion refers to homogenously distributed nanotubes in a colloidal state also including small bundles, while solution implies that the nanotubes appear individualized, e.g. the carbon nanotube bundles are exfoliated.

The most widespread noncovalent functionalization method to obtain nanotubes dispersed and dissolved in aqueous media is their encapsulation in surfactant micelles. In general, surfactants can be described as molecules with a hydrophilic region usually referred to as polar head group and a hydrophobic region denoted as tail. Due to this amphiphilicity they tend to adsorb at interfaces and self-organize into supramolecular structures.

Three adsorption mechanisms of surfactants onto SWCNTs have been proposed as depicted by Fig. 1.4. In analogy to the epitaxial adsorption of surfactants on graphite, specific self-alignment as cylindrical micelles (Fig. 1.4a) or hemimicelles (Fig. 1.4b) has been suggested [24, 25]. More recently, structureless random adsorption has been favored [26]. In this case, no preferred arrangement of the head and tail groups stabilizes the dispersion/solution (Fig. 1.4c).

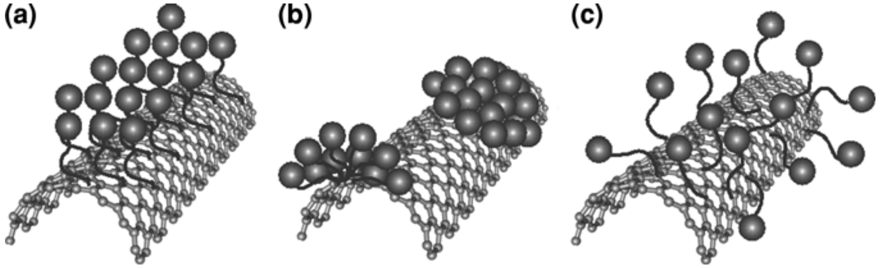

Fig. 1.4 Adsorption of surfactants: **a** SWCNTs encapsulated in a cylindrical micelle by an aligned adsorption of the amphiphiles, **b** hemimicellar adsorption, (**c**) random adsorption. (Reprinted with permission from Wiley VCH: [192])

According to the unzippering mechanism proposed by Strano et al. [27], nanotubes are isolated from bundles by ultrasonication in the presence of a surfactant (Fig. 1.5). During the first step, the energy input by ultrasonication provides high local sheer forces, resulting in dangling ends in the nanotube bundles (Fig. 1.5b) which become adsorption sites for surfactants preventing the loosened tubes from reaggregation (Fig. 1.5c). Due to the movement of the partly individualized nanotubes relative to the bundle, the surfactant continuously progresses along the nanotube length resulting in the isolation of the individual tube (Fig. 1.5d). Hereby, an equilibrium is established between free individuals and bundled aggregates limiting the concentration of stably individualized SWCNTs.

The exfoliation of SWCNTs is specifically important for their characterization. A cornerstone in nanotube characterization has been laid by O'Connell et al. who have first reported on the observation of nanotube fluorescence across the bandgap of semiconducting SWCNTs [24]. This subject will be further discussed in Sect. 1.4.2.

Surfactants are usually classified according to the nature of the head charge, e.g. anionic, cationic, non-ionic and zwitterionic. A variety of nanotube surfactants (Scheme 1.1) has been investigated including the most common detergents sodium dodecyl benzene sulfonate (SDBS) [28–32], sodium dodecyl sulfate (SDS) [24, 25, 28, 32–34], lithium dodecyl sulfate (LDS) [35], the bile salts sodium deoxycholate (SDC) [29, 31, 32, 36, 37], sodium taurodeoxycholate (STDC)[29] and sodium cholate (SC)[29, 31, 32, 36, 37] as representatives of anionic surfactants, dodecyltrimethylammonium bromide (DTAB), tetradecyl trimethyl ammonium bromide (TTAP), hexadecyltrimethylammonium bromide (HTAB) among cationic surfactants [38] and TritonX-100 [28, 29], Tween-20, Tween-40 and Tween-60 as non-ionic surfactants [38].

As briefly summarized in the section above, the results concerning the adsorption mechanism of detergents on the SWCNT scaffold partly appear contradictionary, nicely demonstrating that the supramolecular arrangement on the SWCNTs and thus the resulting dispersion efficiency and stability is highly sensitive to the environment and the dispersion parameters, e.g. ultrasonication

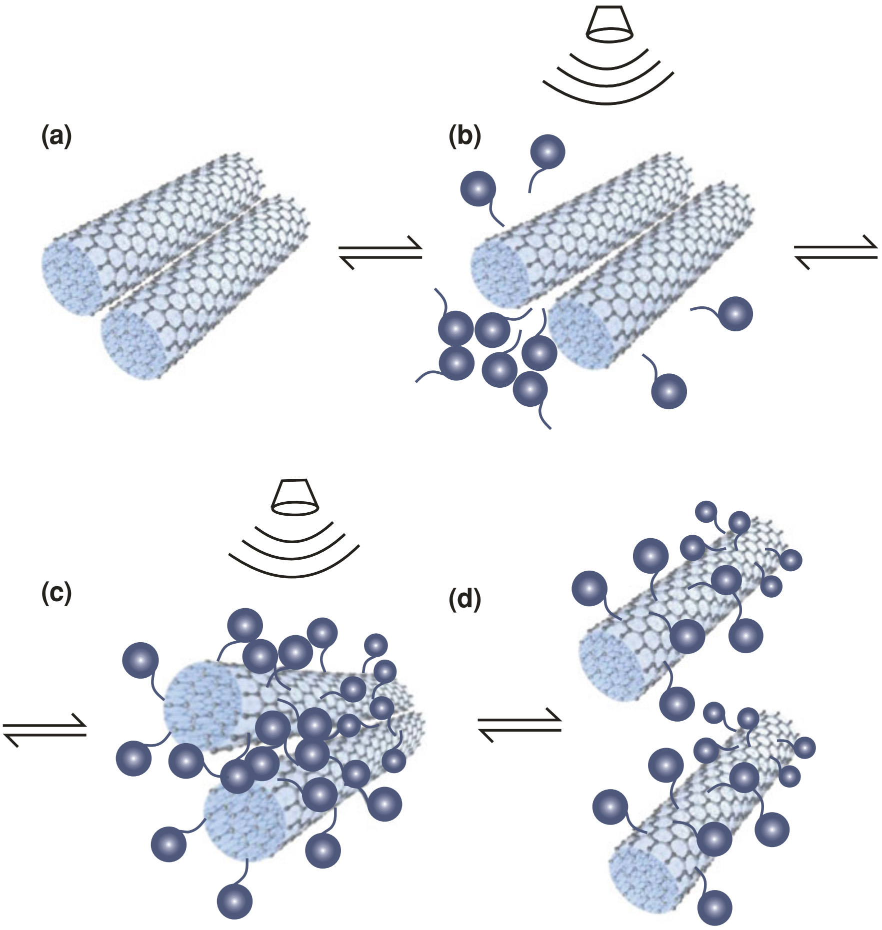

Fig. 1.5 Mechanism of nanotube exfoliation from bundles with the aid of a surfactant and ultrasonication according to the unzippering mechanism [27]. (Reprinted with permission from Wiley VCH: [192])

power and time [39], centrifugation or precipitation conditions, temperature, presence of salts etc. Furthermore, it has been shown that the concentration of the nanotube [40], as well as the detergent [41, 42] has a tremendous impact on both, the quality of the dispersion and the general dispersion behavior. The composition of the pristine nanotube material (amount of impurities, diameter distribution, etc.) constitutes a further impediment towards comparability [39].

In a systematic study, the effects of purification, sonication time and surfactant concentration on the dispersability of SWCNTs in an aqueous solution of SDBS have been investigated [30]. It has been revealed that the purification method has an impact on the surface properties of the nanotubes, e.g. the point of zero charge (PZC). However, the introduced positive or negative charges on the nanotubes,

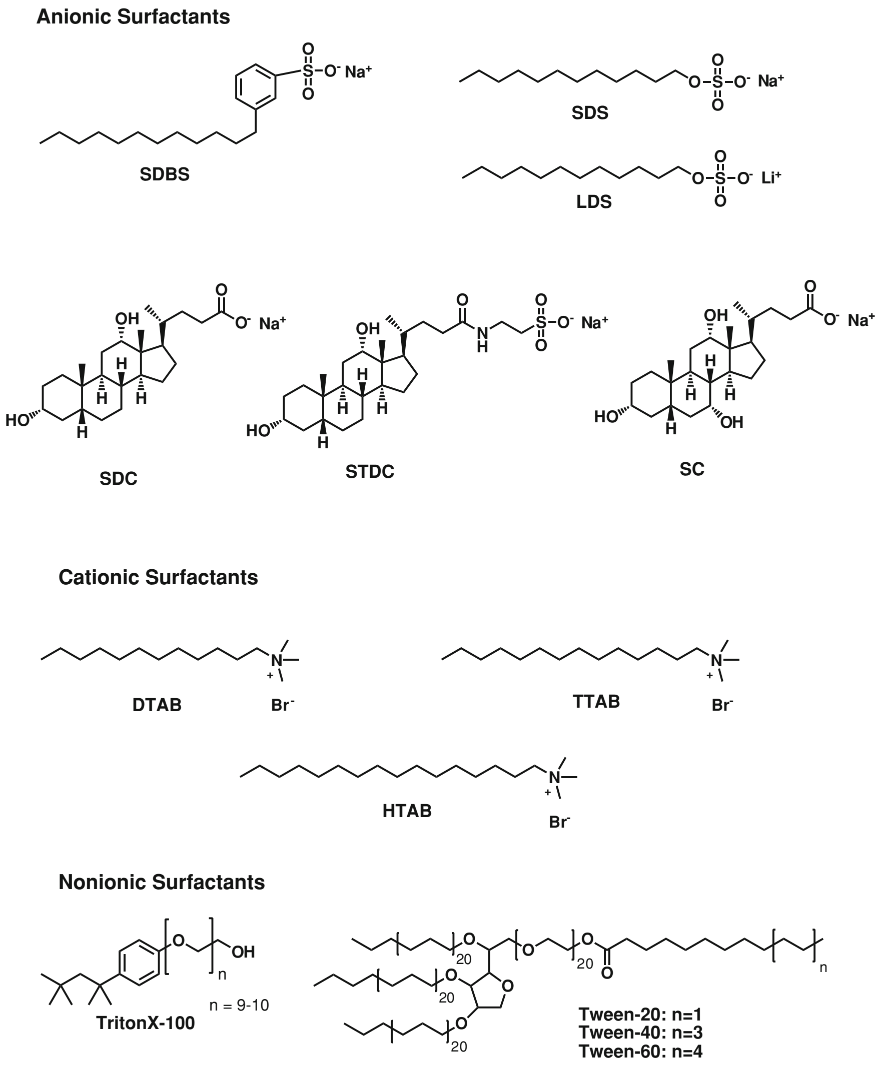

Scheme 1.1 Structures of the most common SWCNT surfactants

being dependent on the pH, only influence the interaction with the negatively charged SDBS molecules at pH values far from the PZC, indicating that the nanotube-detergent interactions are hydrophobic in nature. Further adsorption studies have shown that, at saturation, the detergent molecules cover the nanotubes as monolayer with the tails oriented vertically on the surface (tails on configuration) [30]. This indicates that the nanotubes are rather dispersed by adsorption of the SDBS molecules than by enclosing the SWCNTs in cylindrical micelles. It has also been pointed out that the sonication time plays a key role in nanotube

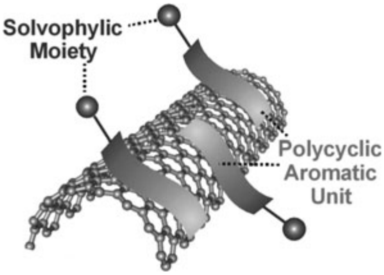

Fig. 1.6 Concept of nanotube dispersion by polycyclic aromatic compounds equipped with a solvophylic moiety. (Reprinted with permission from Wiley VCH: [192])

dispersion and dissolution, as dispersion remained ineffective without the aid of sonication. Finally, the investigations have unveiled that nanotubes can be dispersed in an aqueous solution of SDBS below the critical micelle concentration (cmc) of SDBS further underlining that the formation of micelles is not a requirement for dispersability. A dispersion efficiency maximum is reached at SDBS concentrations [SDBS] = 2.5 mM (0.87 wt%) under the experimental conditions chosen by the authors.

Additionally to the readily available detergents, bifunctional polycyclic aromatic compounds are also excellent candidates for the dispersion/dissolution of nanotubes. In principle, a strong and specific interaction with the nanotube can be ensured via π-π-stacking which is, in many cases, favorable over the non-specific hydrophobic interaction being exploited by detergents. Water solubility is provided by solvophylic moieties covalently attached to the aromatic backbone of the dispersant (Fig. 1.6).

Pyrene derivatives, especially trimethyl-(2-oxo-2-pyrene-1-yl-ethyl)-ammonium bromide **Pyrene1** are prominent examples nicely underlining the effectiveness of this concept. It has been demonstrated that **Pyrene1** is capable of dispersing and individualizing both as-produced and purified SWCNTs under mild experimental conditions [43, 44]. Since it has been found that **Pyrene1** is an excellent nanotube solubilizer, the pyrene moiety has widely been applied as noncovalent anchoring group, for instance, for fullerenes, proteins, porphyrins and metal nanoparticles (ref. [45] and references therein).

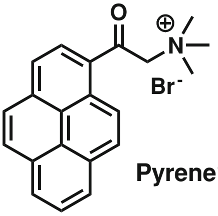

Pyrene1

Additionally to the pyrene moiety, other anchoring groups such as naphthalene, [46] or porphyrins have been used [47, 48] to induce dispersion in aqueous media and to allow the construction of nanotube-based donor–acceptor hybrids [48–50].

Until recently, only limited research has thus far focused on the dispersion of nanotubes in organic solvents compared to water-based systems. Since carbon nanotubes are hydrophobic, they are expected to be wetted by organic solvents as opposed to aqueous media. However, pristine CNTs are colloidally dispersed only in a limited number of solvents, e.g. *o*-dichlorobenzene (ODCB)[51–55], *N*-methyl-2-pyrrolidone (NMP)[56–60], *N, N*-dimethylformamide (DMF)[56–61] and *N,N*-dimethylacetamide (DMA) [57, 60]. Even though dispersion in such solvents is convenient, it is important to note that the stability of the dispersion is usually poor being accompanied by the formation of nanotube aggregates within hours or days.

Within the past years, Coleman and co-workers gained remarkable insights in the dispersion of nanotubes in solvents in the absence of any dispersant [62]. Considering nanotubes as large solute molecules, standard solution theory can be applied. Thus, SWCNTs would be soluble when their enthalpy of mixing $\Delta\bar{H}_{\mathrm{mix}}$ is negative. Since the enthalpy of mixing can also be expressed by the Hildebrand solubility parameters (Hildebrand-Scatchard expression), it can be concluded that dispersion is favored when the solubility parameter of the solvent matches that of the SWCNTs (the solute). The Hildebrand solubility parameter, however, only takes into account the dispersive contributions and not the polar and hydrogen bonding interactions which are manifested in the Hansen solubility parameters. The unambiguous consequence is that the energetic cost of dispersion is minimized when all three Hansen parameters of the solvent match those of the solute. Commonly, in solubility theory, a dispersion can be considered a solution when the free energy of mixing $\Delta\bar{G}_{\mathrm{mix}}$ is negative. For many systems, a large entropy of mixing $\Delta\bar{S}_{\mathrm{mix}}$ which contributes to the free energy of mixing results in a negative free energy. Since nanotubes are large and rigid, the entropy of mixing is comparatively small so that the enthalpy of mixing $\Delta\bar{H}_{\mathrm{mix}}$ is the crucial factor to determine the solubility. Inspired by the finding that SWCNTs can be debundled by dilution in NMP [63], this solvent has been chosen for further investigations and the development of a detailed thermodynamic analysis [64] paving the way towards true solutions of SWCNTs in rather common solvents. An extensive solvent screening then allowed estimating the Hansen solubility parameters of pristine SWCNTs and further developing the solubility model [65]. Based on these theories, new solvents for nanotubes have been proposed and investigated [66]. Significantly, *N*-cyclohexyl pyrrolidone and 1-benzyl-2-pyrrolidinone have been described as highly promising solvents with dispersion and exfoliation rates approaching those of the common detergent SDBS. However, it has been pointed out by the authors, that the model still remains imperfect, as some solvents with the correct Hansen parameters are not capable of dispersing SWCNTs which is in marked contrast to solubility theory so that a deeper understanding of solvent-nanotube interactions still needs to be created.

Similarly to the concept of dispersion of nanotubes in aqueous media by the addition of dispersants, the dispersability of nanotubes in organic solvents can also be increased by designed additives. However, one main driving force for dispersion in aqueous media, namely the hydrophobic effect, is not exploited in this case. Nonetheless, some examples exist, for example porphyrin derivatives which have also shown to promote successful dispersion of nanotubes in nonaqueous media [67–74].

Additionally to the monomeric dispersion additives described above, natural [75–81] or synthetic polymers [19, 45, 82–85] are commonly applied for the dispersion of SWCNTs in aqueous and organic media. However, the use of polymeric materials is associated with one major drawback, as the complete post-process removal of the dispersant is not possible so that this topic is not further discussed within this thesis.

As has already been mentioned, SWCNT dispersion and solubilization does not only overcome one of the major hurdles in nanotube research, but it also provides the foundation to address the next step towards SWCNT-based technology, e.g. efficient SWCNT sorting according to diameter and/or chirality. Since exfoliation and individualization of nanotubes is a pre-condition for any separation approach, the success of the sorting technology ultimately depends on the quality of the dispersion.

1.3 Post-Production SWCNT Separation

1.3.1 Overview of Sorting Approaches

Even though the extraordinary potential of carbon nanotubes as new super materials especially in CNT-based electronics had been recognized soon after their discovery, integration of millions of nanotubes in functional circuits can thus far be merely considered a vision, as nanotube samples with defined electronic classification, or preferably single chirality with defined length are a prerequisite. Despite recent progresses in the field of controlled nanotube production [21], it is reasonable that this goal may not be achieved by controlled synthesis alone by considering the following aspects: SWCNTs are grown from metal catalyst particles widely defining their diameter. However, the futility of the exact chirality control by predefined catalyst particle size during synthesis can be imagined by recognizing that the diameter difference between a (10,10)-metallic and a (9,11)-semiconducting SWCNTs is merely 0.03 Å. Furthermore, the high temperatures during nanotube production presumably induce thermal vibrations allowing variations in the SWCNT diameters even for identically sized catalyst particles. Thus, the development of post-synthetic separation techniques such as electrophoresis, chromatography, density gradient ultracentrifugation and selective interaction is deemed necessary and has received considerable attention in nanotube research [86–88].

Among electrophoretic techniques, alternating current (a.c.) dielectrophoresis holds most promise, as nanotube separation by electronic type may be accomplished. It has been demonstrated that metallic nanotubes are selectively deposited between the electrodes in an a.c. field, when a nanotube dispersion in an aqueous solution of sodium dodecyl sulfate is applied [89]. Upon subjecting nanotubes to an external electric field, a dipole moment is induced resulting in a translational motion along the field gradient which depends both on the dielectric constant of the nanotubes ε_p and solvent medium ε_S. The static dielectric constant for semiconducting HiPco nanotubes has been calculated to be lower than 5, while that of metallic SWCNTs has been estimated to be around 1000 [90]. Since the dielectric constant of the solvent, in this case an aqueous solution of sodium dodecyl sulfate, is around 80, semiconducting nanotubes exhibit a negative dielectrophoretic force, e.g. they move towards the low electric field region, while the elctrophoretic force in the case of metallic nanotubes is positive so that they move towards the high field region. By investigating the deposited material by incident-light dark-field microscopy it has been shown that the Rayleigh scattered light is polarized perpendicular to the electrode revealing the alignment of the nanotubes.

Even though dielectrophoretic separation is capable of sorting SWCNTs by electronic properties, the method suffers from the disadvantage of limited throughput. Furthermore, the fact that SWCNTs are deposited simultaneously to the separation strongly constrains the flexibility. Nonetheless, dielectric spectroscopy on SWCNT suspensions allows rapid and accurate determination of both the dielectric properties of the surfactant encapsulated SWCNTs, as well as the proportions of metallic and semiconducting nanotubes [91]. Several attempts have focused on upscaling the original separation setup by using larger electrodes [92] or making use of dielectrophoretic field flow-fractionation [93]. However, electrophoresis will certainly not fulfill the criteria of nanotube separation in bulk quantities.

Chromatographic techniques are well established in chemistry and biology to separate materials on the molecular scale. Thus, it is not surprising that evaluating the suitability of chromatographic techniques for the separation and purification of nanotubes has commenced soon after their discovery. However, attempts seemed to be little fruitful until the first chromatography-based separation has been reported in 2003 [76]. The approach relies on the supramolecular aggregation of DNA that enables SWCNT sorting by ion exchange chromatography. When nanotubes are wrapped with an appropriate single-stranded DNA, the electrostatics of the SWCNT-DNA hybrid in the ion exchange column is dependent on the nanotube diameter or the electronic properties [76]. The optical properties of the separated SWCNTs in the respective fractions are so striking that they can be observed as distinguishable colors by the naked eye. As the initial results have been convoluted by differences in lengths, an improved sorting with the aid of size exclusion chromatography has been subsequently developed [77]. In a groundbreaking study, it has recently been demonstrated that single chirality sorting of 12 different (n,m)-SWCNTs can be achieved by utilizing the appropriate DNA sequence [94]. The major obstacle for this methodology, however, is the utilization of designed DNA sequences on the one hand and the low throughput similarly to electrophoretic sorting on the other hand. Furthermore, DNA cannot be removed from the SWCNT sidewall after separation, as it wraps around the SWCNT scaffold due to its polymeric nature. Finally, the majority of work has been carried out with SWCNTs of diameters smaller than 1.2 nm so that the proof of widespread applicability of this technique is still lacking.

In a different approach, it has been revealed that surfactant encapsulated semiconducting SWCNTs exhibit an enhanced adsorption towards agarose gel [95]. Thus, metallic SWCNTs could be squeezed from a frozen block of agarose gel where a mixture of SWCNTs has initially been loaded [96]. This methodology certainly holds great potential, as it appears to be easily scalable. However, in order to further improve sorting efficiencies and separation yields, a deeper understanding in the underlying interactions will be necessary.

In the following sections, the two remaining separation techniques based on noncovalent interactions, e.g. density gradient ultracentrifugation and selective dispersion shall be discussed in-depth, as they hold most promise and are directly related to the subject of this thesis.

1.3.2 Density Gradient Ultracentrifugation

Density gradient ultracentrifugation (DGU) in general exploits subtle differences in the buoyant density of the material to be separated. In principle, the sample is loaded into an aqueous solution with a known density gradient established by a gradient medium such as iodixanol, nycodenz or sucrose. Upon applying a centrifugal force, the species travel towards their respective isopycnic points, e.g. the position where their density is equal to that of the gradient. The spatially separated bands can then be fractionated.

If differences in the buoyant density were merely related to the diameter of the nanotube, larger diameter SWCNTs would have lower densities than smaller diameter nanotubes. However, as described by a hydrodynamic model [97], the thickness and hydration of the surfactant coating, as well as the eventual filling of the nanotubes with water [98], strongly alters the buoyant density. The choice of the surfactant is a crucial aspect for the nanotube sorting criteria by DGU. When a surfactant is chosen which uniformly coats all nanotubes equally, the sorting is related to the diameter. In this case, the density increases with increasing diameter (Fig. 1.7). If nanotubes are dispersed in a surfactant, or a combination of surfactants that exhibit preferences for some (n, m)-species, separation by properties beyond geometrical aspects, e.g. sorting by electronic structure may be achieved.

In a first report, enrichment of DNA-wrapped HiPco [99] and CoMoCAT [100] SWCNTs by diameter has been described. [101] Further works focusing on SWCNTs dispersed in conventional detergent solutions have demonstrated the versatility of the DGU approach [102–112]. Multiple possibilities for sorting of CoMoCAT, laser ablation and arc discharge SWCNTs according to diameter or electronic properties exist up to now, so that merely a few shall be summarized here. For example, sodium cholate encapsulated CoMoCAT nanotubes can be sorted by diameter as evidenced by the evolution of visibly colored bands [102]. Due to the high optical purity of the fractions, investigations concerning the photoluminescence quantum yields could be carried out revealing that the quantum yields exceed 1 % which is by a factor of 5 higher than previously reported for aqueous nanotube dispersions [103, 104].

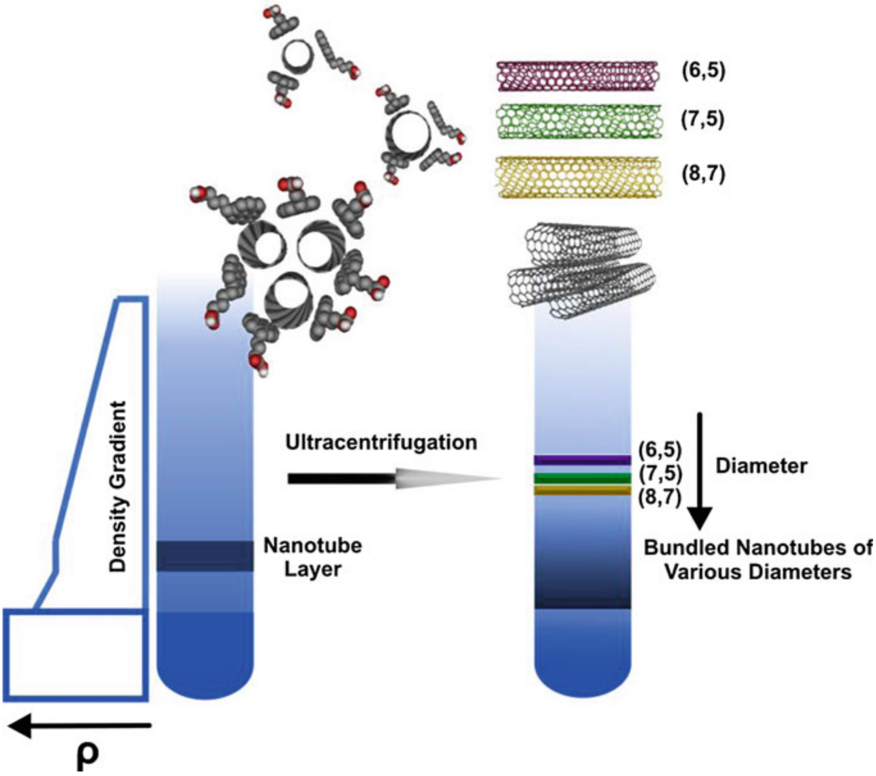

Fig. 1.7 Concept of density gradient ultracentrifugation of SWCNTs. (**a**) Prior to ultracentrifugation surfactant encapsulated nanotubes are injected into an approximately linear density gradient. In the centrifugal field, the nanotubes move to their respective isopycnic points in the centrifuge vial resulting in their separation according to diameter (or electronic properties). (Reprinted with permission from Wiley VCH: [192])

Electronic type specific separation has been achieved by the use of surfactant mixtures of SC and SDS. Most remarkably the position of the metallic and semiconducting fractions, respectively can be tailored by changing the ratio of the two surfactants, e.g. semiconducting nanotubes have a lower density when sodium cholate is the main surfactant [102, 113], while metallic nanotubes show a lower density with SDS as main surfactant and SC as co-surfactant [105, 109, 110, 114, 115]. The metallic fractions have been applied to the preparation of colored semitransparent conductive coatings with colors varying between cyan, magenta and yellow, depending on the composition of the starting material [105, 109, 110, 114, 115]. The semiconducting counterparts allowed the fabrication of thin film nanotube transistors [113, 116, 117]. Furthermore an assignment of the (*n*,*m*) indices is possible by the use of an aberration corrected transmission electron microscopic study [109].

As has been mentioned above, the sorting of SWCNTs according to their electronic type in DGU has been attributed to inequivalent binding of two surfactants as a function of nanotube polarizability and therefore their electronic properties. This principle has been confirmed by electronic type specific sorting of narrowly distributed (*n*, *m*) SWCNTs by iterative centrifugation steps in a SDS-SC surfactant mixture without the aid of a density gradient [106]. However, an adsorption model that accounts for the different surfactant arrangement on metallic and semiconducting SWCNTs has not yet been proposed. Nonetheless, progress towards understanding the role of co-surfactants in DGU based separations has recently been achieved [118]. Diameter sorting of SWCNTs produced by the alcohol catalytic chemical vapor deposition [119] has been improved by a modified co-surfactant DGU, where SWCNTs were initially dispersed in SDC and loaded into a gradient containing SDS. The refined separation resulted in the formation of a full rainbow of colored layers after DGU. It has been attributed to the co-adsorption of SDS to the SWCNT surface which is already partly occupied by SDC. As the packing density of SDC on the nanotube scaffold presumably varies with the diameter of the SWCNTs, the co-adsorption enhances the variation in the buoyant density as a function of tube diameter. Even though this explanation is highly reasonable, the investigation by alternative characterization methods is deemed necessary. Furthermore, the model does not account for differences in the buoyant density in SDS-SC co-surfactant DGU for sorting according to electronic type.

The density gradient medium commonly chosen for SWCNT-DGU is iodixanol which has the disadvantage of being equipped with iodine atoms potentially acting as electron acceptors. Furthermore, iodixanol is an expensive reagent and a rather large molecule causing problems when removing the gradient medium from the nanotube sample. Consequently, other gradient media deserve some attention. Recently, it has been demonstrated that electronic-type sorting also occurs in sucrose as gradient medium when temperature and surfactant concentration is adjusted [108].

Even though significant progress in DGU-based separations has been achieved, the sorting of the commonly used HiPco SWCNTs has shown to be difficult. The major challenge in (*n*, *m*)-sorting of HiPco SWCNTs is related to the presence of multiple species that differ only slightly in diameter and have thus nearly equal buoyant densities. Sorting according to electronic type without modification of the standard procedures has also been problematic, but has been overcome by the use of a three component surfactant mixture comprised of SDC, SC and SDS [120]. As HiPco SWCNTs can conveniently be characterized by Raman spectroscopy (as will be outlined in Sect. 1.4.3), the improved sorting technique enabled the first bulk characterization of the separated material by Raman spectroscopy. Recently, two significant variations of the commonly used DGU procedure have been reported which are potentially capable of overcoming the obstacle of the separation of HiPco SWCNTs by (*n*, *m*)-type. One approach exploits the higher packing density of SDS on the nanotubes with increasing electrolyte concentration [111, 121]. For this purpose, varying amounts of NaCl have been added prior to DGU which resulted in the separation of HiPco SWCNTs according to their electronic type, as SDS presumably preferentially adsorbs on metallic SWCNTs [122]. The second approach utilizes a nonlinear density gradient directly addressing the problem of isolating specific chiralities in the regime of diverse chiralities and similar diameters [123]. The successful improvement of the DGU sorting performance relied on the use of carefully chosen nonlinear gradients resulting in spatially spreading the bands of interest. Experimental conditions have hereby been optimized by the construction of a device capable of measuring the SWCNT fluorescence in the centrifugation vial without the need for fractionation. Thus, highly polydisperse HiPco SWCNT samples have successfully been enriched in 10 different (*n*, *m*)-species. It also enabled the SWCNT separation according to helicity, e.g. left and right handed species of the same chirality. The sorting according to helicity has previously been observed for CoMoCAT and arc discharge SWCNTs with the aid of SC as chiral surfactant in a linear gradient, even though with lower performance and flexibility with respect to the (*n*, *m*) chirality [124].

Finally, it is worthwhile mentioning that DGU on functionalized SWCNTs has revealed that the density of the covalently functionalized nanotubes is altered allowing separation of functionalized from nonfunctionalized SWCNTs which is an important step for precise reaction control [125]. Length sorting of nanotubes in DGU has also been reported by exploiting the transient motion regime, as opposed to the equilibrium regime which is approached for diameter and electronic-type sorting [126, 127].

Due to the combination of comparatively low cost, scalability, easy operability and especially flexibility with respect to the SWCNT pristine material and sorting criteria, the DGU approach has evolved to the most commonly used technique among researchers to separate as-grown SWCNTs to satisfy their needs in extensively probing and utilizing the properties of this highly potent material. However, the major drawback of DGU is still the low yield which can be traced back to insufficient exfoliation and individualization efficiencies of commercially available surfactants. Another critical issue is related to the deeper understanding of the supramolecular arrangement of the dispersants on the SWCNT surface which will hinge on the ability to tune the efficiency of sorting.

1.3.3 Selective Dispersion

Additionally to the design of separation techniques, focus has been laid on the exploration of selective interaction of various molecules with SWCNTs according to electronic type, diameter and/or chirality. Most frequently, as differences between various (*n*, *m*)-SWCNTs can be amplified by selective interaction they are used to aid the separation process. However, selective interaction does not necessarily result in enrichment of certain nanotube species without the additional use of the well established separation techniques described above—a scenario that would be considered as selective dispersion. Since the sorting techniques rely on special equipment and are often characterized by a low throughput, especially in the cases of electrophoresis and chromatography, the ideal separation scenario would indeed involve selective dispersion. The sparingly known examples shall be summarized in the following.

Selective interaction of SWCNTs produced by different techniques with fluorene based polymers has been extensively investigated [128–131]. Hereby, different polymers have been shown to discriminate between nanotube species either by diameter or chiral angle. Upon dispersion of the nanotubes in toluene/ polymer solutions, significant alterations of the nanotube photoluminescence features have been observed reflecting selective interaction depending on the polymer structure. Based on the optical properties of the nanotube dispersions, it has been concluded that PFO (poly(9,9-dioctylfluorenyl-2,7-diyl) [128–131], and PFH-A (poly[(9,9-dihexylfluorenyl-2,7-diyl)-*co*-(9,19-anthracene)])[129] preferentially individualize SWCNTs with high chiral angle (>24.5°), while PFO-BT (poly[9,9-dioctylfluorenyl-2,7-diyl)-co-1,4-benzo-{2,1'-3}-thiadiazole)])[128, 129, 131] exhibits diameter selective exfoliation in the range of 1.02–1.06 nm.

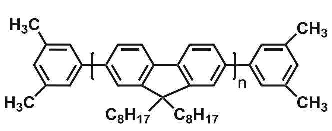

PFO

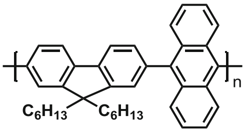

PFH-A

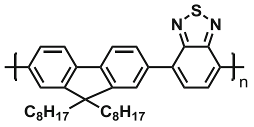

PFO-BT

However, the selective interaction is dependent on the solvent used for the dispersion. It has furthermore been revealed that overall solubilization follows the opposite trend to selective interaction, as more flexible conformations of the polymers allow more nanotubes to be dispersed, while at the same time reducing the selectivity [131]. Additionally, PFO has been used as extracting agent for semiconducting SWCNTs in toluene assisted by ultracentrifugation allowing the fabrication of improved nanotube based field-effect transistors (FET) [132].

Among biomolecules, a variety of additives have been suggested to promote selective interactions with specific SWCNTs. For example, SWCNTs can be threaded by large-ring cyclodextrins providing water solubility on the one hand and partial discrimination with respect to diameter on the other hand [133]. In a similar approach, diameter sorting has been achieved by reversible cyclization of designed peptides [134]. Artificial peptides containing thiol groups on the N and C terminus are capable of solubilizing and encircling SWCNTs within a certain diameter range (depending on the size of the peptide) by controlled formation of disulfide bonds with the advantage of avoiding dissociation of the peptide by the introduction of a covalent bond. Furthermore, individually suspended SWCNTs in aqueous media by adsorption of phosphatidylcholine are enriched in smaller diameter nanotubes [135].

Selective noncovalent functionalization of semiconducting nanotubes has been realized by porphyrin chemistry involving 5,10,15,20-tetrakis(hexadecyloxyphenyl)-21*H*, 23*H*-porphyrin (THPP) [136]. Upon redispersing noncovalently functionalized SWCNTs in THF, it has been shown that the suspended nanotubes are enriched in semiconducting species, while the precipitate is enchriched in metallic SWCNTs after repeated extractions.

Recently, the interaction of the common redox cofactor flavin mononucleotide with SWCNTs has been investigated [137, 138]. Due to cooperative hydrogen bonding between adjacent flavin moieties adsorbed on the SWCNT via π-π-stacking interaction, a helical ribbon organizes around the nanotube backbone, as has been demonstrated by high resolution transmission electron microscopy. Most interestingly, a strong chirality dependency in the interaction has been unveiled by replacing the flavin dispersant with SDBS. This strongly selective interaction was exploited for the enrichment of the (8,6) nanotubes (85 % enrichment value). For this purpose, an appropriate amount of SDBS was added to nanotubes dispersed in a solution of flavin mononucleotide to yield replacement of the flavin moieties on all chiralities except for the (8,6) nanotube. Since it has previously been reported that SDS suspended SWCNTs can be precipitated out of solution by addition of NaCl [139], all nanotubes being enclosed in SDBS micelles could be flocculated by the addition of NaCl to yield a nanotube sample highly enriched in a single chirality to remain in suspension.

Another approach to achieve diameter selective enrichment of SWCNTs is presented in the concept of selective dispersion of the nanotube material by tweezer-shaped molecules consisting of an anchor moiety shaped like a folded ribbon to ensure diameter dependence (Fig. 1.8). To allow the dispersion of the SWCNTs (commonly in water), the tweezer should also be equipped with solvophyilc moieties, either on the tweezer branches (Fig. 1.8a), or on the rigid bridging unit (Fig. 1.8b).

In principle, a rigid unit bridging two aromatic anchor groups such as pentacene (**Tweezer 2**) [140] or dihydronaphthopentaphene (**Tweezer 3**)[141] results in the formation of tweezer-type molecules capable of selectively interacting with the SWCNT scaffold. Responding to a growing interest, the experimental results have furthermore been supported by density functional theory calculations [142]. The nanotweezer principle has been expanded to the extraction of optically pure SWCNTs with the aid of chiral diporphyrins (**Tweezer 1**) [143–145]. Thus, left and right-handed mirror images of chiral nanotubes can be separated yielding nanotube dispersions being distinguishable by circular dichroism after removal of the chiral extracting agents. Variation of the tweezer pattern recently resulted in a simultaneous discrimination of handedness and diameter enabling the enrichment of a single enantiomer of the (6,5)-SWCNT [146].

1.4 Characterization of Carbon Nanotubes

In addition to the development of dispersion and separation scenarios, researchers have been challenged by the search for reliable SWCNT characterization techniques enabling the detailed investigation of pristine and processed nanotube

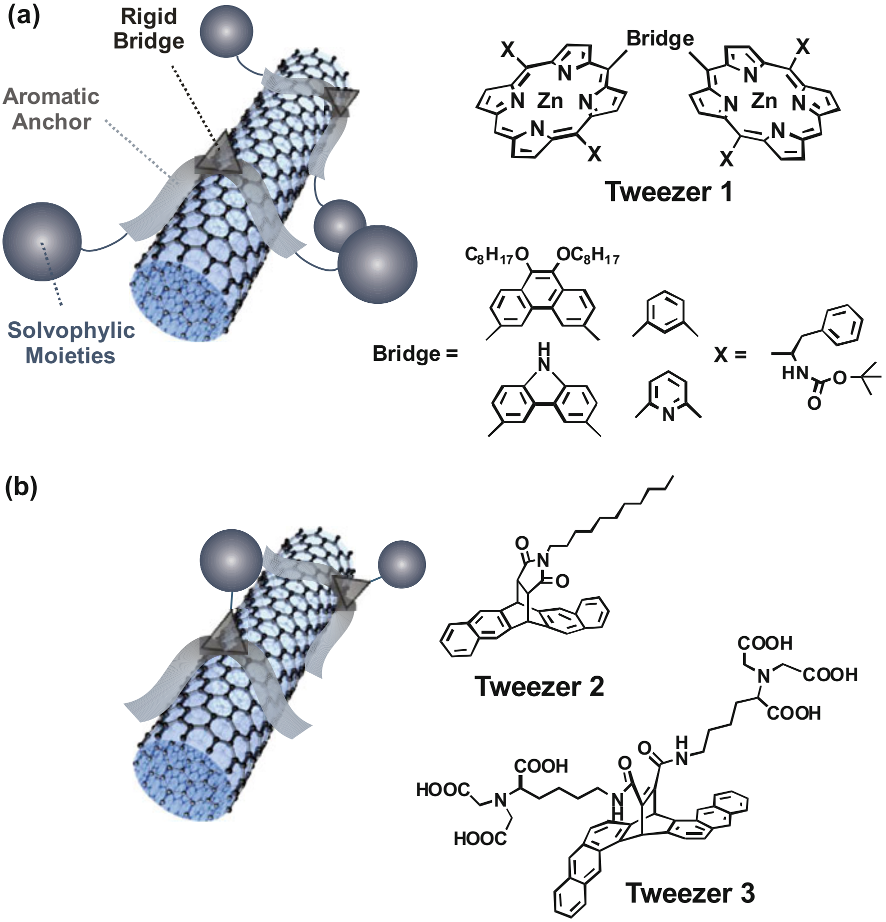

Fig. 1.8 Schematic representation of the selective dispersion by designed nanotweezer molecules equipped with aromatic anchor groups bridged by a rigid unit

samples. Some of the most important characterization techniques shall be summarized in the following.

1.4.1 Absorption Spectroscopy

UV/Vis/nIR absorption spectroscopy has proven to be a powerful tool in SWCNT characterization, as a high information density related to the physical and electronic properties of the SWCNT sample is accessible by a readily available and inexpensive technique. In a first approximation, the optical transitions between the

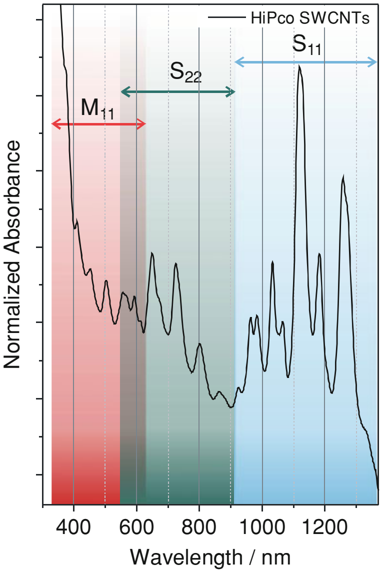

Fig. 1.9 Typical UV/Vis/nIR absorption spectrum of HiPco SWCNT dispersed in an aqueous solution of SDBS (1 wt%) after ultracentrifugation. Metallic M_{11} transitions are indicated by the *red* shaded background, semiconducting S_{22} and S_{11} transitions by the *green* and *blue* colored shaded background, respectively

van Hove singularities (see Sect. 1.1) are probed which are directly related to the chirality of the SWCNT. Thus, absorption spectroscopy in principle allows for the determination of the composition of the material and the distribution of the (*n*,*m*)-species in the bulk sample [147]. A typical absorption spectrum of HiPco SWCNTs dispersed in an aqueous solution of SDBS (1 wt%) after ultracentrifugation is displayed in Fig. 1.9. The metallic M_{11} transitions arise in the UV/Vis region from 350-620 nm partly overlapping with the second semiconducting S_{22}, ranging from 550-900 nm. In the nIR region, the first semiconducting S_{11} transitions are observed.

It has furthermore been revealed by experiment [148] and theoretical calculations [149] that the optical transitions are excitonic in nature, e.g. that bound electron-hole pairs are formed after the excitation. This process is the foundation for the SWCNT nIR fluorescence which will be discussed in Sect. 1.4.2 [24]. Quite surprisingly, the formation of bound dark excitons has also been revealed for metallic SWCNTs [150]. As a consequence, the experimentally observed optical transitions are lower in energy than the energy gap between the van Hove singularities determined by tight binding calculations.

Despite the possibility of (*n*, *m*)-assignment, the determination of the relative (*n*, *m*)-distribution is not straight forward. One major drawback is associated with broadening, red-shift and loss of optical absorption features upon bundling of the nanotubes [24]. In principle this can be traced back to the introduction of allowed states below the excited states in the DOS, or from a more chemical point of view, due to the mixing of orbitals in nanotube bundles. Consequently, the transition energies are highly susceptible to the environment of the nanotubes by bundling effects, as well as of covalent or noncovalent functionalization. Significantly, the metallic transitions are less affected than the semiconducting transitions imposing tremendous problems in determining the (n, m)-distributions of a given sample [151]. The ability to produce samples comprised of exclusively individualized SWCNTs by DGU has partly overcome the problems in determining the (n, m)-distributions and enabled to propose a new procedure to estimate the metallic to semiconductor ratio in SWCNT dispersions on the foundation of absorption spectroscopy [115].

Nonetheless, optical absorption spectroscopy has evolved to a highly important characterization technique, as it is, first of all, the quickest possibility to determine the dispersion efficiency of a given solvent or surfactant system [56, 63]. Commonly, the nanotube dispersion is centrifuged to remove coarse aggregates and insoluble material and the supernatant after centrifugation is analyzed. The ratio of the initial SWCNT concentration to the SWCNT concentration in the supernatant after centrifugation can be regarded as dispersion efficiency. The nanotube concentration in the supernatant can either be calculated from the extinction coefficient of the SCWNT sample [152, 153] or from the ratio of the SWCNT absorbance at a specific wavelength prior to and after centrifugation [63, 154]. The second methodology, however, should only be applied to highly homogenous dispersions where an alteration of the absorption spectra due to scattering effects can be excluded.

Finally, it is worth mentioning that absorption spectroscopy on SWCNTs can be used to evaluate the purity and individualization degree of the sample by determining the ratio of the integrated resonant features arising from the excitonic transitions to the integrated area of the non-resonant background attributed to amorphous and bundled material (resonant ratio) [155, 156].

Throughout this thesis the absorbance is expressed as optical density per cm of path length (OD/cm^{-1}).

1.4.2 Emission Spectroscopy

The ability to produce stable SWCNT dispersions containing individualized nanotubes by the aid of surfactants has first enabled the study of the nanotube nIR fluorescence in 2002 [24]. Hereby, the optical excitation of the S_{22} transition by visible light is followed by rapid electronic relaxation into the S_{11} level prior to emission. The formation of bound excitons results in nIR fluorescence [157] with exciton mobilities of 140–240 nm (depending on the surfactant coating) [158]. Even though excitonic transitions are also induced in metallic SWCNTs, no nIR fluorescence is observed, as the excitons follow a radiationless decay path due to the absence of a band gap [150]. As a consequence, SWCNT nIR fluorescence is absent in metallic SWCNTs, as well as in bundled SWCNTs due to the electronic communication between neighbouring nanotubes in a bundle [24]. Only small bundles not containing metallic SWCNTs still exhibit nIR fluorescence with

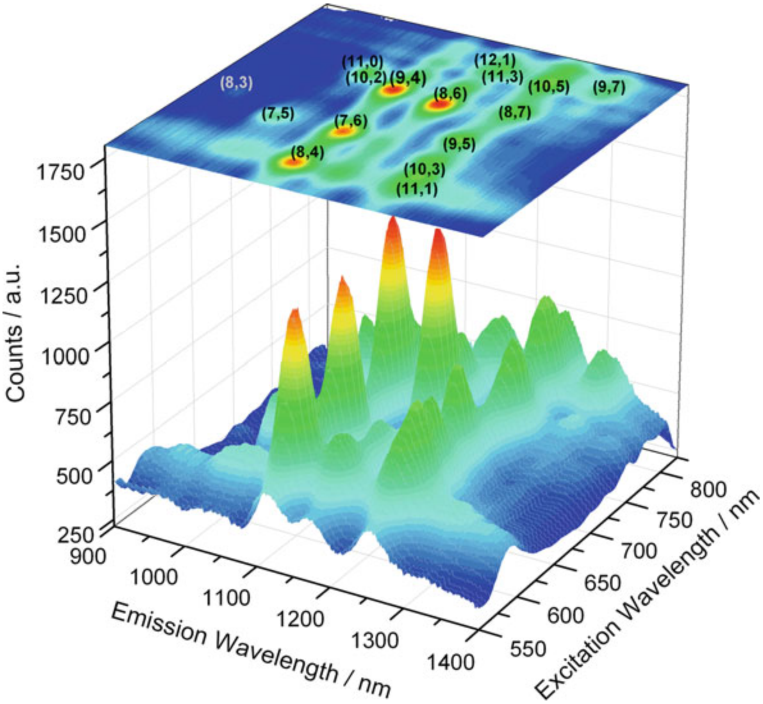

Fig. 1.10 Typical excitation-emission profile of HiPco SWCNT dispersed in an aqueous solution of SDBS (1 wt%) after ultracentrifugation. Commonly, the peaks are transferred to a 2D contour plot at the top of the image. The (*n*, *m*) indices of the most abundant nanotubes species in the sample are marked in the contour plot

characteristic emission *vs.* excitation peaks arising from an exciton energy transfer from large band gap tubes to smaller band gap tubes [159].

Due to the chirality dependent variations in the electronic properties and directly related to that, the optical characteristics of SWCNTs, the measurement of excitation *vs.* emission profiles of SWCNT dispersions has been established as powerful technique to investigate the (*n*, *m*)-distribution of bulk samples. A typical contour plot of HiPco SWCNTs dispersed in an aqueous solution of SDBS (1 wt%) after ultracentrifugation is presented in Fig. 1.10. Owing to the extensive investigations of the group of Bruce Weisman, the various excitation *vs.* emission peaks can precisely be assigned to the chirality of the SWCNT, as also marked in Fig. 1.10 [24, 160].

However, apart from the obstacle that only semiconducting SWCNTs can be probed, another serious drawback arises, as the SWCNT nIR emission is highly sensitive to the dielectric environment around the nanotube and may by quenched or altered by the presence of oxygen [161], metal ions [162] or aromatic compounds adsorbed on the nanotube surface [129, 131, 137, 163]. Consequently, it has been demonstrated that shielding the nanotubes from the environment by a homogenous surfactant coverage results in highly fluorescent SWCNT samples [164, 165]. Additionally, lengths effects have a large impact on the optical response of SWCNTs (both emission and absorption)[166] due to the high exciton mobilities [158].

Nonetheless, emission spectroscopy is the most frequently used technique in the characterization of noncovalently functionalized SWCNTs, especially with regard to the determination of the (n, m)-distribution (of the semiconducting components) within the sample.

1.4.3 Raman Spectroscopy

Even though Raman spectroscopy is the most important and versatile technique for the characterization of covalently functionalized SWCNTs [167], it is of less significance for the investigation of noncovalently functionalized SWCNTs. Thus, it shall only be briefly discussed within this section.

First of all, it is important to note that Raman spectroscopy on CNTs is based on a resonant Raman scattering process, e.g. the Raman signals are strongly enhanced, when the excitation energy matches the energy of an optical transition (see DOS Sect. 1.1 and absorption spectroscopy Sect. 1.4.1). Thus, only the dipole allowed optical transitions occurring between the matching van Hove singularties of the valence and the conduction band excited by the given laser energy are detected. Accordingly, Raman spectroscopy of an ensemble of SWCNTs is sensitive to the subset of nanotubes where the resonant condition is fulfilled resulting in a strong dependency of the Raman spectra on the excitation wavelength [168, 169]. The excitation energies in relation to the SWCNT diameter are summarized in the so-called *Kataura* plot which has first been established from theoretical calculations [170] and subsequently revised by experimental studies [160, 171–174].

A typical Raman spectrum of a bulk sample of HiPco SWCNTs recorded at an excitation wavelength of 633 nm is displayed in Fig. 1.11. In the low energy region of the spectrum (150–350 cm^{-1} shift from the elastically scattered light) the so-called radial breathing modes (RBMs) evolve (green color code in Fig. 1.12) arising from the symmetrical vibration of all atoms radially in phase normal to the SWCNT axis. These modes are only dependent on the diameter of the SWCNT and not on the chirality of the nanotubes. The wavenumber ω_{RBM} is inversely related to the SWCNT diameter d according to Eq. 1.3:

$$\omega_{\mathrm{RBM}} = \frac{A}{d} + B \qquad (1.3)$$

For the constants A and B, different values have been reported. In the case of the diameter assignment in the inset in Fig. 1.11, the values of $A = 204\ \mathrm{cm}^{-1}$ and $\mathrm{B} = 27\ \mathrm{cm}^{-1}$ have been used which have been established from measurements on

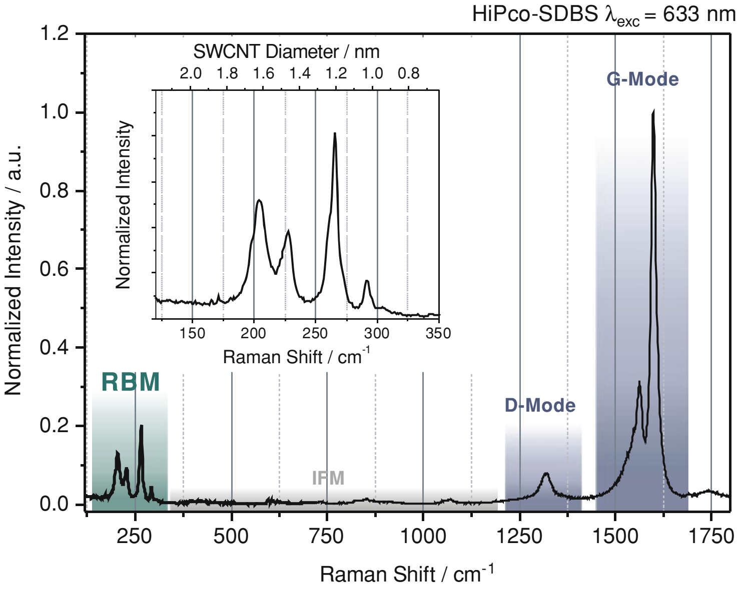

Fig. 1.11 Typical Raman spectrum of a bulk HiPco SWCNT sample after dispersion in aqueous SDBS solution (1 wt %) and filtration recorded at an excitation wavelength of 633 nm. In the lower energy region (*green* color code), the characteristic radial breathing modes (RBM) evolve which are also presented as inset. In the high energy region (*blue* color code) the defect induced D-mode and the graphitic G-mode are discernable. The so-called interfrequency modes (IFM) appear in the energy region between the RBMs and high energy modes (*grey* color code)

free standing SWCNTs [175]. Upon combining the information obtained from the resonant excitement at the given laser energy and the energy of the respective RBM which is directly related to the diameter of the nanotubes, (*n*, *m*)-assignment of the RBM signals is in principle possible by the aid of the *Kataura* plot.

The tangential, or high energy modes in the Raman spectra (blue color code), are commonly the most intense bands and form the so-called G-mode originating from the tangential E_{2g} vibrations in the graphitic honeycomb lattice which is typically observed at around 1580 cm^{-1}. The G-mode comprises six vibrational modes of different symmetry each of them exhibiting characteristic diameter dependency [176–178]. A detailed discussion is omitted within this thesis [167].

The third dominant band in the Raman spectra of SWCNTs (and graphite) is the defect induced D-mode at 1300–1400 cm^{-1} which is in first approximation associated with the introduction of sp^3 carbon atoms in the sp^2 honeycomb lattice such as kinks, ends, oxidative defects or anchor points for covalently attached functional groups. Thus, the ratio of the D- to G-mode with respect to the as-produced material can in principle be used to estimate the degree of functionalization of covalently derivatized SWCNTs rendering Raman spectroscopy the most important and versatile characterization technique for covalent SWCNT chemistry. However, the origin of the D-mode, as well as the use of the D/G-ratio for the determination of the degree of functionalization in covalent SWCNT chemistry is still a source of discussion as summarized in a review article related to that subject [167]. Additionally, a number of peaks with lower intensity arise in the intermediate region between the RBMs and the D-mode (interfrequency modes, IFM) [179]. However, they are not commonly used for the bulk characterization of nanotubes, neither in covalent SWCNT chemistry, nor in SWCNT dispersion and separation.

Especially with regard to the possibility of a (n, m)-index assignment on the foundation of the *Kataura* plot, Raman spectroscopy is thus a highly potent characterization technique for the determination of the bulk composition of the SWCNT material. It is therefore also important for the investigation of sorted SWCNTs (for examples by the techniques described in Sect. 1.3). However, Raman spectroscopy is less frequently used in this research area compared to absorption and emission spectroscopy due to the following major drawbacks associated with this technique.

1. Even though information about metallic SWCNTs can be extracted which are not captured by emission spectroscopy, the complete determination of the material composition according to the (n,m)-species by Raman spectroscopy is a tedious task. Due to the resonant nature of the Raman scattering on SWCNTs, a precise evaluation of all (n, m)-species is only accessible, when the excitation of the sample is screened from 400–900 nm. In practice, this is time consuming on the one hand and the experimental prerequisite, e.g. a laser source with tunable energy, is not readily available on the other hand.
2. Furthermore, it has been shown that environmental effects such as sample morphology have a tremendous impact on the Raman spectra [180, 181]. As has already been mentioned in Sect. 1.4.1, the optical transitions of the SWCNTs are broadened and red-shifted in SWCNT bundles compared to individual, deaggregated SWCNTs. Accordingly, the resonant enhancement of SWCNTs at a fixed laser energy varies with the degree of bundling and debundling in the sample. Practically, this effect is often a source of data misinterpretation in Raman spectroscopy, as the available laser energies are often restricted so that changes in the Raman RBM region may be assigned to changes in the (n, m)-distribution, even though they might be produced by differences in the sample morphology. Even though the morphology of the SWCNT sample can be examined by microscopic techniques such as atomic force microscopy (AFM, see Sect. 1.4.4) the correlation of the Raman spectra to the morphology is not straight forward.

1.4.4 Atomic Force Microscopy

Atomic force microscopy (AFM) has evolved to a standard technique in the characterization of especially noncovalently functionalized and dispersed

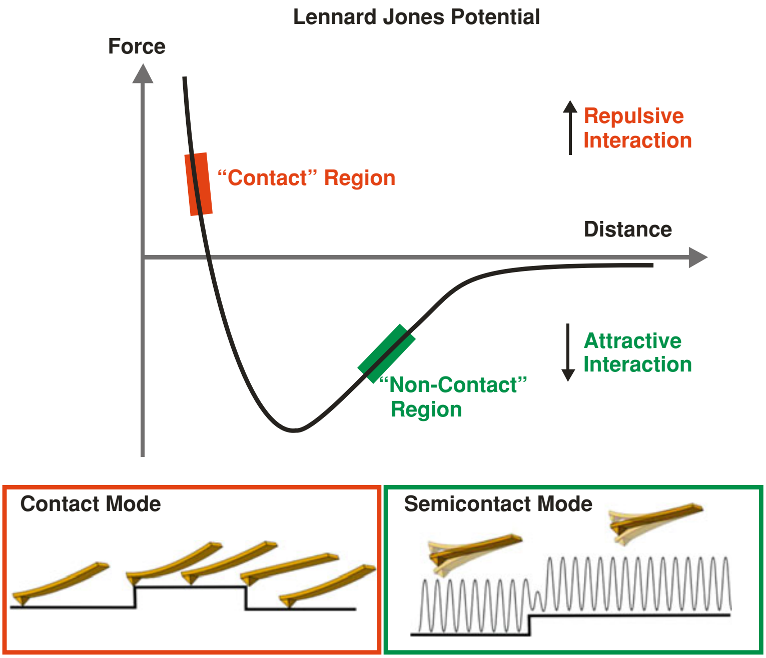

Fig. 1.12 Schematic representation of the force regime in the Lennard Jones potential exploited for contact (*red*) and noncontact (*green*) AFM imaging and the illustration of the respective scanning modes

SWCNTs, as information on the sample morphology and an impression on the quality of the sample can be extracted.

AFM is a scanning-tip technique capable of resolving height differences below 1 nm by detecting small forces (smaller than 1 nN) between the sample surface and a flexible cantilever that is scanning over the surface. The reflection of a laser focused on the top side of the cantilever is detected by a photodiode. The signal is directly related to the motion of the cantilever, e.g. either directly to the topography (contact mode) or the oscillation of the cantilever due to adhesion or repulsion with the surface (noncontact mode).

As described by the *Lennard Jones* potential (Fig. 1.12), the interaction force between two objects is a function of their distance. In AFM contact mode the regime of the repulsive forces is exploited by keeping the cantilever deflection fixed so that a constant force is applied. Thus, the AFM probe directly follows the topography. In semicontact or noncontact mode, the cantilever oscillates close to its resonance frequency. The changes in oscillation are then converted to the topographic information to yield the corresponding height image. Alternatively, the changes in oscillation according to their adhesive or repulsive nature can be expressed in the so-called phase imaging mode, where the contrast of the image predominantly arises from changes in the material's composition [182, 183].

In the case of CNTs, the sample is commonly deposited onto a silicon wafer from solution/dispersion by spincasting, dropcasting or dipcoating. Most frequently, the height images recorded in semicontact mode are analyzed, as scanning in contact mode may result in manipulation of the nanotube morphology—an observation that has been used to investigate mechanical properties of CNTs [184]. AFM analysis has tremendously gained in importance for SWCNT characterization, as it not only allows to obtain an impression on the sample purity, e.g. to estimate the amount of spherical contaminants, but it is also frequently used for the determination of the degree of individualization of the SWCNTs in the sample by statistical AFM analysis [63, 64, 153, 154, 185–187]. Even though, measurements are carried out on air-dried samples, the effects of surface adhesion and drying effects are negligible [63, 185] so that the determination of the height of the rod-like SWCNTs enables to draw conclusions of the bundle size distributions of the SWCNTs in the dispersions. In the case of samples with predominantly individualized SWCNTs, analysis of the SWCNT length is also possible [126, 127, 188].

1.4.5 Zeta Potential

Since the stabilization of nanotubes by ionic surfactants in an aqueous dispersion relies on the electrostatic repulsion between adsorbed surfactant molecules, a SWCNT-surfactant complex may be regarded as classical colloidal system. Generally, the electrostatic repulsion is quantified by the potential in the vicinity of the SWCNT surface, e.g. the zeta potential ζ.

The zeta potential is defined as the potential of a solid surface at the shear plane of the surrounding liquid [189]. A solid surface binds one or more layers of liquid molecules and ions more or less tightly, as illustrated in Fig. 1.13 for a negatively charged particle. Around the particle an electrical double layer is formed (Stern layer) with strongly bound ions. This inner layer is surrounded by a diffuse layer of loosely bound ions and solvent molecules which are slipped off from the surface, when the particle moves. The potential at the hydrodynamic slipping plane is defined as the zeta potential.

For electrostatic reasons, colloidal particles exhibiting zeta potentials greater than 15 mV or smaller than -15 mV are expected to be stable so that maximizing the zeta potential would ultimately be related to increasing the stability of the dispersion. Since the zeta potential scales with the level of charging on a surfactant coated surface, this would mean that increasing the packing density of surfactants on the surface is highly favorable. Based on preliminary research on the zeta potential of aqueous nanotube dispersions [190], Coleman and co-workers [35] have been able to relate the zeta potential of detergent coated SWCNTs to the quality of the dispersion. By a detailed AFM analysis on nanotubes dispersed in SDBS, SDS, LDS, TTAP, SC and fairy liquid (a common kitchen surfactant) they have quantified the quality of the dispersion by four parameters: the saturation value (at low concentration) of the root-mean-square bundle diameter, the

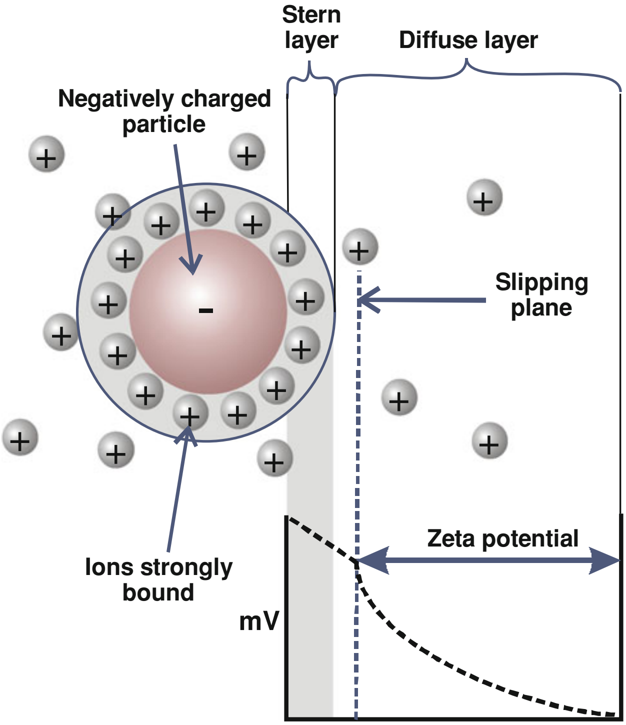

Fig. 1.13 Schematic illustration of the definition of the zeta potential as the potential on the hydrodynamic slipping plane of the diffuse zone of counterions surrounding the Helmholtz double layer around a charged particle

maximum value of the total number of dispersed objects per unit volume of dispersion, the saturation value (at low concentration) of the number fraction of individual tubes and the maximum value of the number of individual nanotubes per unit volume of dispersion. They have included the four parameters in a metric, allowing quantification of the quality of the dispersion. The dispersion quality metric scales very well with the zeta potential decreasing in the following order: SDS > LDS > SDBS > TTAB > SC > fairy liquid.

In a preliminary study, White et al. [190]. have demonstrated that the zeta potential of a dispersion of nanotubes in SDS augments with increasing the SDS concentration (for a fixed nanotube concentration). Furthermore they have shown that the zeta potential is increased when reducing the chain length of the detergent. Both observations are consistent with the zeta potential scaling with the total charge density in the vicinity of the nanotube. Typical values of the zeta potential in the study range from -20 mV for the SC solution to −72 mV for the LDS dispersion (for a nanotube concentration of 0.065 g/l) [35]. It has clearly been outlined that the dispersion quality can presumably be significantly improved by using surfactants coating the nanotubes to give hybrids with magnitudes of the zeta potential of 100 mV and higher.

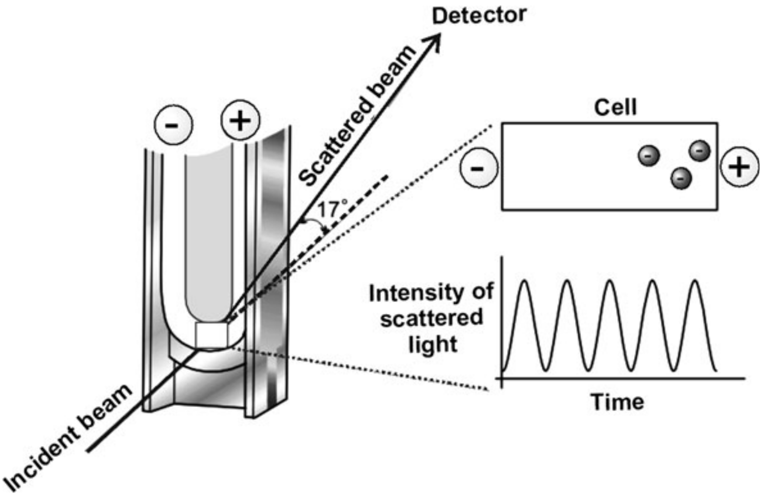

Fig. 1.14 Schematic representation of the experimental setup for the determination of the zeta potential by the electrophoretic mobility of the particles with laser Doppler velocimetry

Since the zeta potential is directly related to the movement of the particle in an electrical field, it is experimentally determined by measuring the electrophoretic mobility by laser *Doppler* velocimetry [191]. In principle, the frequency of the scattered light (which is dependent on the movement of the particles in an electrical field) of an incident laser beam is combined with the frequency of the reference beam passing through the cell without being scattered. Due to constructive and destructive interference of the two beams, an intensity signal is created which is directly proportional to the speed of the particles (Fig. 1.14).

The zeta potential ζ is related to the measured electrophoretic mobility μ according to the *Smoluchowski* approximation (Eq. 1.4):

$$\mu = \frac{\zeta \varepsilon_m V}{4\pi\eta D} \tag{1.4}$$

where V is the applied voltage, η is the viscosity of the solution, ε_m is the dielectric constant of the medium and D is the electrode separation. Despite the fact that the *Smoluchowski* approximation is only rigorously valid for spherical particles, it is applied for the analysis of SWCNTs [35, 190] due to default of a description for cylindrical particles such as nanotubes.

1.4.6 Hurdles in Nanotube Characterization

Due to the polydispersity and insolubility of as-produced SWCNTs, no standard characterization techniques of the toolbox of organic chemists, such as nuclear magnetic resonance spectroscopy, mass spectrometry or elemental analysis can conveniently be applied to the precise analysis of nanotubes. Furthermore, different questions arise in nano science compared to traditional organic chemistry so that alternative characterization techniques are sought for.

The methodologies described above only present a cross-section of available scenarios for the investigation of noncovalently or covalently functionalized nanotubes presented in literature. Numerous other techniques such as thermogravimetric analysis, photoelectron spectroscopy, IR spectroscopy, transient absorption spectroscopy, tip enhanced Raman spectroscopy, tip enhanced near field optical microscopy, scanning electron microscopy, transmission electron microscopy, scanning tunneling microscopy, dynamic light scattering and small angle neutron scattering among others may be used. Accordingly, a manifoldness of analytical techniques exists and may be applied to nanotube characterization. However, it is exactly this diversity that renders nanotube characterization and evaluation of dispersion, sorting or functionalization sequences highly challenging, as no standard protocol for the precise analysis has yet been established.

Taken as individual methods, every characterization technique has its own limitations and restrictions. The greatest hurdles have already been addressed in the sections above and shall be summarized and discussed in the following. Absorption spectroscopy is a readily available and versatile characterization technique for high quality SWCNT dispersions. The ratio of the resonant peaks to the non-resonant background can in principle be taken as a measure for the degree of nanotube bundling. However, the presence of amorphous carbon impurities in the sample also contributes to the nonresonant background thus convoluting the precise analysis. The (n,m)-assignment by optical absorption spectroscopy is also problematic due to the occurrence of multiple overlapping bands. Furthermore, environmental effects such as bundling or the influence of adsorbed species due to van der Waals, π-π-stacking or charge transfer interactions result in changes in the transition energies of the nanotubes which are reflected by peak broadening and peak shifting.

The latter effect is even more critical in the characterization of SWCNTs by their nIR emission, as fluorescence spectroscopy is highly sensitive to the dielectric environment of the nanotubes. Additionally, only individualized semiconducting SWCNTs can be probed in emission spectroscopy so that no complete bulk characterization of the dispersion is possible, especially with regard to the metallic nanotube species.

The metallic SWCNTs can efficiently be analyzed by Raman spectroscopy. However, a precise Raman analysis involves screening the excitation wavelength due to the resonant nature of the scattering process. Furthermore, Raman spectra are commonly recorded from the solid material and are thus strongly dependent on the sample morphology.

The SWCNT morphology can be analyzed by AFM, at least on samples deposited on wafers. Since AFM is a scanning technique, the morphology can only be probed locally on the wafer. The wafers are usually not homogenously covered by the nanotubes so that an impression on the sample morphology can only be obtained when multiple images are recorded. Thus, the characterization is rather time consuming, especially due to the fact that areas of interest are not easily spotted.

Last, but not least, zeta potential can be used to investigate the quality of nanotube dispersions. However, no information on the (*n*,*m*)-distribution is obtained and only little research on the zeta potential of solubilized nanotubes has thus far been carried out. Additionally, no approximation for the calculation of the zeta potential from the electrophoretic mobility in the case of cylindrical objects has been developed.

Considering these aspects, it is obvious that a complete picture of the nanotube sample with regard to dispersion quality, underlying interactions and material composition is only accessible when the information of multiple characterization techniques are combined. However, up to now, no direct correlation to unify different spectroscopic and microscopic techniques is available for the bulk characterization without the need for expensive equipment (such as tip enhanced Raman spectroscopy).

Thus, in order to shed light into the structure-property relationship of SWCNT-surfactant complexes, the quality of the SWCNT dispersions and the investigation of nanotube sorting efficiencies, it is unambiguously necessary to improve the reliability and comparability of SWCNT characterization.

References

1. S. Iijima, Nature **354**, 56–58 (1991)
2. A. Hirsch, Angew. Chem. Int. Ed. **41**, 1853–1859 (2002)
3. H.W. Kroto, J.R. Heath, S.C. O'Brien, R.F. Curl, R.E. Smalley, Nature **318**, 162–163 (1985)
4. A. Hirsch, M. Brettreich, *Fullerenes–Chemistry and Reations* (Wiley, Weinheim, 2005)
5. K.S. Novoselov, A.K. Geim, S.V. Morozov, D. Jiang, Y. Zhang, S.V. Dubonos, I.V. Grigorieva, A.A. Firsov, Science **306**, 666–669 (2004)
6. A.K. Geim, K.S. Novoselov, Nat. Mater. **6**, 183–191 (2007)
7. M.S. Dresselhaus, G. Dresselhaus, P. Avouris, *Carbon Nanotubes: Synthesis, Structure, Properties, and Applications* (Springer, Berlin, 2001)
8. K. Tanaka, T. Yamabe, K. Fukui, *The Science and Technology of Carbon Nanotubes* (Elsevier, Oxford, 1999)
9. M.J. O'Connell (ed.), *Carbon Nanotubes: Properties and Applications* (CRC Press LLC, Boca Raton, 2006)
10. S. Reich, C. Thomsen, J. Maultzsch, *Carbon Nanotubes: Basic Concepts and Physical Properties* (Wiley, Weinheim, 2004)
11. A. Jorio, G. Dresselhaus, M.S. Dresselhaus, *Carbon Nanotubes: Advanced Topics in the Synthesis, Structure, Properties and Applications* (Springer, Berlin, 2007)
12. R. Saito, M.S. Dresselhaus, G. Dresselhaus, *Physical Properties of Carbon Nanotubes* (World Scientific Pub Co, London, 1998)
13. L. Kelly, M. Meyyappan, *Carbon Nanotubes: Science and Applications* (CRC Press Inc, Boca Raton, 2004)
14. M.S. Dresselhaus, G. Dresselhaus, R. Saito, Phys. Rev. B Condens. Matter **45**, 6234–6242 (1992)
15. A. Jung, Dissertation, University of Erlangen-Nürnberg (Erlangen), 2007

16. R. Saito, M. Fujita, G. Dresselhaus, M.S. Dresselhaus, Phys. Rev. B Condens. Matter **46**, 1804–1811 (1992)
17. R.H. Baughman, A.A. Zakhidov, W.A. de Heer, Science **297**, 787–792 (2002)
18. P. Avouris, Acc. Chem. Res. **35**, 1026–1034 (2002)
19. L. Vaisman, H.D. Wagner, G. Marom, Adv. Colloid Interface Sci. **128–130**, 37–46 (2006)
20. N. Grossiord, J. Loos, O. Regev, C.E. Koning, Chem. Mater. **18**, 1089–1099 (2006)
21. N. Grobert, Mater. Today **10**, 28–35 (2007)
22. L.A. Girifalco, M. Hodak, R.S. Lee, Phys. Rev. B **62**, 13104–13110 (2000)
23. S. Nuriel, L. Liu, A.H. Barber, H.D. Wagner, Chem. Phys. Lett. **404**, 263–266 (2005)
24. M.J. O'Connell, S.M. Bachilo, C.B. Huffman, V.C. Moore, M.S. Strano, E.H. Haroz, K.L. Rialon, P.J. Boul, W.H. Noon, C. Kittrell, J. Ma, R.H. Hauge, R.B. Weisman, R.E. Smalley, Science **297**, 593–596 (2002)
25. C. Richard, F. Balavoine, P. Schultz, T.W. Ebbesen, C. Mioskowski, Science **300**, 775–778 (2003)
26. K. Yurekli, C.A. Mitchell, R. Krishnamoorti, J. Am. Chem. Soc. **126**, 9902–9903 (2004)
27. M.S. Strano, V.C. Moore, M.K. Miller, M.J. Allen, E.H. Haroz, C. Kittrell, R.H. Hauge, R.E. Smalley, J. Nanosci. Nanotechnol. **3**, 81–86 (2003)
28. M.F. Islam, E. Rojas, D.M. Bergey, A.T. Johnson, A.G. Yodh, Nano Lett. **3**, 269–273 (2003)
29. W. Wenseleers, I.I. Vlasov, E. Goovaerts, E.D. Obraztsova, A.S. Lobach, A. Bouwen, Adv. Funct. Mater. **14**, 1105–1112 (2004)
30. O. Matarredona, H. Rhoads, Z. Li, J.H. Harwell, L. Balzano, D.E. Resasco, J. Phys. Chem. B **107**, 13357–13367 (2003)
31. T. Okazaki, T. Saito, K. Matsuura, S. Ohshima, M. Yumura, S. Iijima, Nano Lett. **5**, 2618–2623 (2005)
32. R. Haggenmueller, S.S. Rahatekar, J.A. Fagan, J. Chun, M.L. Becker, R.R. Naik, T. Krauss, L. Carlson, J.F. Kadla, P.C. Trulove, D.F. Fox, H.C. DeLong, Z. Fang, S.O. Kelley, J.W. Gilman, Langmuir **24**, 5070–5078 (2008)
33. L. Jiang, L. Gao, J. Sun, J. Colloid Interface Sci. **260**, 89–94 (2003)
34. N.R. Tummala, A. Striolo, ACS Nano **3**, 595–602 (2009)
35. Z. Sun, V. Nicolosi, D. Rickard, S.D. Bergin, D. Aherne, J.N. Coleman, J. Phys. Chem. C **112**, 10692–10699 (2008)
36. A. Ishibashi, N. Nakashima, Bull. Chem. Soc. Jpn. **79**, 357–359 (2006)
37. A. Ishibashi, N. Nakashima, Chem. Eur. J. **12**, 7595–7602 (2006)
38. V.C. Moore, M.S. Strano, E.H. Haroz, R.H. Hauge, R.E. Smalley, J. Schmidt, Y. Talmon, Nano Lett. **3**, 1379–1382 (2003)
39. N. Grossiord, O. Regev, J. Loos, J. Meuldijk, C.E. Koning, Anal. Chem. **77**, 5135–5139 (2005)
40. B.R. Priya, H.J. Byrne, J. Phys. Chem. C **112**, 332–337 (2008)
41. J.-Y. Shin, T. Premkumar, K.E. Geckeler, Chem. Eur. J. **14**, 6044–6048 (2008)
42. S. Utsumi, M. Kanamaru, H. Honda, H. Kanoh, H. Tanaka, T. Ohkubo, H. Sakai, M. Abe, K. Kaneko, J. Colloid Interface Sci. **308**, 276–284 (2007)
43. N. Nakashima, Y. Tomonari, H. Murakami, *Chem. Lett.* pp. 638–639, (2002)
44. Y. Tomonari, H. Murakami, N. Nakashima, Chem. Eur. J. **12**, 4027–4034 (2006)
45. T. Fujigaya, N. Nakashima, Polym. J. **40**, 577–589 (2008)
46. H. Paloniemi, T. Aeaeritalo, T. Laiho, H. Liuke, N. Kocharova, K. Haapakka, F. Terzi, R. Seeber, J. Lukkari, J. Phys. Chem. B **109**, 8634–8642 (2005)
47. J. Chen, C.P. Collier, J. Phys. Chem. B **109**, 7605–7609 (2005)
48. D.M. Guldi, G.M.A. Rahman, N. Jux, N. Tagmatarchis, M. Prato, Angew. Chem. Int. Ed. **43**, 5526–5530 (2004)
49. D.M. Guldi, G.N.A. Rahman, J. Ramey, M. Marcaccio, D. Paolucci, F. Paolucci, S. Qin, W.T. Ford, D. Balbinot, N. Jux, N. Tagmatarchis, M. Prato, *Chem. Commun.* pp. 2034–2035, (2004)
50. Y.-L. Zhao, J.F. Stoddart, Acc. Chem. Res. **42**, 1161–1171 (2009)

51. M.R. Diehl, S.N. Yaliraki, R.A. Beckman, M. Barahona, J.R. Heath, Angew. Chem. Int. Ed. **41**, 353–356 (2002)
52. J. L. Bahr, E. T. Mickelson, M. J. Bronikowski, R. E. Smalley, J. M. Tour, *Chem. Commun.* pp. 193–194 (2001)
53. S. Niyogi, M.A. Hamon, D.E. Perea, C.B. Kang, B. Zhao, S.K. Pal, A.E. Wyant, M.E. Itkis, R.C. Haddon, J. Phys. Chem. B **107**, 8799–8804 (2003)
54. D.S. Kim, D. Nepal, K.E. Geckeler, Small **1**, 1117–1124 (2005)
55. S.B. Fagan, A.G. Souza Filho, J.O.G. Lima, J. Mendes Filho, O.P. Ferreira, I.O. Mazali, O.L. Alves, M.S. Dresselhaus, Nano Lett. **4**, 1285–1288 (2004)
56. K.D. Ausman, R. Piner, O. Lourie, R.S. Ruoff, M. Korobov, J. Phys. Chem. B **104**, 8911–8915 (2000)
57. B.J. Landi, H.J. Ruf, J.J. Worman, R.P. Raffaelle, J. Phys. Chem. B **108**, 17089–17095 (2004)
58. J. Liu, M.J. Casavant, M. Cox, D.A. Walters, P. Boul, W. Lu, A.J. Rimberg, K.A. Smith, D.T. Colbert, R.E. Smalley, Chem. Phys. Lett. **303**, 125–129 (1999)
59. C.A. Furtado, U.J. Kim, H.R. Gutierrez, L. Pan, E.C. Dickey, P.C. Eklund, J. Am. Chem. Soc. **126**, 6095–6105 (2004)
60. J. Wang, W.J. Blau, J. Phys. Chem. C **112**, 2298–2303 (2008)
61. Q. Cheng, S. Debnath, E. Gregan, H.J. Byrne, J. Phys. Chem. C **112**, 20154–20158 (2008)
62. J.N. Coleman, Adv. Funct. Mater. **19**, 3680–3695 (2009)
63. S. Giordani, S.D. Bergin, V. Nicolosi, S. Lebedkin, M.M. Kappes, W.J. Blau, J.N. Coleman, J. Phys. Chem. B **110**, 15708–15718 (2006)
64. S.D. Bergin, V. Nicolosi, P.V. Streich, S. Giordani, Z. Sun, A.H. Windle, P. Ryan, N.P.P. Niraj, Z.-T.T. Wang, L. Carpenter, W.J. Blau, J.J. Boland, J.P. Hamilton, J.N. Coleman, Adv. Mater. **20**, 1876–1881 (2008)
65. S.D. Bergin, Z. Sun, D. Rickard, P.V. Streich, J.P. Hamilton, J.N. Coleman, ACS Nano **3**, 2340–2350 (2009)
66. S.D. Bergin, Z.-Y. Sun, P. Streich, J. Hamilton, J.N. Coleman, J. Phys. Chem. C **114**, 231–237 (2010)
67. T.G. Hedderman, S.M. Keogh, G. Chambers, H.J. Byrne, J. Phys. Chem. B **108**, 18860–18865 (2004)
68. S.I. Pascu, N. Kuganathan, L.H. Tong, R.M.J. Jacobs, P.J. Barnard, B.T. Chu, Y. Huh, G. Tobias, C.G. Salzmann, J.K.M. Sanders, M.L.H. Green, J.C. Green, J. Mater. Chem. **18**, 2781–2788 (2008)
69. H. Murakami, T. Nomura, N. Nakashima, Chem. Phys. Lett. **378**, 481–485 (2003)
70. A. Ikeda, Y. Tanaka, K. Nobusawa, J.-I. Kikuchi, Langmuir **23**, 10913–10915 (2007)
71. K. Nobusawa, A. Ikeda, J.-i. Kikuchi, S.-i. Kawano, N. Fujita, S. Shinkai, Angew. Chem. Int. Ed. **47**, 4577–4580 (2008)
72. K.K. Kim, S.-M. Yoon, J.-Y. Choi, J. Lee, B.-K. Kim, J.M. Kim, J.-H. Lee, U. Paik, M.H. Park, C.W. Yang, K.H. An, Y. Chung, Y.H. Lee, Adv. Funct. Mater. **17**, 1775–1783 (2007)
73. A. Mateo-Alonso, C. Ehli, K.H. Chen, D.M. Guldi, M. Prato, J. Phys. Chem. A **111**, 12669–12673 (2007)
74. J.-H. Lee, S.-M. Yoon, K.K. Kim, I.-S. Cha, Y.J. Park, J.-Y. Choi, Y.H. Lee, U. Paik, J. Phys. Chem. C **112**, 15267–15273 (2008)
75. N. Nakashima, S. Okuzono, H. Murakami, T. Nakai, K. Yoshikawa, Chem. Lett. **32**, 456–457 (2003)
76. M. Zheng, A. Jagota, E.D. Semke, B.A. Diner, R.S. McLean, S.R. Lustig, R.E. Richardson, N.G. Tassi, Nat. Mater. **2**, 338–342 (2003)
77. X. Tu, M. Zheng, Nano Res. **1**, 185–194 (2008)
78. F. Balavoine, P. Schultz, C. Richard, V. Mallouh, T.W. Ebbesen, C. Mioskowski, Angew. Chem. Int. Ed. **38**, 1912–1915 (1999)
79. R. Bandyopadhyaya, E. Nativ-Roth, O. Regev, R. Yerushalmi-Rozen, Nano Lett. **2**, 25–28 (2002)

80. G.R. Dieckmann, A.B. Dalton, P.A. Johnson, J. Razal, J. Chen, G.M. Giordano, E. Munoz, I.H. Musselman, R.H. Baughman, R.K. Draper, J. Am. Chem. Soc. **125**, 1770–1777 (2003)
81. M.S. Arnold, M.O. Guler, M.C. Hersam, S.I. Stupp, Langmuir **21**, 4705–4709 (2005)
82. D.B. Romero, M. Carrard, W. De Heer, L. Zuppiroli, Adv. Mater. **8**, 899–902 (1996)
83. N. Nakashima, T. Fujigaya, Chem. Lett. **36**, 692–697 (2007)
84. D. Tasis, N. Tagmatarchis, A. Bianco, M. Prato, Chem. Rev. **106**, 1105–1136 (2006)
85. A. Hirsch, O. Vostrowsky, Top. Curr. Chem. **245**, 193–237 (2005)
86. M.C. Hersam, Nat. Nanotechnol. **3**, 387–394 (2008)
87. R. Krupke, F. Hennrich, Adv. Eng. Mater. **7**, 111–116 (2005)
88. S. Banerjee, T. Hemraj-Benny, S.S. Wong, J. Nanosci. Nanotechnol. **5**, 841–855 (2005)
89. R. Krupke, F. Hennrich, v. Lohneysen Hilbert, M. Kappes, *Science* **301**, 344–347, (2003)
90. L.X. Benedict, S.G. Louie, M.L. Cohen, Phys. Rev. B: Condens. Matter **52**, 8541–8549 (1995)
91. N. Mureau, E. Mendoza, S.R.P. Silva, K.F. Hoettges, M.P. Hughes, *Appl. Phys. Lett.* **88**, 243109/243101–243109/243103, (2006)
92. T. Lutz, K.J. Donovan, Carbon **43**, 2508–2513 (2005)
93. H. Peng, N.T. Alvarez, C. Kittrell, R.H. Hauge, H.K. Schmidt, J. Am. Chem. Soc. **128**, 8396–8397 (2006)
94. X. Tu, S. Manohar, A. Jagota, M. Zheng, Nature **460**, 250–253 (2009)
95. T. Tanaka, H. Jin, Y. Miyata, H. Kataura, *Appl. Phys. Express*, **1**, 114001/114001–114001/114003, (2008)
96. T. Tanaka, H. Jin, Y. Miyata, S. Fujii, H. Suga, Y. Naitoh, T. Minari, T. Miyadera, K. Tsukagoshi, H. Kataura, Nano Lett. **9**, 1497–1500 (2009)
97. N. Nair, W.-J. Kim, R.D. Braatz, M.S. Strano, Langmuir **24**, 1790–1795 (2008)
98. F. Hennrich, K. Arnold, S. Lebedkin, A. Quintilla, W. Wenzel, M.M. Kappes, phys. stat. so. (b) **244**, 3896–3900 (2007)
99. M.J. Bronikowski, P.A. Willis, D.T. Colbert, K.A. Smith, R.E. Smalley, J. Vac. Sci. Technol., A **19**, 1800–1805 (2001)
100. B. Kitiyanan, W.E. Alvarez, J.H. Harwell, D.E. Resasco, Chem. Phys. Lett. **317**, 497–503 (2000)
101. M.S. Arnold, S.I. Stupp, M.C. Hersam, Nano Lett. **5**, 713–718 (2005)
102. M.S. Arnold, A.A. Green, J.F. Hulvat, S.I. Stupp, M.C. Hersam, Nat. Nanotechnol. **1**, 60–65 (2006)
103. J. Crochet, M. Clemens, T. Hertel, J. Am. Chem. Soc. **129**, 8058–8059 (2007)
104. J. Crochet, M. Clemens, T. Hertel, phys. stat. sol. (b) **244**, 3964–3968 (2007)
105. Y. Miyata, K. Yanagi, Y. Maniwa, H. Kataura, J. Phys. Chem. C **112**, 3591–3596 (2008)
106. L. Wei, B. Wang, T.H. Goh, L.-J. Li, Y. Yang, M.B. Chan-Park, Y. Chen, J. Phys. Chem. B **112**, 2771–2774 (2008)
107. K. Yanagi, Y. Miyata, H. Kataura, *Appl. Phys. Express* **1**, 034003/034001–034003/034003 (2008)
108. K. Yanagi, T. Iitsuka, S. Fujii, H. Kataura, J. Phys. Chem. C **112**, 18889–18894 (2008)
109. Y. Sato, K. Yanagi, Y. Miyata, K. Suenaga, H. Kataura, S. Iijima, Nano Lett. **8**, 3151–3154 (2008)
110. Y. Miyata, K. Yanagi, Y. Maniwa, H. Kataura, Phys. stat. sol. (b) **245**, 2233–2238 (2008)
111. S. Niyogi, C. G. Densmore, S. K. Doorn, *J. Am. Chem. Soc.* (2009)
112. R. Fleurier, J.-S. Lauret, U. Lopez, A. Loiseau, Adv. Funct. Mater. **19**, 2219–2223 (2009)
113. C.W. Lee, C.-H. Weng, L. Wei, Y. Chen, M.B. Chan-Park, C.-H. Tsai, K.-C. Leou, C.H.P. Poa, J. Wang, L.-J. Li, J. Phys. Chem. C **112**, 12089–12091 (2008)
114. A.A. Green, M.C. Hersam, Nano Lett. **8**, 1417–1422 (2008)
115. Y. Miyata, K. Yanagi, Y. Maniwa, H. Kataura, J. Phys. Chem. C **112**, 13187–13191 (2008)
116. M. Engel, J.P. Small, M. Steiner, M. Freitag, A.A. Green, M.C. Hersam, P. Avouris, ACS Nano **2**, 2445–2452 (2008)
117. L. Nougaret, H. Happy, G. Dambrine, V. Derycke, J. P. Bourgoin, A. A. Green, M. C. Hersam, *Appl. Phys. Lett.* **94**, 243505/243501–243505/243503 (2009)

118. P. Zhao, E. Einarsson, R. Xiang, Y. Murakami, S. Maruyama, J. Phys. Chem. C **114**, 4831–4834 (2010)
119. Y. Miyauchi, S. Chiashi, Y. Murakami, Y. Hayashida, S. Maruyama, Chem. Phys. Lett. **387**, 198–203 (2004)
120. E.H. Haroz, W.D. Rice, B.Y. Lu, S. Ghosh, R.H. Hauge, R.B. Weisman, S.K. Doorn, J. Kono, ACS Nano **4**, 1955–1962 (2010)
121. S. Niyogi, C.G. Densmore, S.K. Doorn, J. Am. Chem. Soc. **131**, 1144–1153 (2009)
122. K. Moshammer, F. Hennrich, M.M. Kappes, Nano Res. **2**, 599–606 (2009)
123. S. Ghosh, S.M. Bachilo, R.B. Weisman, Nat. Nanotechnol. **5**, 443–450 (2010)
124. A. Green, M. Duch, M. Hersam, Nano Res. **2**, 69–77 (2009)
125. W.-J. Kim, N. Nair, C.Y. Lee, M.S. Strano, J. Phys. Chem. C **112**, 7326–7331 (2008)
126. J.A. Fagan, M.L. Becker, J. Chun, E.K. Hobbie, Adv. Mater. **20**, 1609–1613 (2008)
127. J.A. Fagan, M.L. Becker, J. Chun, P. Nie, B.J. Bauer, J.R. Simpson, A. Hight-Walker, E.K. Hobbie, Langmuir **24**, 13880–13889 (2008)
128. A. Nish, J.-Y. Hwang, J. Doig, R.J. Nicholas, Nat. Nanotechnol. **2**, 640–646 (2007)
129. F. Chen, B. Wang, Y. Chen, L.-J. Li, Nano Lett. **7**, 3013–3017 (2007)
130. F. Hennrich, S. Lebedkin, M.M. Kappes, phys. stat. sol. (b) **245**, 1951–1953 (2008)
131. J.-Y. Hwang, A. Nish, J. Doig, S. Douven, C.-W. Chen, L.-C. Chen, R.J. Nicholas, J. Am. Chem. Soc. **130**, 3543–3553 (2008)
132. N. Izard, S. Kazaoui, K. Hata, T. Okazaki, T. Saito, S. Iijima, N. Minami, *Appl. Phys. Lett.* **92**, 243112/243111–243112/243113 (2008)
133. H. Dodziuk, A. Ejchart, W. Anczewski, H. Ueda, E. Krinichnaya, G. Dolgonos, W. Kutner, *Chem. Commun.* pp. 986–987 (2003)
134. A. Ortiz-Acevedo, H. Xie, V. Zorbas, W.M. Sampson, A.B. Dalton, R.H. Baughman, R.K. Draper, I.H. Musselman, G.R. Dieckmann, J. Am. Chem. Soc. **127**, 9512–9517 (2005)
135. D. Tasis, K. Papagelis, D. Douroumis, J.R. Smith, N. Bouropoulos, D.G. Fatouros, J. Nanosci. Nanotechnol. **8**, 420–423 (2008)
136. H. Li, B. Zhou, Y. Lin, L. Gu, W. Wang, K.A.S. Fernando, S. Kumar, L.F. Allard, Y.-P. Sun, J. Am. Chem. Soc. **126**, 1014–1015 (2004)
137. S.-Y. Ju, J. Doll, I. Sharma, F. Papadimitrakopoulos, Nat. Nanotechnol. **3**, 356–362 (2008)
138. C.S. Lin, R.Q. Zhang, T.A. Niehaus, T. Frauenheim, J. Phys. Chem. C **111**, 4069–4073 (2007)
139. S. Niyogi, S. Boukhalfa, S.B. Chikkannanavar, T.J. McDonald, M.J. Heben, S.K. Doorn, J. Am. Chem. Soc. **129**, 1898–1899 (2007)
140. R.M. Tromp, A. Afzali, M. Freitag, D.B. Mitzi, Z. Chen, Nano Lett. **8**, 469–472 (2008)
141. R. Marquis, K. Kulikiewicz, S. Lebedkin, M. M. Kappes, C. Mioskowski, S. Meunier, A. Wagner, *Chem. Eur. J.* **15**, 11187–11196, S11187/11181–S11187/11185 (2009)
142. J. Zhou, H. Li, J. Lu, G. Luo, L. Lai, R. Qin, L. Wang, S. Nagase, Z. Gao, W. Mei, G. Li, D. Yu, S. Sanvito, Nano Res. **3**, 296–306 (2010)
143. X. Peng, N. Komatsu, T. Kimura, A. Osuka, ACS Nano **2**, 2045–2050 (2008)
144. X. Peng, N. Komatsu, T. Kimura, A. Osuka, J. Am. Chem. Soc. **129**, 15947–15953 (2007)
145. X. Peng, N. Komatsu, S. Bhattacharya, T. Shimawaki, S. Aonuma, T. Kimura, A. Osuka, Nat. Nanotechnol. **2**, 361–365 (2007)
146. F. Wang, K. Matsuda, A.F.M.M. Rahman, X. Peng, T. Kimura, N. Komatsu, J. Am. Chem. Soc. **132**, 10876–10881 (2010)
147. S.M. Bachilo, M.S. Strano, C. Kittrell, R.H. Hauge, R.E. Smalley, R.B. Weisman, Science **298**, 2361–2366 (2002)
148. F. Wang, G. Dukovic, L.E. Brus, T.F. Heinz, Science **308**, 838–841 (2005)
149. C. D. Spataru, S. Ismail-Beigi, L. X. Benedict, S. G. Louie, *Phys. Rev. Lett.* **92**, 077402/077401–077402/077404 (2004)
150. J. Deslippe, C.D. Spataru, D. Prendergast, S.G. Louie, Nano Lett. **7**, 1626–1630 (2007)
151. H. Huang, H. Kajiura, R. Maruyama, K. Kadono, K. Noda, J. Phys. Chem. B **110**, 4686–4690 (2006)

152. B. Zhao, M.E. Itkis, S. Niyogi, H. Hu, J. Zhang, R.C. Haddon, J. Phys. Chem. B **108**, 8136–8141 (2004)
153. S.D. Bergin, V. Nicolosi, H. Cathcart, M. Lotya, D. Rickard, Z. Sun, W.J. Blau, J.N. Coleman, J. Phys. Chem. C **112**, 972–977 (2008)
154. V. Nicolosi, H. Cathcart, A.R. Dalton, D. Aherne, G.R. Dieckmann, J.N. Coleman, Biomacromolecules **9**, 598–602 (2008)
155. M.E. Itkis, D.E. Perea, S. Niyogi, S.M. Rickard, M.A. Hamon, H. Hu, B. Zhao, R.C. Haddon, Nano Lett. **3**, 309–314 (2003)
156. B. Zhao, M.E. Itkis, S. Niyogi, H. Hu, D.E. Perea, R.C. Haddon, J. Nanosci. Nanotechnol. **4**, 995–1004 (2004)
157. M. Jones, C. Engtrakul, W. K. Metzger, R. J. Ellingson, A. J. Nozik, M. J. Heben, G. Rumbles, *Phys. Rev. B* **71**, 115426/115421–115426/115429 (2005)
158. A.J. Siitonen, D.A. Tsyboulski, S.M. Bachilo, R.B. Weisman, Nano Lett. **10**, 1595–1599 (2010)
159. P.H. Tan, A.G. Rozhin, T. Hasan, P. Hu, V. Scardaci, W.I. Milne, A.C. Ferrari, *Phys. Rev. Lett.* **99**, 137402/137401–137402/137404 (2007)
160. R.B. Weisman, S.M. Bachilo, Nano Lett. **3**, 1235–1238 (2003)
161. H. Cathcart, V. Nicolosi, J.M. Hughes, W.J. Blau, J.M. Kelly, S.J. Quinn, J.N. Coleman, J. Am. Chem. Soc. **130**, 12734–12744 (2008)
162. J.J. Brege, C. Gallaway, A.R. Barron, J. Phys. Chem. C **111**, 17812–17820 (2007)
163. R. Marquis, C. Greco, I. Sadokierska, S. Lebedkin, M.M. Kappes, T. Michel, L. Alvarez, J.-L. Sauvajol, S. Meunier, C. Mioskowski, Nano Lett. **8**, 1830–1835 (2008)
164. D.A. Tsyboulski, E.L. Bakota, L.S. Witus, J.-D.R. Rocha, J.D. Hartgerink, R.B. Weisman, J. Am. Chem. Soc. **130**, 17134–17140 (2008)
165. S.-Y. Ju, W.P. Kopcha, F. Papadimitrakopoulos, Science **323**, 1319–1323 (2009)
166. J.A. Fagan, J.R. Simpson, B.J. Bauer, S.H. De Paoli Lacerda, M.L. Becker, J. Chun, K.B. Migler, A.R. Hight Walker, E.K. Hobbie, J. Am. Chem. Soc. **129**, 10607–10612 (2007)
167. R. Graupner, J. Raman Spectrosc. **38**, 673–683 (2007)
168. L. Alvarez, A. Righi, T. Guillard, S. Rols, E. Anglaret, D. Laplaze, J.L. Sauvajol, Chem. Phys. Lett. **316**, 186–190 (2000)
169. S.K. Doorn, D.A. Heller, P.W. Barone, M.L. Usrey, M.S. Strano, Appl. Phys. A **78**, 1147–1155 (2004)
170. H. Kataura, Y. Kumazawa, Y. Maniwa, I. Umezu, S. Suzuki, Y. Ohtsuka, Y. Achiba, Synth. Met. **103**, 2555–2558 (1999)
171. M.S. Strano, J. Am. Chem. Soc. **125**, 16148–16153 (2003)
172. H. Telg, J. Maultzsch, S. Reich, F. Hennrich, C. Thomsen, *Phys. Rev. Lett.* **93**, 177401/177401–177401/177404 (2004)
173. J. Maultzsch, H. Telg, S. Reich, C. Thomsen, *Phys. Rev. B* **72**, 205438/205431–205438/205416 (2005)
174. A. Jorio, P.T. Araujo, S.K. Doorn, S. Maruyama, H. Chacham, M.A. Pimenta, phys. stat. sol. (b) **243**, 3117–3121 (2006)
175. J.C. Meyer, M. Paillet, T. Michel, A. Moreac, A. Neumann, G.S. Duesberg, S. Roth, J.-L. Sauvajol, *Phys. Rev. Lett.* **95**, 217401/217401–217401/217404 (2005)
176. V.N. Popov, P. Lambin, *Phys. Rev. B* **73**, 085407/085401–085407/085409 (2006)
177. O. Dubay, G. Kresse, H. Kuzmany, *Phys. Rev. Lett.* **88**, 235506/235501–235506/235504 (2002)
178. A. Jorio, A.G. Souza Filho, G. Dresselhaus, M.S. Dresselhaus, A.K. Swan, M. S. Unlu, B. B. Goldberg, M.A. Pimenta, J.H. Hafner, C.M. Lieber, R. Saito, *Phys. Rev. B* **65**, 155412/155411–155412/155419 (2002)
179. Z. Luo, F. Papadimitrakopoulos, S.K. Doorn, *Phys. Rev. B* **75**, 205438/205431–205438/205437 (2007)
180. L.M. Ericson, P.E. Pehrsson, J. Phys. Chem. B **109**, 20276–20280 (2005)
181. C. Fantini, A. Jorio, M. Souza, M.S. Strano, M.S. Dresselhaus, M.A. Pimenta, *Phys. Rev. Lett.* **93**, 147406/147401–147406/147404 (2004)

182. G. Bar, Y. Thomann, M.H. Whangbo, Langmuir **14**, 1219–1226 (1998)
183. O.P. Behrend, L. Odoni, J.L. Loubet, N.A. Burnham, Appl. Phys. Lett. **75**, 2551–2553 (1999)
184. M.R. Falvo, G.J. Clary, R.M. Taylor 2nd, V. Chi, F.P. Brooks Jr, S. Washburn, R. Superfine, Nature **389**, 582–584 (1997)
185. H. Cathcart, S. Quinn, V. Nicolosi, J.M. Kelly, W.J. Blau, J.N. Coleman, J. Phys. Chem. C **111**, 66–74 (2007)
186. J. Amiran, V. Nicolosi, S.D. Bergin, U. Khan, P.E. Lyons, J.N. Coleman, J. Phys. Chem. C **112**, 3519–3524 (2008)
187. H. Cathcart, J.N. Coleman, Chem. Phys. Lett. **474**, 122–126 (2009)
188. X. Huang, R.S. McLean, M. Zheng, Anal. Chem. **77**, 6225–6228 (2005)
189. H.-J. Butt, K. Graf, M. Kappl, *Physics and Chemistry of Interfaces* (Wiley, Weinheim, 2006)
190. B. White, S. Banerjee, S. O'Brien, N.J. Turro, I.P. Herman, J. Phys. Chem. C **111**, 13684–13690 (2007)
191. F. Durst, A. Melling, J.H. Whitelaw, *Principles and Practice of Laser Doppler Anemometry* (Academic, London, 1976)

Chapter 2
Proposal

Despite their unique physical, mechanical and electronic properties single-walled carbon nanotube-based technology has commenced slowly. This can be traced back to two major hurdles namely their poor solubility in common solvents on the one hand and the polydispersity of the as-produced material with regard to diameter, length and chirality on the other hand. SWCNT solubilization can conveniently be achieved by the aid of surfactants noncovalently anchored to the SWCNT surface. The resulting dispersion can be subjected to sorting scenarios recently developed. However, up to now, separation efficiencies and yields are poor as sorting is restricted to individualized SWCNTs. Individualization rates by common surfactants are below 25% (after mild centrifugation) so that novel SWCNT surfactants with superior properties are sought for.

Accordingly, the major focus of this thesis is directed towards the evaluation of novel SWCNT surfactants with perylene bisimide (PBI) anchor groups. The desired amphiphilicity that can be considered as prerequisite for an efficient SWCNT dispersion in aqueous media, is generated by peripheral derivatization with *Newkome*-type dendrimers. The dispersion and individualization efficiencies of a variety of perylene bisimide derivatives are to be compared on the foundation of SWCNT absorption and nIR emission spectroscopy, as well as statistical AFM analysis. Since the PBIs are commonly equipped with carboxylic acid functionalities, the influence of the pH value and the counterion is another point which has to be addressed. In order to establish structure property relationships and to elucidate packing densities of the surfactants on the SWCNT scaffold and the underlying interactions, the characterization is to be expanded to alternative methods such as zeta potential measurements, IR spectroscopy, X-Ray photoelectron spectroscopy (XPS) and the hydrodynamic characterization of the SWCNT-PBI complexes by analytical ultracentrifugation.

On the foundation of these findings, potential selective interactions of the PBI dispersants with certain SWCNT species are to be investigated. For this purpose, a characterization routine based on the techniques outlined in Sect. 1.4 is to be developed. The gained insights and the acquired methodologies are then to be

C. Backes, *Noncovalent Functionalization of Carbon Nanotubes*, Springer Theses,
DOI: 10.1007/978-3-642-27582-1_2,

applied to structural variations of the π-surfactants such as cationic PBIs or pyrene derivatives.

In the second part, the designed surfactants shall be applied for SWCNT separation. Focus is not only to be laid on the use of already established techniques, but also on the design and development of novel separation scenarios accessible by the π-surfactants.

Another obstacle directly related to the polydispersity and poor solubility of the SWCNTs is presented in the characterization of this 1D carbon allotrope. Since no standard protocols can be followed, commonly evidence from multiple characterization techniques is cumulated to gain a comprehensive picture of noncovalently (or covalently) derivatized SWCNTs. Hereby, it is highly challenging to correlate the information obtained from the manifold spectroscopic and microscopic techniques. Accordingly, the improvement of SWCNT characterization and the development of reliable analytical protocols is another topic which is addressed by this thesis.

Chapter 3
Results and Discussion

3.1 SWCNT Surfactant Design: Solubilization by Aromatic Amphiphiles

3.1.1 The Versatility of Perylene Bisimide Derivatives

In the first section, the suitability of seven different perylene bisimide derivatives (**1**–**7**) with respect to nanotube dispersion and exfoliation in water has been investigated (Scheme 3.1) [1, 2]. The syntheses of these systems is described in the literature [2, 3]. As outlined by numerous studies [4–12], the inclusion of polycyclic aromatic units in nanotube dispersion additives enhances the interaction with the aromatic nanotube scaffold in comparison to classical detergents where the interaction is limited to *van der Waals* attraction.

In general, solubility of the perylene derivatives has been ensured by peripheral derivatization with first and second generation *Newkome*-type dendrimers, except for **7** being equipped with two sulfonic acid groups. The perylene derivatives may be classified as bolaamphiphilic **1**, **2**, **7** or amphiphilic **3**, **4**, **5**, **6** depending on their substitution pattern. The amphiphile **4** equipped with a first generation *Newkome*-type dendrimer does not exhibit sufficient water solubility and was therefore excluded from the study on SWCNT dispersion [3].

In order to evaluate the importance of the dendritic substituents for nanotube dispersion, the symmetric sulfonic acid perylene derivative **7** has also been subjected to the analysis of SWCNT dispersion**.** Furthermore the solubilization of nanotubes by the amphiphile **8** was investigated consisting of a second generation *Newkome*-type dendrimer and a C14-alkyl chain to underline the necessity of the perylene unit for efficient dispersion of nanotubes. To allow comparison with previous works concerned with nanotube dispersability and solubilization, the commonly used surfactant SDBS [13–19] has been chosen as reference, as it is has shown to yield highly stable nanotube dispersions with very little preference for certain nanotube diameters [20] or chiralities [14, 19].

C. Backes, *Noncovalent Functionalization of Carbon Nanotubes*, Springer Theses,
DOI: 10.1007/978-3-642-27582-1_3, © Springer-Verlag Berlin Heidelberg 2012

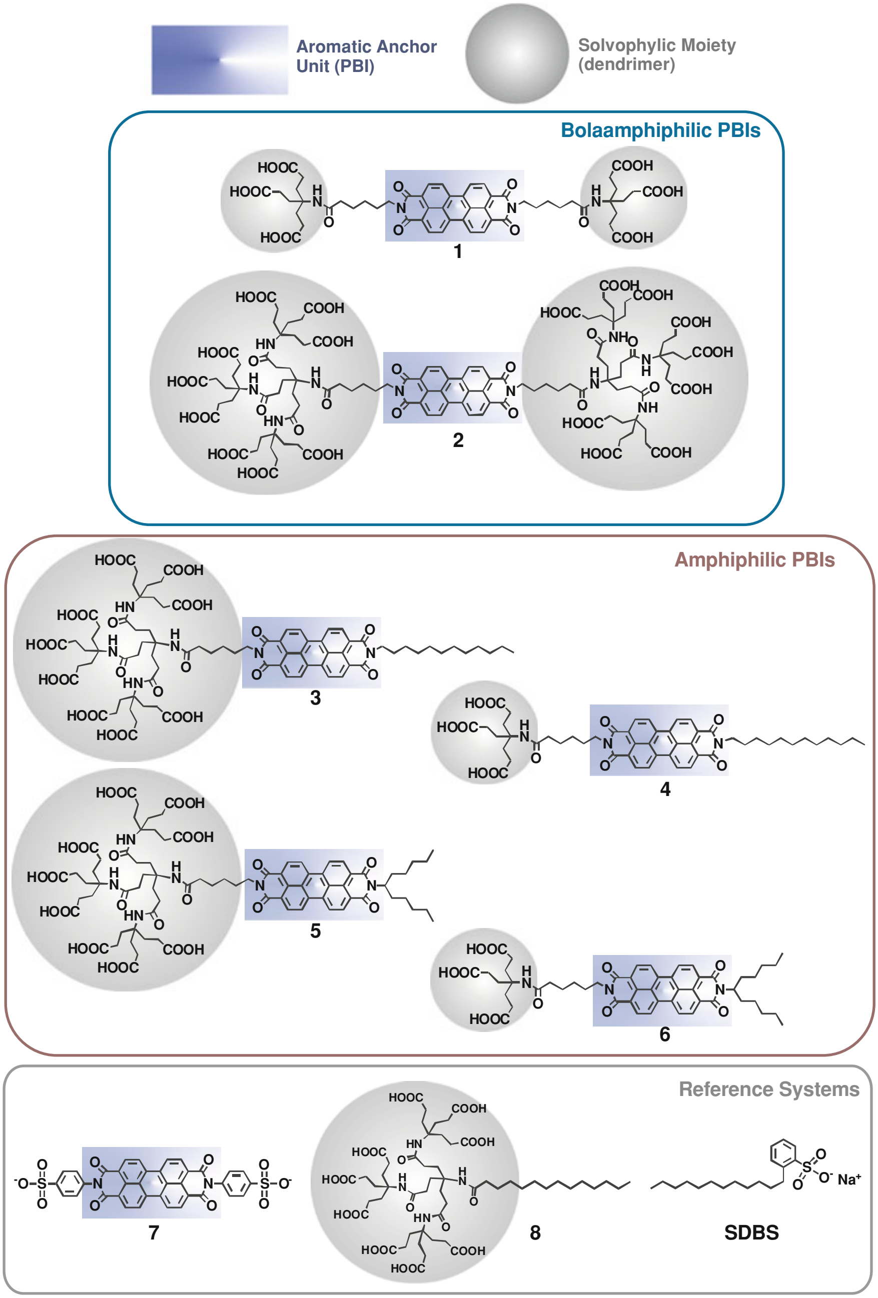

Scheme 3.1 Structures of the perylene bisimide derivatives and the reference systems applied for the dispersion of HiPco SWCNTs. The anchor unit to the SWCNT surface is indicated by the *blue squares*, the solvophylic moieties by the *grey circles*

3.1.1.1 Overview of SWCNT Dispersability

In a typical nanotube dispersion experiment, HiPco SWCNTs were added to an aqueous solution of the surfactant at constant surfactant concentrations of 0.1 g L^{-1} for the designed systems (above the critical micelle concentration in all cases), followed by sonication (30 min) and mild centrifugation (30 min, 15 krpm) in order to remove coarse aggregates and insoluble material. The supernatant after centrifugation containing the stably dispersed nanotubes was then subjected to spectroscopic and microscopic characterization. Significantly, SWCNTs are not dispersable by a buffered aqueous solution of **8** demonstrating the importance of the perylene unit as aromatic anchor to the nanotube surface. Furthermore, it is important to note that a buffered aqueous solution of **7** is also not capable of dispersing SWCNTs, as the negative charges of the sulfonic acid groups are located too close to the perylene core which results in insufficient interaction of the anchor group with the nanotubes. Thus, **7** and **8** were excluded from further studies.

In the case of **1**, **2**, **3**, **5** and **6**, the nanotubes are homogenously dispersed for a nanotube to perylene (SWCNT:Per) ratio of approximately 2:1 by weight as determined by the stepwise addition of a perylene stock solution to nanotubes dispersed in a buffer solution (pH = 7). The presence of the characteristic SWCNT transitions in the absorption spectrum with a ratio SWCNT:**3** = 3.4:1 reveals that this ratio is sufficient to induce SWCNT dispersion (Fig. 3.1a). However, as only individualized semiconducting SWCNTs exhibit nIR emission, the absence of SWCNT fluorescence at this ratio (Fig. 3.1b) indicates that a higher concentration of the perylene dispersant is required to also promote exfoliation of the SWCNT bundles. The nIR fluorescence of the SWCNTs is detected at SWCNT:**3** ratios lower than 2:1 (blue trace in Fig. 3.1b). Accordingly, individualization starts at a SWCNT:**3** ratio of 2:1 [1].

Since the threshold concentration of the perylene dispersant necessary for the efficient SWCNT solubilization slightly varies as a function of substituent and pH, a ratio of SWCNT:Per = 1:1 by weight was chosen in the following comparative study in all cases which is well above the minimum perylene concentration for efficient individualization. Figure 3.2 depicts the supernatant solutions of nanotubes dispersed in buffered aqueous solutions of the five perylene derivatives after centrifugation for pH = 7 (phosphate buffer) and pH = 10 (borate buffer), respectively. As indicated by the different colors of the vials in Fig. 3.2, the amount of nanotubes remaining in the supernatant after centrifugation is dependent on the structure of the perylene derivative on the one hand and the buffer medium (pH) on the other hand. For quantification of the amount of nanotubes stably dispersed, the solutions were subjected to UV/Vis/nIR absorption spectroscopic studies.

UV/Vis/nIR absorption spectroscopy is a highly versatile tool for SWCNT characterization, as it can be used to calculate the nanotube concentration in a given sample on the basis of the optical density of the dispersion. The concentrations of nanotubes in the supernatant dispersions after centrifugation in buffered

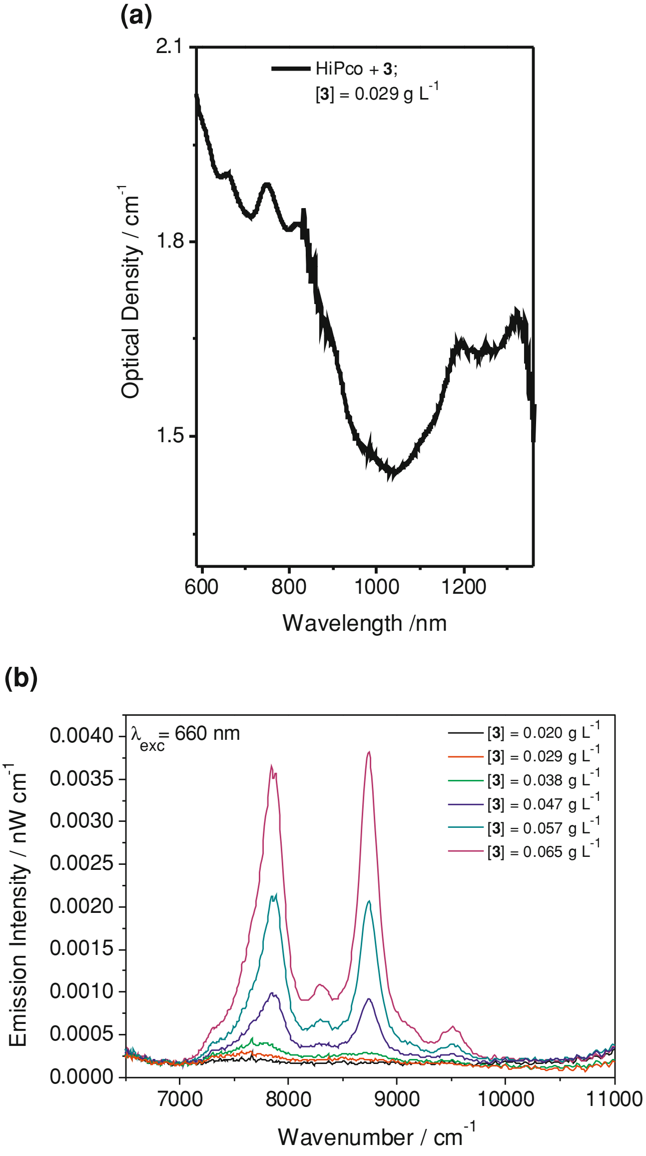

Fig. 3.1 **a** UV/Vis/nIR absorption spectrum after the addition of a 0.1 wt% buffered aqueous solution of **3** to SWCNTs in buffer (pH = 7, [SWCNT] = 0.1 g L^{-1}); the total amount of **3** added corresponds to a concentration of [**3**] = 0.029 g L^{-1}. The homogeneity of the dispersion is reflected by the presence of the characteristic SWCNT transitions. The region below 600 nm is omitted due to the absorption of the perylene core. **b** As recorded fluorescence spectra ($\lambda_{exc} = 660$ nm) of the addition of a 0.1 wt% buffered aqueous solution of **3** to SWCNTs in buffer (pH = 7, [SWCNT] = 0.10 g L^{-1}); the total amount of **3** added corresponds to a concentration of [**3**] = 0.065 g L^{-1}. Individualization of the nanotubes starts to occur when the concentration of **3** exceeds 0.047 g L^{-1}

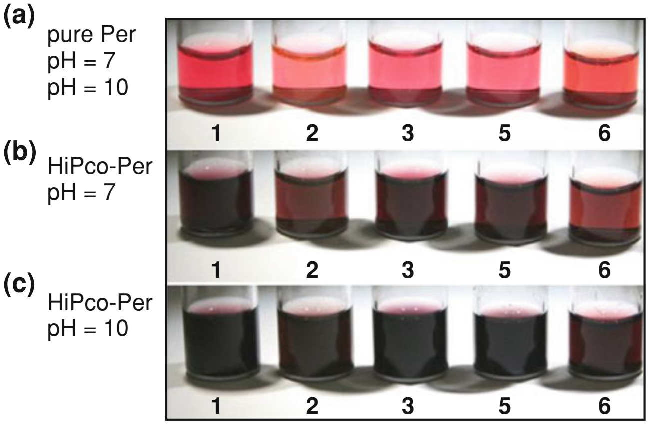

Fig. 3.2 Photograph of **a** buffered aqueous solutions of the perylenes **1**, **2**, **3**, **5** and **6** and **b** HiPco SWCNTs dispersed in aqueous solutions of the perylene derivatives after centrifugation at pH = 7. **c** at pH = 10, respectively. The initial concentration of SWCNTs was 0.1 g L^{-1} with a SWCNT:Per ratio of 1:1 by weight. (Reproduced with permission from Wiley–VCH, Ref. [2])

Table 3.1 Calculated nanotube concentrations in the supernatant of SWCNT-Per after centrifugation and the corresponding dispersion efficiencies in %. In all cases, the initial nanotube and perylene concentration, respectively, is 0.1 g L^{-1}. The concentration of SDBS is 10.0 g L^{-1}

		1	2	3	5	6	SDBS
[SWCNT]/g L^{-1}	pH = 7	0.033	0.023	0.034	0.031	0.018	0.068
		(33%)	(23%)	(34%)	(31%)	(18%)	(68%)
	pH = 10	0.066	0.039	0.073	0.073	0.033	0.069
		(66%)	(39%)	(73%)	(73%)	(33%)	(69%)

aqueous solutions (pH = 7 and 10) of the perylene derivatives are summarized in Table 3.1. They have been calculated from the absorption coefficient of the nanotubes at 740 nm which was determined to be 435 L mol^{-1} cm^{-1} (3625 L g^{-1} m^{-1}) for an aqueous dispersion of HiPco SWCNTs in SDBS-phosphate buffer (pH = 7) and 476 L mol^{-1} cm^{-1} (3967 Lg^{-1} m^{-1}) for an aqueous dispersion of HiPco SWCNTs in SDBS-borate buffer (pH = 10), respectively.

It is important to note that the initial concentration of SDBS is by a factor of 100 higher than the concentration of the perylenes, as nanotube dispersion has shown to be highly effective for SDBS concentrations of 1 wt% (10 g L^{-1}) [16]. A direct comparison of the actual exfoliation power of the perylenes with SDBS is therefore not possible. However, the experiment with SDBS can be used to set up a benchmark for nanotube dispersion. As outlined by Table 3.1, the concentration of nanotubes after centrifugation in the case of the perylene derivatives **1**, **3** and **5** is approximately equal with about 31–34% of nanotubes being stably dispersed after centrifugation. For the sterically demanding bolaamphiphile **2** the nanotube concentration in the supernatant is reduced by a factor of 1.4. The smallest perylene derivative **6** bearing only one first generation dendrimer shows the lowest dispersion capability with 18% of the nanotubes remaining after centrifugation (factor of 1.8 lower compared to **1**, **3** and **5**).

Most interestingly, the nanotube concentration in the supernatant is dependent on the buffer medium. At pH = 10, the concentration of the nanotubes stably dispersed in the buffered solutions of the different perylene derivatives is increased by a factor of 2. Significantly, for SDBS the concentration of the nanotubes remaining in the supernatant after centrifugation is approximately equal. At pH = 10, the concentration of nanotubes dispersed in **3** and **5** even exceeds the concentration of nanotubes in SDBS despite the 100 times lower concentration of the perylene surfactant underlining the high dispersion capability of the perylene derivatives.

At first glance, it might not be surprising that the nanotube dispersability is increased at higher pH for the perylene derivatives, as it is tempting to argue that a higher pH leads to complete deprotonation of the carboxylic acid functionalities in the substituents of the perylene derivatives [21]. Thus, an increase in pH would result in an increased net charge of the dispersant which ultimately leads to increased dispersion efficiency if the same surfactant packing density on the nanotube surface is assumed. However, multiple effects may contribute to the different dispersion behavior at pH = 7 and pH = 10, respectively, so that a well-grounded discussion is postponed at this point.

3.1.1.2 Optical Properties of the SWCNT: Surfactant Dispersions

The intensity of the nanotube absorption yields information on the total amount of SWCNTs dispersed, covering bundled and exfoliated SWNTs. However, bundled nanotubes tend to exhibit broadened and red-shifted optical nanotube transitions [22]. As revealed by Fig. 3.3a, nanotubes dispersed in aqueous solutions of the perylene derivatives (pH = 7) show reasonably well resolved absorption features indicating the presence of exfoliated nanotubes [22]. The absorption spectra normalized to the minimum of the corresponding SWCNT-Per dispersions at pH = 7 and pH = 10, respectively, are virtually identical as exemplary shown for SWCNT-**2** (Fig. 3.3b). Compared to nanotubes dispersed in a solution of SDBS, the nanotube transitions in general appear broadened and red-shifted, being either indicative for a lower degree of exfoliation or an alteration of the excitonic states due to an increased accessibility of the nanotube to the aqueous environment [23, 24] or π-π-stacking interactions with the perylene unit [4, 5].

In this regard, it is interesting to note that the transitions for SWCNT-**6** (magenta trace in Fig. 3.3a) do not exhibit such a pronounced shift in comparison to SDBS despite the low dispersion efficiency of this perylene derivative. Furthermore, the structure of the nanotube absorption pattern is similar to the reference of SWCNT-SDBS. Thus, the adsorption of **6** onto the sidewall of the nanotube is presumably similar to the micellar arrangement of the SDBS

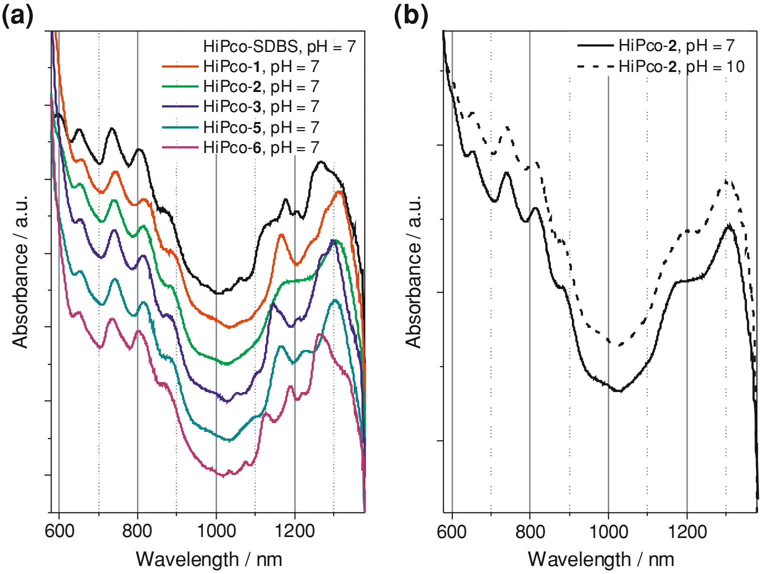

Fig. 3.3 **a** Optical absorption spectra (normalized to the minimum) of SWCNTs dispersed in aqueous solutions of the different perylene derivatives (SWCNT:Per = 1:1 by weight, $[SWCNT]_i = 0.1\ g\ L^{-1}$) compared to nanotubes dispersed in SDBS (1 wt%, $[SWCNT]_i = 0.1\ g\ L^{-1}$). **b** Optical absorption spectra (normalized to the minimum) of SWCNTs dispersed in aqueous solutions of Per2 at pH = 7 and pH = 10 (SWCNT:Per = 1:1 by weight, $[SWCNT]_i = 0.1\ g\ L^{-1}$). In all cases, the supernatant after centrifugation is displayed and the spectra are offset for clarity. (Reproduced with permission from Wiley–VCH, reference 2)

molecules, as no π-π-stacking interaction of the perylene unit is evidenced by optical absorption spectroscopy in the case of **6**.

Absorption spectroscopy is also highly versatile for the characterization of aqueous perylene dye solutions, as the ratio of the 0→0 (around 550 nm) to the 0→1 (around 500 nm) transition is directly related to the degree of perylene aggregation: While monomeric PBIs exhibit normal Franck–Condon progression with $A^{0\rightarrow}/A^{0\rightarrow 1} \approx 1.6$, aggregated PBIs have inversed intensity distributions among their vibronic states with $A^{0\rightarrow 0}/A^{0\rightarrow 1} \leq 0.7$ [25–27]. The $A^{0\rightarrow 0}/A^{0\rightarrow 1}$ transitions of the PBIs at a concentration of $0.1\ g\ L^{-1}$ in the absence and presence of HiPco SWCNTs are summarized in Table 3.2.

Obviously, the least sterically hindered amphiphilic perylene **6** shows the strongest self-aggregation ($A^{0\rightarrow 0}/A^{0\rightarrow 1} = 0.4$), followed by the bolaamphiphile equipped with the first generation dendrimers **1** ($A^{0\rightarrow 0}/A^{0\rightarrow 1} = 0.5$). The amphiphilic perylenes with the second generation dendrimers **3** and **5** are also predominantly self-aggregated at the concentration investigated with $A^{0\rightarrow 0}/A^{0\rightarrow 1} = 0.6$. In contrast, the highly bulky bolaamphiphile **2** with two sterically demanding substituents exhibits a low degree of self-aggregation with $A^{0\rightarrow 0}/A^{0\rightarrow 1} = 1.1$.

Table 3.2 Tabulated values of the ratios of $A^{0\rightarrow 0}/A^{0\rightarrow 1}$ of the perylene transitions in the absence and presence of HiPco SWCNT in buffered solutions at pH = 7 and pH = 10, respectively

	1	2	3	5	6
$A^{0\rightarrow 0}/A^{0\rightarrow 1}$ in the absence of HiPco SWCNTs	0.5	1.1	0.6	0.6	0.4
$A^{0\rightarrow 0}/A^{0\rightarrow 1}$ in the presence of HiPco SWCNTs pH = 7	0.9	1.2	1.0	0.8	0.5
$A^{0\rightarrow 0}/A^{0\rightarrow 1}$ in the presence of HiPco SWCNTs pH = 10	0.9	1.1	1.1	0.9	0.5

The difference in the perylene $A^{0\rightarrow 0}/A^{0\rightarrow 1}$ ratios in the presence of SWCNTs is striking as exemplarily depicted in the case of **3** in Fig. 3.4a. In general, the ratios $A^{0\rightarrow 0}/A^{0\rightarrow 1}$ of the perylene transitions are increased when the perylene moiety is anchored to the SWCNT scaffold (Table 3.2). In the case of perylene **6** the ratio is only slightly changed (from 0.4 to 0.5) indicating that this perylene derivative is not sufficiently interacting with the SWCNT surface to induce alterations of the perylene transitions. In the case of perylene derivative **2** carrying two bulky second generation *Newkome*-type dendrimers also virtually no difference in the $A^{0\rightarrow 0}/A^{0\rightarrow 1}$ ratios in the presence and absence of SWCNT is discernable. This can be traced back to the less pronounced self-aggregation of the derivative in the absence of SWCNT as described above. In all other cases, the perylene transitions approach the normal Franck–Condon progression indicating that the perylene derivatives adsorb onto the nanotubes as monomeric species.

It should in principle be possible to determine the amount of free perylene and adsorbed perylene on the foundation of the perylene bands. However, a precise quantification is not possible due to the underlying SWCNT M_{11} background which convolutes the analysis. Furthermore, the actual concentration of the perylene derivatives in the SWCNT supernatant dispersions is unknown, as the dispersants are partly removed by the centrifugation process. Since the aggregation behavior of the perylene derivatives is dependent on the concentration of the molecules [3] no appropriate reference experiment can be set up so that attempts to quantify the amount of free bulk perylene are carried out. Nonetheless, the interaction of the perylene derivatives with the SWCNT scaffold can be qualitatively mapped by the ratios of the perylene bands.

An influence of the buffer medium on the ratios $A^{0\rightarrow 0}/A^{0\rightarrow 1}$ of the perylene transitions in the presence of SWCNTs can also be extracted from Table 3.2 in cases of the amphiphilic derivatives **3** and **5**. Obviously, the amount of free perylene is decreased upon nanotube addition in pH = 10 compared to pH = 7 as indicated by the higher $A^{0\rightarrow 0}/A^{0\rightarrow 1}$ ratios. Further support of this conclusion is derived from the peak position of the perylene peaks which appear red-shifted upon adsorption to the SWCNT surface. The perylene absorption bands are red-shifted by 5 nm (0.021 eV) in the phosphate buffer solution (pH = 7) and 10 nm (0.041 eV) in the borate buffer solution (pH = 10), respectively.

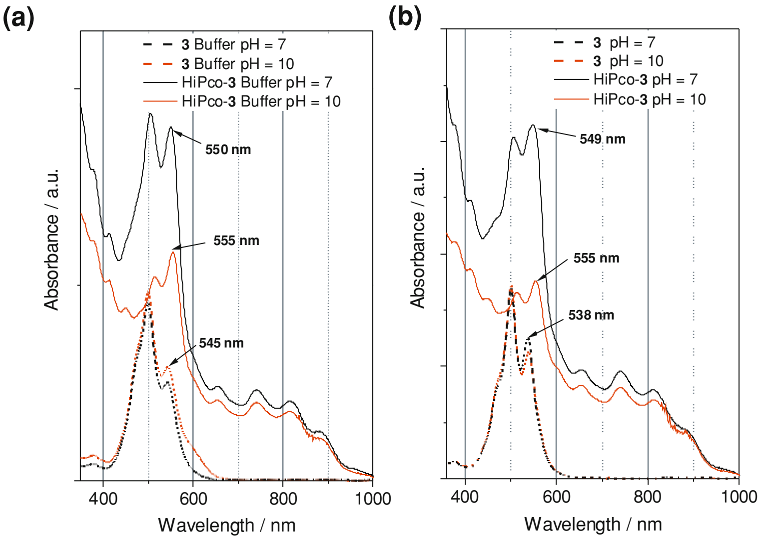

Fig. 3.4 Optical absorption spectra (normalized to the minimum at 1030 nm) of SWCNTs dispersed in aqueous solutions of **3** at pH = 7 and pH = 10 (SWCNT:Per = 1:1 by weight, $[\mathrm{SWCNT}]_i = 0.05\ \mathrm{g\ L^{-1}}$). In both cases, the supernatant after centrifugation is displayed: **a** buffer medium, **b** no buffer. (Reproduced with permission from Wiley–VCH, reference 2)

In order to evaluate whether the observed increased perylene-nanotube interaction at pH = 10 is dependent on the use of different buffer media (phosphate and borate buffer, respectively), or whether it is an effect induced by the change in pH, a second sample has been prepared by adjusting the pH with a sodium hydroxide solution to 7 and 10, respectively (Fig. 3.4b). Even though the differences in the ratio of the $0 \rightarrow 1$ perylene transition to the $0 \rightarrow 0$ transition is not as striking as in the case of the buffered samples, the increased π-π-stacking interaction of the perylene to the nanotube π-surface is still reflected by the red-shift of the perylene absorption bands (0.05 eV at pH = 7 and 0.07 eV at pH = 10).

This behavior is somewhat counterintuitive, as it implies that the amount of adsorbed perylene is increased at pH = 10 compared to pH = 7. If the net negative charge of the perylene molecules was increased at higher pH, the Coulomb repulsion between the adsorbed perylene molecules on the nanotube surface would be increased which would presumably be accompanied with the opposite behavior, namely, a decrease of the amount of adsorbed perylene at elevated pH. Even if the counterions shield the Coulomb repulsion between adjacent molecules, this would not account for a higher adsorption rate.

The qualitatively increased adsorption of perylene molecules onto the nanotube sidewall at higher pH can be traced back to two possible explanations: (1) the surface area of the nanotubes is increased due to a higher degree of debundling for SWCNT-Per in borate buffer (pH = 10) or (2) the interaction of the perylene moiety with the nanotube surface is stronger, as the nanotubes themselves are

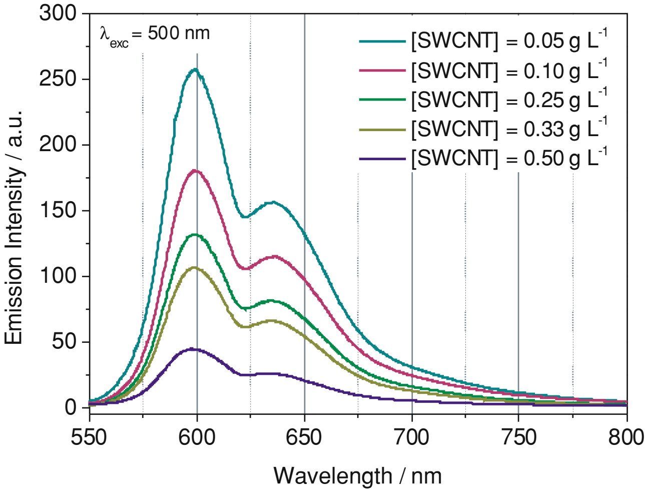

Fig. 3.5 Fluorescence spectra of an aqueous solution of SWCNT-**3** with $\lambda_{exc} = 500$ nm at different SWCNT concentrations. (Reproduced with permission from Wiley–VCH, reference 2)

partially negatively charged at pH values above their point of zero charge [16]. Since it has been shown in an independent study that a charge transfer from SWCNTs to the electron poor perylene moiety takes place [28], the introduction of negative charges on the SWCNTs could potentially strengthen this charge transfer interaction. Both explanations shall be evaluated later on.

In summary, the dispersion ability of the perylene derivatives according to UV/Vis/nIR absorption spectroscopy follows the order $3 > 1 > 5 > 2 > 6$ at pH $= 7$ and $3 = 5 > 1 > 2 > 6$ at pH $= 10$. The π-π-stacking interaction of the perylene unit is reflected in the optical absorption spectra of SWCNT-**1**, SWCNT-**2**, SWCNT-**3** and SWCNT-**5** in contrast to aqueous nanotube dispersions of **6** and SDBS.

The SWCNT-Per dispersions are furthermore an ideal system for emission spectroscopic studies, as both the SWCNT, as well as the perylene dispersants exhibit fluorescence. Emission spectra upon excitation of the perylene unit with $\lambda_{exc} = 500$ nm with varying amounts of SWCNTs dispersed in an aqueous perylene solution (0.1 g L^{-1}) reveal that the emission intensity of the perylene dye is subsequently reduced with increasing concentrations of SWCNTs as exemplarily depicted in the case of **3** in Fig. 3.5 [1]. This is attributed to the fact that upon increasing the concentration of SWCNTs, the concentration of free perylene responsible for the emission is decreased, as more perylene is adsorbed on the surface of the nanotube. In addition, an innerfilter effect [29] of the nanotubes could also contribute to the observed decrease of emission intensity. Elimination of the innerfilter effect in this experiment is not trivial, as the usual methodology to overcome this problem involves dilution of the samples to the same nanotube concentration. However, diluting the SWCNT-**3** dispersions would also result in an alteration of the perylene fluorescence, as the emission of **3** is highly dependent on the aggregation state of the perylene itself: A concentration dependent fluorescence study of **3** revealed that the emission intensity reaches a maximum at concentrations of approximately 5×10^{-5} M. At higher concentrations however, the fluorescence is subsequently quenched due to the self aggregation of the perylene moieties [3].

As outlined in Sect. 1.4.2, photoluminescence spectroscopy is furthermore a powerful tool in nanotube characterization as fluorescence is mapped from excitonic band gap transitions in exfoliated semiconducting nanotubes, allowing precise (n, m)-assignments of the semiconducting nanotube species [30, 31]. However, fluorescence spectroscopy is highly sensitive to the dielectric environment around the nanotube and may be quenched or altered by the presence of oxygen [32], metal ions [33] or aromatic compounds adsorbed on the nanotube surface [9, 11, 12, 34].

The fluorescence spectroscopic investigation of the SWCNT-Per composites [2] involves dilution of the dispersions by a buffer solution to the same optical density of 0.26 cm^{-1} ([SWCNT] = 0.006 g L^{-1}) to account for attenuation of the fluorescence intensity by the innerfilter effect [29]. Even though it has been revealed that nanotubes may be spontaneously exfoliated upon dilution on the time scale of days [23, 29, 35, 36], which would also influence the fluorescence intensity, this effect is negligible in this case, as spectra were recorded immediately after dilution not allowing the nanotube dispersions to equilibrate with the altered surroundings.

The nIR emission of the HiPco-Per dispersions were collected at two excitation wavelength ($\lambda_{\text{exc}} = 660$ and 785 nm) after degassing the dispersions by nitrogen. As revealed by Fig. 3.6 and Table 3.3, the nanotube emission intensity is dependent on the structure of the perylene derivative. Furthermore, the emission pattern is strongly attenuated when compared to nanotubes dispersed in a solution of SDBS. A detailed discussion of this fact is postponed to Sect. 3.1.3.

In contrast to absorption spectroscopy, the pH only has a minor impact on the nanotube nIR emission. Upon comparing nanotubes dispersed in SDBS, the nIR emission intensity and pattern is virtually identical for buffered solutions at $\text{pH} = 7$ and $\text{pH} = 10$. The nIR emission intensity is slightly reduced for the $\text{pH} = 10$ solutions. However, no changes in spectral position and or pattern are observed.

In general, the nanotube emission intensity is decreased for SWCNT-Per compared to nanotubes dispersed in SDBS. Similar to the red-shifted absorption features this may be either attributed to the π-π-stacking and charge transfer interaction of the nanotube to the perylene core or to the lack of debundling. To elucidate this issue, the determination of the individualization degrees needs to be determined (see Sect. 3.1.1.3).

Since the dispersants investigated all bear the same nanotube anchor group, namely the perylene unit, it is quite surprising that the nanotube emission intensity and pattern depends on the structure of the perylene derivative. In the case of **6**, the nanotube emission pattern strongly resembles the pattern of nanotubes dispersed in a buffered aqueous solution of SDBS, as demonstrated by the normalized emission

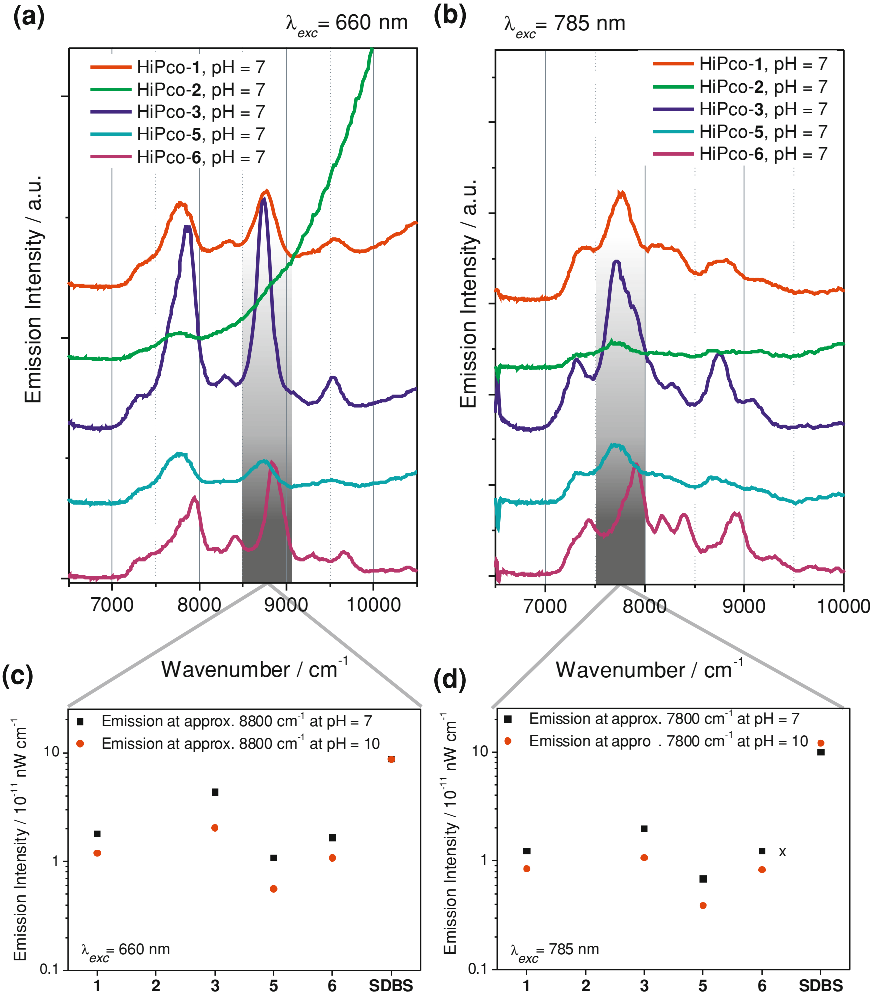

Fig. 3.6 As recorded nIR emission spectra of SWCNTs dispersed in aqueous solutions of the different perylene derivatives (SWCNT:Per = 1:1 by weight, [SWCNT] = 0.006 g L^{-1}) at pH = 7. **a** $\lambda_{exc} = 660$ nm, **b** $\lambda_{exc} = 785$ nm. In all cases, the supernatant after centrifugation was diluted to an optical density of 0.26 cm^{-1} at 740 nm and degassed by bubbling nitrogen prior to acquisition of the spectra. Spectral offset for clarity. In the *bottom* section the recorded emission intensities for the major peaks (*shaded areas*) are plotted versus the different surfactants at pH = 7 and pH = 10, respectively: **c** $\lambda_{exc} = 660$ nm, **d** $\lambda_{exc} = 785$ nm. (Reproduced with permission from Wiley–VCH, reference 2)

spectra presented in Fig. 3.7. This observation is in agreement with the optical absorption spectra and indicates that **6** follows a different supramolecular aggregation on the nanotube scaffold compared to the perylenes **1**, **3** and **5**. This can be attributed to a reduced π-π-stacking interaction, as **6** forms highly stable micelles

Table 3.3 Tabulated maximum nIR emission intensity (I) and peak position (ν) for HiPco tubes dispersed in buffered aqueous solutions (pH = 7) of the perylene derivatives and SDBS ([SWCNT] = 0.006 g L^{-1}, [Per] = 0.006 g L^{-1}, [SDBS] = 10 g L^{-1})

	λ_{exc} = 660 nm				λ_{exc} = 785 nm	
	ν (cm^{-1})	I (nW/cm^{-1})	ν (cm^{-1})	I (nW/cm^{-1})	ν (cm^{-1})	I (nW/cm^{-1})
SDBS	8899	1.83×10^{-10}	8005	8.69×10^{-11}	7944	1.00×10^{-10}
1	8770	2.04×10^{-11}	7780	1.79×10^{-11}	7763	1.23×10^{-11}
2	–	–	–	–	–	–
3	8739	4.86×10^{-11}	7839	4.32×10^{-11}	7713	1.97×10^{-11}
5	8738	9.34×10^{-12}	7771	1.06×10^{-11}	7696	6.93×10^{-12}
6	8834	2.40×10^{-11}	7934	1.66×10^{-11}	7908	1.23×10^{-11}

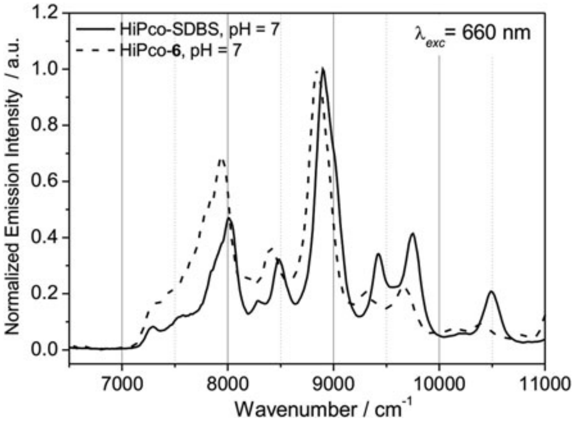

Fig. 3.7 nIR emission spectra (normalized to the maximum) of SWCNTs dispersed in aqueous solutions of **6** and SDBS (SWCNT:Per = 1:1 by weight, [SWCNT] = 0.006 g L^{-1}, [SDBS] = 10 g L^{-1}) at λ_{exc} = 660 nm. In all cases, the supernatant after centrifugation was diluted to an optical density of 0.26 cm^{-1} at 740 nm and degassed by bubbling nitrogen prior to acquisition of the spectra. (Reproduced with permission from Wiley–VCH, reference 2)

due to the comparatively small charged head group (First generation *Newkome*-type dendrimer) so that adsorption to the nanotube sidewall via the non-polar alky chain is presumably favored over the adsorption of the perylene core.

Furthermore, it is important to note that the nanotube emission is completely quenched in the case of perylene **2**. On the one hand, this might again reflect a different supramolecular adsorption of perylene **2** compared to **1**, **3** and **5**, as **2** is equipped with two bulky second generation *Newkome*-type dendrimers which hinders its self aggregation, e.g. formation of stable and well defined micelles, as already revealed by cryo-TEM imaging [3]. On the other hand, fluorescence quenching may be induced by an increased net charge density in the nanotube surrounding, as solubilization is ensured by 18 carboxylate entities opposed to 6 for perylene **1** and 9 for perylenes **3** and **5**.

In summary, nIR emission decreases in the order of $\mathbf{3} > \mathbf{1} = \mathbf{6} > \mathbf{5} > \mathbf{2}$ (totally quenched). Since the emission intensity is highly sensitive to the structure of the perylene derivatives it is suggested that the mechanism of nanotube emission quenching is not merely based on the π-π-stacking interaction of the perylene core, as no pronounced changes would then be expected by the variation of the substituents in the perylene periphery. Either the aggregation state of the nanotubes dispersed in the different perylene derivatives varies significantly (individualization degrees), or this attenuation occurs due to changes in the dielectric medium of the nanotubes, e.g. different charge density which influences the dynamic fluorescence quenching, as shall be elucidated by the determination of the zeta potential of the SWCNT-Per dispersions.

3.1.1.3 Exfoliation and Surfactant Packing Density

In colloidal science, the zeta potential ζ is defined as the electric potential at the hydrodynamic slip plane of the diffuse zone of counterions surrounding the Helmholtz double layer of a dispersed object (see Sect. 1.4.5). The ζ-potential is often used as an index of the magnitude of electrostatic interaction between colloidal particles and can therefore be regarded as a measure for the stability of the dispersion. In the case of nanotube dispersions it can directly be related to the potential in the vicinity of the bound ions at the surface of the nanotubes. Recently, White et al. [37] and Coleman et al. [38] have correlated the zeta potential of surfactant stabilized nanotubes to the dispersion stability. As outlined by Coleman et al. [38], the ideal nanotube surfactant should yield high magnitudes of the zeta potential—either negative or positive (dependent on the head charge of the surfactant). Thus, if the dispersion ability is to be maximized, the surfactants need to be highly charged, tightly packed, of low molecular weight (to maximize the packing density) and exhibit strong binding to the nanotube in order to minimize the fraction of free surfactant at a given concentration, shielding the repulsive interaction between the dispersed nanotubes.

The perylene derivatives presumably fulfill three of the four criteria: they are highly charged, can be tightly packed onto the nanotube surface and are strongly interacting with the nanotube. However, they suffer from the drawback of high molecular weight as opposed to the established detergents such as SDBS. In accordance with the theoretical prediction, the experimentally determined magnitude of the zeta potential (average of ten measurements) of the SWCNT-Per composites (Fig. 3.8) is comparable to SWCNT-SDBS under equal experimental conditions (sonication and centrifugation parameters, aqueous medium) [2].

Upon comparing the zeta potential for HiPco-SDBS in non-buffered opposed to buffered media, it becomes apparent that the presence of the increased ionic strength in the buffer medium and directly related to that the larger pool of positive counterions significantly decreases the magnitude of the zeta potential, as the

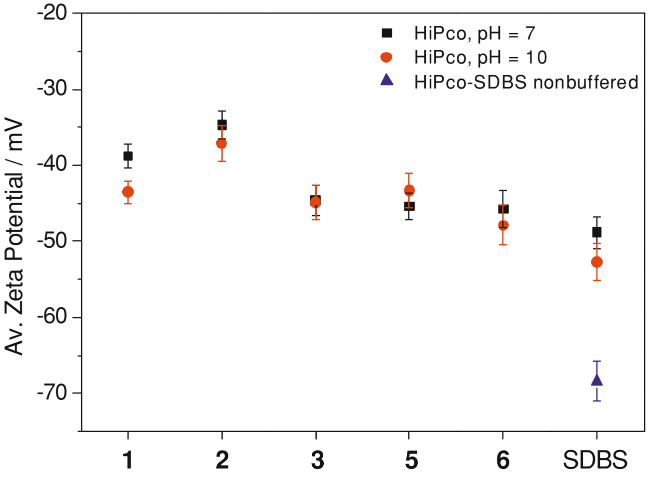

Fig. 3.8 Zeta potential of the SWCNT-Per dispersions compared to SWCNT-SDBS at pH = 7, as well as pH = 10. The error bars are derived from the standard deviation over ten measurements. (Reproduced with permission from Wiley–VCH, reference 2)

counter charges become partly localized at the hydrodynamic slip plane. This phenomenon should be kept in mind when regarding zeta potential values of the HiPco-Per dispersions which are in the same range as those of HiPco-SDBS in buffered media.

The determination of the zeta potential in a comparative study of different nanotube surfactants can also be used to qualitatively estimate the packing density (number of surfactant molecules per unit nanotube) of the dispersant. Since a dispersion of SWCNTs in the smallest PBI **6** being equipped with three carboxylic acid functionalities yields similar values for the zeta potential with respect to the other perylene derivatives, the packing density has to be highest for the derivative **6**. The zeta potential of the nanotube dispersion in the derivative **2** with 18 carboxylic acid functionalities is lower in magnitude so that it can be concluded that the PBI **2** is least densely packed on the nanotube backbone. In summary, the packing density of the perylene molecules onto the SWCNT scaffold decreases in the order **6** (3 COOH) > **1** (6 COOH) > **3** (9 COOH) = **5** (9 COOH) > **2** (18 COOH). Most interestingly, there is no direct correlation to the nanotube fluorescence intensity which should be inversely related to the packing density (more perylene molecules per unit nanotube should lead to a more pronounced quenching of the nanotube fluorescence). In fact, the nanotube fluorescence is totally quenched when dispersed with **2**, which is least densely packed.

In general, the pH only has a minor impact on the zeta potential of SWCNT-Per dispersions. Therefore, it can be concluded that the packing density of the perylene molecules on the nanotube surface is slightly reduced upon increasing the pH, as the charge density is approximately equal while the net charge of the surfactant molecules themselves is increased due to a complete deprotonation of the carboxylic acid groups. Thus the observed increase in nanotube dispersability and the related increase in the amount of perylene adsorbed at higher pH is attributed to a higher degree of exfoliation, as shall further be evaluated by AFM analysis.

In summary, the zeta potential measurements yield valuable information: (1) the charge density in the vicinity of the nanotube is similar for all the dispersions in the different perylene derivatives, presumably because the packing density of the perylene derivatives is governed by inter-perylene Coulombic repulsion, except for perylene **2** where packing may additionally be reduced due to steric effects. On the example of **2** as nanotube surfactant, it can nicely be followed that the nanotube emission intensity can neither be correlated with the charge density in the vicinity of the nanotube, nor with the packing density of the perylene molecules. It is therefore proposed that the nanotube emission properties are traced back to variations in the supramolecular aggregation of the surfactant molecules on the nanotube surface. (2) An increase in pH does not result in a significant change of the zeta potential. Thus, the observation that more perylene molecules are adsorbed on the nanotube surface at higher pH is most probably related to a higher degree of SWCNT debundling which increases the surface area of the nanotubes. In order to further clarify the dispersion mechanisms especially with respect to nanotube exfoliation and the assembly of the perylene derivatives on the nanotube sidewall, the suspensions have been subjected to an atomic force microscopic investigation.

AFM can be applied to the determination of height distributions in nanotube samples and directly related to that, the degree of SWCNT debundling. Since dispersion by the amphiphilic perylenes **3** and **5** has shown to be quite similar, the microscopic investigation focuses on a comparative study of nanotube dispersions by **1**, **2**, **3** and **6**. In order to determine the number fraction of individual nanotubes N_I/N_T being a measure for the surfactant capability, a statistical AFM analysis of the AFM images recorded in tapping mode has been performed with minimum 350 counts at pH 7 and 250 counts at pH 10, respectively. For the determination of N_I/N_T, the number of nanotube objects with less than 1.4 nm in height has been divided by the total number of counts of all nanotubes (individuals and bundles of varying size/height).

As revealed by the statistical analysis of the bundle size distribution, the number of fraction of individualized nanotubes N_I/N_T increases in the order $\mathbf{1} > \mathbf{3} > \mathbf{2} > \mathbf{6}$ at pH = 7 (Fig. 3.9). In the case of the supernatant of nanotubes dispersed in a buffered aqueous solution (pH = 7) of **1**, 44% of the nanotubes have been found to be exfoliated, while for **3**, N_I/N_T is 35%. Even though fewer nanotubes are individualized in the case of **2** (22%), the fraction is still higher than for nanotubes dispersed in an aqueous solution of SDBS under similar experimental conditions (14%) which forms micelles with a radius of 2.97 nm [39] that allows the inclusion of small nanotube bundles [40]. The lowest degree of individualization (12.7%) has been observed for the system SWCNT-**6**, where the dispersion can be attributed to a micellar mechanism which is based on a less specific interaction than an individualization by the π-surfactants.

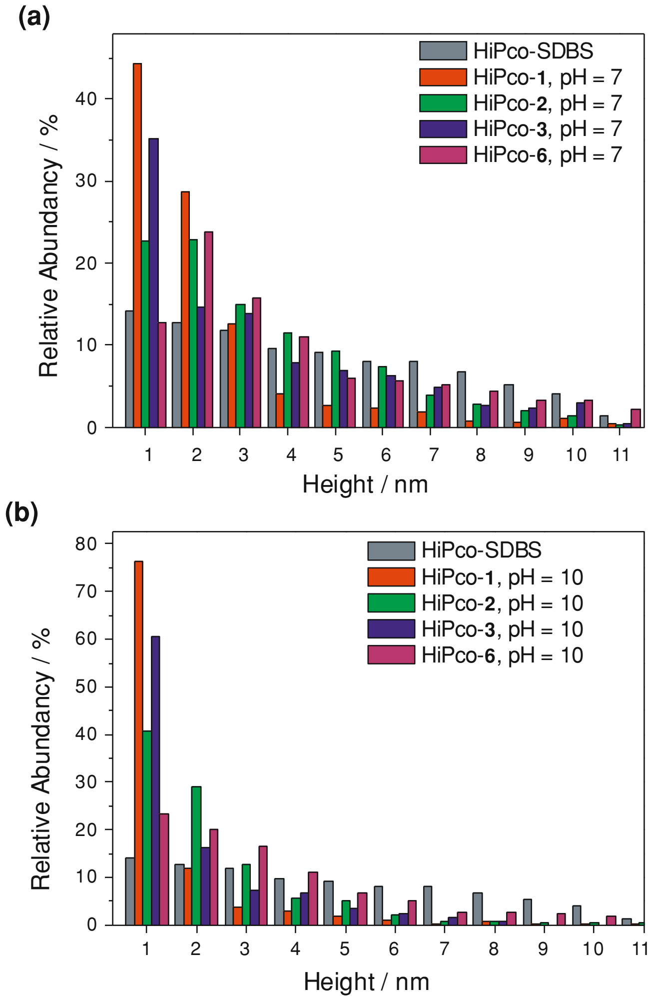

Fig. 3.9 Histograms of the bundle size distributions of nanotubes dispersed in buffered aqueous solutions of **1**, **2**, **3** and **6** ([SWCNT]:[Per] = 1:1, [Per] = 0. 1 g L^{-1}) compared to nanotubes dispersed in SDBS ([SDBS] = 0.01 wt%, [SWCNT] = 0.02 g L^{-1}) derived from statistical AFM analysis after spincasting the dispersions. **a** pH = 7, **b** pH = 10. (Reproduced with permission from Wiley–VCH, reference 2)

Even though AFM is measured on dried samples, the influence of surface adhesion and drying effects is presumably negligible [23, 36]. However, drying effects cannot generally be excluded so that a SWCNT-Per dispersion (HiPco-**3**) was vitrified and subjected to cryo-TEM imaging. Figure 3.10 depicts cryo-TEM images of SWCNTs dispersed in a buffered aqueous solution of **3,** as well as SWCNTs dispersed in an aqueous solution of SDBS [1].

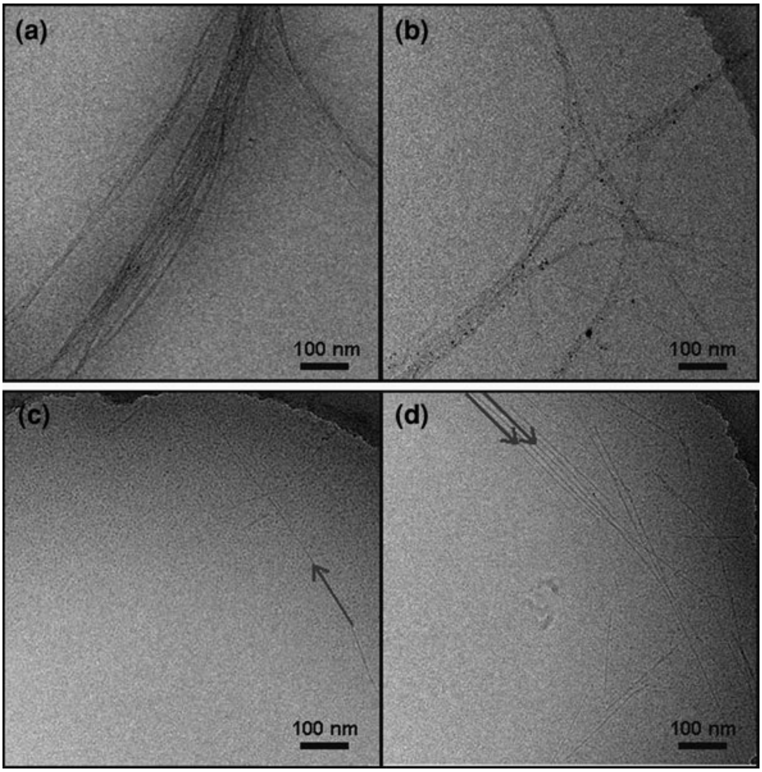

Fig. 3.10 Representative cryo-TEM images of **a**, **b** SWCNT dispersed in SDBS ([SWCNT] = 0.243 g L^{-1}, $[SDBS]_i$ = 10 g L^{-1}) **c**, **d** SWCNT-**3** ([SWCNT] = 0.172 g L^{-1}, $[Per]_i$ = 1 g L^{-1}). The images were recorded from the supernatant after centrifugation in all cases. The *arrows* in c and d serve as optical guide to the very well dispersed SWCNTs in the perylene dispersion. (Reproduced with permission from the American Chemical Society, reference 1)

In contrast to AFM, a high concentration of SWCNTs in solution is desired in order to facilitate the measurement. Thus, a nanotube concentration of 0.243 g L^{-1} for SWCNTs dispersed in a solution of SDBS and a concentration of 0.172 g L^{-1} for SWCNT-**3** was used. As shown by previous cryo-TEM investigations on nanotubes [41–45], the SWCNTs aggregates appear to be extraordinarily straight and long (up to several µm in length) compared to an atomic force microscopic view, where nanotubes tend to coil up due to surface adhesion with the wafer upon drying. The SWCNTs dispersed in SDBS appear as partly individualized tubes, as well as of bundles of up to 20 tubes (Fig. 3.10a, b). In contrast, the nanotubes in SWCNT-**3** appear to be individualized to a higher degree (Fig. 3.10c, d). The overall bundle size is also reduced (about 5 individual tubes). In both cases, surfactant micelles are observed in the background.

Besides, the sidewalls of the nanotubes are decorated with small particles of high density. Presumably, those are iron catalyst impurities present in the pristine SWCNT material [41, 43–45]. An investigation concerning dispersion of SWCNTs in various surfactants by Moore et al. [42] has revealed via cryo-TEM imaging that the amount of the catalytic impurities is drastically reduced by ultracentrifugation. Remarkably, the amount of catalyst particles adsorbed on the SWCNT surface appears to be strongly reduced in SWCNT-**3** compared to SWCNT dispersed in a solution of SDBS without the need for ultracentrifugation, indicating that in the case of **3**, dispersion is restricted to SWCNTs, while a solution of SDBS also disperses a significant amount of impurities. Qualitatively, the cryo-TEM imaging confirms the observations of the AFM study.

As has already been proposed on the foundation of the spectroscopic and zeta potential investigations, the degree of nanotube individualization is increased by 55–58% in the solutions at pH = 10 compared to pH = 7 (Fig. 3.9b) according to the statistical AFM analysis. In the case of SWCNT dispersion by **1**, the degree of exfoliation reaches 76% at pH = 10 with 66% of the starting material being present in the supernatant after centrifugation as deduced from the absorption spectra (Table 3.1). Thus, most strikingly, approximately 50% of the nanotubes in the pristine solid material are individualized by mild ultrasonication with the aid of the designed water soluble PBI surfactant **1**. This superior exfoliation power can be considered as a corner stone for following separation approaches, e.g. by density gradient ultracentrifugation, where nanotube individualization is a fundamental prerequisite.

However, the question arises why the fraction of individualized nanotubes increases dramatically for the perylene based surfactants at pH = 10 compared to pH = 7, even though the charge density on the nanotube surface is approximately equal, as concluded from the zeta potential measurements (Fig. 3.8). It is proposed that the more efficient exfoliation can be traced back to an increased repulsion between adsorbed perylene molecules on adjacent nanotubes in a bundle during the sonication induced unzippering [46] (Fig. 3.11a). At pH = 10 the carboxylic acid functionalities of the perylene derivatives are completely deprotonated [21] so that the head groups bear a higher negative net charge. This results in a stronger inter-perylene Coulombic repulsion. On the one hand this leads to a lower surfactant packing density along the nanotube which is unfavorable for the dispersion. However, on the other hand, the sonication induced exfoliation is rendered more effective, as the head groups of the perylene surfactants on adjacent nanotubes are also subjected to stronger repulsive forces. Most probably, the presence of a π-π-stacking moiety such as the perylene unit is unambiguous for the increased dispersion and exfoliation efficiency, as a strong interaction of the surfactant with the nanotube scaffold can be considered as a prerequisite.

Additionally, the free perylene micelles are presumably less stable at pH = 10 when the carboxylic acid groups of the polar head are completely deprotonated (Fig. 3.11b). This may also lead to an enhanced adsorption rate to the nanotube backbone. Furthermore, the presence of salts in the buffered solutions (Na_2HPO_4 and KH_2PO_4 in the case of pH = 7 and KBO_3 and NaCl in the case of pH = 10,

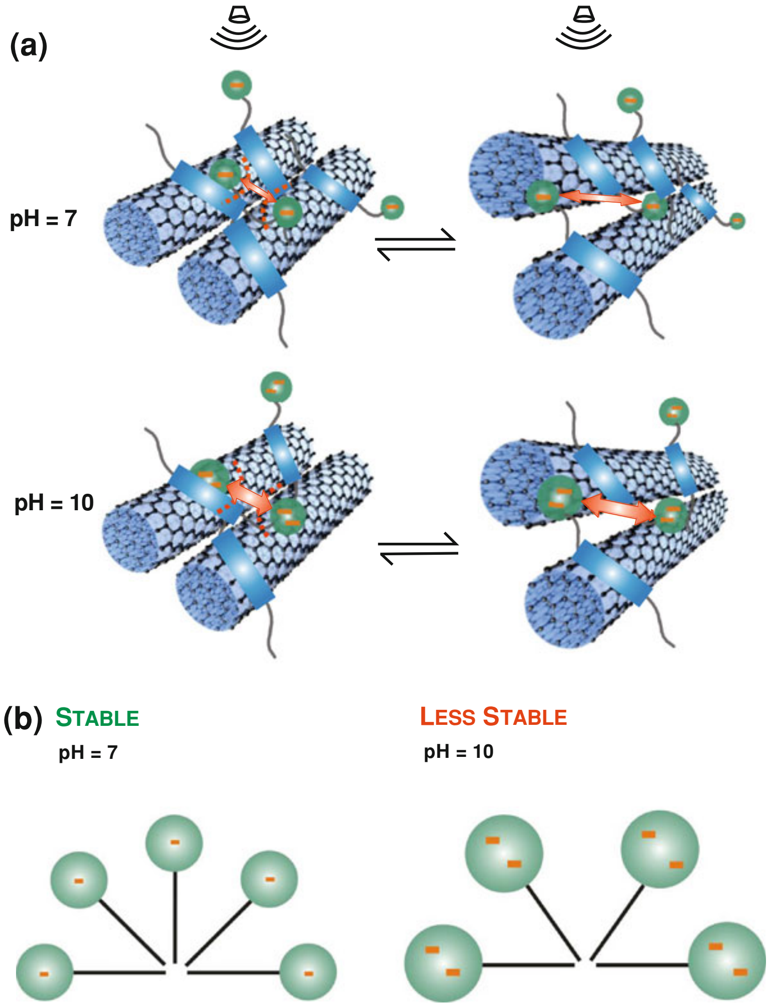

Fig. 3.11 **a** Schematic representation of the proposed mechanism for the increased debundling efficiency of the perylene derivatives at pH = 10 being based on an increased inter-perylene Coulombic repulsion between surfactant molecules adsorbed on adjacent nanotubes during sonication induced unzippering. **b** Schematic representation of the decreased micelle stability upon increasing the charge of the polar head groups. (Reproduced with permission from Wiley–VCH, reference 2)

respectively) may induce differences in the hydration shell of the dispersed carbon nanotubes.

In the following, the puzzling issue of the SWCNT-Per emission properties is addressed again which could not be explained by a variation in the charge density in the vicinity of the nanotubes, packing density of the surfactants or the number of individualized nanotubes in the samples; obviously, a significant amount of nanotubes is exfoliated when dispersed by perylene **2** even though the fluorescence of SWCNT-**2** is totally quenched (Fig. 3.6). Furthermore N_I/N_T also does not correlate with the emission intensity for SWCNT-**1** compared to SWCNT-**3** (a higher amount of individualized nanotubes has been observed for SWCNT-**1**, although the fluorescence intensity is lower for SWCNT-**1** when compared to SWCNT-**3**). Since the zeta potential for the HiPco-perylene dispersions does not significantly deviate for the different perylene derivatives, the charge density in the vicinity of the nanotubes cannot be responsible for such a dramatic alteration of the fluorescence.

Recently, Coleman et al. [32] and Weisman et al. [47] have been able to demonstrate that the fluorescence intensity of an aqueous nanotube dispersion mediated by DNA or peptides, respectively, is widely influenced by the homogeneity of the coverage around the nanotube. It has been proposed that less uniform coatings lead to accelerated exciton decay, as the nanotube surface may be temporarily exposed to perturbations in the surrounding solution. This has been further verified by the group of Papadimitrakopoulos [48].

In order to elucidate whether the variations in emission efficiencies is related to the uniformity of the coating and thus the supramolecular arrangement of the perylene derivatives, analysis of the AFM phase images was performed. AFM phase imaging is the secondary imaging mode of an AFM operating in tapping mode going beyond topographical data. By the aid of phase imaging, variation in composition, adhesion, friction or viscoelasticity can be detected so that phase imaging is a powerful tool to detect differences in materials' properties such as identification of different components in composite materials [49–54]. In studies related to nanotubes, AFM phase imaging has for example been used to supply insights in the ordered helical wrapping of single-stranded DNA strands around the nanotube scaffold [55, 56]. In AFM phase imaging the phase lag between the periodic signal that drives the cantilever and the oscillation of the cantilever is mapped. The changes in the phase lag can be often related to changes in the materials' properties.

Figure 3.12 depicts typical AFM phase images of SWCNT-**1**, SWCNT-**2**, SWCNT-**3** and SWCNT-**6** (pH = 7). Additionally to nanotubes which appear uniformly coated, areas of not-homogenously coated nanotubes (exemplarily marked by the arrows in Fig. 3.12) are observed which give rise to a higher contrast in the images (black regions/aggregates) attributed to perylene aggregates in the cases of **1**, **2** and **3**. The coating uniformity is therefore reflected in the ratio of the area of perylene A_{Per} to the total area of all objects A_{total} (the lower the ratio, the more homogenous is the coating). For the determination of A_{Per} the area of the black aggregates on the SWCNTs has been measured by grain size analysis. This area was added to the area of the objects giving rise to a lighter contrast obtained by shifting the analysis boundary to yield A_{total}. It is important to note that analysis is restricted to AFM images where no free perylene or buffer is mapped. Since a significant amount of not-nanotube objects is always observed for SWCNT-**6** even after rinsing the wafers with deionized water, the analysis of the phase images could not be performed in this case. This observation is attributed to the formation

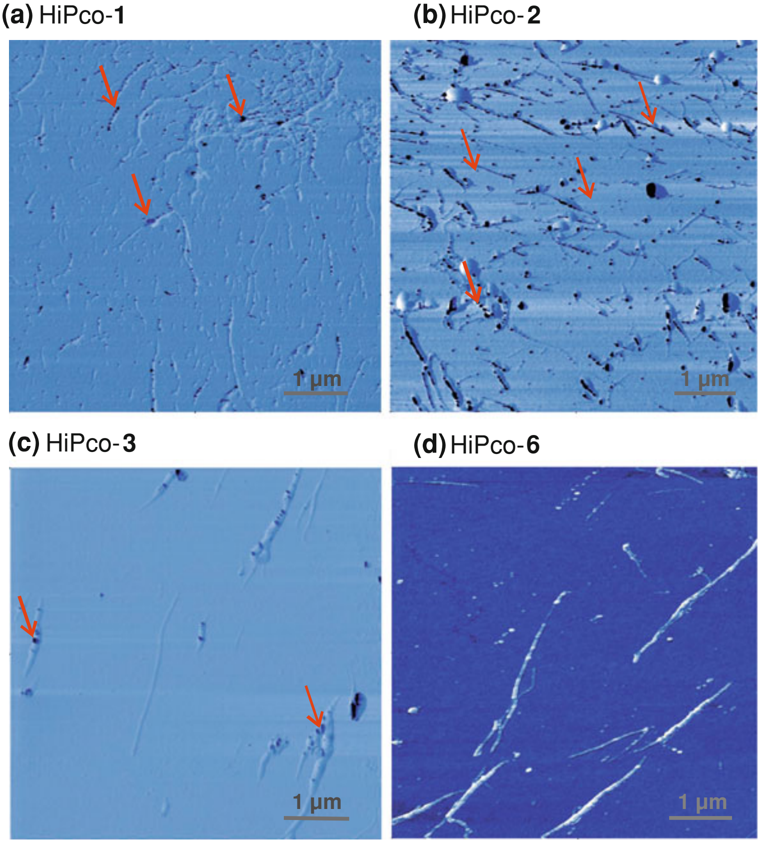

Fig. 3.12 Representative AFM phase images of **a** SWCNT-**1**, **b** SWCNT-**2**, **c** SWCNT-**3** and **d** SWCNT-**6** (pH = 7) showing "bare" nanotubes and nanotubes that are inhomogenously covered marked by the *arrows*. In the case of SWCNT-**6**, no inhomogeneities along the nanotubes are observed. (Reproduced with permission from Wiley–VCH, reference 2)

of highly stable perylene micelles, which remain adsorbed on the polar SiO_2 wafer surface. However, qualitatively, no phase contrast between the nanotube surface and the free perylene is apparent being indicative for a highly homogenous covering of the nanotube backbone by the perylene derivative **6**.

Comparison of the ratios A_{Per}/A_{total} for SWCNT-**1**, SWCNT-**2** and SWCNT-**3** reveals that SWCNT-**3** yields the lowest ratio A_{Per}/A_{total} (20.4%), followed by SWCNT-**1** (33.5%) and SWCNT-**2** (41.1%). Thus, it can be concluded that the SWCNTs are most homogenously covered by the amphiphilic perylene derivative **3** and least for the bolaamphiphile **2** carrying highly bulky substituents. This is in complete agreement with the nanotube fluorescence intensity of the SWCNT-Per dispersions, as fluorescence intensity also increases in the order **2** < **1** < **3** further

Table 3.4 Composition of **1** and **2**, as well as the respective HiPco-Per samples according to the XPS survey spectra. A direct comparison of the perylene derivatives in the absence of SWCNTs is not possible due to sample charging upon irradiation with X-rays

	C1s (%)	O1s (%)	N1s (%)
1 calculated	71.8	23.1	5.1
1	69	22	3.8
HiPco-**1**	66	28	5.5
2 calculated	66.6	27.6	5.7
2	82	13	2.7
HiPco-**2**	70.5	23	4.8

supporting the suggestion that less homogenous coatings lead to accelerated exciton decays.

In an attempt to further elucidate the packing densities and homogeneity of the surfactant coverage, dried SWCNT-Per samples have been subjected to X-ray photoelectron spectroscopy (XPS). In photo electron spectroscopy, a solid sample is irradiated by monochromatic light and the energy distribution of the photo emitted electrons is detected which allows to determine the electron's binding energy prior to the excitation. When X-rays are used the atomic core levels are accessible so that the surface elemental composition can be determined. This is highly versatile in SWCNT derivatization with hetero atoms, as functionalization degrees can thus be estimated [57–60]. Additionally, chemical shifts may be observed, as the exact binding energy of an element is characteristic to its dielectric environment. The binding energy is directly related to the charge on the atom, e.g. an increasing positive charge yields increased binding energies of the core level [61]. Accordingly, XPS is widely applied for the characterization of covalently functionalized SWCNTs [57–60].

However, XPS is no standard characterization technique to gain insights in SWCNT surfactant interactions, so that first investigations have focused on the bolaamphiphilic perylene derivatives **1** and **2**. This can be traced back to the fact that this technique is extremely surface sensitive due to the small inelastic mean free path of the photoelectrons in the order of a few Ångströms [61]. Sample preparation involved dispersion of the SWCNTs in buffered aqueous solutions (pH = 7) of **1** and **2**, respectively, according to the procedure outlined above and in the experimental section. The resulting homogenous dark red solution was micro filtrated (cellulose nitrate, 0.2 µm pore size), washed with 50 mL deionized water and dried under vacuum at 70°C.

The experimentally derived material compositions according to the XPS survey spectra are summarized in Table 3.4 and compared to the calculated values of the pure perylene derivatives. Unfortunately, the perylene derivatives in the absence of SWCNTs were charged upon the X-ray irradiation. In order to compensate the charging, the samples have additionally been irradiated with low energetic electrons. This leads to a partial decomposition of the material on the one hand and a

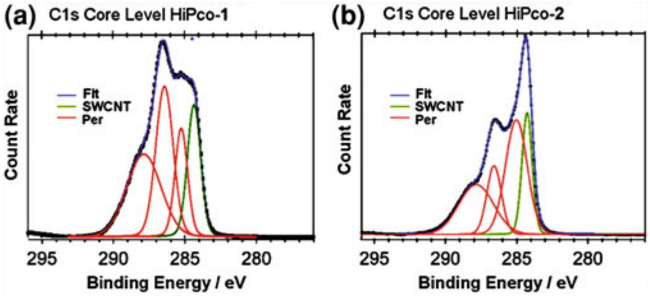

Fig. 3.13 XPS core level spectra of **a** HiPco SWCNTs dispersed by **1** and **b** HiPco SWCNTs dispersed by **2**. In both cases the dispersions have been microfiltrated, washed with deionized water and dried

downshift of the binding energies on the other hand so that no direct comparison is possible.

In both cases of HiPco-Per, only minor contributions from the SWCNTs can be detected, as the experimentally derived surface composition matches the calculated composition of the respective perylene derivatives very closely. This nicely reflects the surface sensitivity of the measurement and reveals that the perylene surfactants almost completely cover the SWCNT scaffold in the dried samples. Nonetheless, subtle differences arise which shall be discussed in the context of the C1 s core level spectra which are depicted in Fig. 3.13.

The C1s core level spectra have to be interpreted with care and should not be overrated due to the presence of multiple carbon species such as acid and amide C = O, imide C = O, sp^3 alkyl carbon, as well as aromatic sp^2 carbon. At least four carbon species can be clearly identified as indicated by the fitted plots in Fig. 3.13. The carbon species with the lowest binding energy of 284.5 eV is attributed to the aromatic carbon atoms of the SWCNTs and the perylene core. The species with higher binding energies of 285.5, 286.5, 288 eV can be assigned to the alkyl carbon atoms, the imide carbon atoms and the carboxyl, as well as amide carbon atoms, respectively and accordingly unambiguously stem from the perylene surfactants. Even though it has been reported that SWCNT doping induces shifts in the C1s core level spectra [5, 62], this issue shall not be discussed due to the multiple overlapping bands in the C1s spectra which cannot be completely deconvoluted and the lack of well-grounded comparison to the perylene surfactant material in the absence of SWCNTs as described above.

Nonetheless, valuable information can be extracted from the XPS measurements. In the case of the smaller bolaamphiphilic perylene dispersant **1** only a vanishing contribution of the SWCNT can be detected in HiPco-**1** as indicated by the surface composition summarized in Table 3.4, as well as from the SWCNT core level peak which is manifested as shoulder in the C1s core level spectrum in Fig. 3.13a. In the case of the sterically demanding bolaamphiphile **2**, the SWCNT surface is less homogenously covered which is reflected in a more pronounced

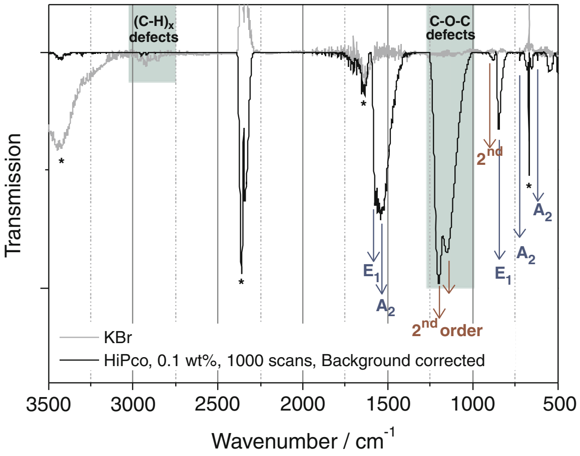

Fig. 3.14 Transmission IR spectrum of pristine SWCNTs in KBr after background subtraction. The KBr reference spectrum is also displayed. The SWCNT active-phonons [66] are indicated by the *blue* and *red arrows*, the vibrations that may attributed to defects are indicated by the *green shaded* background

SWCNT core level peak (Fig. 3.13b), as well as a higher overall carbon content (Table 3.4). Accordingly, the XPS data nicely underline the conclusions drawn on the foundation of the microscopic and spectroscopic investigations above.

Even though XPS demonstrates that the surfactants almost completely cover the SWCNT scaffold in the dried state and are not removed by washing the samples, no quantification of the SWCNT to perylene ratio is accessible due to the pronounced intrinsic surface sensitivity of the measurement. However, a methodology to precisely determine the surfactant packing density quantitatively would be highly desirable as it would greatly facilitate the interpretation of the spectroscopic characterization on the one hand and concomitantly provide a deeper understanding for a future SWCNT surfactant design on the other hand.

To further address this issue, detailed IR spectroscopic investigations have been carried out, as will be summarized in the following. Since the perylene derivatives, as well as the SWCNTs are expected to possess a variety of IR active phonons depending on their chirality [63–65] which have also been observed experimentally [66], it could be envisaged that the ratio of the SWCNTs to the perylene dispersants can be quantified by IR spectroscopy.

In a first set of initial experiments, the optimal conditions for the IR spectroscopic investigation on SWCNTs have been set up. Attempts to measure the IR spectra in attenuated total reflectance failed, presumably due to the high refractive index of nanotubes. Therefore, samples have been prepared by grinding the SWCNTs with KBr with the aid of a ball mill. It has been found that well resolved spectra are obtained by using a nanotube concentration of 0.1 wt% of the as-received material in KBr. In any case, 0.175 g of KBr were pressed to yield the pellets that were immediately subjected to the measurement. A representative background corrected IR spectrum of the pristine HiPco SWCNTs with a resolution of 4 cm^{-1} and 1000 scans is presented in Fig. 3.14.

Please note that a background correction is unambiguously necessary due to the presence of optical SWCNT transitions in the IR region [66]. Despite numerous reports on IR spectroscopy of SWCNTs [63–65, 67–69], a clear identification of the peaks with respect to the calculated IR active phonons has not been possible until 2005 [66]. Based on this work of Eklund et al. [66], a careful peak assignment can be carried out. In agreement with the literature, numerous sharp peaks attributed to A_{2u} and E_{1u}-active phonons arise as indicated by the blue arrows in Fig. 3.14. Furthermore, second order combination modes marked by the red arrows appear. The most dominant peak centered at 1170 cm^{-1}, however, presumably cannot be traced back to IR-active modes in a perfect sp^2 carbon lattice of a nanotube, but rather C–O–C vibrations of defects in the nanotube scaffold. Similarly, broad signals in this region have also been observed experimentally by Eklund and co-workers [66], but have vanished after high temperature vacuum annealing. Since IR spectroscopy in the case of this thesis is used to study non-covalent interaction of the SWCNTs with the designed perylene based surfactants in the bulk material, the origin of the IR active peaks on a molecular scale is not the significant criterion—as long as the peaks stem from the pristine nanotube material.

Bearing this in mind, samples were prepared by grinding different ratios of perylene surfactants and pristine HiPco SWCNTs (P0343). Some representative spectra with **1** as perylene additive are presented in Fig. 3.15. In the as recorded spectra (Fig. 3.15a) the most characteristic peaks have been assigned. The aromatic and aliphatic stretching vibrations (C–H st) of the perylene derivative, as well as the C–H deformation modes (C–H δ) of the dendritic substituents are clearly discernable. Furthermore, three characteristic C = O stretching modes (C = O st) appear corresponding to the imide, carboxylic acid and amide functionalities, respectively. Since the deformation mode (N–H δ) is expected to appear in virtually the same spectral region as the aryl C–C skeletal vibration (arC–C) no clear identification is possible in this case. The arylic C–H deformation modes (arC–H δ) additionally are observed in the low energy region of the spectrum.

Most importantly, all characteristic vibrations are also detected in the samples where SWCNTs were added to the KBr prior to the pellet fabrication. As nicely demonstrated in the normalized spectra displayed in Fig. 3.15b, the perylene signals are superimposed onto the peaks previously attributed to the as-received SWCNT material. By increasing the SWCNT concentration in the pellets, the broad signal centered at 1140 cm^{-1} (denoted as peak 2) subsequently increases with respect to the perylene C = O stretching vibration at 1695 cm^{-1} (denoted as peak 1). Thus, it is possible to plot the intensity ratio of peak 2 to peak 1 as a function of the SWCNT to perylene ratio. As demonstrated in Fig. 3.16, an approximately linear relationship is deduced for both perylene **1** (Fig. 3.16a) and perylene **2** (Fig. 3.16b).

With the aid of the calibration lines, unknown ratios of perylene surfactant to SWCNT can in principle be determined as illustrated for a variety of cases in the following. Samples were prepared by dispersing HiPco SWCNTs in buffered

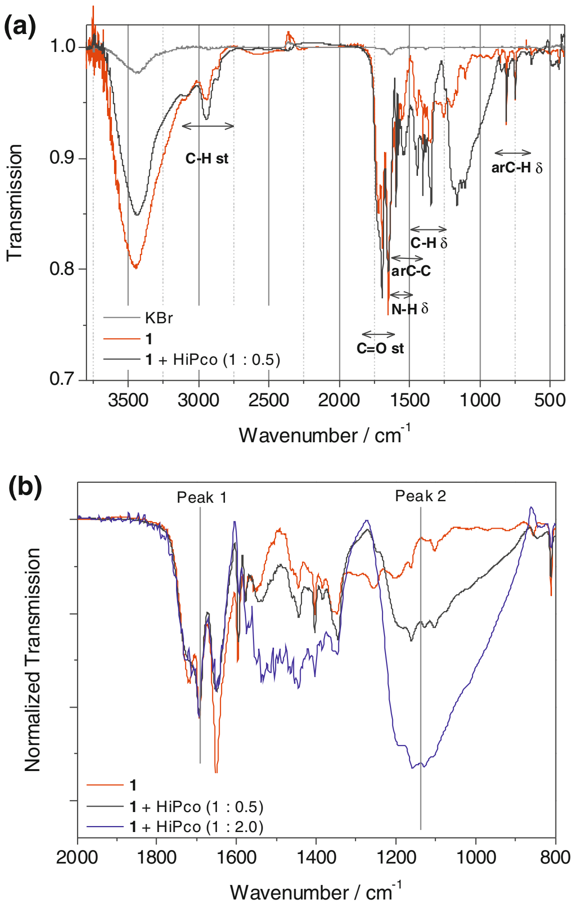

Fig. 3.15 **a** As recorded transmission IR spectra of the perylene derivative **1** in KBr and SWCNTs and **1** in KBr (with a ratio of 1:0.5 by mass). **b** Magnified view of the IR spectra normalized to peak 1 in the presence and absence of HiPco SWCNTs

solutions of **1** and **2** (pH = 7) as described before. One part of the resulting homogenous dispersion was filtrated (cellulose nitrate, 0.2 μm pore size), washed with 50 mL deionized water and dried under vacuum at 70°C. The second part of the dispersion was centrifuged and the supernatant (hereafter denoted as S) and the precipitate (denoted as P) were both processed analogously. The large particles of dried SWCNTs were pestled and afterwards grinded with KBr (SWCNT concentration 0.3 wt%) by ball milling prior to fabrication of the pellets which were then subjected to IR spectroscopy.

The ratios of peak 2 to peak 1 and the ratio of the SWCNT:Per in the samples deduced from the calibration lines are summarized in Table 3.5. To further elucidate the role of the pH value upon dispersion with aid of the designed surfactants which has already been extensively discussed within this chapter, the HiPco SWCNTs dispersed in buffered aqueous solutions of **1** and **2**, respectively, at pH = 10 have also been analyzed.

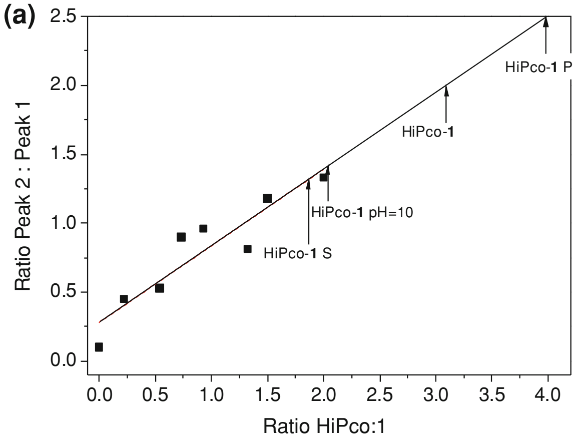

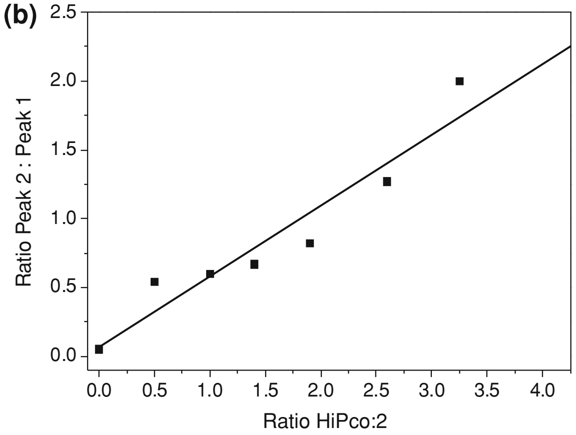

Fig. 3.16 Relationship of the intensity ratio of peak 2:peak 1 defined in Fig. 3.15 to the ratio of SWCNT:Per. **a** perylene derivative **1** (peak 1 at 1695 and peak 2 at 1140 cm^{-1}) and **b** perylene derivative **2** (peak 1 at 1710 and peak 2 at 1123 cm^{-1})

Table 3.5 Tabulated peak ratios from the IR spectra of HiPco-**1** (pH = 7 and pH = 10), HiPco-**1** S and HiPco-**1** P, as well as the ratios of SWCNT:Per according to the calibration lines depicted in Fig. 3.16

	Peak 2:Peak 1	Ratio of SWCNT:Per
HiPco-**1** pH = 7	2.0	3.1:1
HiPco-**1** S pH = 7	1.3	1.9:1
HiPco-**1** P pH = 7	2.5	4.0:1
HiPco-**1** pH = 10	1.4	2.0:1

On the foundation of IR spectroscopy, the ratio of HiPco SWCNT to perylene **1** was determined to be 2:1—an absolutely realistic value, as it has been shown that dispersion at higher SWCNT:Per ratios, e.g. lower perylene content is insufficient for the dispersion of nanotubes (compare Fig. 3.1). The precipitate is characterized by a much lower perylene content (ratio SWCNT:Per = 4:1) due to the decreased surface area in bundles opposed to individualized SWCNTs. Surely, this observation is accompanied by the reasoning that nanotubes with a lower perylene content are not stabilized in aqueous solution and therefore precipitate.

The dispersion in buffered media at pH = 10 (HiPco-**1** pH = 10) is characterized by a much higher content of perylene compared to the dispersion at pH = 7 ((HiPco-**1** pH = 7), e.g. HiPco:**1** approaches the value for the supernatant after centrifugation of the pH = 7 dispersion with 2:1. This is attributed to an increased surface area due to the higher degree of SWCNT individualization as deduced from the AFM analysis (Fig. 3.9). Please note that it has been found by AFM that the amount of exfoliated SWCNTs has been increased by 55–58% in the pH = 10 dispersions. Significantly, the amount of perylene surfactant has been increased by 64% in the dispersion at pH = 10 (e.g. the ratio of HiPco:Per has decreased by 55%) further emphasizing that the IR spectroscopic analysis yields realistic ratios and can indeed by applied to the quantitative determination of the SWCNT:surfactant ratios in the bulk material.

However, the IR spectroscopic investigation still suffers from the drawback that it may not be applied to any SWCNT-surfactant system, as illustrated in the case of perylene **2**. It has previously been revealed in this chapter that the packing density of the derivative **2** is drastically lower compared the structural analogue due to the sterically and especially electro statically demanding second generation *Newkome*-type dendrimers in the periphery of the perylene anchor group. Even though the characteristic perylene vibrations can be identified in the HiPco-**2** spectra, their intensity relative to the SWCNT bands is too low to be used for quantification. An example is depicted in Fig. 3.17b. Nonetheless, the IR spectroscopic investigation for the quantification of SWCNT to surfactant ratios has been fruitful, especially as it can be in principle applied to any functional group giving rise to characteristic IR spectra.

Furthermore, it is interesting to note that the spectra obtained from grinding the SWCNT pristine material together with the perylene derivatives in comparison to the spectra obtained after filtrating and drying the actual dispersions are not identical with respect to peak position and shape. Representative spectra for HiPco-**1** and HiPco-**2** are depicted in Fig. 3.17a, b, respectively.

As denoted by the black arrows in Fig. 3.17, two peaks arise in the HiPco-**1** spectrum at 1280 and 843 cm^{-1} which are not present in the spectrum of **1** or HiPco+**1**. Furthermore, a slight blueshift of the SWCNT band at 1170 cm^{-1} appears. A similar trend is observed in the case of HiPco-**2,** as bands at 1284 and 843 cm^{-1} appear when the perylene moiety is in contact with the SWCNT scaffold in contrast to spectra where both components have been mixed. The spectra indicate that an interaction between the perylene moiety and the SWCNT scaffold can be observed by IR spectroscopy. However, further investigations concerning this subject are deemed necessary.

In summary, IR spectroscopy is a useful characterization technique, as the ratio of nanotube to perylene in the dried samples can be determined quantitatively. This methodology bears the advantage that it involves a readily available technique and that it is in principle applicable to any covalently or noncovalently

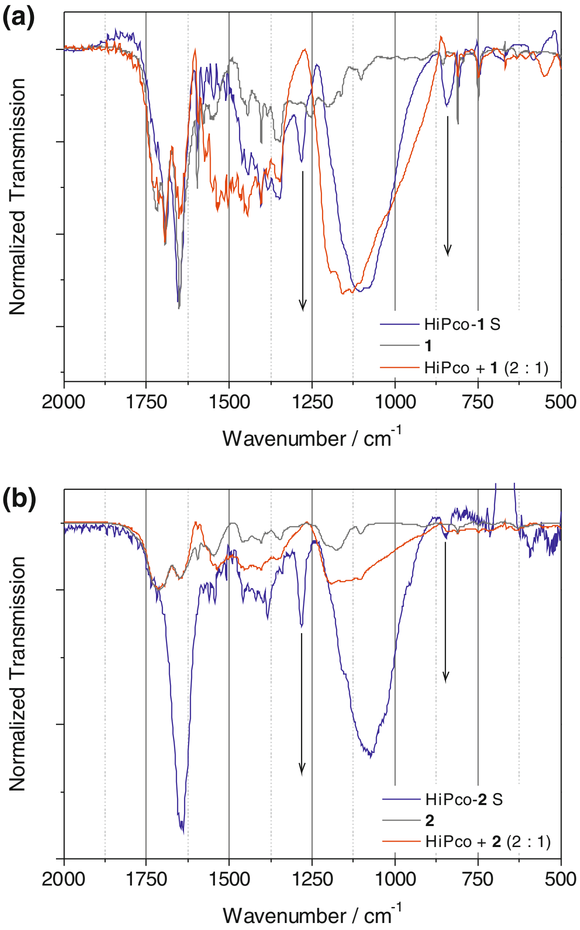

Fig. 3.17 Transmission IR spectra normalized to the C = O vibration at 1695 cm^{-1} of Per, Per in the presence of HiPco SWCNTs by grinding SWCNTs and the perylene derivative in KBr) and a dried dispersion of HiPco-Per S after filtration and drying. **a** Spectra with the perylene derivative **1** and **b** spectra with the perylene derivative **2**

bound species, as long as characteristic IR active phonons are present. However, the situation in the dried state may not precisely reflect the packing densities in solution, as a partial desorption and/or rearrangement on the SWCNT surface may be induced by sample processing which involves filtration, washing and drying. Therefore, considerable attention shall be directed towards the characterization of the dispersions by analytical ultracentrifugation in solution (Sect. 3.1.2).

Nonetheless, the results obtained from the variety of characterization techniques including absorption and emission spectroscopy, zeta potential, AFM, XPS and IR spectroscopy nicely underline the complex situation in SWCNT dispersion, especially with the aid of π-surfactants such as the perylene derivatives. A number of factors such as structure of the perylene derivative, as well as sonication and centrifugation conditions, concentration (or rather concentration ratios) of surfactant and SWCNTs and other environmental effects such as pH influence the quality of the dispersion and have an impact on the dispersion efficiencies. In the following, another important factor for understanding SWCNT dispersion shall be investigated, e.g. the effect of the counterions on the carboxy-terminated perylene surfactants.

3.1.1.4 The Effect of the Counterion

It has long been known in classical colloidal sciences that the counterion influences the self-aggregation behavior of amphiphiles [70]. However, such an effect has never been investigated in presence of SWCNTs, nor has it been studied whether the counterion influences dispersion efficiencies or individualization rates. It was furthermore recently shown that the counterion effects the self-aggregation behavior of amphiphilic carboxylates into ordered micelles and superlattices in a rather unexpected fashion, as in contrast to classical surfactants, Na^+ possesses the highest affinity to the carboxylates followed by Li^+ and K^+ (the “classical order” would be Li^+–Na^+–K^+) [70].

Accordingly, the question arises, whether the self-aggregation of the perylene surfactants can also be tuned by the presence of the counterion and whether an impact on SWCNT dispersability is discernable [71]. On the foundation of the results discussed in the previous sections, it may be postulated that a less pronounced self-aggregation of the surfactant possibly increases the dispersion efficiencies. Tailoring the self-aggregation by screening the counterion can be regarded as ideal model scenario to elucidate this suggestion, as the same surfactant molecule can be used albeit with different self-aggregation behavior.

Focus is directed towards the bolaamphiphilic perylene derivative **1** equipped with two first generation *Newkome*-type dendrimers. Water solubility of **1** is provided after deprotonation of the carboxylic acid functionalities in the periphery of the perylene core. Thus, commonly, buffered aqueous solutions are investigated, where the perylene derivative is strongly self-aggregating, down to concentrations of 10^{-7} M [3]. In contrast to the previous investigations, no buffer has been used in the following, as the influence of different counterions (Na^+, K^+, Li^+) on the aggregation behavior at low ionic strengths was to be investigated. The stock solutions at $pH = 7$ were prepared by titrating **1** in H_2O (10^{-4} M) with six equivalents of the hydroxide of the respective counterions. The resulting solutions were then subjected to optical absorption and emission spectroscopy, as exemplarily depicted with Na^+ as counterion in Fig. 3.18.

As can be followed in the absorption spectra (Fig. 3.18a), the perylene signature undergoes a dramatic change upon dilution in the non-buffered medium, where aggregation is in general dramatically decreased compared to the buffered medium with higher ionic strengths due to a reduction of charge screening effects. The ratio $A^{0\rightarrow0}$ to $A^{0\rightarrow1}$ of the perylene transitions upon dilution can be fitted to an exponential decay curve with the “decay constant” t being a measure for the tendency of the PBIs to aggregate. The portion of aggregated to monomeric species is shifted to lower $A^{0\rightarrow0}/A^{0\rightarrow1}$ ratios, e.g. more aggregates, at lower

Fig. 3.18 **a** Absorption and **b** emission spectra ($\lambda_{\text{exc}} = 500$ nm) of **1** at different concentrations with 6 equivalents of Na^+ as counterion per mole of perylene dye. (Reproduced with permission from the Royal Society of Chemistry, reference 71)

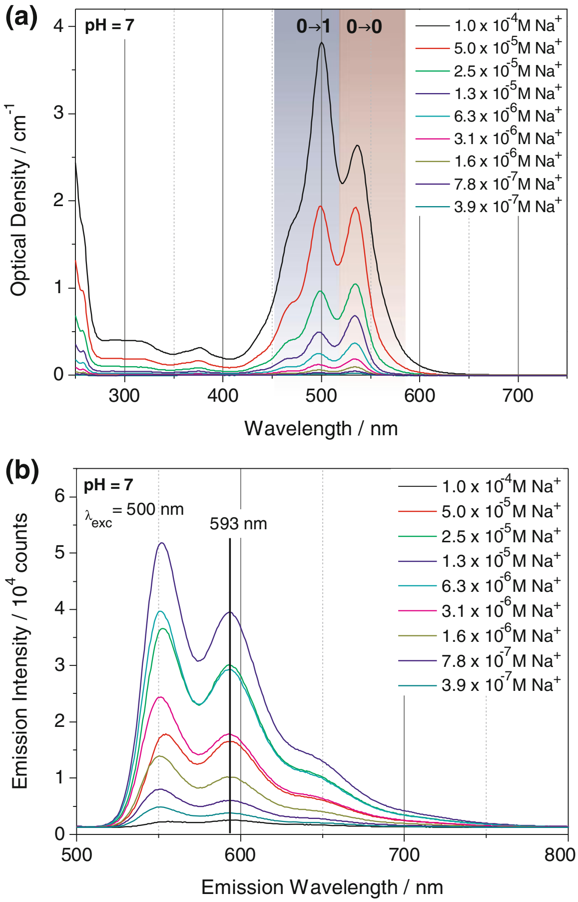

perylene concentrations with Na^+ as counterions giving rise to lower decay constants (Fig. 3.19).

As summarized in Fig. 3.19a, the decay constants increase in the order Na^+–Li^+–K^+. It can thus be concluded that the perylene aggregation proceeds at lower perylene concentrations with Na^+ as counterion, followed by Li^+ and K^+. In a second series of experiments, the pH was increased to 11 by the addition of the respective hydroxide solutions. On the one hand, this ensures a complete deprotonation of the carboxylic acid functionalities of **1** and concomitantly increases the concentration of the counterions. The evolution of the ratio of the perylene $A^{0\rightarrow0}$ to $A^{0\rightarrow1}$ transitions is depicted in Fig. 3.19b. Qualitatively, the same trend is observed as at pH = 7, namely Na^+ exhibits the highest affinity to **1** followed by Li^+ and K^+. The overall decay constants are decreased by a factor of 1.65 ± 0.08 in comparison to the solution at neutral pH—an observation that can be explained

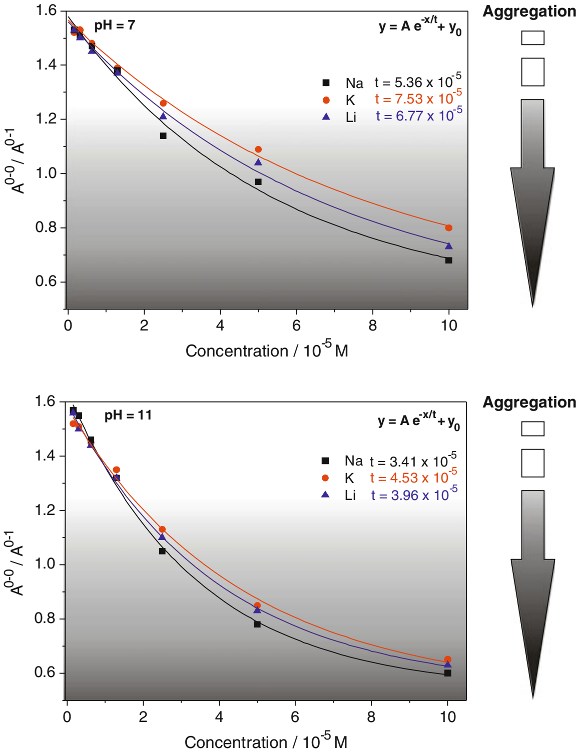

Fig. 3.19 Evolution of the $A^{0\rightarrow0}/A^{0\rightarrow1}$ transitions of **1** in the presence of Na^+, K^+ and Li^+ as counterion at **a** pH = 7 and **b** pH = 11, respectively. The lower the ratio of the $A^{0\rightarrow0}/A^{0\rightarrow1}$, the higher is the degree of aggregation in the perylene sample as indicated by the *arrow*. (Reproduced with permission from the Royal Society of Chemistry, reference 71)

in terms of an increased concentration of the respective counterions resulting in a stronger aggregation tendency.

An important criterion to describe the aggregation behavior of molecules into superstructures is the critical micelle concentration (cmc) being defined as the lowest concentration at which micelles are formed. In the case of PBIs, it can be conveniently determined by the evolution of the perylene emission intensities at different concentrations. The perylene emission arises predominantly from monomeric species so that it does not follow a linear slope when aggregates are formed. The emission intensity at 593 nm was followed (as indicated in Fig. 3.18b), concentrations up to 10^{-4} M have been investigated. At high concentrations, the emission intensity is decreased by innerfilter effects, e.g. an emitted photon is absorbed by neighboring perylene molecules in the solution. However, at 593 nm the innerfilter effect is negligible, as the PBI does not absorb light of this energy.

The PBI emission intensity with Na^+ as counterion at pH = 7 is exemplarily depicted in Fig. 3.20a. At concentrations below the cmc, the emission intensity of **1** increases linearly with the concentration (dashed line in Fig. 3.20). Above the cmc, the data points can be fitted to an exponential decay curve (solid line). The cmc is thus the intersection of both functions as denoted by the arrow in

Fig. 3.20 **a** Determination of the critical micelle concentration (cmc) from the emission intensity at 593 nm where innerfilter effects are negligible, as indicated in the absorption spectra in Fig. 3.18a. The first five data points can be fitted linearly. The next four data points follow an exponential decay curve. The intersection of the extrapolated fit curves yields the cmc. **b** Comparison of the evolution of the emission intensity at pH = 7 and pH = 11 with Na^+ as counterion. (Reproduced with permission from the Royal Society of Chemistry, reference 71)

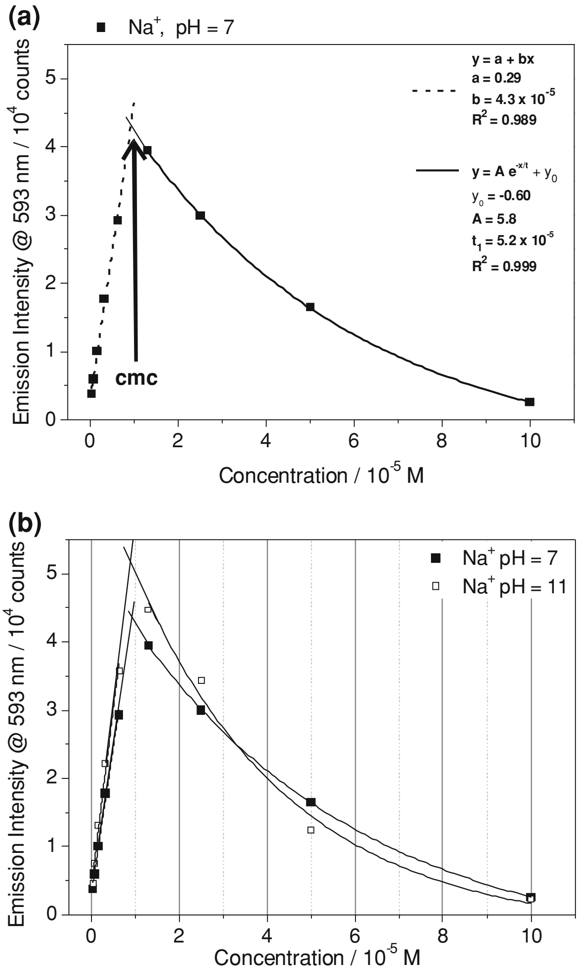

Fig. 3.20a. The results from the determination of the cmc of **1** with Na^+, Li^+ and K^+ at pH = 7 and pH = 11 according to the procedure described above are summarized in Table 3.6.

Significantly, the cmc is lowest with Na^+ as counterion, followed by Li^+ and K^+. This observation is in complete agreement with the decay curves of the absorption spectra where an enhanced affinity of Na^+ has already been proposed within this manuscript, as well as with the investigations on carboxylic amphiphiles published previously [70].

Upon comparing the solutions prepared at pH = 7 and pH = 11, it is striking that the cmc is not dependent on the ionic strength, but only on the nature of the counterion, as it is equal in all cases for pH = 7 and pH = 11. However, similarly to the absorption spectroscopic investigation, the decay constants of the emission

Table 3.6 Critical micelle concentrations of **1** determined as outlined in Fig. 3.20 with Na^+, Li^+ and K^+ as counterions being a measure for the affinity of the respective counterions to the carboxylic acid groups of **1**

	cmc (Na^+)	cmc (Li^+)	cmc (K^+)
pH = 7	0.94×10^{-5} M	1.12×10^{-5} M	1.18×10^{-5} M
pH = 11	0.94×10^{-5} M	1.13×10^{-5} M	1.19×10^{-5} M

Table 3.7 SWCNT dispersion efficiencies of **1** with different counterions determined on the foundation of absorption spectroscopic data. The initial nanotube concentration c_i was kept constant and the concentration in the supernatant after centrifugation c_S has been calculated from the optical density at 735 nm and the extinction coefficient of HiPco SWCNTs [2]. The initial perylene concentration in all experiments was 5×10^{-5} M

		c_i(HiPco) (g L^{-1})	Optical density at 735 nm (cm^{-1})	c_S(HiPco)	Dispersion efficiency (%)
Na^+	pH = 7	0.05	0.92	0.025	50
	pH = 11	0.05	0.88	0.024	48
Li^+	pH = 7	0.05	0.90	0.025	50
	pH = 11	0.05	1.23	0.034	64
K^+	pH = 7	0.05	0.90	0.025	50
	pH = 11	0.05	1.59	0.044	88

intensity *vs.* concentration above the cmc are lower at pH = 11 compared to pH = 7 indicating that the perylene aggregation proceeds more rapidly at pH = 11 where the concentration of the respective counterions is higher (Fig. 3.20b).

As can be concluded from the experiments analyzed above, the PBI **1** has an increased tendency to aggregate in the presence of Na^+ ions compared to the other alkali metal ions Li^+ and K^+. Since the perylene derivative **1** is an excellent SWCNT dispersant, the question arises whether the nature of the counterion not only influences the perylene self-aggregation, but also the aggregation on the SWCNT scaffold which ultimately influences the dispersion efficiency. To shed light into this question, 0.05 g L^{-1} HiPco SWCNTs were immersed into the 5×10^{-5} M solutions of **1**. The ratio of PBI to SWCNT is thus approximately 1:1 by mass and therefore similar to the conditions previously applied for the investigations in buffered media. After sonication (20 min, bath type sonicator), the resulting dispersions have been mildly centrifuged (15 krpm, 30 min) in order to remove coarse aggregates. The concentration in the supernatant calculated from the extinction coefficients of HiPco SWCNTs in aqueous media as a measure for the dispersion efficiency of the surfactant with the respective counterions are summarized in Table 3.7. Interestingly, the counterion does not influence the dispersion efficiency at pH = 7 at all. In all cases 50% of the pristine SWCNT material is stably dispersed by **1** in the supernatant after centrifugation. As comparison to the values in buffered media (33%, Table 3.1), the dispersion efficiency is increased, as **1** is less prone to self aggregation and thus presumably more easily accessible to adsorption on the SWCNT scaffold.

Therefore, one might expect that the dispersion efficiency is increased when counterions are used which lead to a reduced perylene aggregation in comparison to Na^+, e.g. Li^+ or even more pronounced K^+. Even though no effect in the concentration range has been observed at pH = 7, the influence of the counterion becomes clearly discernable in the pH = 11 solutions. A pronounced counterion effect is detectable when approaching higher concentrations of the counterion at pH = 11. Thus, not only the pH value (as discussed in Sect. 3.1.1.3), but also the counterion influences the surfactant capabilities of the perylene based additives. Most significantly the dispersion efficiencies with Li^+ as counterion are increased to 64% and to even 88% with K^+ as counterion under basic conditions with **1** as dispersant (Table 3.7).

To conclude this chapter, it has been demonstrated that the counterion strongly affects the self-aggregation behaviour of perylene carboxylates. On the foundation of absorption and emission spectroscopy, it has been revealed that Na^+ is more strongly bound to the carboxylic acid functionalities of the PBI **1** compared to Li^+ and K^+ leading to a more pronounced self-aggregation. Thus the aggregation behaviour of perylene carboxylates can be tuned by the presence of the respective counterions. To demonstrate the importance of such effects, the SWCNT surfactant capability of **1** in dependency of the counterion and the pH has been investigated by absorption spectroscopy. Understanding the interaction of **1** with different counterions has thus enabled to increase SWCNT dispersion efficiencies of the designed perylene based surfactant to 88% by using K^+ as counterion, as perylene self-aggregation is suppressed in this case.

3.1.2 Characterization of SWCNT-Surfactant Dispersions by Analytical Ultracentrifugation

3.1.2.1 Tracing the Interactions in a Surfactant-Intercalant Approach

In an attempt to further increase the dispersion efficiencies of the designed perylene derivatives, a dispersion concept originally proposed by Paik and co-workers [72] involving the use of a small intercalant molecule additionally to the dispersant has been applied. Since the designed perylene surfactants carry rather bulky dendritic substituents in the periphery in order to ensure their water solubility, it is reasonable to suggest that these large molecules cannot easily slip between adjacent SWCNTs in a bundle during the sonication induced unzippering. Accordingly, the additional use of a small intercalant molecule such as perylene tetracarboxylic acid dianhydride (PTCDA) which should also possess a high affinity to the SWCNTs [73] may increase the overall dispersability, even though PTCDA itself is insoluble in aqueous media.

Table 3.8 Tabulated optical densities at 740 nm ($OD_{740\ nm}$) of the SWCNT-**3**-PTCDA supernatant dispersions after centrifugation and the corresponding calculated nanotube concentrations. In all cases, the initial nanotube concentration is 0.1 g L^{-1}

	pH = 7		pH = 10	
	$OD_{740\ nm}$ (cm^{-1})	[SWCNT]/g L^{-1} (%)	$OD_{740\ nm}$	[SWCNT]/g L^{-1} (%)
HiPco-**3**-PTCDA (2:3:0)	1.4	0.039, 39	1.9	0.048, 48
HiPco -**3**-PTCDA (2:3:1)	2.0	0.054, 54	2.8	0.071, 71
HiPco -**3**-PTCDA (2:3:2)	2.3	0.064, 64	3.5	0.088, 88

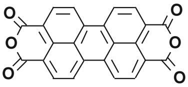

PTCDA

In order to evaluate this concept, dispersions have been prepared with varying ratios of the perylene surfactant **3** and the intercalant PTCDA in buffered solutions of pH = 7 and pH = 10, respectively [74]. HiPco SWCNTs with a constant concentration of 0.1 g L^{-1} have been immersed in the aqueous solutions. The mixtures have been sonicated (30 min, bath type) and centrifuged (15 krpm, 30 min) in order to remove coarse SWCNT aggregates and insoluble PTCDA. The optical densities at 740 nm of the supernatant solutions are summarized in Table 3.8.

In all cases the dispersion efficiencies were increased by the addition of PTCDA. The efficacy of the two-component dispersant system is underlined by the fact that up to 88% of the initial SWCNTs are stably dispersed at pH = 10 with a **3**:PTCDA ratio of 3:2 (by weight). Considering that the HiPco SWCNTs used in this study have a purity of 95%, it becomes clear that the dispersion of the nanotubes in aqueous media is almost quantitative in this case. However, further investigations are deemed necessary to understand the role of PTCDA in the dispersion process. With respect to the efficacy of this novel two component surfactant-intercalant dispersant system, it is worth noting that it has also been applied to the dispersion of graphite to yield graphene stabilized in aqueous media. Initial results obtained by absorption spectroscopy, AFM and Raman have been highly promising. However, no further focus has been directed towards this independent area of research within this thesis.

The optical absorption spectra of the HiPco-**3**-PTCDA dispersions (at pH = 7 and pH = 10) are displayed in Fig. 3.21. All SWCNT dispersions have been diluted 1:1 with the respective buffered aqueous solutions of **3** ([**3**] = 0.15 g L^{-1}) prior to acquisition of the spectra. Even though no relative changes in the excitonic SWCNT transitions are discernable, the absorption spectra yield valuable information with regard to the perylene absorption bands.

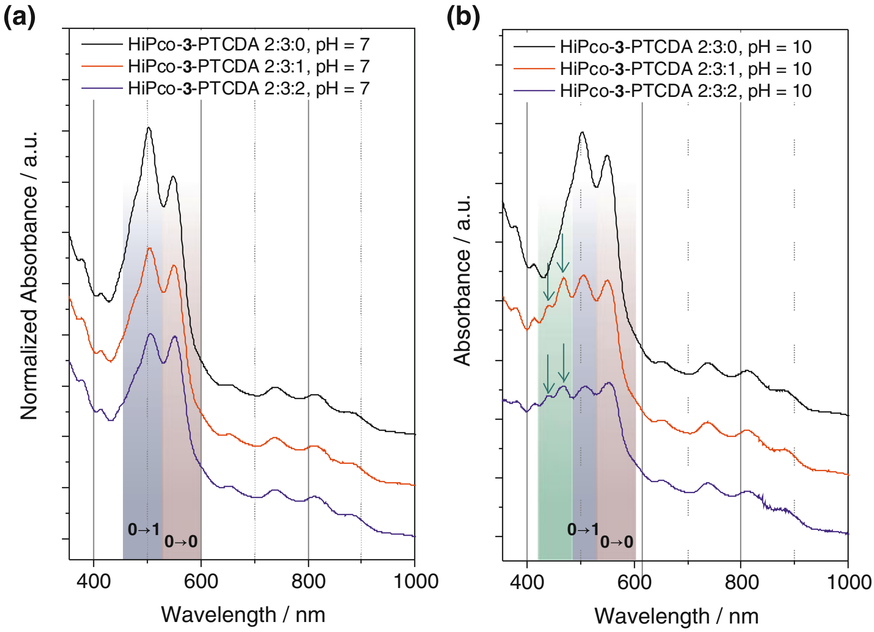

Fig. 3.21 Optical absorption spectra (normalized to the minimum) of the SWCNT absorbance at 1020 nm dispersed in buffered aqueous solutions of **3** (0.15 g L^{-1}) with and without the addition of PTCDA ($[SWCNT]_i = 0.1$ g L^{-1}). In all cases, the supernatant after centrifugation was diluted 1:1 by volume with the buffered aqueous solution of **3**. The spectra are offset for clarity. **a** pH = 7, **b** pH = 10. The perylene surfactant transitions are marked by the *blue* and *red* shaded background. The *green* color indicates the absorption bands attributed to the addition of PTCDA

As already discussed extensively in Sect. 3.1.1, the peaks centered at 500 and 550 nm are attributed to the perylene 0→1 (blue shaded background in Fig. 3.12) and 0→0 transitions (red shaded background), respectively. The intensity ratio of the perylene transitions can qualitatively be used as measure for the degree of perylene aggregation. A relative increase of the 0→1 transition with respect to the 0→0 indicates the presence of an increased amount of monomeric perylene species. Since the perylene surfactants adsorb to the SWCNT scaffold as monomeric species, such a change in the perylene transitions as discernable in the samples where PTCDA has initially been added (red and blue traces) is indicative for an enhanced interaction with the SWCNTs. This can be rationalized in terms of an increased surface area of the nanotubes, as more nanotubes are efficiently dispersed and exfoliated by the addition of the PTCDA intercalant as indicated by the increased dispersion efficiencies.

Furthermore, additional bands centered at 438 and 465 nm arise in the absorbance spectra of the SWCNT-**3**-PTCDA dispersions at pH = 10 (marked by the greed shaded background in Fig. 3.21b). These may be attributed to the presence of PTCDA adsorbed on the SWCNTs or stabilized by free surfactant **3**. However, both explanations are strongly challenged by the observation that no such species have been detected in the $pH = 7$ dispersions. Despite the extraordinary dispersion efficiencies of this two component surfactant system, a variety of questions remain unanswered, as a convincing resolution of the colloidal structures in the dispersion cannot be captured from steady state absorption spectroscopy. For example, it is not clear whether PTCDA is adsorbed onto the SWCNT scaffold or whether it is stabilized by free surfactant micelles of **3**. The absence of the absorption peaks that may be assigned to PTCDA in the $pH = 7$ solutions is also a puzzling issue.

Thus it would be highly desirable to directly visualize the different colloidal systems of the dispersion. An ideal characterization tool to elucidate the role of PTCDA is found in analytical ultracentrifugation with a multiwavelength detector, where full absorption spectra $c(\lambda)$ at each radial position r at each time step t during the sedimentation process can be mapped. Since the different components of the dispersion such as SWCNT-**3**, free bulk micelles of **3** and presumably other colloids involving PTCDA possess unique absorption characteristics, the visualization of their distinct sedimentation profiles will allow attribution to molecular interactions without the need for complex hydrodynamic modeling. Ideally, the dispersion can fully be analyzed in a single experiment [74].

In order to elucidate the complex interactions in the dispersion, band sedimentation in a multiwavelength analytical ultracentrifuge (MWL AUC) has been carried out which is essentially a spectrometer/CCD synchronized to centrifugal fractionation.[1] The process, raw data and evaluation results are summarized in Fig. 3.22. The SWCNT dispersion was placed in the sample reservoir of a vinograd cell. These cells open a small capillary when the pressure rises during the increasing centrifugal acceleration. This leads to the overlayering of sample (HiPco-**3**-PTCDA with an initial ratio of 2:3:2 in H_2O/buffer $pH = 10$) onto the solvent column of higher density (in this case a 1:1 mixture of H_2O and D_2O) at a radial position of 6.33 cm. Data acquisition started as soon as the final rotational frequency of 55,000 rpm was reached and continued for 78 min, generating 131 snapshots of the fractionation process with a radial step size of 50 μm and 45 s intervals. The full experiment can be captured by a movie in a few seconds and perfectly visualizes the fractionation of fast and slowly sedimenting colloids with very distinct absorption profiles. One of the snapshots from this movie is shown in Fig. 3.22c, where radial Range 1 is defined for the fast moving colloids which sedimented after 7 min already half way to the bottom of the cell on the right. Radial Range 2 defines the slowly sedimenting colloids.

In order to extract the absorption profiles of the different components individual snapshots were chosen and the absorption $c(r,\lambda)$ was integrated over the radial ranges (r) as indicated. The fast moving colloids are best captured at the very beginning (First minute, Fig. 3.22b). The Range 1a (6.5–6.8 cm) is defined with the integrated absorption profile in Fig. 3.22e. This profile is characteristic for the

---

[1] Special thanks is credited to Dr. W. Wohlleben from BASF SE for providing the opportunity to carry out the experiments on the designed MWL AUCand for the help with the data evaluation.

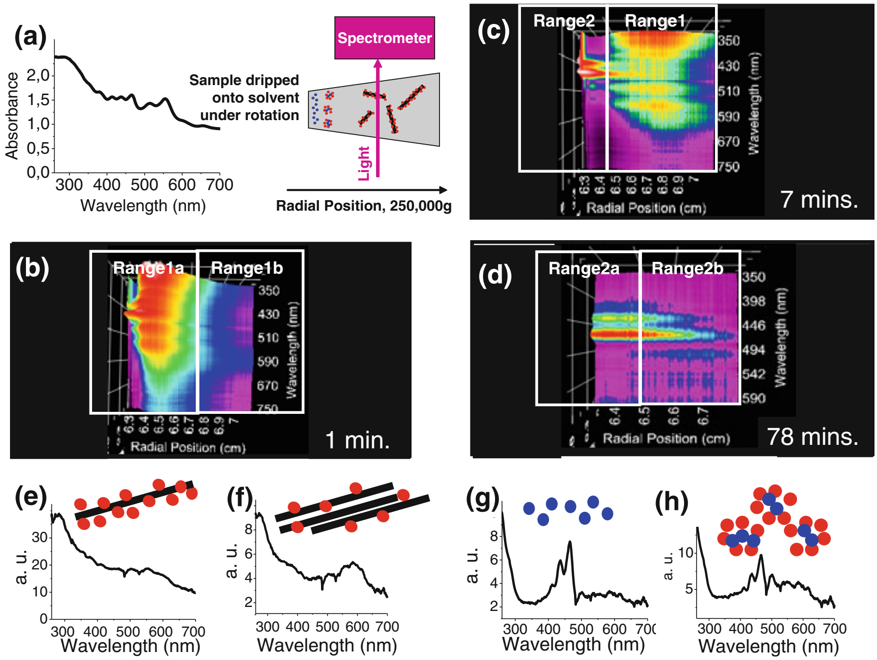

Fig. 3.22 Process, raw data and evaluation of wavelength-resolved band sedimentation. **a** Initial absorption of the CNT dispersion, whereof 15 µL are layered onto the solvent during speed-up of the centrifugal force, which acts in radial direction. Repeated snapshots of $c(r, \lambda)$ are acquired by fast radial scanning of a spectrometer; **b** snapshot at first minute, where only fast moving colloids are visible, evaluated as ranges 1a and 1b; **c** snapshot at seventh minute, where the fractionation of fast (Range 1) and slow (Range 2) sedimenting colloids with their distinct absorption profiles is best visualized; **d** snapshot at 78th minute, where a substructure within the slow colloids appears, evaluated as range 2a and 2b; **e**–**h** integration of the ranges, attributed to **e** individualized CNT with attached surfactant and **f** CNT bundles with few surfactant molecules attached, **g** hydrolyzed intercalant, **h** intercalant—surfactant micelles. (Reproduced with permission from Wiley–VCH, reference 74)

main fraction of the dispersion, namely individualized CNTs encapsulated by the perylene surfactant **3** with its 0→1 transition at 500 nm and its 0→0 transition at 550 nm, respectively. In Range 1b, colloids sedimenting faster than the individualized SWCNTs (6.8–7.1 cm) are also captured. Their absorption profile (Fig. 3.22f) contains comparatively less surfactant in relation to SWCNTs, attributed to a decreased accessible surface area in SWCNT bundles.

The absorption profiles of the slowly sedimenting colloids extracted from the last scan (78th min, Fig. 3.22d) visualize that also the slowly sedimenting colloids are composed of two discrete fractions. One fraction with an absorption peak at 500 nm does sediment (6.55–7.1 cm, range 2b), but another fraction without that absorption component (6.3–6.55 cm, Range 2a) virtually stands still except for some diffusional broadening. The absorption profile of Range 2b (Fig. 3.22h) contains the typical absorption peaks of the perylene surfactant **3** and is hence attributed to surfactant micelles.

The origin of the rather unexpected, but very distinct component of the non-sedimenting Range 2a is puzzling. Its absorption profile (Fig. 3.22g) contains only the peaks originally attributed to the intercalant PTCDA, with vanishing traces of the surfactant **3**. The observation that the absorbance peaks at 438 and 465 nm that may be assigned to PTCDA correspond to a molecule neither associated with perylene surfactant micelles, nor with the sedimenting CNTs strongly suggests that this species is not the PTCDA intercalant, as PTCDA is highly self-aggregating and not water soluble without stabilization.

It is proposed that under the basic conditions employed in the experiment (buffer pH = 10), the anhydride functionalities are opened to yield the corresponding perylene tetracarboxylic acid (PTC). PTCDA presumably initially acts as intercalant during the sonication induced exfoliation of the nanotubes. During the sonication process PTCDA comes in contact with the nanotube surface where it is intermittently adsorbed by π-π-stacking interactions. As PTCDA is a rather small molecule compared to the surfactant **3**, it may also slip between the adjacent nanotubes in large bundles therefore increasing the amount of stably dispersed CNT material. For the pH = 7 dispersions, where no traces of PTCDA have been detected in the stable CNT dispersions, the PTCDA intercalant is presumably replaced by the surfactant **3** resulting in re-aggregation with the remaining bulk PTCDA and thus sedimentation during pre-centrifugation. In the case of the pH = 10 dispersions, the PTCDA is exposed to the basic environment while being adsorbed on the nanotube where it is hydrolyzed to yield the perylene tetracarboxylic acid. Since the experiment is carried out under basic conditions, the carboxylic acid groups of PTC are deprotonated and thus negatively charged. In contrast to the surfactant **3** the charges are located directly next to the aromatic unit (perylene moiety) serving as anchor group to the CNTs so that the π-π stacking interaction is no longer ensured resulting in desorption of the PTC. This explanation is in line with the observation that the structurally similar perylene derivative **7** is not capable of dispersing SWCNTs as described in Sect. 3.1.1.1.

To further evaluate this hypothesis, we have immersed the PTCDA in aqueous media at different pH values. As depicted in Fig. 3.23a, the two main absorption bands centered at 438 and 465 nm appear under basic conditions after sonication for 30 min and stirring the sample for 3 days, while the anhydride functionalities are obviously stable at pH = 7, e.g. no absorption peaks are detected after centrifugation.

Interestingly, in an initial control experiment involving sonication of PTCDA in a buffered aqueous solution of the perylene surfactant in the absence of nanotubes followed by mild sonication and characterization by absorption spectroscopy, no traces of the perylene tetra carboxylic acid have been detected. However, if the sample was left to equilibrate for at least 24 h prior to the centrifugation step, the peaks attributed to the perylene tetracarboxylic acid clearly evolved (Fig. 3.23b). Obviously the presence of nanotubes increases the rate of anhydride hydrolysis, as the PTC is discernable in the supernatant already after 30 min of sonication

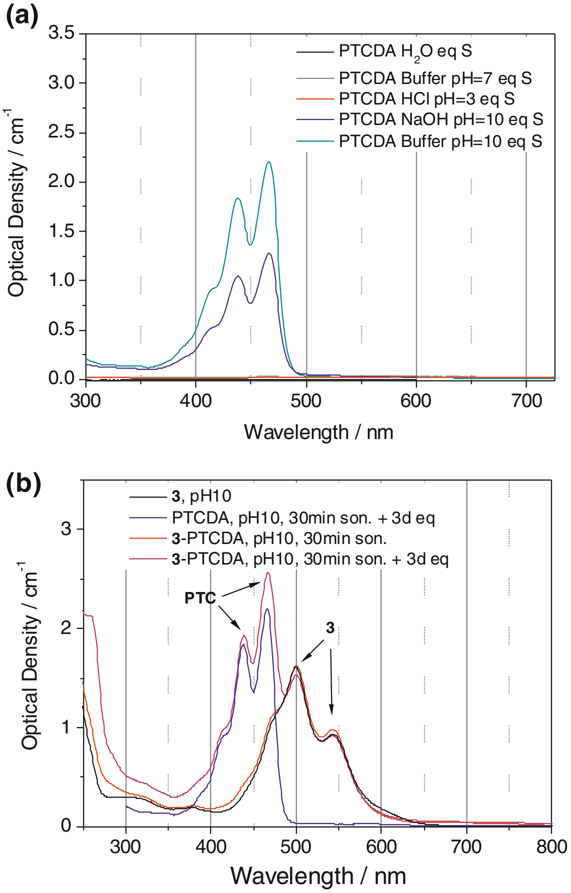

Fig. 3.23 **a** As recorded optical absorption spectra of PTCDA (0.1 g L^{-1}) immersed in aqueous solutions at different pH values. The pH was either adjusted by addition of HCl or NaOH, respectively, or by the use of a buffer solution. In all cases, the supernatant (S) after centrifugation is displayed after 30 min of sonication and 3 d of stirring the mixture (at room temperature) prior to centrifugation, e.g. allowing the system to equilibrate (designated as eq). **b** As recorded optical absorption spectra of **1** (0.15 g L^{-1}), PTCDA (0.1 g L^{-1}) and mixtures of both in buffered aqueous solutions at pH = 10. In all cases, the supernatant after centrifugation is displayed. The peaks centered at 438 nm and 465 nm attributed to perylene tetracarboxylic acid only evolve if the sample was given 3 d to equilibrate for the anhydride to be hydrolyzed

indicating that the PTCDA truly intermittently adsorbs to the SWCNT scaffold where it is exposed to the basic environment.

In summary, dispersion efficiencies of SWCNTs could be significantly increased by a highly efficient two-component surfactant system. The complex, multicomponent absorption spectrum (Fig. 3.21) and the unknown underlying interactions could not be interpreted by bulk characterization techniques. However, in a single measurement with the MWL AUC the existence of distinct components has been visualized and their absorption profiles during their sedimentation have been extracted (Fig. 3.22e–h). Evidence was provided that PTCDA is hydrolyzed at higher pH after executing its role as intercalant. It is suggested that PTCDA is adsorbed on the SWCNT scaffold by π-π-stacking interaction only intermittently. As PTCDA is a rather small molecule it may slip between the adjacent nanotubes in large bundles therefore assisting the exfoliation and increasing the amount of stably dispersed SWCNT material. When being exposed to a basic environment, the PTCDA is hydrolyzed while being adsorbed on the nanotube backbone to yield the perylene tetracarboxylic acid which in turn desorbs from the SWCNT surface. By the use of a unique centrifuge spectrometer recording the entire UV/Vis absorption during fractionation of $\sim 10^{10}$ colloids, this complex SWCNT dispersion could be analyzed in a single experiment. Beyond this application, analytical ultracentrifugation is certainly a highly potent characterization technique for SWCNT dispersions, which can be regarded as classical colloidal systems. In principle, this gives access to their hydrodynamic characterization on the foundation of sedimentation experiments as will be outlined in the following.

3.1.2.2 Hydrodynamic Characterization of Various SWCNT-Surfactant Systems

Even though centrifugation is widely applied in SWCNT research, quantitative studies on the hydrodynamic properties of surfactant encapsulated SWCNTs during centrifugation are only scarcely spread. Nair et al. have used a hydrodynamic model to describe the motion of SWCNTs in a centrifugal field [75]. However, the study was based on the buoyant densities and the spreading of the nanotubes close to their isopycnic points. Since the buoyant density also includes a large hydration shell, it is not possible to draw conclusions on the mass and volume of the surfactant layer without the hydration shell.

In an alternative approach, Hersam and co-workers [76] have characterized the hydrodynamic properties of sodium cholate encapsulated CoMoCAT SWCNTs by the aid of an analytical ultracentrifugation. This allowed a more direct investigation, as the hydration layer which has convoluted the results of Nair et al. does not need to be considered in this case, as its density is approximately equal to the density of water. Thus, the sedimentation velocity of a SWCNT-surfactant complex depends on the anhydrous partial specific volume.

In general, the sedimentation velocity of particles in a centrifugal field is determined by the sedimentation and diffusion coefficients, as well as the hydrodynamic frictional coefficients. It can be measured by analytical ultracentrifugation where the temporal and spatial distribution of the sedimenting species can be directly detected in situ, e.g. by absorption spectroscopy (Fig. 3.24). Other optics such as interference, turbidity, *Schlieren* and X-ray are available for in situ detection [77, 78], but absorption is most suitable for nanotube characterization.

As outlined by Hersam et al. [76], the classical technique of differential sedimentation in H_2O and D_2O [79, 80] can be applied also to nanotubes. The determination of the sedimentation, diffusion and hydrodynamic frictional coefficients [81] in H_2O and D_2O enables the calculation of the anhydrous molar volume of the surfactant encapsulated SWCNTs. Based on this result, conclusions on the linear packing density of the surfactant on the nanotube surface can be drawn. For detailed explanations on the theoretical background, please see the corresponding Ref. [76].

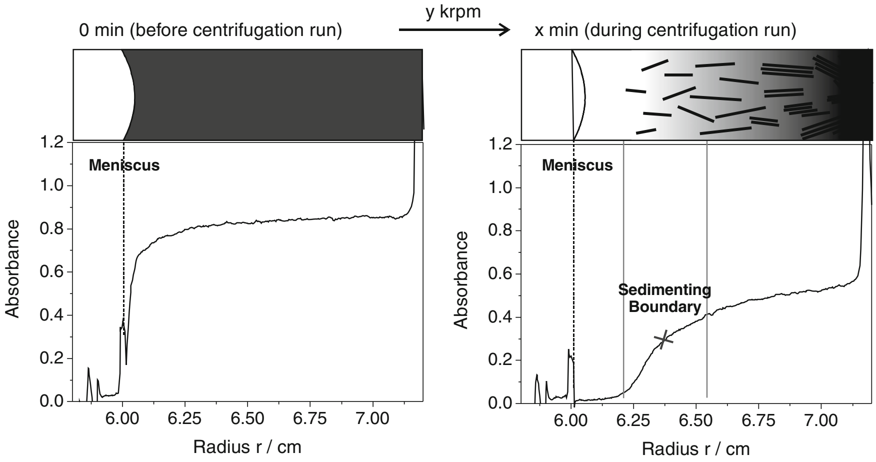

Fig. 3.24 Schematic representation of SWCNTs in an analytical ultracentrifuge cell (*top panels*) before and at a certain time during the centrifugation. The corresponding plots of absorbance *versus* radius of the cell are displayed in the *bottom* graphs. The meniscus of the solution is identified by an artificial peak in the optical density (*dashed line*) and the sedimenting boundary is found between the *vertical solid lines*, marked by the symbol X. (Reproduced with permission from Wiley–VCH, reference 82)

On the foundation of the study of Hersam and co-workers [76], the hydrodynamic properties of different SWCNT-surfactant systems have been compared as summarized in the following in order to aid the understanding of the interaction of SWCNTs and surfactant molecules in solution which is of uttermost importance for the design of novel, potent SWCNT dispersants. On the basis of the sedimentation rates in water and deuterated water, respectively, the anhydrous specific volumina of SWCNT dispersed in aqueous solutions of the commercially available surfactants sodium cholate (SC) and sodium dodecy benzene sulfonate (SDBS), as well as the three designed perylene based surfactants **1**, **2** and **3** have been determined [82].

The dispersions were prepared by immersing SWCNTs in aqueous solutions of SC and SDBS (10 g L^{-1}) or buffered aqueous solutions (phosphate buffer, pH = 7) of the perylene bisimide derivatives ([Per]:[SWCNT] = 1:1), respectively. Focus was directed to SWCNTs produced by high pressure carbon monoxide decomposition (HiPco) and by cobalt-molybdenum catalysis (CoMoCAT). The dispersions were mildly pre-centrifuged (30 min, 15,000 rpm) in order to remove coarse aggregates and large SWCNT bundles. The top 70% of the supernatant were collected and, if necessary, diluted with the respective surfactant solution to an optical density of approximately 1 cm^{-1} at 740 nm. In contrast to the study of Hersam et al. [76] the pristine SWCNT material was not sorted by diameter via DGU.

The aqueous dispersions were loaded into two-hole Epon cells and subjected to ultra-centrifugation at 40 krpm (25°C). The spatial and temporal distribution of the

SWCNT-surfactant complex was followed by in situ measurements of the absorbance profiles. The thus determined concentration profiles c(r, t, λ) are 3-dimensional [30] and show the expected redistribution upon time when nanotubes are sedimenting as exemplary depicted for HiPco-**3** (H_2O) in Fig. 3.25. Initially, at $t = 0$ the concentration of SWCNTs is uniform along the centrifuge cell. During centrifugation, a net sedimentation of the nanotubes occurs from smaller to larger radii so that the top of the cell becomes depleted of nanotubes, i.e. the optical density is reduced resulting in the development of a boundary (e.g. blue trace in Fig. 3.25a). With increasing time, the boundary broadens and moves towards the bottom of the cell (e.g. black trace). The temporal snapshot in Fig. 3.25b shows perylene-encapsulated nanotubes around 6.5 cm and free perylene micelles close to the meniscus at 6 cm, respectively. It is in fact the primordial advantage of the analytical ultracentrifuge that due to the fractionating measurement principle small colloids (individualized nanotubes) are characterized without any perturbation by the larger colloids (bundles). Bundles sediment faster than individual nanotubes, so that they are removed before detection of individualized SWCNTs starts which sediment significantly slower.

The sedimentation coefficient s, diffusion D and the hydrodynamic frictional f coefficients, specifically the frictional ratios $f f_0^{-1}$ are obtained by fitting the experimental c(r, t) profiles to the multi-component Lamm equation by appropriate programs such as SEDFIT [81, 83, 84].

The sedimentation coefficient s is an instrument-independent measure of the sedimentation speed u, reduced by the centrifugal acceleration: $s = u/\omega^2 r$, where ω is the rotational frequency and r the average radius of the measurement cell from the center of rotation ($r = 6.5$ cm in Beckman XLI machines) [77, 78]. The frictional ratios $f f_0^{-1}$ compares the frictional force acting on a solute with the frictional force acting on a sphere of equal volume. Any deviation from $f f_0^{-1} = 1$ indicates a non-compact, non-spherical morphology [77, 78]. In order to understand the uncertainties in the evaluation procedure, their mathematical basis is also discussed beyond the use of SEDFIT in the study by Hersam et al. [76].

The evaluation first optimizes a volume-weighted distribution of sedimentation coefficients for best fit to the experimental movie of fractionation. In this step, SEDFIT makes use of the temporal evolution of a broadening sedimentation boundary: polydispersity broadening scales linear with time, but diffusion broadening scales with time$^{1/2}$. Subsequently, a regularization procedure assesses automatically whether small changes of the obtained best fit are statistically relevant on the 0.98 confidence level, and reports as final result the average distribution of all statistically indiscernible distributions [81, 84].

The distribution of sedimentation coefficients c (s) is a robust result, which is over-determined because apparent coefficients s^* can be obtained already from a single snapshot, neglecting diffusion. Details of the shape of the c(s) distribution are deconvoluted from diffusion, i.e. are correlated with the frictional ratios. The frictional ratio is obtained only from a global evaluation of the shape evolution of the sedimenting boundary among all snapshots. A 2D fit of both s and $f f_0^{-1}$ multiplies the degrees of freedom and inherently optimizes the quality of the fit.

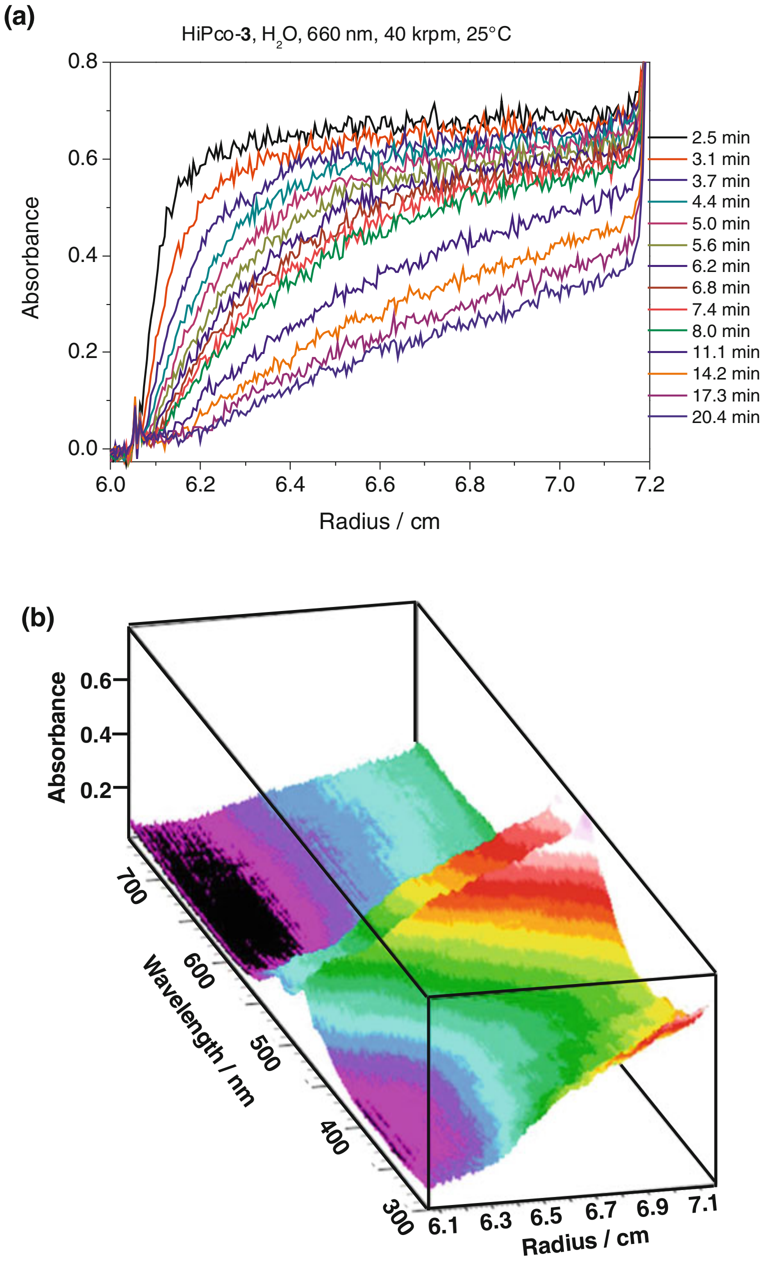

Fig. 3.25 Experimental raw data of HiPco-**3** sedimentation at 40 krpm in H_2O; **a** Concentration c(r, t) profiles at 660 nm detection. The steep rises at 6.0 and 7.17 cm mark the meniscus and the *bottom* of the cell, respectively. **b** Snapshot of c(r, λ) after 32 min. (Reproduced with permission from Wiley–VCH, reference 82)

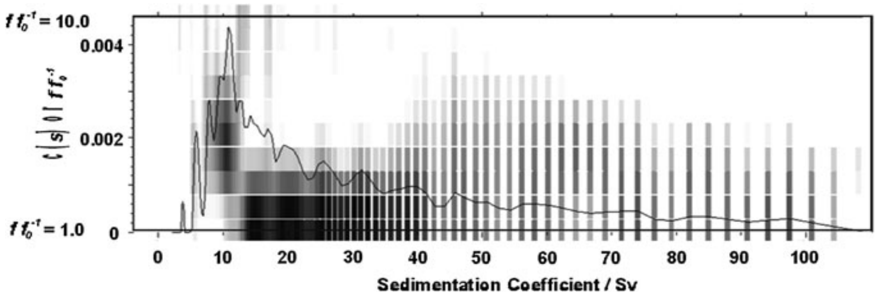

Fig. 3.26 2D-results of frictional ratio and sedimentation coefficient for HiPco-SC in D_2O. The individualized CNTs have a clearly extended configuration with $f f_0^{-1}$ around 5, while the entangled CNTs have a more compact morphology with lower $f f_0^{-1}$. The fitting range for s was 2–120 Sv (log spacing) with $f f_0^{-1}$ from 1 to 10

A 2D grid of 10 values for $f f_0^{-1}$ and 120 values for s is computationally affordable with less than an hour fitting time on a standard PC. The grid spacing in s is chosen to be logarithmic in order to enhance the resolution and the fitting penalty by quadratic deviation in the region of the individualized nanotubes. Results on $f f_0^{-1}$ depend on the rotational frequency chosen for the experiment, because the relative influence of polydispersity and diffusion on the boundary broadening changes with the effective duration of the experiment. The anhydrous specific volume is another caveat. It is experimentally derived from comparison of the sedimentation coefficients s in H_2O and D_2O, but before that, must be specified in the fit to obtain the sedimentation coefficients. The value of was set to 0.5 $cm^3\ g^{-1}$ in the fits, but identical results are obtained for of 0.3 and 0.8 $cm^3\ g^{-1}$.

A typical result is shown in Fig. 3.26. Consistently larger values of $f f_0^{-1}$ for the first peak of slowly sedimenting signals are obtained, identified with individualized nanotubes. Integration over this peak only eliminates any contribution by bundles in the following evaluations. Note that this option is not available in ensemble methods such as fluorescence spectroscopy, dynamic light scattering, zeta-potential, small angle X-ray or neutron scattering etc. Over all experiments, the individualized nanotubes exhibit $f f_0^{-1} = 4.8 \pm 1.8$ (H_2O) and 3.8 ± 1.6 (D_2O), which is a large difference between the averages. The average of the differences is even larger with 40% deviation between frictional ratios fitted from H_2O and D_2O experiments of the same nanotube-surfactant system. This indicates a weak reliability of the shape analysis. Unfortunately, the combined uncertainty from sedimentation coefficient and frictional ratio leads to an even larger average deviation (55%) in the molar masses from H_2O and D_2O experiments. The reason for the discrepancies is the stronger influence of diffusion in the D_2O experiment (all at the same rotational speed), giving SEDFIT the mathematical freedom to model diffusion by low masses alone.

In the majority of experiments, a commercial Beckman Coulter XLA ultracentrifuge was used where only up to three single wavelengths can be recorded. There, the spatial and temporal distribution of the sedimenting species at the

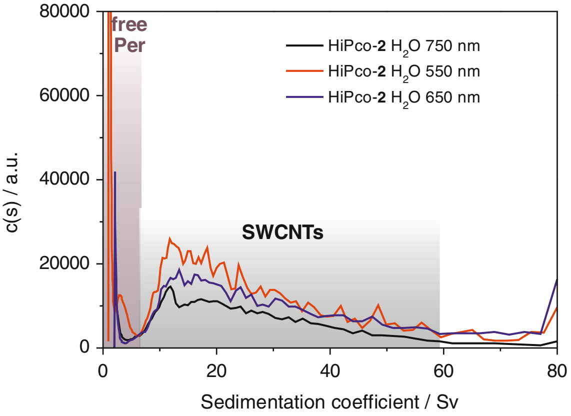

Fig. 3.27 c(s) distributions of the sedimentation of HiPco-**2** in H_2O at three different wavelengths. At 550 and 650 nm, the sedimentation of the free perylene micelles is discernable at sedimentation coefficients below 5 Sv (marked by the *red shaded* background) in addition to the sedimentation of the HiPco-**2** complex (marked by the *grey shaded* background). The sedimentation coefficients of the species attributed to nanotubes is independent on the wavelength. (Reproduced with permission from Wiley–VCH, reference 82)

wavelength 550 nm was followed. At this wavelength, both the nanotubes and the perylene surfactants are captured in a single measurement (but not the SC or SDBS surfactant micelles). Figure 3.27 exemplarily depicts the c(s) distributions of HiPco-**2** at three different wavelength (550, 650, 750 nm). Obviously, hardly any difference in the regime of the sedimentation coefficients attributed to the nanotube species (above 10 Sv) is discernable. This is to be expected for the broad absorption spectrum of nanotubes. However, in the case of 550 and 650 nm, very slowly sedimenting species attributed to free perylene micelles are present. Thus, at a suitable wavelength such as 550 nm, the hydrodynamic characterization of the free surfactant and the nanotube surfactant complexes can be carried out in one experiment.

Table 3.9 gives an overview of the as obtained sedimentation coefficients, anhydrous molar mass M, frictional ratios ff_0^{-1} and anhydrous specific volumina $\bar{v}$ of the SWCNT-surfactant complexes investigated.

From the sedimentation coefficients in water and deuterated water, the anhydrous specific volume of the SWCNT-surfactant complexes can be calculated. The results are also summarized in Table 3.9. Based on the assumption of equivalent surfactant adsorption in water and deuterated water (which is quite reasonable, as surfactant adsorption on the nanotube scaffold is mainly driven by the hydrophobic effect), the anhydrous specific volume $\bar{v}$ can be expressed as

$$\bar{v} = \frac{\eta_H s_H - \eta_D s_D}{\eta_H s_H \rho_D - \eta_D s_D \rho_H} \tag{3.1}$$

Table 3.9 Tabulated data of the sedimentation coefficients s, frictional ratios ff_0^{-1}, anhydrous molar mass M and anhydrous specific volume $\bar{v}$ of the systems investigated

		Sedimentation coefficient s/Sv	Anhydrous molar mass M/kDa	Frictional ratioff_0^{-1}	Anhydrous specific volume $\bar{v}$/cm^{3}g^{-1}
CoMoCAT- SC	H_2O	13.0	750	5.4	0.56
	D_2O	9.2	440	3.8	
HiPco-SC	H_2O	16.6	500	2.9	0.65
	D_2O	10.9	860	5.1	
HiPco-SDBS	H_2O	15.4	1500	6.4	0.83
	D_2O	6.1	210	3.6	
HiPco-1	H_2O	26.6	770	2.7	0.81
	D_2O	11.8	440	3.0	
HiPco-2	H_2O	18.7	2700	4.2	0.69
	D_2O	11.7	510	1.3	
HiPco-3	H_2O	25.8	1600	7.0	0.75
	D_2O	14.8	1100	5.7	

where η is the viscosity of the solvent, ρ is its density and the subscripts H and D denote water and deuterated water, respectively.

Before discussing subtle differences in the sedimentation coefficients with different nanotube surfactants, first of all, the sedimentation velocities in water and deuterated water, respectively, deserve some attention. In all cases, the sedimentation velocity in D_2O is much slower than in H_2O (Fig. 3.28). This can be attributed to the fact that the density of dispersed individualized SWCNTs is greater than 1 so that it matches the density of D_2O (1.104 g cm^{-3} at 25°C) more closely than the density of water (0.998 g cm^{-3}). The anhydrous densities of the individualized component of the SWCNT-surfactant dispersions are measured to be between 1.1 and 1.8 g cm^{-3} (the density is inversely proportional to the anhydrous specific volume summarized in Table 3.9).

Interestingly, the amount of bundled SWCNT species appears to be reduced in case of the samples dispersed in deuterated water, as the peaks with higher sedimentation coefficients are smaller in comparison to the main peak of the individualized nanotubes. This is especially striking in the c(s) distribution of CoMoCAT-SC (Fig. 3.28). This impression is further supported by the observation that all samples in D_2O have intrinsically been of higher optical density, e.g. higher nanotube concentration after the first centrifugation step compared to the samples prepared in water, although the initial nanotube concentration was constant.

Upon comparing the HiPco to the CoMoCAT pristine material, striking difference appear in the c(s) distributions as exemplarily shown for SWCNT-SC (Fig. 3.29). First of all, the s-value distribution attributed to the individualized nanotubes is much broader for the HiPco material compared to the CoMoCAT SWCNTs. This is not surprising, as the diameter and lengths distributions of the HiPco samples are significantly broader, while being much narrower in case of the

Fig. 3.28 c(*s*) distribution for **a** CoMoCAT-SC in H_2O and D_2O and **b** HiPco-SC in H_2O and D_2O derived from fitting the experimental data from the XLA with the model of continuous c(*s*) distribution with logarithmic steps from 5 to 130 Sv with $\bar{v}$ set to 0.6 and ff_0^{-1} to 5. (Reproduced with permission from Wiley–VCH, reference 82)

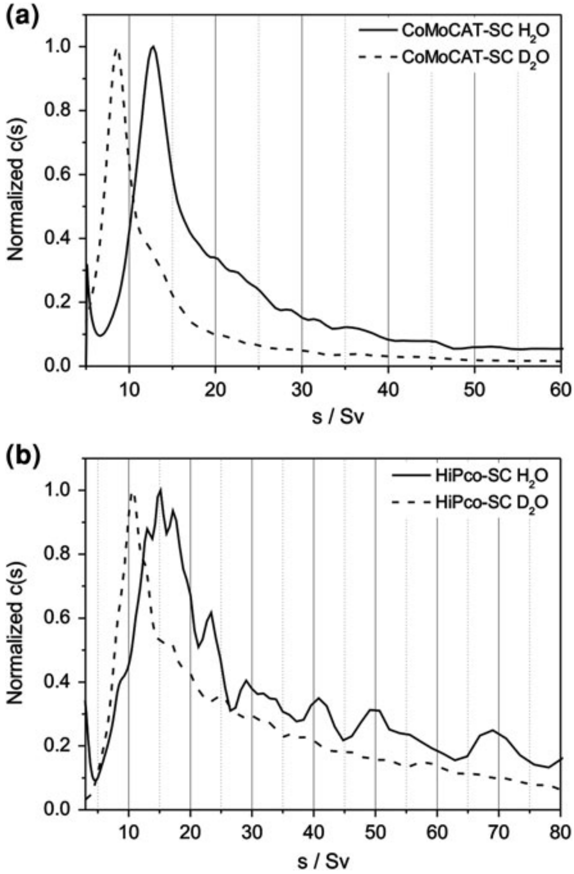

Fig. 3.29 c(*s*) distribution for CoMoCAT-SC and HiPco-SC in H_2O derived from fitting the experimental data from the XLA with the model of continuous c(*s*) distribution. (Reproduced with permission from Wiley–VCH, reference 82)

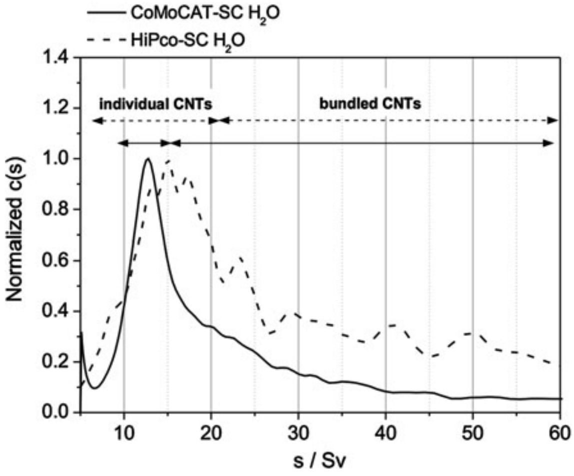

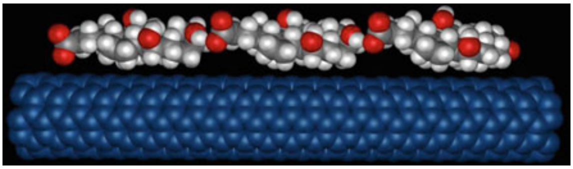

Fig. 3.30 Schematic representation of the adsorption of sodium cholate molecules on the surface of a (6, 5)-nanotube. (Reproduced with permission from Wiley–VCH, reference 82)

CoMoCAT nanotubes. Thus, HiPco SWCNTs are characterized by a broader *s*-value distribution and higher sedimentation coefficients in average.

In the following, comparisons of the anhydrous specific volumina of the SWCNT-surfactant complexes are drawn as foundation for understanding the underlying noncovalent interactions. Regarding the classical surfactants SC and SDBS, significant differences in the anhydrous molar volumina of the HiPco-surfactant complexes have been determined namely the anhydrous specific molar volume with SDBS as surfactant is larger as with SC.

The adsorption of SC has already been extensively studied in the AUC investigation of Hersam and co-workers [76]. It has been revealed that SC is densely packed on the nanotube surface with a linear surfactant density of 3.6 molecules per nm of SWCNT surface. The six-membered carbon rings are believed to stack to the nanotube sidewall with the apolar side not containing the hydroxyl functionalities facing the SWCNT surface (Fig. 3.30). Considering the anhydrous diameter of the (6, 5)-SWCNT-SC complex which was found to be 1.8 nm and the diameter of the (6, 5)-nanotube (0.75 nm), the diameter contribution of one surfactant molecule adsorbed is 0.53 nm.

In contrast to SC the adsorption of SDBS is strongly dependent on the concentration of the surfactant. Even though it has been demonstrated that SDBS is capable of dispersing SWCNTs even at 0.1 cmc (cmc = 1.2 mM = 0.4 g L^{-1}) [13], the concentration of SDBS is most commonly kept higher (10–20 g L^{-1}) as the debundling is more efficient at concentrations of around 14 g L^{-1} (33 times the cmc) [15]. This observation can be attributed to the fact that the orientation of the SDBS molecules on the nanotube surface can either be in a so-called “tails on” conformation (Fig. 3.31a) or “head to tail” with the SDBS molecules being arranged parallel to the nanotube surface (Fig. 3.31b). At low SDBS concentrations the head to tail configuration is favored, while the SDBS molecules tend to “stand upright” at higher concentrations.

Within this thesis, a SDBS concentration of 10 g L^{-1} was chosen so that theoretically, the “tails on” configuration is favored. In this case the diameter of SWCNT-SDBS is expected be approximately d(SWCNT) + 2 (2.4 nm) + *van der Waals* distance, while it is d(SWCNT) + 2 (0.53 nm) for SWCNT-SC [13, 15]. This agrees well with the calculated anhydrous specific molar volume derived from the sedimentation coefficients in water and deuterated water, as $\bar{v}$ (HiPco-SC) was found to be 0.63 cm^3 g^{-1} opposed to 0.83 cm^3 g^{-1} for HiPco-

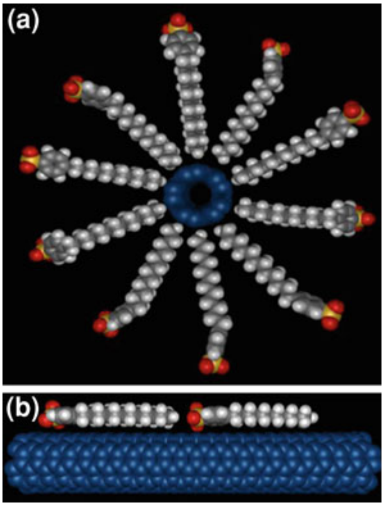

Fig. 3.31 Schematic illustration of the possible adsorption mechanisms of SDBS on a graphitic surface; **a** "tails on" configuration, **b** "head to tail" configuration. (Reproduced with permission from Wiley–VCH, reference 82)

SDBS (Table 3.9). However, it is important to note that additional to the nanotube and SDBS concentration, the nanotube diameter and the ionic strength of the solution also has an impact on the conformation of the detergent on the nanotube surface [85]. Nonetheless, the determination of the anhydrous specific volume by differential sedimentation can be regarded as versatile tool to shed light into the adsorption behavior of various surfactants.

Concerning an analysis of the average sedimentation coefficients *s* attributed to individualized SWCNTs, no significant deviations for HiPco-SC and HiPco-SDBS, respectively, have been determined. However, they appear to be much higher for the HiPco-Per dispersions. On the one hand, the higher sedimentation coefficients could be attributed to a lower degree of debundling in HiPco-Per. However, statistical AFM analysis on the HiPco-Per dispersions has revealed superior degrees of individualization opposed to HiPco-SDBS (Sect. 3.1.1.3). Additionally, the first peak in the c (*s*) distributions attributed to individualized nanotubes has been chosen for analysis which widely eliminates the contribution from bundled nanotubes. On the other hand, it is quite reasonable that individualized SWCNT-Per complexes sediment quicker compared to SWCNT-SC and SWCNT-SDBS, as the perylenes possess higher molecular weight. Even though the molecular weight of the surfactant has a minor impact on the sedimentation rates of metaloxide nanoclusters [86], the situation is different in the case of nanotubes, as SWCNTs are characterized by very high surface areas with low molecular weight. Thus, the molecular weight of the surfactant adsorbed even at moderate packing densities is expected to strongly influence the sedimentation coefficients. Thus, it is not surprising that the sedimentation coefficients in the case of HiPco-Per are increased to values above 20 Sv in H_2O.

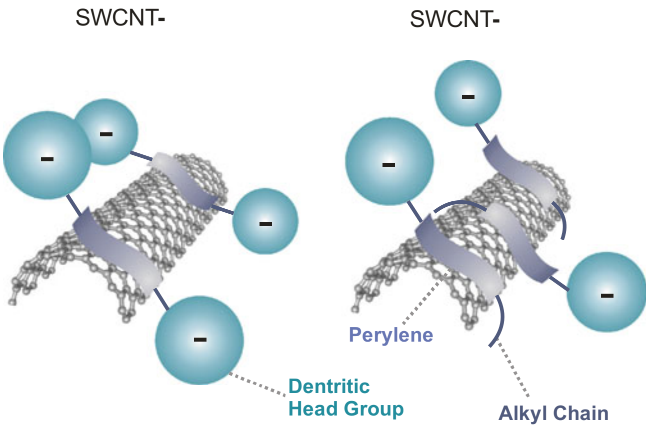

Fig. 3.32 Schematic illustration of possible adsorption of the perylene derivatives **2** and **3**. The packing density of the amphiphile can be strongly enhanced compared to the bolaamphiphile, as an alternating arrangement of alkyl groups and dendritic head groups is possible. (Reproduced with permission from Wiley–VCH, reference 82)

Furthermore, the anhydrous molar specific volumina of the SWCNT-Per complexes deserve some attention, as they are strongly related to the packing density (the number of surfactant molecules per nm nanotube) of the surfactant on the SWCNT scaffold. Upon comparing the two bolaamphiphilic perylene derivatives **1** and **2**, striking differences appear in the anhydrous molar volumina. Even though the bulky bolaamphiphile **2** is larger, e.g. it possesses higher molecular weight, the anhydrous molar volume of SWCNT-**2** (0.69 $cm^3\ g^{-1}$) is strongly reduced compared to SWCNT-**1** (0.81 $cm^3\ g^{-1}$) as summarized in Table 3.9. This fact is attributed to a much lower packing density of the surfactant on the SWCNT surface which has already been indicated by zeta potential measurements and IR spectroscopy (Sect. 3.1.1.3). This observation can be understood in terms of a much higher inter perylene Coulombic repulsion, as **2** is equipped with two second generation *Newkome*-type dendrimers with 9 carboxylic acid groups on both sides of the perylene anchor group. In contrast, **1** bears two first generation *Newkome*-type dendrimers with three carboxylic acid groups on both sides of the perylene core leading to a much reduced Coulombic repulsion. Accordingly, the perylene surfactant **1** can be more densely packed on the nanotube surface due to the reduced charge density of the polar head groups.

The result for the anhydrous molar volume of SWCNT-**3** nicely completes the picture. In contrast to the bolaamphiphile **2**, the derivative **3** is an amphiphilic molecule where one second generation *Newkome*-type dendrimer has been substituted by an alkyl chain. Thus, the surfactant can be arranged on the nanotube surface in such a way that the bulky head groups and the alkyl chains are alternating, as schematically depicted in Fig. 3.32. Thus, the amphiphilic perylene derivative **3** can be more densely packed on the nanotube scaffold compared to **2** which is nicely reflected in the higher anhydrous molar volume (0.75 $cm^3\ g^{-1}$). This adsorption pattern also accounts for the observation that the perylene surfactant **3** covers the nanotube surface more homogenously compared to the bolaamphiphiles giving rise to a more intense SWCNT nIR emission (compare Sect. 3.1.1.3).

A more precise modeling of the perylene adsorption in the SWCNT scaffold on the foundation of the hydrodynamic characterization by AUC is not practicable. This can be traced back to the given uncertainties in the experimental values for $f\ f_0^{-1}$ and M which puts the application of hydrodynamic models such as the 'smooth-surfactant-cylinder' of Hersam et al. [76] at fray. Furthermore, those surfactants that do not collapse flat onto the nanotube surface such as the perylene surfactants do not match the flat cylinder model and unphysical (e.g. negative) values for the ligand packing density appear. In contrast, the anhydrous specific volume is a reliable result that involves little modeling and results directly from the over-determined sedimentation coefficients.

Within this chapter it has been demonstrated that analytical ultracentrifugation, especially with multi-wavelength analysis for selective detection of different fractions, is a powerful tool for giving insights into the packing density and therefore the adsorption of different surfactants on the nanotube surface. From the experimentally determined sedimentation rates in water and deuterated water, the anhydrous specific volume of the SWCNT-surfactant complexes has been extracted. The difference in the diameter distributions of the pristine SWCNT material, e.g. HiPco and CoMoCAT SWCNTs is reflected by a broadened c(s)-distribution in the case of the more polydisperse HiPco nanotubes. A comparison of SDBS and SC as surfactants has furthermore been related to the adsorption mechanisms previously discussed in literature [13, 15, 76]. It has been revealed that SDBS favors the "tails on" configuration for the surfactant concentration investigated (10 $g\ L^{-1}$). From the series of nanotube-surfactant complexes it is concluded that hydrodynamic modeling is not universally applicable, unless data from multiple rotational speeds are evaluated globally in order to suppress uncertainties in diffusion coefficients.

Concerning the analysis of the HiPco-Per dispersions, further evidence has been provided that the bulky bolaamphiphilic derivative **2** is least densely organized on the nanotube scaffold which is reflected in a rather low anhydrous molar volume (0.69 $cm^3\ g^{-1}$). Among perylene surfactants, the smallest derivative **1** is most densely adsorbed on the nanotube backbone with an anhydrous molar volume of 0.85 $cm^3\ g^{-1}$. These findings agree well with previous discussions on the foundation of zeta potential measurements and IR spectroscopic investigations. Furthermore, the amphiphilic derivative **3** yields a much higher anhydrous molar volume compared to the bolaamphiphile **2** which can be rationalized by a simple adsorption picture where the orientation of alkyl chains and hydrophilic head groups alternates allowing a more dense arrangement.

3.1.3 *Enhanced Adsorption Affinity of Anionic Perylene Surfactants towards Smaller Diameter SWCNTs*

3.1.3.1 Indications for Selective Interaction

Even though the extensive characterization described and analyzed above was able to shed light into the dispersion efficiencies and the adsorption mechanism of the designed perylene based surfactants, as well as the structure property relationship of the SWCNT-Per dispersions, one issue has not been considered so far, namely a possible selective interactions of the π-surfactants with certain (*n*, *m*)-SWCNT species. As outlined in the introduction, selective SWCNT dispersion is to be considered as ideal SWCNT sorting scenario owing to its simplicity and the great potential of scalability. However, convincing examples of this separation methodology are scarce, as the underlying selective interactions are not well captured on a fundamental and molecular scale.

In the case of the perylene surfactants, selective interaction is indicated by detailed emission spectroscopic investigations as will be discussed exemplarily with the amphiphilic derivative **3** as dispersant [1]. As already revealed in Sect. 3.1.1, SWCNT nIR emission intensity is drastically reduced in the HiPco-Per dispersions compared to HiPco-SDBS. Part of this fluorescence loss was attributed to the adsorption of the π-stacking perylene core, as well as to the homogeneity of the surfactant coverage for different perylene derivatives. The peak position of the remaining fluorescence is additionally strongly attenuated in comparison to HiPco-SDBS as illustrated in the 3D excitation-emission plots presented in Fig. 3.33. The relative peak shifts in HiPco-**3** (indicated by the red squares and black shaded backgrounds in Fig. 3.33b) can be plotted as a function of SWCNT diameter to yield the graph presented in Fig. 3.34. The SWCNT emission appears predominantly red-shifted when the perylene surfactant is adsorbed. The barthochromic shift is much more pronounced for smaller diameter, e.g. larger band gap SWCNTs. Thus, one may conclude that the interaction of the perylene core to the SWCNT surface depends on the electronic properties of the SWCNT species.

Even though adsorption of an aromatic unit to the nanotube scaffold is often accompanied with red-shifted emission and absorption [4, 9, 10, 24, 48, 87] the nature of this shift can be attributed to an increased exposure of the nanotube to the environment or to an alteration of the exciton binding energy by π-π-stacking interaction with the surfactant [88]. Recently, Papadimitrakopoulos et al. have studied the fluorescence of SWCNTs dispersed in various organic solvents by a flavin based surfactant [48]. They were able to relate a part of the red-shifted nanotube emission to bundling and debundling effects, uniformity of surfactant coverage and adsorption of the aromatic compound. They have shown that the flavin based dispersion in toluene favors a highly uniform surfactant coverage shielding the nanotubes from the environment and therefore resulting in a superior nanotube emission quantum yields. However, it is interesting to note that the nanotube emission in this case was still red-shifted compared to nanotubes

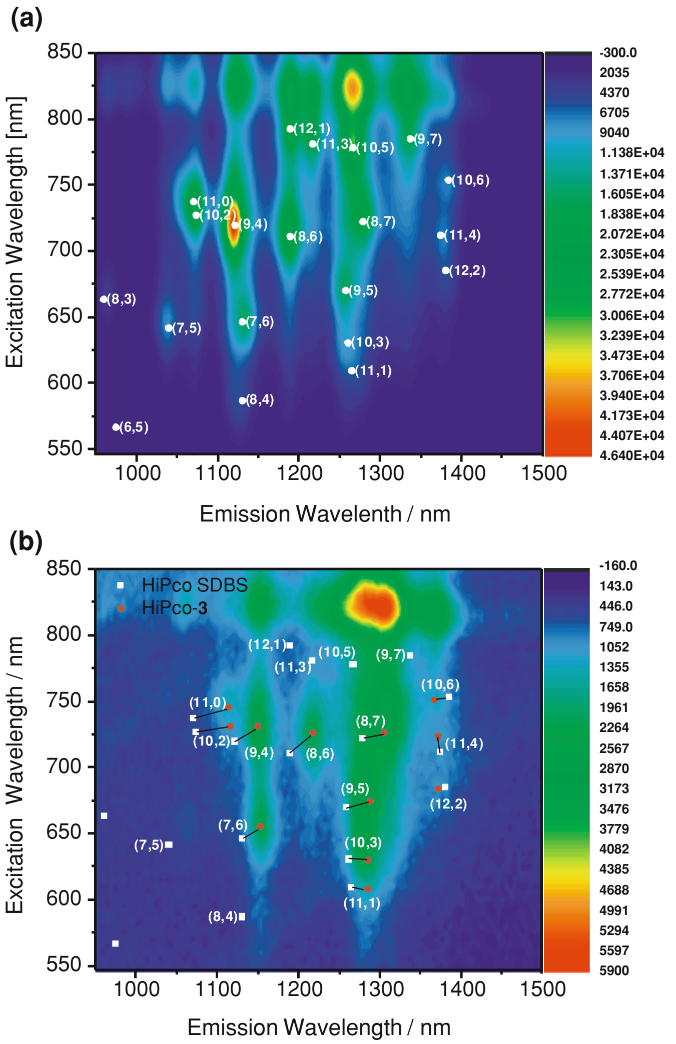

Fig. 3.33 Photoluminescence maps—with increasing intensity from blue to green to yellow and to red—of **a** SWCNT-SDBS **b** SWCNT-**3**. For both samples, the dispersions were centrifuged until an optical density of 0.4 cm^{-1} (at 740 nm) was reached corresponding to a nanotube concentration of 0.01 g L^{-1}. The peak positions in HiPco-**3** are significantly shifted in comparison to HiPco-SDBS as indicated by the *red circles* and *white squares*. (Reproduced with permission from the American Chemical Society, reference 1)

dispersed in SDBS being indicative for a contribution based on the π-π-stacking interaction. However, this explanation would not account for the observed dependency of the SWCNT emission shift on the nanotube diameter.

Since it has been shown by Guldi and co-workers that adsorption of the electron poor perylene unit leads to p-type doping of the nanotubes [89] it is tempting to

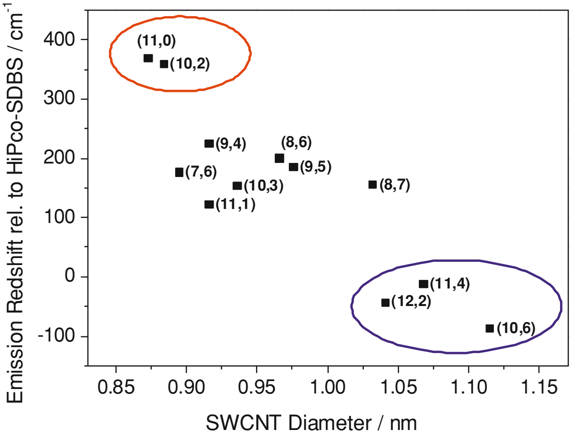

Fig. 3.34 Relation of the magnitude of the emission peak shift to the diameter of the nanotube. Positive values denote a *red*-shift, while negative values correspond to a *blue*-shift. (Reproduced with permission from the American Chemical Society, reference 1)

argue that the fluorescence is bleached and shifted due to the electron transfer from the nanotube to the perylene unit which has previously also been well documented by O'Connell et al. in the case of the addition of an organic acceptor molecule to a dispersion of SWCNTs in SDS [90]. However, in their study, O'Connell and co-workers demonstrated that the addition of the acceptor molecule to the nanotubes dispersion results in nanotube fluorescence bleaching with the larger diameter, e.g. smaller band gap nanotubes being affected first, as the charge transfer from the SWCNT to the organic acceptor is more efficient in the case of the smaller band gap nanotubes [90]. This observation ultimately indicates a stronger interaction of the larger diameter nanotubes with the electron acceptor molecules.

In this regard, it is possible to explain the more pronounced red-shift of SWCNT-Per complexes for smaller diameter nanotubes in two ways. On the one hand, the increased red-shift may be attributed to a less homogenous perylene coverage for smaller diameter nanotubes resulting in a more pronounced CNT exposure to the aqueous environment and therefore a more pronounced red-shift. This behavior would be related to a lower affinity of the perylene surfactant to smaller diameter nanotubes. On the other hand, the perylene surfactant may exhibit a stronger interaction with the smaller diameter nanotubes resulting in a higher packing density on the nanotube scaffold. This may cause stronger red-shifting of the nanotube emission by the enhanced π-π-stacking contribution on smaller diameter nanotubes.

In order to elucidate and understand the rather complex emission properties in the SWCNT-Per dispersions which are indicative for selective interaction or rather differences in surfactant packing density in dependency of SWCNT diameter further investigations are deemed necessary [91]. One possibility to probe relative changes in the packing density of charged surfactants on the nanotube surface is the determination of the zeta potential ζ as already presented in Sect. 3.1.1.3. Since the interest has been directed to variations of packing density on with different diameters, CoMoCAT and HiPco SWCNTs have been compared in the

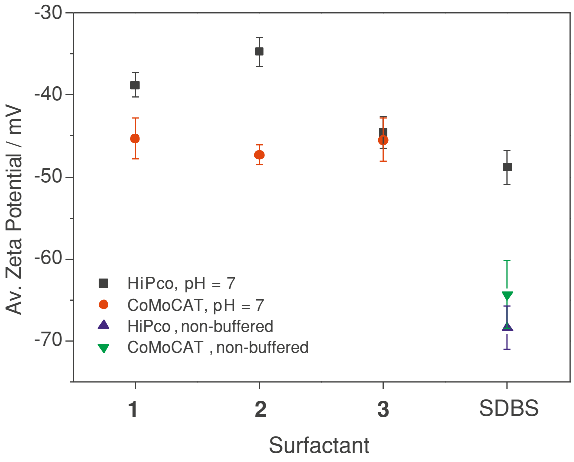

Fig. 3.35 Zeta potential of HiPco and CoMoCAT SWCNTs dispersed in buffered solutions of the perylene derivatives **1–3** (pH = 7) compared to SWCNT-SDBS (non-buffered). The error bars are derived from the standard deviation over ten measurements. (Reproduced with permission from Wiley–VCH, reference 91)

following. CoMoCAT SWCNTs are characterized by a smaller and narrower diameter distribution (0.7–0.9 nm) compared to HiPco SWCNTs (0.8–1.4 nm). The average results of ten zeta potential measurements of the HiPco and CoMoCAT dispersed by the aid of the perylene surfactants **1**, **2** and **3** in buffered aqueous media (pH = 7) compared to SWCNT-SDBS (in nonbuffered media) are summarized in Fig. 3.35. As already discussed in context with Fig. 3.8, the zeta potential is lower in magnitude in the buffered media due to charge screening effects arising from the pool of counterions. Those effects shall not be discussed in this section, as focus is directed towards differences in the zeta potential of HiPco and CoMoCAT SWCNTs.

Upon comparing HiPco to CoMoCAT SWCNTs, only minor differences are observed in the magnitude of the zeta potential with SDBS as surfactant. The zeta potential of CoMoCAT is slightly reduced in magnitude presumably due to the higher curvature allowing only a smaller amount of SDBS molecules to adsorb per unit length nanotube. This trend is inversed for the perylene surfactants, especially in the case of the bolaamphiphiles **1** and **2**. The magnitude of the zeta potential for nanotubes dispersed in **2** is increased from −34.7 mV for HiPco nanotubes to −47.3 mV for CoMoCAT nanotubes. This strongly indicates that the packing of the bolaamphiphile **2** carrying highly bulky substituents can be strongly enhanced for smaller diameter nanotubes such as CoMoCAT. A similar behavior has been observed for **1**, although not as pronounced.

As illustrated in Sect. 3.1.2, the packing densities of surfactants can be deduced from the determination of the anhydrous specific volume on the foundation of the sedimentation coefficients by means of analytical ultracentrifugation. Since the differences between the zeta potential of HiPco and CoMoCAT SWCNTs has been most striking in the case of the bolaamphiphilic surfactant **2**, the corresponding dispersions have been subjected to AUC in water and deuterated water (Table 3.10).

Table 3.10 Tabulated data of the sedimentation coefficients s in H_2O and D_2O (denoted by the subscripts H and D, respectively) and anhydrous specific volume $\bar{v}$ of the systems investigated

	Sedimentation coefficient H_2O s_H (Sv)	Sedimentation coefficient D_2O s_D [Sv]	Anhydrous specific volume $\bar{v}$ (cm^3 g^{-1})
CoMoCAT- SC	13.0	9.2	0.56
HiPco-SC	16.6	10.9	0.65
CoMoCAT-2	15.7	8.7	0.74
HiPco-2	18.7	11.7	0.69

In the case of sodium cholate as nanotube surfactant, the differences in the anhydrous specific volumina $\bar{v}$ of CoMoCAT and HiPco SWCNTs, respectively, nicely account for the variations in the diameter distributions of the pristine nanotube material. CoMoCAT nanotubes are characterized by a much narrower diameter distribution with a mean diameter centered at 0.8 nm opposed to HiPco nanotubes with a mean average diameter of 1.1 nm which is 38% larger in average. Thus, the anhydrous molar volume of CoMoCAT-SC is smaller by 0.09 cm^3 g^{-1} compared to HiPco-SC (assuming the equal packing density of sodium cholate onto the SWCNT surface).

Most importantly, the situation is different with the perylene derivative **2** as nanotube surfactant. In this case, the anhydrous specific volume $\bar{v}$ of the nanotube surfactant complex is higher for CoMoCAT nanotubes, even though their mean diameter is lower compared to HiPco nanotubes. This striking deviation derived for **2** as surfactant compared to SC as surfactant points towards a change in the supramolecular arrangement of the perylene surfactants on smaller diameter nanotubes. The adsorption geometry of the surfactant has to be altered in such a way that more perylene molecules can be adsorbed per length unit of SWCNT in the case of smaller diameter tubes, as has already been indicated by the zeta potential measurements. Even though two independent characterization techniques strongly indicate an enhanced adsorption affinity of the anionic perylene surfactants on smaller diameter SWCNTs, additional proof would be desirable.

3.1.3.2 Replacement Titrations with Sodium Dodecyl Benzene Sulfonate as Cosurfactant

It has been shown by Papadimitrakopoulos and co-workers that a replacement of a monomeric π-surfactant can be achieved by the subsequent addition of SDBS unveiling the selective interaction of the initial surfactant [9]. In the following this procedure has been adapted to the designed perylene based surfactants.

The replacement can be captured by absorption and emission spectroscopy, as the initially altered SWCNT optical transitions are recovered [9]. Interestingly, in the case of the perylene derivatives, Raman spectroscopy can also be used to probe the successful replacement [1]. Figure 3.36 displays the high energy region of the

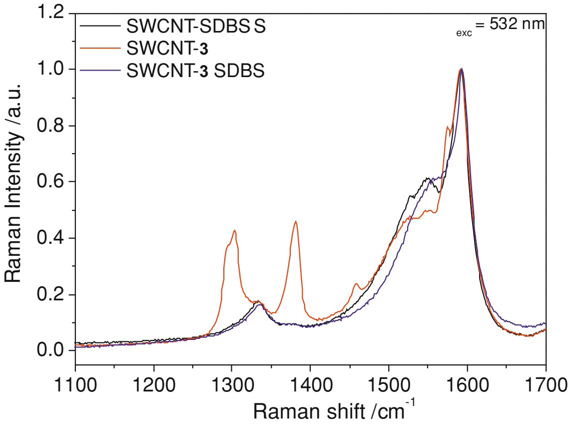

Fig. 3.36 Raman spectra of the filtrated supernatant of HiPco SWCNTs dispersed in an aqueous solution of SDBS (SWCNT-SDBS S) in comparison to the filtrated supernatant of HiPco SWCNTs dispersed in a buffered aqueous solution of **3** before (SWCNT-**3** S) and after replacement with SDBS (SWCNT-**3** S SDBS) with an excitation wavelength of 532 nm. All spectra have been normalized to the G-band at 1580 cm^{-1}

Raman spectra of the filtrated supernatant of HiPco SWCNTs dispersed in an aqueous solution of SDBS (SWCNT-SDBS S) in comparison to the filtrated supernatant of HiPco SWCNTs dispersed in a buffered aqueous solution of **3** before (SWCNT-**3** S) and after replacement with SDBS (SWCNT-**3** S SDBS) with an excitation wavelength of 532 nm.

Raman spectra have been recorded from the solid, as the fluorescence of free bulk perylene impedes with the acquisition in solution. Similarly, Raman spectra from the pure perylene derivatives in the absence of SWCNTs could not be recorded due to the strong fluorescence background. Accordingly, the detection of the perylene Raman signals at 1309, 1389, 1465 and 1582 cm^{-1} not only proves the presence of the perylene surfactant after filtration (which has also been demonstrated by XPS and IR spectroscopy in Sect. 3.1.1.3), but also nicely documents the interaction of the perylene core with the SWCNT scaffold. If there was no communication between the perylene anchor group with the SWCNT scaffold, the fluorescence of the perylene would not be quenched and would thus also impede with the Raman spectroscopic investigation. Significantly, no traces of the perylene surfactant are detected with 633 and 785 nm excitation, as the aromatic anchoring group is not resonantly excited at the other two wavelengths probed. Even though the observation that the Raman signals of the perylene moiety can be mapped concomitantly with the SWCNTs at an excitation of 532 nm has been of minor importance for this thesis, it has very recently been the foundation for tracing the interactions of perylene derivatives with graphene [92]. The absence of the perylene Raman peaks in the spectrum after addition of SDBS (blue trace in Fig. 3.36) unambiguously evidences the successful replacement of the designed surfactant **3** by SDBS.

In order to reveal a potential enhanced interaction of the designed perylene surfactants to SWCNTs of smaller diameters, e.g. larger bandgaps, the replacement of the dispersants **1**, **2** and **3** has been followed by subsequent addition of an aqueous stock solution of SDBS (10 g L^{-1}) [91]. Such a subsequent replacement of the perylene derivative from the nanotube sidewall can experimentally by followed by absorption (Fig. 3.37) and (nIR) emission spectroscopy (Fig. 3.38).

As described previously within this thesis (Sect. 3.1.1.2), the unbound perylene surfactants **1** and **3** are predominantly self-aggregated in solution, e.g. they form stable micelles giving rise to an absorption spectrum with $A^{0\to0}/A^{0\to1} \leq 0.7$. When adsorbed to the nanotube sidewall, the absorption pattern resembles that of the monomeric PBIs. However, the perylene transitions are red-shifted when the perylene molecules are associated with the nanotubes. Thus, it can be concluded from the perylene transitions presented in the absorption spectra in Fig. 3.38 that the concentration of free perylene is minimized in the HiPco-Per dispersions (red traces).

The replacement of the perylene dispersants **1** and **3** from the nanotube sidewall can nicely be followed by the changes induced in the perylene transitions, as the pattern is subsequently switched from the "monomeric", that is nanotube adsorbed signature to the self-aggregated form of the free perylene micelles upon addition of SDBS. In the case of the bulky bolaamphiphilic derivative **2**, the changes are less clearly discernable, as unbound perylene **2** has a lower tendency to form stable micelles with an inversed intensity distribution among the vibronic states. Thus, only a slight blue-shift of the perylene transitions is observed during the SDBS replacement titration.

Concerning the evolution of the SWCNT nIR emission, in general, upon substitution of the perylene surfactant by SDBS, the initially quenched nanotube fluorescence is subsequently recovered and blue-shifted (Fig. 3.38).

To further evaluate the replacement, the evolution of three different fluorescence peaks (at 1025, 1125, 1250 nm) corresponding to small (diameter = 0.83 nm, (7, 5)-SWCNT), medium (diameter = 0.89 nm, (7, 6)-SWCNT) and large diameter (diameter = 0.98 nm, (9, 5)-SWCNT) nanotubes, respectively, upon the addition of SDBS is compared in Fig. 3.39. The data points have been fitted to a sigmoidal curve (Boltzmann fit) yielding the respective inflection points marked by the vertical lines in Fig. 3.39. The emission of the (9, 5)-SWCNT in recovered first, followed by (7, 6) and (7, 5). Obviously, the perylene surfactant is first replaced from the larger diameter nanotubes (blue trace) and then from the smaller diameter nanotubes (red trace) in the HiPco sample for all perylene derivatives. This strongly supports the conclusion drawn from the zeta potential measurements, e.g. that the affinity of the perylene surfactant is higher for smaller diameter nanotubes.

As discernable in the fluorescence spectra of Fig. 3.38, the emission of the perylene unit (onset at low wavelengths) is slightly convoluting the data, especially for HiPco-**2** (Fig. 3.38b). However, as the evolution of the nanotube emission peaks are considered relative to the perylene background, the replacement information can still be extracted.

Since the evolution of the fluorescence spectra during the replacement titration may be strongly dependent on the preparation conditions such as nanotube concentration, perylene concentration and the presence of varying amounts of bundles due to the ultrasonication and centrifugation processing, the fluorescence titrations

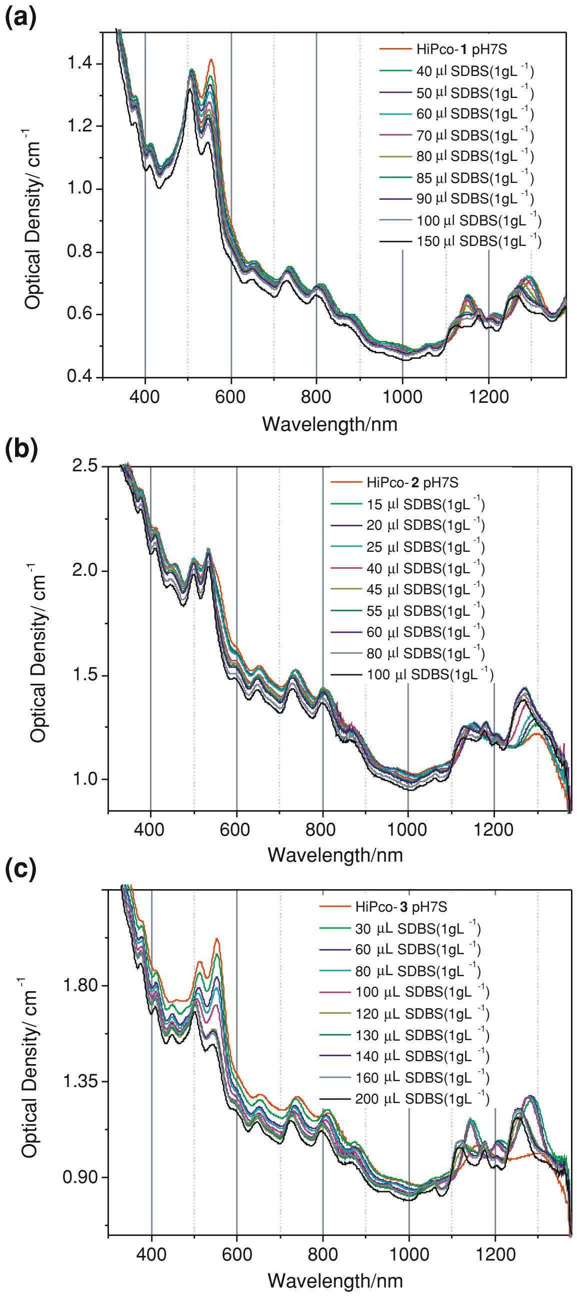

Fig. 3.37 As recorded absorption spectra of the addition of SDBS to buffered aqueous solutions of HiPco-Per ($[\mathrm{Per}]_i = 0.1$ g L^{-1}). **a** SWCNT-**1** ($[\mathrm{SWCNT}] = 0.052$ g L^{-1}), **b** SWCNT-**2** ($[\mathrm{SWCNT}] = 0.042$ g L^{-1}) and **c** SWCNT-**3** ($[\mathrm{SWCNT}] = 0.040$ g L^{-1}). The nanotube concentrations have been calculated from the optical densities at 740 nm and the corresponding extinction coefficient of the HiPco SWCNTs. (Reproduced with permission from Wiley–VCH, reference 91)

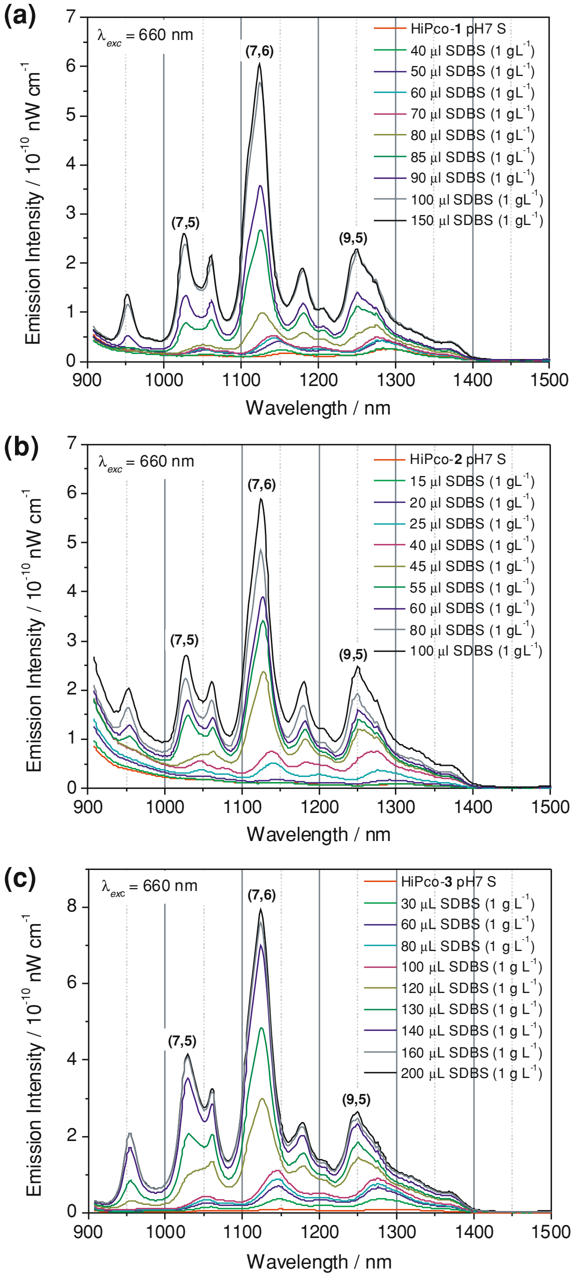

Fig. 3.38 As recorded fluorescence spectra at $\lambda_{\mathrm{exc}} = 660$ nm of the addition of SDBS to buffered aqueous solutions of HiPco-Per ($[\mathrm{Per}]_i = 0.1$ g L^{-1}). **a** SWCNT-**1** ($[\mathrm{SWCNT}] = 0.052$ g L^{-1}), **b** SWCNT-**2** ($[\mathrm{SWCNT}] = 0.042$ g L^{-1}) and **c** SWCNT-**3** ($[\mathrm{SWCNT}] = 0.040$ g L^{-1}). (Reproduced with permission from Wiley–VCH, reference 91)

have been repeated with different initial perylene concentrations, but constant initial nanotube concentrations. In the following only the nanotube concentrations in the supernatant after centrifugation (calculated from the optical densities in the

Fig. 3.39 Evolution of the nanotube emission intensity upon addition of SDBS to HiPco-Per for three different fluorescence peaks corresponding to small diameter (7, 5), medium diameter (7, 6) and larger diameter (9, 5) HiPco-SWCNTs. **a** HiPco-**1**, **b** HiPco-**2** and **c** HiPco-**3**. (Reproduced with permission from Wiley–VCH, reference 91)

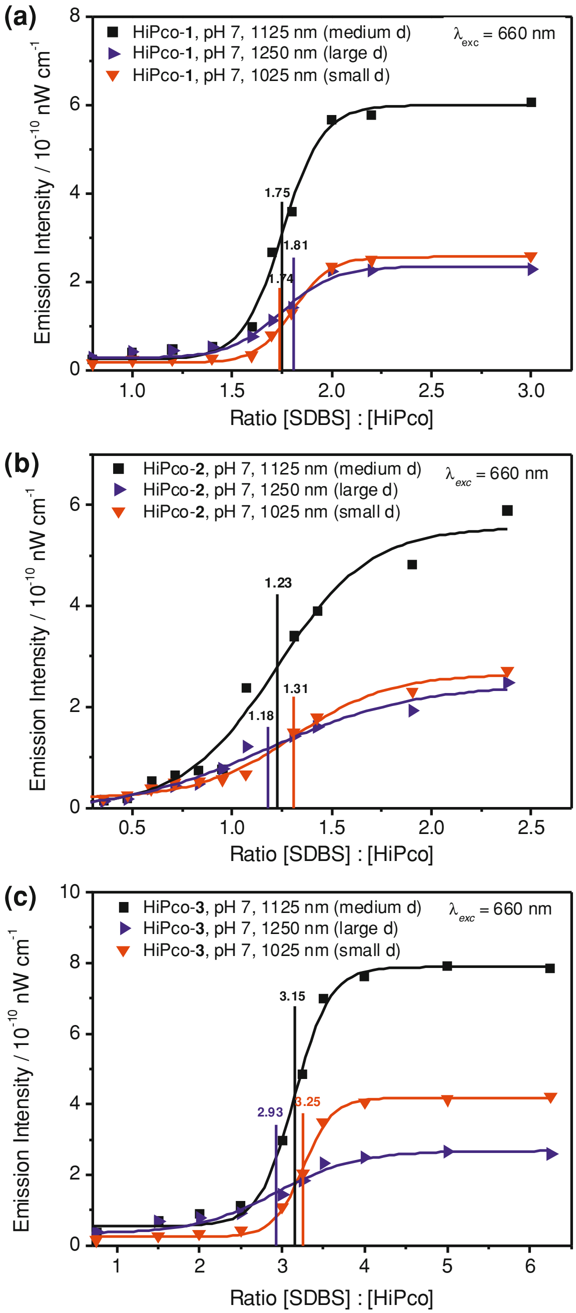

Table 3.11 Inflection points (IP) of the replacement titrations for small (7, 5), medium (7, 6) and large (9, 5) diameter HiPco SWCNTs as indicated in figure 3.39 and the SWCNT, as well as perylene concentrations in the respective experiments

Per	[Per]/g L^{-1}	[HiPco]/g L^{-1}	IP (7, 5) SWCNT		IP (7, 6) SWCNT		IP (9, 5) SWCNT	
				Mean value		Mean value		Mean value
1	0.1	0.052	1.81	1.88	1.75	1.82	1.74	1.81
	0.2	0.021	1.96		1.89		1.89	
	0.5	0.024	1.87		1.81		1.79	
2	0.1	0.042	1.31	1.34	1.23	1.23	1.18	1.17
	0.2	0.023	1.41		1.26		1.17	
	0.5	0.017	1.31		1.21		1.17	
3	0.1	0.043	3.25	3.35	3.15	3.15	2.93	2.93
	0.1	0.054	3.00		2.71		2.31	
	0.1	0.049	3.77		3.59		3.54	
	0.2	0.016	6.58		6.49		6.42	
	0.5	0.0056	39.7		38.8		38.0	

absorption spectra) shall be considered which vary in this series of experiments. The inflection points (IP) of the replacement titrations as indicated in Fig. 3.39 and the corresponding concentrations of perylene and nanotube are summarized in Table 3.11. The corresponding spectra of the fluorescence titrations, as well as the evolution of the fluorescence intensities can be extracted from the supplementary information of Ref. [91].

As already mentioned above, the concentration of nanotubes in the supernatant after centrifugation is not equal in every experiment due to the preparation of the dispersions involving ultrasonication and centrifugation. This may also lead to different bundle size distributions of the nanotubes in the set of experiments performed here. One might expect that even slight fluctuations in the bundle size distributions arising from the preparation of different samples might have a large impact on the replacement data, as the SWCNT surface area being accessible to the adsorption of the perylene surfactants is significantly reduced in bundles opposed to individualized nanotubes. However, this effect is obviously negligible, as the position of the inflection points summarized in Table 3.11 are well reproducible.

However, the situation is different when the concentration of perylene dispersants is changed, at least in the case of **3**. The concentration of the perylene surfactants in the dispersions has been varied in order to elucidate whether the concentration of free perylene not being bound to the nanotube scaffold influences the position of the inflection point of the titration. In the case of the bolaamphiphilic derivatives **1** and **2**, the inflection point of the titration is independent on the concentration of the perylene dispersant, whereas much more SDBS is required (with respect to the amount of nanotubes dispersed) to induce the replacement of **3** when free perylene is present in the dispersion (compare [**3**] = 0.1, 0.2 and 0.5 g L^{-1}). It may thus be concluded that the amphiphilic perylene derivative **3** is interacting with the structurally similar SDBS molecules so that the SDBS is captured in solution by free perylene micelles. Accordingly, the inflection point of the replacement titration is shifted to higher perylene concentrations. Obviously, this is not the case for the bolaamphiphilic perlyenes **1** and **2**. The formation of mixed micelles of the perylene dispersants with SDBS and other commercially available detergents will be addressed in Sect. 3.1.5.

As a consequence, it is crucial to minimize the amount of free perylene micelles, at least in the case of the amphiphile **3**. Therefore the titration has been performed three times with a perylene concentration of 0.1 g L^{-1}. From the absorption spectra (Fig. 3.37) it can be concluded that the perylene dispersant is predominantly associated with the nanotube surface, as the pattern of the perylene transitions is significantly changed compared to unbound perylene micelles.

Upon comparing the mean values of the inflection points of the titrations of the different perylene dispersants, it is striking that the bulky bolaamphiphile **2** is replaced fastest (as indicated by the lowest values for the inflection points summarized in Table 3.11), followed by **1** and **3**. This can be rationalized in terms of a decreasing packing density of the perylene molecules on the nanotube surface in the order $\mathbf{2} < \mathbf{1} < \mathbf{3}$, as already discussed in Sects. 3.1.1.3 and 3.1.2.2.

In any case, the replacement titrations yielded useful information of the interaction of the perylene dispersants with the nanotubes. Most importantly, it is obvious that all the anionic perylene derivatives investigated are first replaced from larger diameter nanotubes (9, 5), followed by medium (7, 6) and smaller diameter nanotubes (7, 5). This strongly points towards an enhanced adsorption affinity of the perylene dyes towards smaller diameter, e.g. larger band gap nanotubes. This effect is least pronounced for the small bolaamphiphilic derivative **1**, as the differences between the inflection points in the titration of the (n, m) SWCNT are smaller compared to the other perylene derivatives. Thus, evidence arising from three completely independent characterization techniques (zeta potential, hydrodynamic characterization by analytical ultracentrifugation and replacement titrations followed by SWCNT nIR emission) can be cumulated to result in a picture of enhanced adsorption affinity of the anionic perylene derivatives towards smaller diameter SWCNTs.

This observation is not easy to rationalize, however, as the adsorption of the electron poor perylene unit and the thus resulting p-type doping of the SWCNTs would be expected to follow the opposite trend. In the following, an adsorption hypothesis is postulated that would nonetheless account for the enhanced adsorption affinity towards smaller diameter nanotubes (Fig. 3.40).

As presented elsewhere adsorption of the perylene unit leads to permanent p-type doping of the nanotubes [89] (Fig. 3.40a). Hereby, larger diameter SWCNTs are presumably more prone to the electron transfer opposed to smaller diameter nanotubes due to their smaller band gap. Thus the larger diameter SWCNTs are more positively charged. This may lead to an attraction of the negatively charged dendrimer substituents in the periphery which bend towards the nanotube scaffold (Fig. 3.40b). In contrast, this attractive force may be reduced for the smaller diameter nanotubes. Additionally, repulsive Coulombic forces between the two

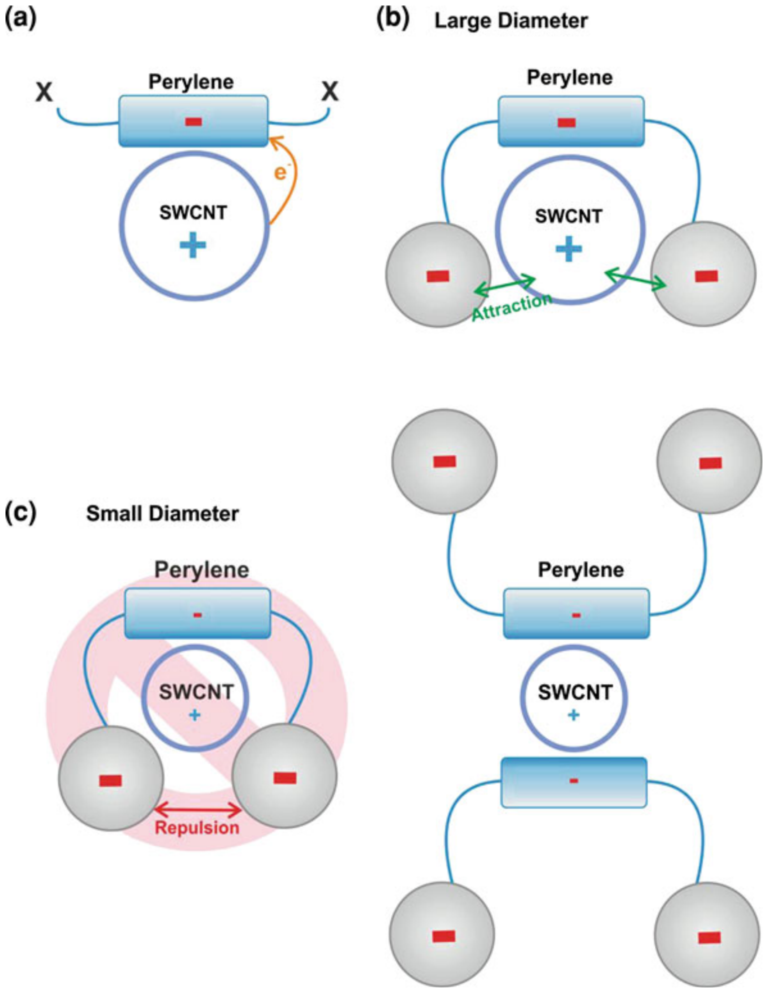

Fig. 3.40 Schematic illustration of the possible adsorption of the perylene bolaamphiphile **2** on larger and smaller diameter SWCNTs. In the case of larger diameter SWCNTs the packing density of the perylene surfactant is reduced due to Coulombic attraction of the p-type doped SWCNTs and the negatively charged *Newkome*-type dendrimer substituents of the perylene surfactant. In the case of smaller diameter nanotubes, the p-type doping is less pronounced rendering the repulsion between the dendrimers the dominant force so that the substituents point away from the nanotube scaffold. This ultimately increases the packing density of the perylene surfactants. (Reproduced with permission from Wiley–VCH, reference 91)

dendrimers on both sides of the perylene moiety may cause the substituents to point into solution, e.g. away from the nanotube surface (Fig. 3.40c). A larger area per unit length of nanotube then remains bare so that more surfactant molecules can be adsorbed leading to a higher packing density onto the nanotube surface.

Even though the adsorption hypothesis presented in Fig. 3.40 explains the experimental observations and is thus quite reasonable, further experiments are deemed necessary such as the investigation of cationic perylene derivatives, as will be addressed in the following chapter. In principle, the elucidation of a potential selective interaction of a perylene based surfactant with analogous structure, but different head charge should clarify the issue of the adsorption hypothesis, as the dendritic head group should not be attracted by the SWCNT surface in this case and accordingly, a cationic derivative should not exhibit an enhanced adsorption affinity towards smaller diameter nanotubes.

3.1.4 SWCNT Dispersion by a Cationic Perylene Based Surfactant

In an attempt to support the adsorption hypothesis of the anionic perylene derivatives, the bolaamphiphilic cationic perylene derivative **9** has received considerable attention. The emphasis has been laid on potential selective interactions of the cationic derivative with SWCNTs of certain diameters which should follow the opposite trend, e.g. preferred arrangement on larger diameter SWCNTs.

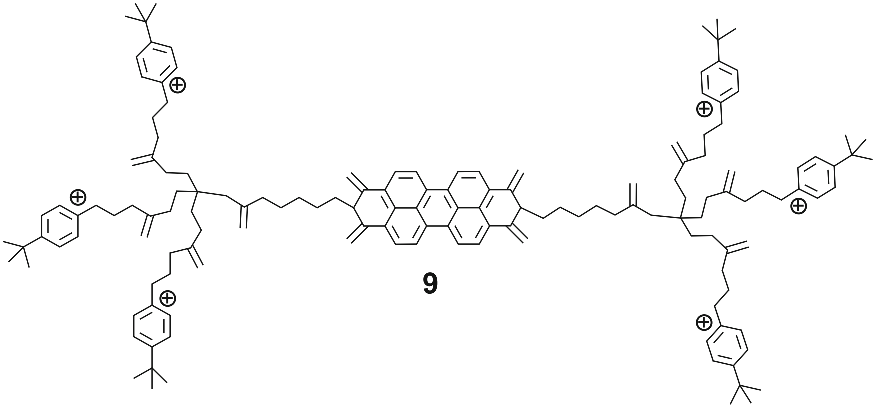

9

In an initial set of experiments, the replacement of the cationic perylene derivative from the SWCNT scaffold by SDBS in analogy to the experiments described in Sect. 3.1.3.2 has been investigated. However, no replacement could be observed by absorption or emission spectroscopy. Most importantly the SWCNT-perylene complex precipitated upon the addition of SDBS (especially striking above the cmc of SDBS) indicating that the charges on the SWCNT surface introduced by the cationic surfactant have been neutralized by the anionic cosurfactant SDBS. This extensive charge screening resulted in an aggregation of the SWCNT-**9** colloids. From the outcome of this experiment, it is obvious that the insights gained from the anionic perylene derivative surfactants cannot be directly transferred to the cationic system.

Table 3.12 Tabulated data of the initial HiPco SWCNT ($[\text{HiPco}]_i$) and perylene surfactant ($[\mathbf{9}]_i$) concentrations and the SWCNT concentrations in the supernatant after centrifugation $[\text{HiPco}]_s$ calculated from the optical densities at 740 nm in the absorption spectra

	$[\text{HiPco}]_i/\text{g L}^{-1}$	$[9]_i/\text{g L}^{-1}$	$[\text{HiPco}]_s/\text{g L}^{-1}$ (%)
Non-buffered pH = 7	0.05	0.1	0.04 (80)
Non-buffered pH = 10	0.05	0.1	0.014 (28)
Non-buffered pH = 3	0.05	0.1	0.015 (30)
Buffered pH = 7	0.05	0.1	0.015 (30)
Buffered pH = 10	0.05	0.1	0
Buffered pH = 3	0.05	0.1	0

Accordingly, the dispersion of SWCNTs by the perylene derivative **9** has been extensively investigated within the bachelor thesis of Sebastian Etschel in 2010 (Department of Chemistry and Pharmacy, Friedrich-Alexander University Erlangen-Nuremberg). The most important findings in context of this thesis shall be summarized in the following.

In a first set of experiments, the SWCNT dispersion efficiencies have been determined in aqueous media at different pH values and with different ionic strengths (comparison of buffered and non-buffered media) as summarized in Table 3.12. The dispersion efficiencies have been calculated from the SWCNT concentration (or rather optical densities) in the supernatant dispersion after mild centrifugation with an initial SWCNT:**9** ratio of 1:2. In general, the dispersion efficiencies are strongly decreased in buffered media (30% at pH = 7) opposed to the non-buffered environment (80% at pH = 7). This can be traced back to charge screening effects of the surfactant head charges by the pool of counterions in solution in buffered media as has already been discussed within this thesis.

The maximum dispersion efficiency with aid of the cationic perylene-based surfactant is reached in non-buffered aqueous media at pH = 7 with 80% of the SWCNT pristine material being stably dispersed. At first glance this value appears extraordinarily high in comparison to the anionic structural analogue **1** (Table 3.1 and Ref. [2]). In this context it should be noted that similar dispersion efficiencies can be achieved with the aid of **1** under ideal dispersion conditions, e.g. basic non-buffered aqueous environment with K^+ as counterion (Table 3.7 and Ref. [71]).

Since the cationic perylene derivative **9** is equipped with permanent positive charges in the dendritic periphery, dispersion of the SWCNTs should be in principle independent on the pH of the surrounding aqueous medium. As discernable from Table 3.12, the pH has a tremendous and unexpected effect on the dispersion efficiencies with aid of the cationic perylene surfactant. The solubilization in acidic media has shown to be rather inefficient in comparison to the scenario at neutral pH. This behavior can be explained in terms of the introduction of positive charges on the nanotubes at pH values below their point of zero charge. This may lead to Coulombic repulsion with approaching cationic surfactants and therefore decreased solubilization in acidic media. Similar results have been obtained by

Resasco and co-workers with SDBS as surfactant in basic environments (above pH = 10) far below the cmc of SDBS [13].

Most strikingly, the dispersion efficiency of the cationic perylene surfactant **9** drops from 80% at pH = 7 to only 28% in basic media (pH = 10). Even though the counterion and concentration of counterions has shown to play a critical role (Sect. 3.1.1.4 and Ref. [71]) for the dispersion of SWCNTs, a larger pool of hydroxyl counterions in the pH = 10 dispersion is not likely to have such a pronounced effect on the dispersion efficiencies. As revealed by a variety of further investigations (see Bachelor thesis Sebastian Etschel), the ester functionalities linking the cationic pyridine moiety to the dendrimer of the head group are not long-term stable in aqueous media. The ester hydrolysis is accelerated by the presence of hydroxyl anions so that the perylene derivative **9** loses its functionality as cationic SWCNT surfactant resulting in decreased dispersion efficiencies. Similarly to the addition of SDBS to the HiPco-**9** dispersion, the partial transformation of **9** to an anionic derivative results in charge neutralization on the SWCNT surface and therefore drastically reduced dispersion efficiencies.

Even though care must be taken when investigating the SWCNT-**9** dispersion due to the potential ester hydrolysis, the results can be considered as qualitatively reliable when the analysis occurs immediately after preparation of the dispersions. Thus, it was possible to deduce the optimal ratio of HiPco SWCNTs to **9** by SWCNT nIR emission, perylene emission and absorption spectroscopy. Interestingly, the ideal ratio of SWCNT:**9** to yield samples with maximum SWCNT individualization rates and minimum concentration of free bulk perylene surfactant was found to be 1:2.4 (by mass). In comparison to the anionic analogue perylene **1** (HiPco:**1** = 2:1 in buffer pH = 7 and 1:1 in buffer pH = 10) qualitatively more perylene is adsorbed on the SWCNT sidewall in case of the cationic derivative **9** pointing towards higher packing densities and better exfoliation of the SWCNTs. This could in principle be rationalized by a supramolecular arrangement of the perylene derivative **9** with the dendritic arms pointing in solution similar to the anionic derivatives with smaller diameter SWCNTs. However, a direct comparison is not possible, as the investigations with the anionic derivatives have been carried out in buffered media opposed to the cationic system.

The ideal preparation conditions (ratio HiPco:**9** = 1:2.4, non-buffered media, pH = 7) have been applied to further investigations focusing on potential selective interactions of the cationic perylene derivative with SWCNTs of certain diameters (or band gaps). Another indication towards a different adsorption behavior of the cationic derivative **9** in comparison to the anionic derivative **1** arises from the SWCNT emission spectra presented in Fig. 3.41. In both cases the concentration of free perylene surfactant has been minimized in order to avoid data convolution by emission of unbound perylene. Even though the SWCNT emission is red-shifted in both cases with respect to the HiPco SWCNTs dispersed in an aqueous solution of SDBS, subtle differences arise for the anionic and cationic perylene based surfactants. For instance, the red-shift of the large diameter (9, 5)-SWCNT (at 1250 nm in HiPco-SDBS) is more pronounced when the cationic derivative is used as dispersant. Additionally, the signals for smaller diameter SWCNTs (with

Fig. 3.41 SWCNT nIR emission spectra after excitation with 660 nm normalized to the respective maximum peaks. In all cases, the supernatant dispersions after mild centrifugation are displayed with an initial SWCNT concentration of 0.05 g L^{-1}. Initial perylene concentrations were [**1**] = 0.05 g L^{-1} (buffer pH = 7) and [**9**] = 0.12 g L^{-1} (non-buffered pH = 7). The concentration of SDBS was 10 g L^{-1}

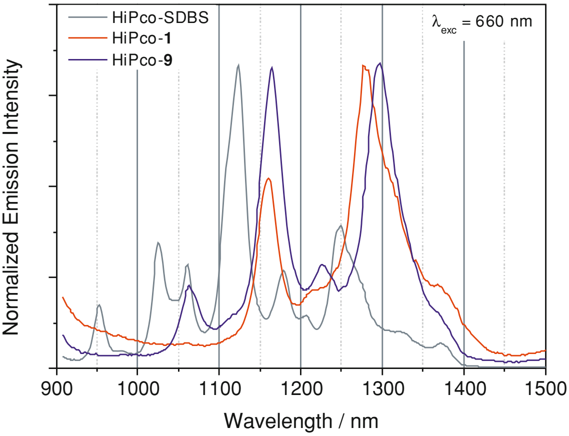

emission peaks below 1100 nm) are not completely quenched (or bleached) in HiPco-**9** as surfactant in contrast to HiPco-**1**.

This qualitative comparison points towards the desired direction, e.g. a different adsorption geometry of the anionic in comparison to the cationic perylene dispersant. However, the emission spectroscopic data at this point should not be overrated, as on the one hand, multiple factors influence the nIR SWCNT emission (as already discussed). On the other hand, no quantitative comparison of the HiPco-**1** and HiPco-**9** spectra is possible due to necessary variations in the preparation conditions (ionic strengths, SWCNT concentrations in the supernatant, perylene dispersant concentrations). Accordingly, further support is sought for.

The most convincing evidence for the enhanced adsorption affinity of the anionic perylene derivatives towards smaller diameter SWCNTs has been found in replacement titrations with the anionic detergent SDBS. It is quite reasonable to assume that a successful replacement can only be promoted with like-charged detergents, e.g. it could be endeavored that a cationic π-surfactant such as **9** can be replaced by a cationic detergent such as DTAB. Accordingly the effect on the optical properties of a HiPco-**9** supernatant dispersion ($[\text{HiPco}]_i = 0.06$ g L^{-1}, $[\mathbf{9}]_i = 0.15$ g L^{-1}) upon subsequent addition of DTAB (as solid) has been investigated.

The absorption spectra of the subsequent addition of DTAB to HiPco-**9** are displayed in Fig. 3.42. The perylene bands originally centered at 510 and 560 nm undergo dramatic changes. Most significantly, a band arises at 530 nm (marked by the green shaded background) which may be attributed to mixed aggregates of **9** and DTAB. A more detailed investigation concerning this subject is presented in Sect. 3.1.5. The perylene band centered at 560 nm (marked by the grey shaded background) which is associated with perylene moieties anchored to the SWCNT scaffold is not altered below a DTAB concentration of 12 g L^{-1} (already well above the cmc). Additionally, the energies of the excitonic SWCNT transitions are not changed, e.g. no peak shifts are observed in the nIR region of the spectrum.

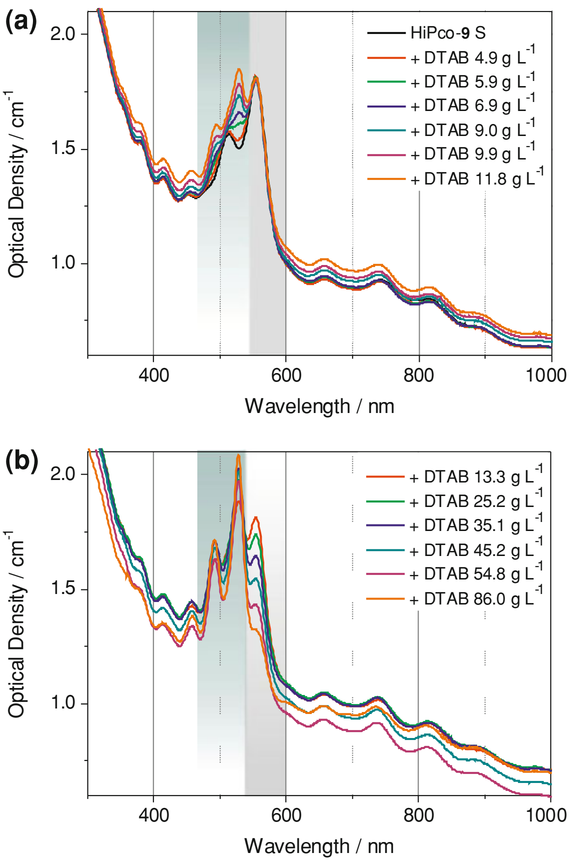

Fig. 3.42 As recorded absorption spectra of the addition of solid DTAB to a supernatant dispersion of HiPco-**9** ([**9**]$_i$ = 0.15 g L^{-1}, [SWCNT]$_i$ = 0.06 g L^{-1}). The supernatant dispersion has been diluted 1:1 with H_2O prior to the addition of DTAB to yield a SWCNT concentration of 0.024 g L^{-1}. The transition associated with perylene anchored to the SWCNT scaffold is indicated by the *grey shaded* background, the transitions that arise by addition of DTAB and may thus be attributed to mixed aggregates of DTAB and perylene **9** are marked by the *green shaded* background. **a** DTAB concentrations below 12 g L^{-1}, **b** DTAB concentrations above 12 g L^{-1}

Both observations can be explained in terms of the formation of mixed micelles of free bulk perylene **9** with DTAB. A replacement from the SWCNT sidewall is not indicated below a DTAB concentration of 12 g L^{-1}.

As revealed by the absorption spectra in Fig. 3.42b, further increasing the concentration of DTAB results in a decrease of the perylene band centered at 560 nm pointing towards a successful removal of the perylene anchoring unit from the SWCNT sidewall. Concomitantly, the perylene band at 530 nm increases, as the free perylene molecules may also interact with DTAB further indicating that a replacement of the cationic perylene derivative has been achieved by the addition of DTAB. However, it is quite surprising that no peak shifts are induced in the characteristic SWCNT transitions, in contrast to the successful replacement of anionic perylene derivatives by SDBS (compare Fig. 3.38). In line with the absorption spectra presented in Fig. 3.42, no peak shift has been observed in the SWCNT nIR emission spectra upon addition of DTAB to HiPco-**9**.

Despite the absence of dominant alterations of the SWCNT transition energies, changes are induced by the addition of DTAB, as most prominent for the spectrum of HiPco-**9** S+DTAB 86.0 g L^{-1}. The SWCNT transitions appear significantly broadened and the absorbance was first decreased and then increased again. Such a behavior can be traced back to aggregation of SWCNTs which may lead to precipitation and the introduction of scattering effects in the absorption spectra. Indeed, flocculation of the SWCNT has been observed after storing the sample at room temperature for 1 h.

Obviously, DTAB is capable of removing the cationic perylene derivative from the SWCNT sidewall. However, a replacement cannot be conveniently followed in the SWCNT absorption and emission in contrast to the replacement of the anionic perylene derivatives by SDBS, as the nanotubes where the cationic dispersant **9** has been removed are not stable in the aqueous solution. They aggregate and finally flocculate so that no changes are captured by their optical characterization.

The reason for this aggregation is not easy to rationalize, as DTAB is a suitable and well known detergent for the solubilization of SWCNTs. However, it has been shown that SWCNT dispersions with the aid of a structural analogue cetyl trimethyl ammonium bromide are not stable in basic media [14]. A pH measurement of the HiPco-**9** S sample after addition of DTAB has revealed a pH value of 12, even though the initial pH before the addition of DTAB was 7. The nature of this increased pH is not clear, but the consequences are striking. On the one hand, the increased pH may induce the precipitation of the nanotubes after the cationic perylene derivative **9** has been removed from the sidewall and replaced by DTAB in analogy to Ref. [14]. On the other hand, the ester of the cationic perylene derivative may be hydrolyzed (as has been shown in the Bachelor thesis of Sebastian Etschel) resulting in the generation of an anionic perylene derivative. Similarly to the addition of SDBS to HiPco-**9** the presence of DTAB would neutralize the surfactant charges on the SWCNT sidewall and induce a precipitation of the material.

Even though the SWCNT flocculation is quite surprising it may in principle be exploited for the separation of SWCNTs if the underlying interaction of the π-surfactant with the SWCNTs is selective for certain (n, m)-species and if the ester hydrolysis is not responsible for the flocculation. This could most conveniently be analyzed by a water soluble cationic perylene derivative which is stable under basic conditions in the future (for example by exchanging the ester with amide functionalities). Further effort towards elucidating the potential replacement, or rather SWCNT flocculation of HiPco-**9** upon the addition of DTAB has not been taken within this thesis.

In summary, the cationic perylene derivative **9** is a powerful surfactant for the solubilization of SWCNTs at neutral pH, especially at low ionic strength. However, the ester functionalities are not long-term stable in aqueous solutions, especially at elevated pH. A selective interaction of the cationic perylene derivative with certain SWCNT species could not conveniently be evidenced, as an attempt to replace the cationic perylene surfactant with DTAB in analogy to the replacements of the anionic derivatives with SDBS yielded complex surfactant and cosurfactant mixtures. Changes in the optical transitions of the nanotubes could not be followed, as the SWCNT flocculated upon the addition of DTAB. Thus, the adsorption hypothesis of the supramolecular arrangement of the anionic perylene derivatives (Fig. 3.40) could not be proven by the investigations with the derivative **9** mainly due to the instability of this derivative in basic media.

The investigations presented in this chapter also pointed towards complex interactions of the designed perylene derivatives with commercially available detergents. Since the supramolecular arrangement of the perylene derivatives in mixed structures with the cosurfactants may also play a significant role during the replacements on the SWCNT surface, the elucidation of these structures and the underlying interactions deserves some attention in the following.

3.1.5 Formation of Mixed Surfactant-Cosurfactant Structures

The perylene bisimide derivatives already introduced within this thesis represent an ideal model substance class for the investigation of the supramolecular arrangement with other surfactants, as their optical properties can be regarded as fingerprint of their aggregation state so that a variety of molecules can be screened for positive or negative interaction by absorption and emission spectroscopy. This will be demonstrated in the following with the anionic bolaamphiphilic perylene derivative **1**, the anionic amphiphilic perylene derivative **3** and the cationic bolaamphiphilic derivative **9**. In each case, a 10^{-5} M buffered aqueous solution of the perylene derivative was mixed 1:1 by volume with an aqueous solution of 1 wt% SDBS, SDS, SC, SDC and DTAB, respectively. In some instances the color of the solutions changed instantaneously in comparison to the reference experiment (dilution of the perylene solutions with water), as summarized by the photographs in Fig. 3.43. The differences are even more striking in the fluorescence photographs (excitation of 366 nm) displayed as second photograph in each sector of Fig. 3.43. An increased fluorescence of the perylene derivatives points to a decreased perylene–perylene interaction and as a consequence to a supramolecular aggregation with the cosurfactant that has been added.

In general, the perylene derivatives are self-aggregated in buffered solutions at the concentration investigated. Qualitatively, the same effects are observed in non-buffered media. However, as solutions of perylene derivative **1** at a concentration of 5×10^{-6} M also contain a significant amount of free, e.g. non-aggregated perylene (compare Fig. 3.18 and 3.19), the changes induced by the cosurfactants are less striking. Therefore, focus is directed towards the buffered solutions in the screening experiments.

From the photographs presented in Fig. 3.43, it can be deduced that the bolaamphiphilic anionic derivative **1** is not significantly interacting with the anionic amphiphiles SDBS and SDS. However, as has already been indicated by the replacement titrations presented in Sect. 3.1.3.2, the amphiphilic derivative **3** is indeed forming mixed aggregates with the amphiphiles SDS and SDSB despite the like head charges. In any case, an interaction is discernable in systems with mixed head charges, for example the anionic perylene derivatives **1** and **3** with DTAB

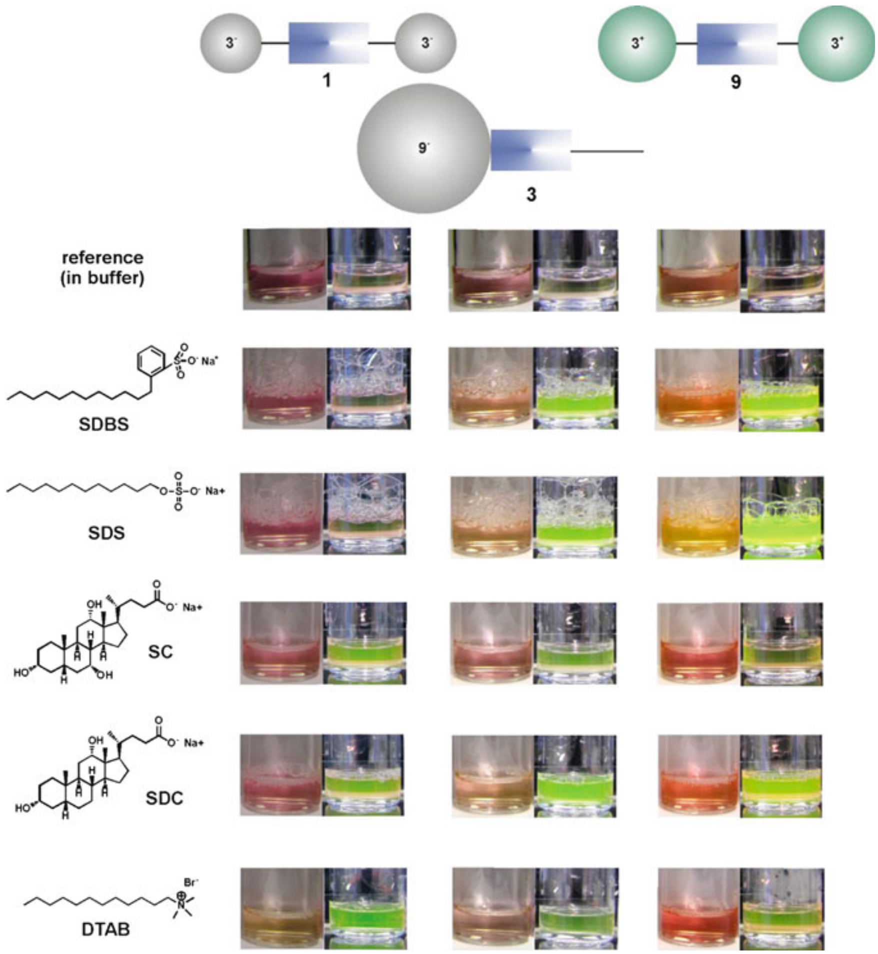

Fig. 3.43 Photographs of the solutions of the perylene derivatives **1**, **3** and **9** (5×10^{-6} M) in the presence of the respective surfactants SDBS, SDS, SC, SDC and DTAB (5 g L^{-1}) under white light illumination and UV irradiation (366 nm). Color changes with respect to the reference solutions (in the absence of a cosurfactant) indicate the formation of mixed supramolecular aggregates

and the cationic perylene derivative **9** with SDS and SDBS. Obviously, the facial amphiphiles SC and SDC interact with every perylene derivative investigated in a similar fashion. In this regard it is interesting to note that the perylene-SDC solutions turn into thixotropic liquids after being stored several days at room temperature.

The system **9**-DTAB yields a rather unexpected result, as no interaction would be endeavored in solutions of a bolaamphiphilic perylene with a like-charged amphiphile. It will be investigated in detail later on in this chapter.

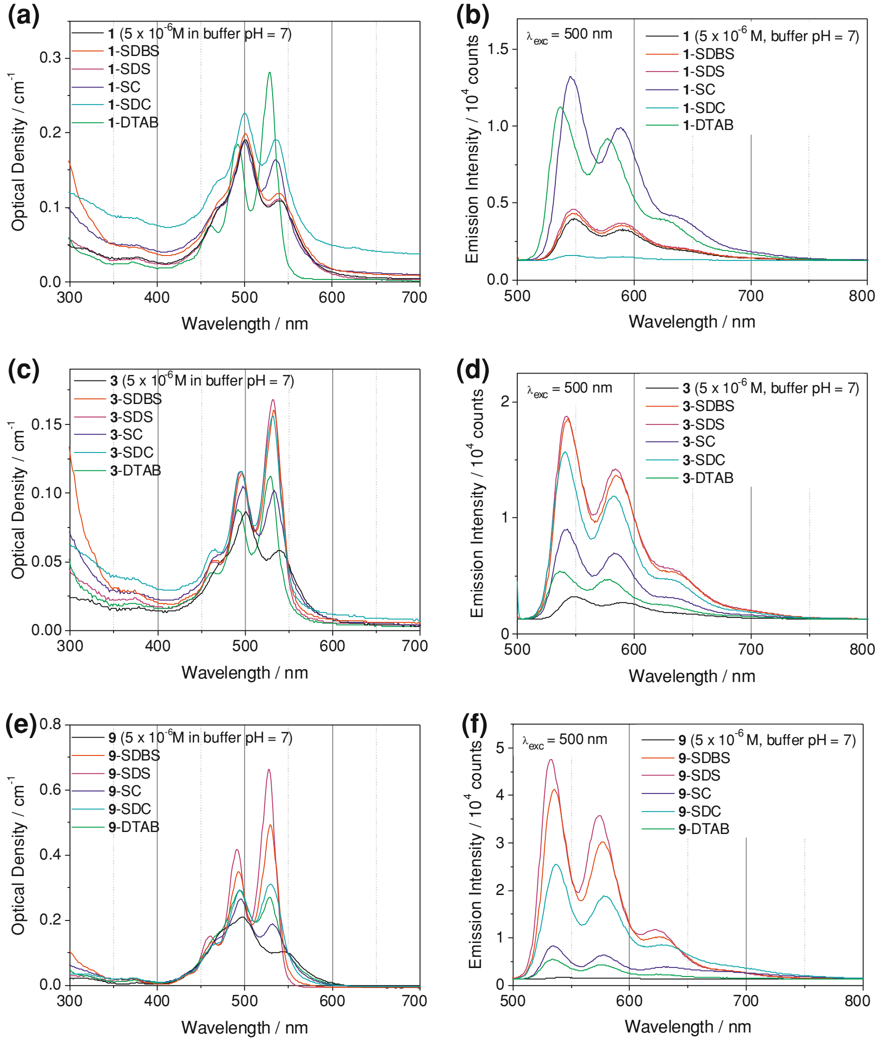

Fig. 3.44 Optical absorption spectra of **a** **1** (5×10^{-6} M) in the presence of the cosurfactants SDBS, SDS, SC, SDC and DTAB ($5\ \mathrm{g\ L^{-1}}$), **c** **3** (5×10^{-6} M) in the presence of the cosurfactants SDBS, SDS, SC, SDC and DTAB ($5\ \mathrm{g\ L^{-1}}$) and **e** **9** (5×10^{-6} M) in the presence of the cosurfactants SDBS, SDS, SC, SDC and DTAB ($5\ \mathrm{g\ L^{-1}}$) in buffered solutions of pH = 7. Figures **b**, **d** and **f** display the corresponding emission spectra with an excitation wavelength of 500 nm

The absorption and emission spectra (excitation of 500 nm) corresponding to the solutions in the photographs of Fig. 3.43 are displayed in Fig. 3.44, as they represent a spectroscopic view of the color changes and the interaction of the perylene derivatives with the cosurfactants.

The absorption features of the perylene derivatives have already been extensively discussed within this thesis and shall therefore only be briefly described in this chapter. In the cases where a pronounced interaction of the perylene derivatives with the cosurfactants is observed, the perylene transitions are changed and resemble the signature of the monomeric species with normal Franck–Condon progression in the absorption spectra (Fig. 3.44a, c and e). The perylene emission intensity is concomitantly increased and slightly blue-shifted with regard to the reference samples in these cases (Figs. 3.44b, d and f) also evidencing reduced perylene–perylene interaction. Please note that the optical properties and the quantum yields of the perylene derivatives can thus be tuned and controlled by the addition of cosurfactants. The only exception from this general trend is the solution of **1**-SDC where very large aggregates are formed within minutes inducing a pronounced scattering in the absorption spectrum (resulting in the non-zero absorption background) and a quenching or bleaching of the perylene emission.

From the surfactant screening presented above, it appears quite surprising that the cationic bolaamphiphile **9** exhibits a pronounced interaction with the surfactant DTAB, while no such aggregation is discernable in the cases of the anionic analogue **1**-SDBS (or **1**-SDS). In order to elucidate this discrepancy, the system has been investigated in more detail. For this purpose, a stepwise addition of solid DTAB to a nonbuffered solution of **9** was followed by absorption and emission spectroscopy. As indicated by the absorption spectra (Fig. 3.45a), no pronounced interaction can be traced below the cmc of DTAB (13 mM [93]). However, above the critical micelle concentration of the cosurfactant (Fig. 3.45b), the perylene bands undergo dramatic changes and are transformed to the pattern of monomeric perylene bisimide derivatives (as has already been indicated in Fig. 3.44e). Qualitatively the same evolution has been observed at higher concentrations of the perylene derivative. However, a higher concentration of DTAB has been necessary to complete the change to the monomeric PBI pattern.

The emission intensity of the perylene unit significantly increases by the addition of DTAB, as exemplarily depicted in the 2D excitation-emission contour plots in Figs. 3.46a and 3.46b. The approximately 3.5-fold increase in emission intensity can best be mapped by the emission spectra with 530 nm excitation presented in Fig. 3.46c. Again, the striking changes occur above the cmc of DTAB in complete agreement with the absorption spectra.

Interestingly, the emission intensity is not only increased in **9**-DTAB (above the cmc of DTAB), but the excitation-emission maximum of the perylene moiety is also slightly blue-shifted compared to the reference system in the absence of DTAB (from excitation 531.5 nm and emission 543 nm to excitation 528.5 nm and emission 531 nm). Despite the fact that the perylene emission in the aqueous solution of **9** predominantly arises from monomeric PBIs, a clear contribution from the self-aggregation arises which is manifested as red-shift compared to the **9**-DTAB solutions where the perylene–perylene interaction has been disrupted by the supramolecular arrangement with the cosurfactant.

Unambiguous evidence that the perylene–perylene interaction has been broken up by the addition of DTAB arises from Figs. 3.46d, e. In the absence of DTAB,

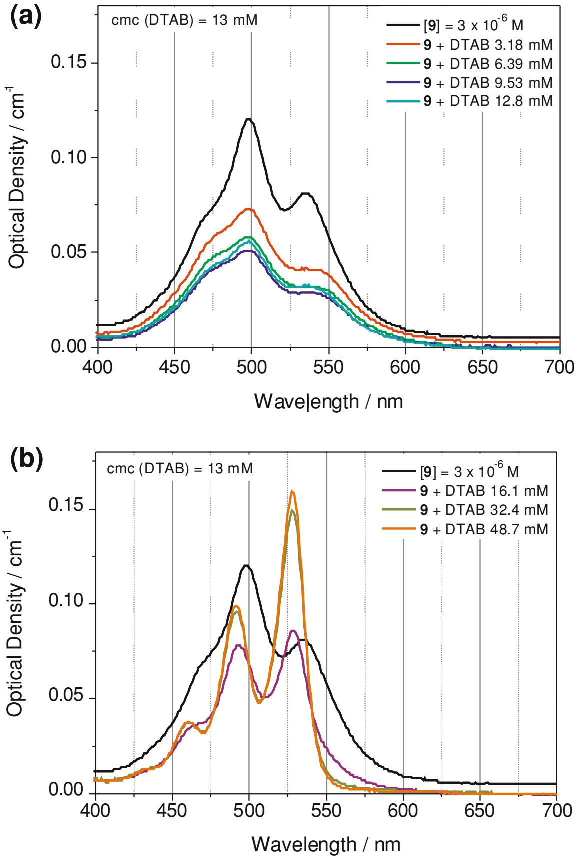

Fig. 3.45 Optical absorption spectra of the subsequent addition of solid DTAB to an aqueous solution of the cationic perylene derivative **9** (3×10^{-6} M). The resulting concentrations of DTAB are indicated in the figure legend. **a** Regime below the cmc of DTAB, **b** Addition steps with DTAB concentrations above its cmc

the perylene derivative **9** is strongly self-aggregating resulting in a significant deviation of the absorption from the excitation spectra (at 530 nm). If the molecules were not self-aggregating, the normalized absorption and excitation spectra should be equal and both should be a mirror image of the emission spectrum—a situation observed after addition of DTAB (Fig. 3.46e).

In order to structurally elucidate the **9**-DTAB complexes, samples have been subjected to cryo-TEM imaging. Since higher concentrations are favorable for this microscopic technique, samples have been prepared with $[\mathbf{9}] = 10^{-4}$ M. The subsequent addition of DTAB has been followed by absorption spectroscopy. DTAB concentrations of 0.012 M (below cmc) and 0.16 M (above cmc) have been chosen as representatives of the perylene **9**-DTAB system above and below the cmc of DTAB. Despite the higher concentrations, the samples are spectroscopically well comparable to the samples **9**+DTAB 12.8 mM and **9**+DTAB 32.4 mM displayed in Figs. 3.45 and 3.46.

Representative cryo-TEM images of an aqueous solution of **9** and the system **9**-DTAB below and above the cmc of DTAB are displayed in Fig. 3.47. The

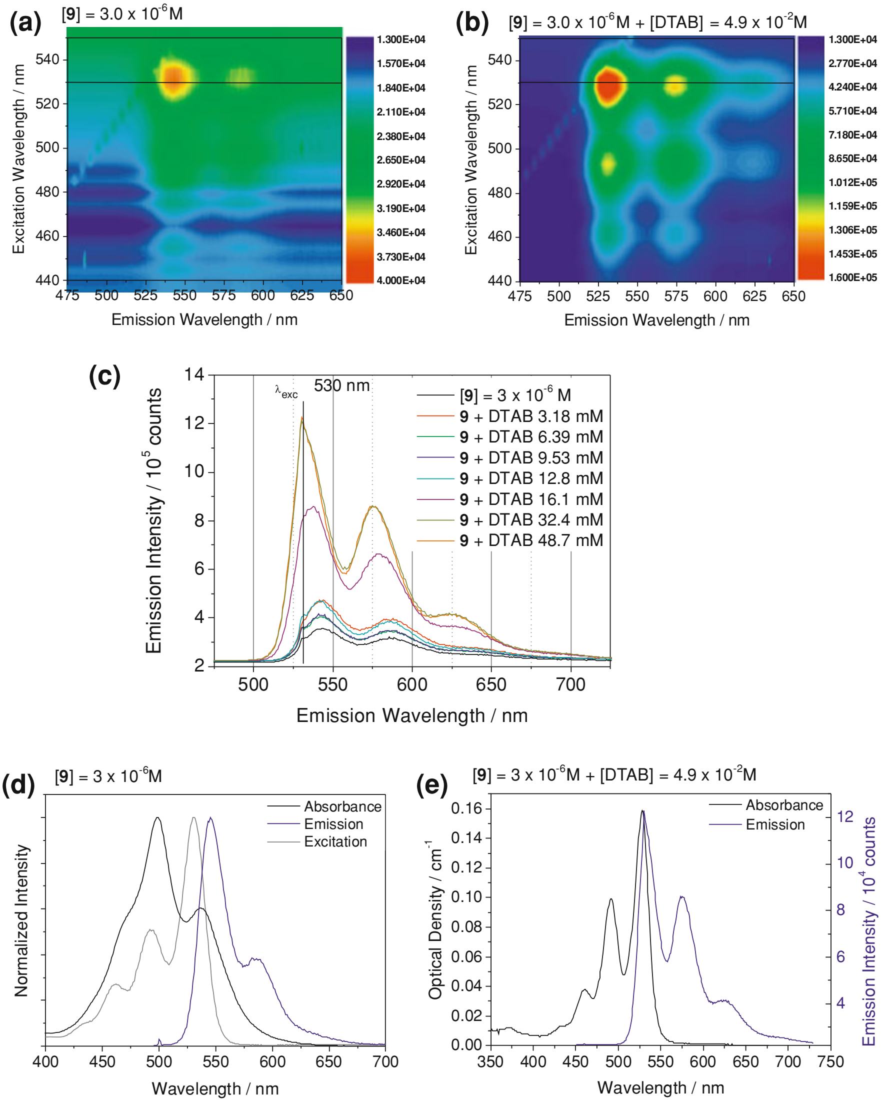

Fig. 3.46 2D excitation-emission profiles of **a** perylene derivative **9** (3×10^{-6} M) and **b** perylene derivative **9** (3×10^{-6} M) after the addition of solid DTAB (4.9×10^{-2} M). **c** Emission spectra of the subsequent addition of DTAB with $\lambda_{\text{exc}} = 530$ nm. The respective concentrations of DTAB are indicated in the figure legend. **d** Plots of normalized absorbance, excitation (530 nm) and emission (530 nm) of **9**. **e** Plots of absorbance and emission of **9**-DTAB

significant structures are indicated by the markings in Figs. 3.47a, c, e. In contrast to the anionic bolaamphiphilic perylene derivatives **1** and **2** [3], the cationic derivative **9** forms aligned fiber-like aggregates with a diameter of

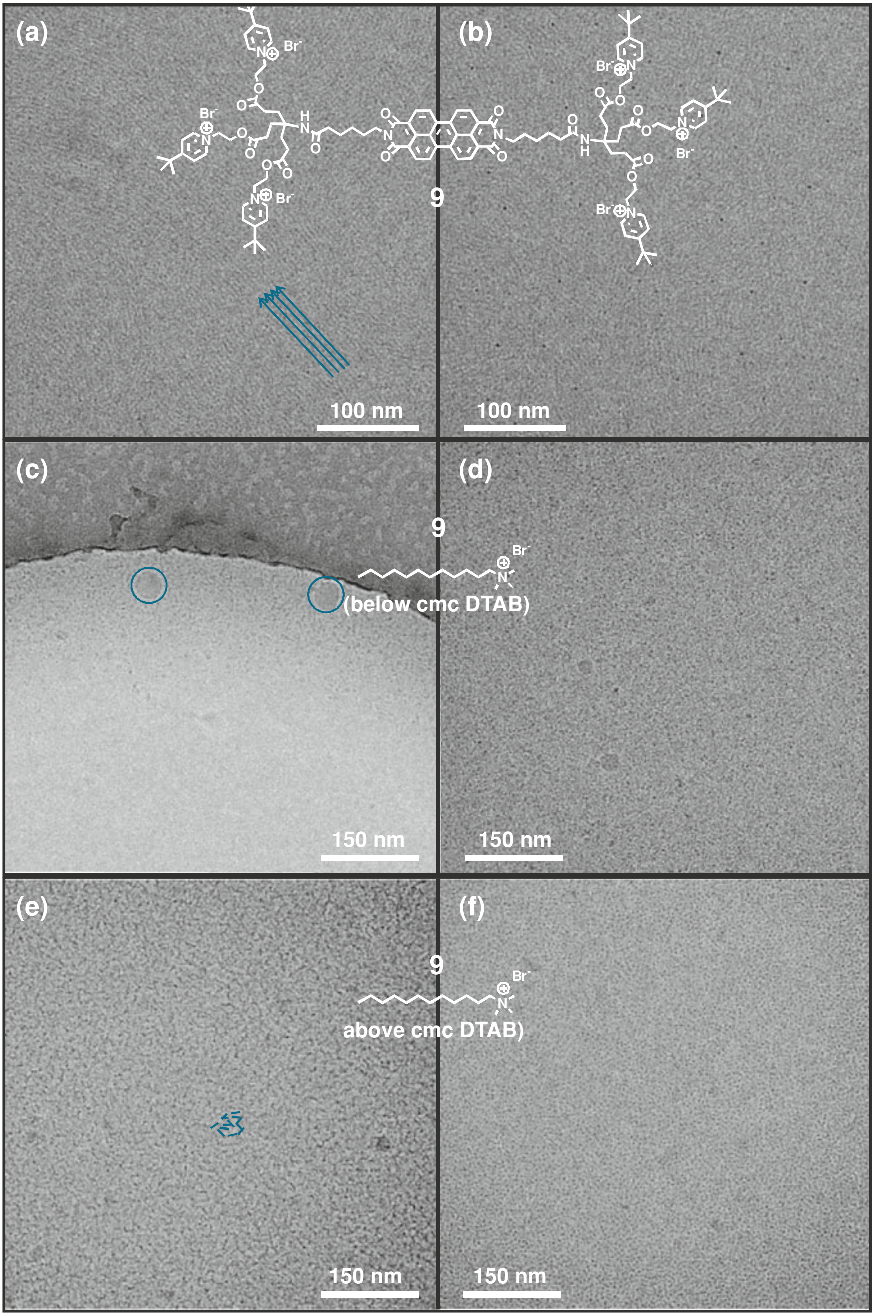

Fig. 3.47 Cryo-TEM images of **a**, **b** an aqueous solution of the cationic perylene derivative **9** ([**9**] = 10^{-4} M), **c**, **d** an aqueous solution of **9**-DTAB below the cmc of DTAB ([**9**] = 10^{-4} M, [DTAB] = 0.012 M) and **e**, **f** an aqueous solution of **9**-DTAB above the cmc of DTAB ([**9**] = 10^{-4} M, [DTAB] = 0.16 M). The significant structures are indicated by the markings in the figures on the *left* hand side

2.8 ± 0.5 nm (Figs. 3.47a, b). The small regions of high contrast especially discernable in Fig. 3.47b can be attributed to the fiber-like aggregates imaged along the axis. After the addition of DTAB, rather inhomogenous spherical aggregates with diameters of approximately 40 nm are formed (Figs. 3.47c, d). The observation that the large objects appear either spheric or ellipsoidic indicates that the structures are vesicles. In the samples **9**-DTAB above the cmc of DTAB, well defined fiber-like micelles with a length of 15 nm are observed (Fig. 3.47e) additionally to the small regular micelles of 4 nm diameter which can be attributed to free DTAB micelles not interacting with perylene (Fig. 3.47f).

Even though the arrangement within these supramolecular aggregates cannot be resolved by cryo-TEM imaging, this technique is highly versatile, as it nicely evidences the structural changes in solution which give rise to the differences in the optical properties of the mixed surfactant-cosurfactant systems. However, the role of the cationic head group remains unclear.

In order to further gain insights in the nature of the supramolecular assembly of **9** and DTAB, a variety of reference experiments have been carried out including the subsequent addition of SDBS to an aqueous solution of **9** and the subsequent addition of DTAB to a buffered aqueous solution of the anionic perylene derivative **1**. In case of the mixed head charge system **9**-SDBS, the absorption cross section of the perylene derivative decreases after the first addition step and is then subsequently recovered with increasing concentrations of SDBS, slightly blue-shifted and the contribution from the $0 \rightarrow 0$ perylene transition (at 540 nm) rises somewhat with respect to the $0 \rightarrow 1$ perylene transition (Fig. 3.48a).

The evolution of the perylene emission followed at an excitation wavelength of 530 nm is characterized by a sudden drop in intensity after the first SDBS addition step. The emission intensity is then recovered subsequently and slightly blue-shifted in comparison to the spectrum in absence of SDBS (Fig. 3.48b) in analogy to the absorption spectra.

In this regard it is interesting to note that the formation of a broad excimer emission band as indicated in the 2D excitation-emission contour plots in Fig. 3.49 is observed at low SDBS concentrations.

Obviously, the oppositely charged SDBS molecules neutralize the charges of the cationic perylene derivative at low SDBS concentrations resulting in an even more pronounced self-aggregation. At higher SDBS concentrations, the system undergoes a structural rearrangement inducing increased fluorescence intensities.

Again, the perylene fluorescence intensity is strongly increased far above the cmc of SDBS (2.8 mM) [94] to yield a maximum emission intensity which is higher by a factor of 3.5 pointing towards a complete breaking up of the perylene–perylene aggregates similarly to the situation presented in **9**-DTAB. It has been known since the 1940s that it is possible to determine the cmc of detergents by following emission quantum yields of self-aggregating fluorophores in aqueous solutions. Accordingly, different dyes have been used to determine the cmc of anionic and cationic detergents by using their optical properties as fingerprint for their aggregation [94, 95]. Hereby, a dye solution can be either used to determine the cmc of anionic or cationic detergents depending on the charge of the dye. This

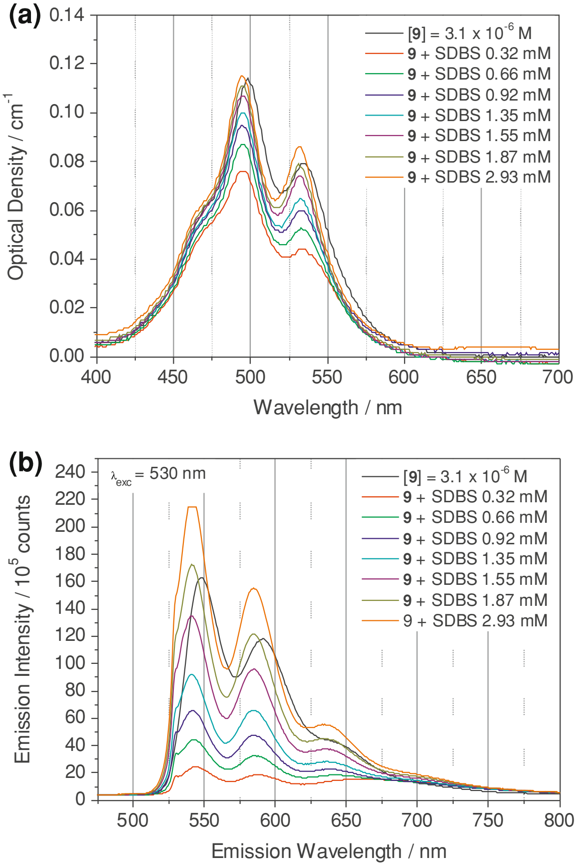

Fig. 3.48 Subsequent addition of solid SDBS to an aqueous solution of perylene derivative **9** ([**9**] = 3.1×10^{-6} M) followed by **a** absorption spectroscopy and **b** emission spectroscopy (λ_{exc} = 530 nm). The concentrations of SDBS are indicated in the figure legends

further underlines the exceptional situation presented by studying the aggregation behavior of the cationic perylene derivative **9**, as a pronounced interaction with both anionic and cationic amphiphiles has been evidenced. Accordingly, it can be envisaged that an interaction additional to the electrostatic forces between the head groups plays a significant role in the aggregation of the cationic perylene derivative with DTAB.

To further evaluate the presence of this interaction beyond electrostatic effects, the subsequent addition of DTAB to the anionic perylene derivative **1** has been investigated. In this surfactant-cosurfactant system, both the electrostatic attraction between the oppositely charged head groups in analogy to **9**-SDBS, as well as the "DTAB-perylene" interaction in analogy to **9**-DTAB can in principle occur.

The optical properties of the perylene derivative **1** at low DTAB concentrations (below 6.4 mM) are characterized by the formation of strong perylene–perylene aggregates (Fig. 3.50). In absorption spectroscopy (Fig. 3.50a) this is reflected by a nonzero background which can be attributed to large scattering particles. In total agreement with this observation, the perylene emission is dramatically reduced in

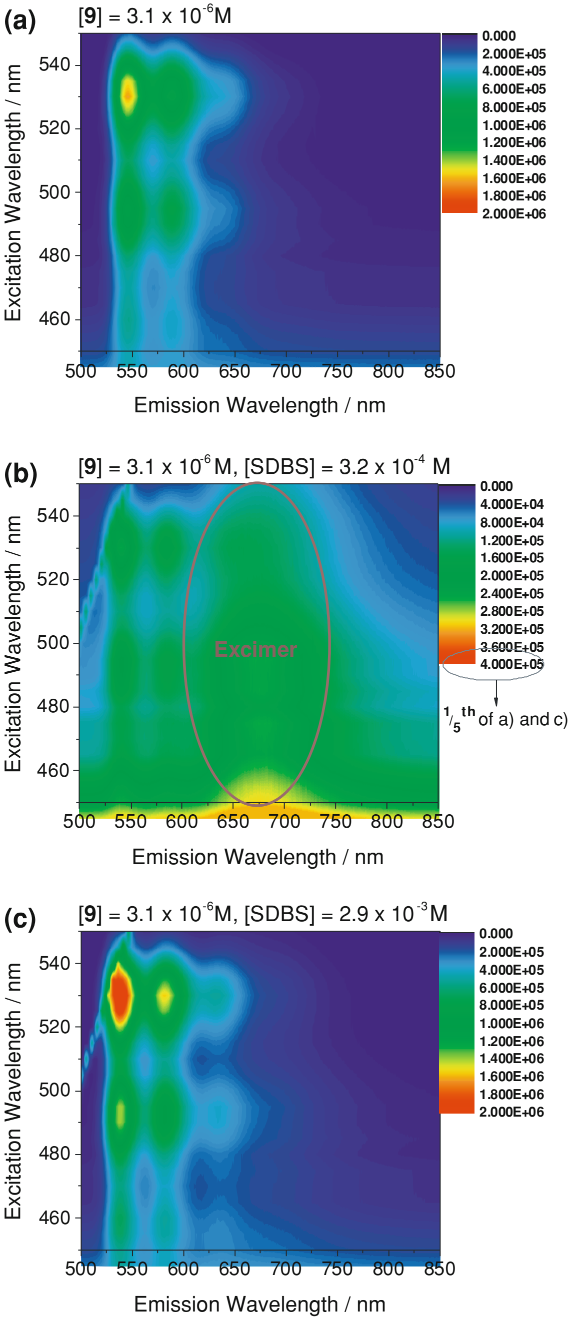

Fig. 3.49 2D excitation-emission contour plots of **a** perylene derivative **9** ([**9**] = 3.1 x 10^{-6} M, **b** **9**-SDBS at low SDBS concentration ([SDBS] = 3.2 × 10^{-4} M) and **c** **9**-SDBS at higher SDBS concentration ([SDBS] = 2.9 × 10^{-3} M). The maximum emission intensity in **b** is reduced by at least a factor of 5

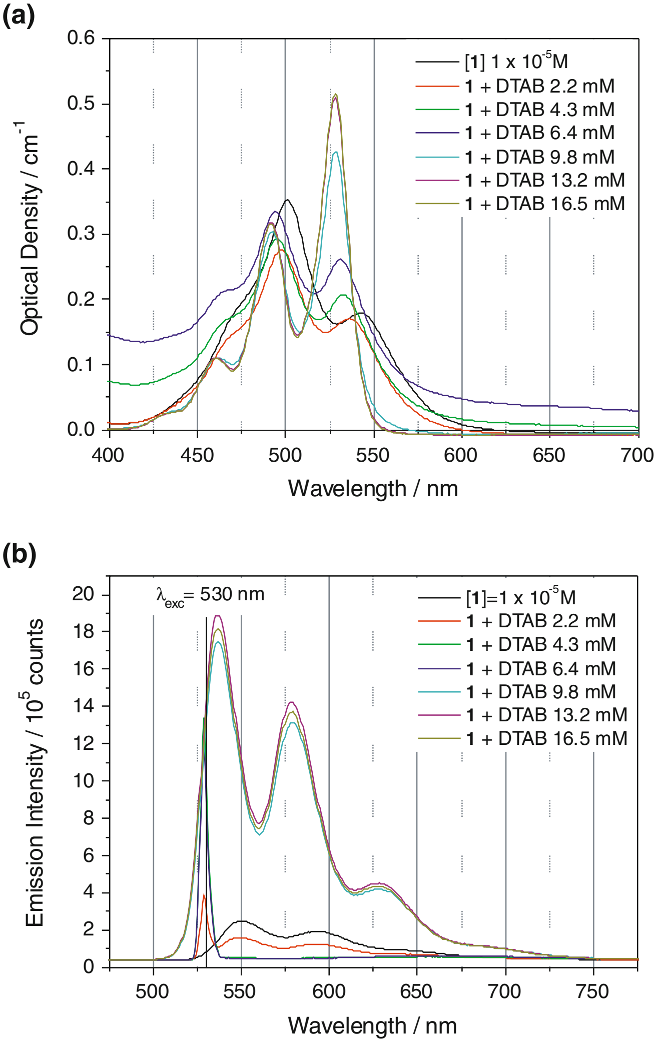

Fig. 3.50 Subsequent addition of solid DTAB to a buffered aqueous solution of perylene derivative **1** ([**1**] = 1.0 × 10^{-5} M) followed by **a** absorption spectroscopy and **b** emission spectroscopy (λ_{exc} = 530 nm). The concentrations of DTAB are indicated in the figure legends

intensity (Fig. 3.50b). This effect is qualitatively similar to the first addition steps of SDBS to the perylene derivative **9** (see Fig. 3.49) and can be traced back to the charge neutralization of the dendritic head groups in the perylene derivative due to the addition of the oppositely charged detergent. Please note that a direct comparison between the two systems is not possible, as the self-aggregation behavior of the perylene derivatives, as well as that of the cosurfactants is different. Furthermore, the perylene concentration is not equal in both sets of experiments and the subsequent addition of DTAB to **1** has been carried out in buffered media opposed to the experiments with the cationic derivative.

Above DTAB concentrations of 9.8 mM the perylene–perylene aggregates are again broken up resulting in an inversion of the perylene bands in the absorption spectra (Fig. 3.50a) to monomeric PBIs with normal Franck–Condon progression. Furthermore, the perylene emission intensity is dramatically increased by a factor of 7.5 compared to the pure perylene derivative solution (Fig. 3.50b). It is important to note that the transition to the optically monomeric perylene derivative occurs at a DTAB concentration significantly below its cmc (13 mM) which is in marked contrast to the previous experiments. Presumably, this can be traced back to the two independent interactions already described within this chapter occurring concomitantly. However, the nature of the non-electrostatic perylene-DTAB interaction is uncertain. Additional experiments such as small angle neutron scattering and time-resolved fluorescence spectroscopy are necessary to further elucidate this phenomenon. Unfortunately, this has been out of the scope of this thesis.

A last set of experiments involving the study of surfactant-cosurfactant systems has been concerned with the supramolecular assembly of the anionic perylene derivative **1** with the cationic perylene derivative **9**. Owing to the oppositely charged head groups and the aromatic perylene cores, the structurally similar PBIs are expected to undergo a very pronounced aggregation. In principle it can be envisaged that the assembly of **1** and **9** can be tailored by changing the pH, as the anionic head charges are dependent on the pH value (due to protonation and deprotonation), while the cationic charges are pH independent. However, as described in Sect. 3.1.4, the cationic perylene derivative is not stable in basic media. Therefore, investigations have been restricted to neutral pH.

The supramolecular assembly of **1** and **9** at neutral pH (buffered medium) is evidenced by absorption and emission spectroscopy (Fig. 3.51). The absorption spectra presented in Fig. 3.51a display the profiles of **1**, **9** and the equimolar mixture of both derivatives. The dashed plot is derived from the mathematical sum of the individual spectra (divided by 2). Significantly, it is not equal to the recorded spectrum of the mixture indicating that the perylene derivatives are interacting with each other. Further support is derived from emission spectroscopy. In general, the emission intensity of **1**–**9** is significantly reduced pointing towards a stronger aggregation of the perylene moieties. The normalized spectra displayed in Fig. 3.51b furthermore reveal that the predominant emission in **1**–**9** arises from an excimer band. Most strikingly, the excitation spectrum of the excimer species (720 nm) presented in Fig. 3.51c strongly resembles the absorption spectrum of **1**–**9**. Thus, monomeric species only have a minor contribution to the optical properties in buffered aqueous solutions of **1**–**9** pointing to a very pronounced self-assembly.

In order to obtain an impression on the structure and aggregate sizes of the mixed PBI assemblies, a solution of **1**–**9** has been subjected to cryo-TEM imaging. Only inhomogenous, large, not well defined objects with sizes exceeding 150 nm

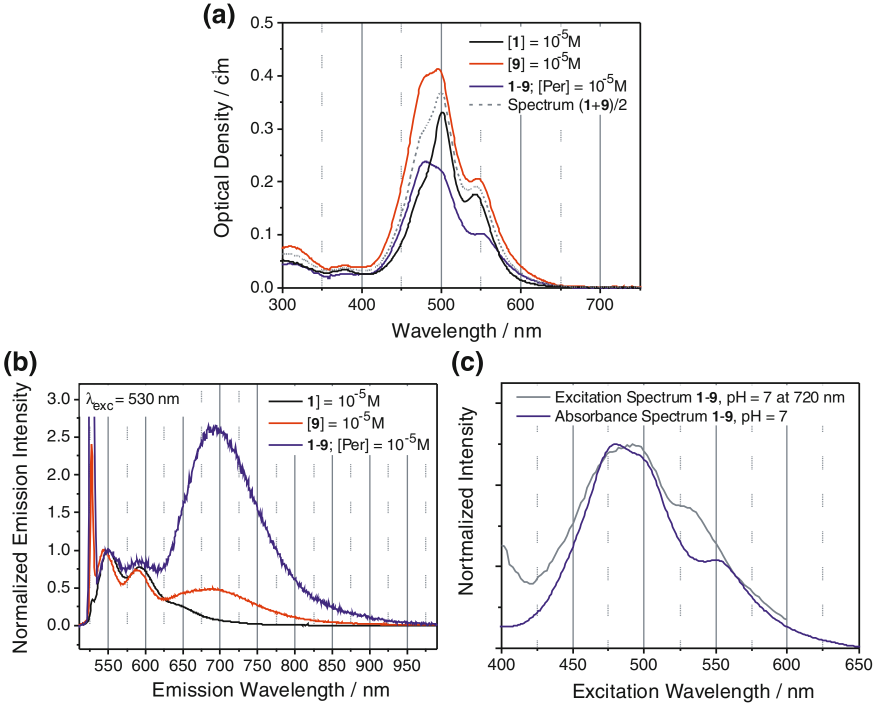

Fig. 3.51 **a** Absorption spectra of aqueous solutions of **1** and **9** compared to the spectrum of the equimolar mixture of both perylene derivatives (**1**–**9**). The *dashed line* represents the mathematical sum (devided by two) of the individual spectra of **1** and **9**. **b** Emission spectra of the solutions of **1**, **9** and **1**–**9** normalized to the local maximum at 550 nm recorded with $\lambda_{\mathrm{exc}} = 530$ nm. **c** Direct comparison of the excitation spectrum of the excimer species (720 nm) with the absorption spectrum of **1**–**9**

have been recorded so that no further attempts to resolve the underlying interactions have been carried out within this thesis.

In summary, detailed optical characterization on mixed perylene surfactant—detergent systems have laid the foundation for an in-depth understanding of the underlying supramolecular interactions. The perylene dyes represent an ideal model system, as their aggregation state can be qualitatively observed by absorption and emission spectroscopy. From a screening of different perylene derivative cosurfactant systems, it has been found that DTAB interacts with every perylene derivative under investigation independent on its head charge or structure. A variety of experiments has been performed in order to trace this interaction that appears to be independent on electrostatic forces. However, further investigations by different and independent techniques will be necessary to complete the picture. The very pronounced supramolecular assembly of the two structural analogues (albeit with opposite head charges) perylene **1** and **9** has also been captured by absorption and emission spectroscopy.

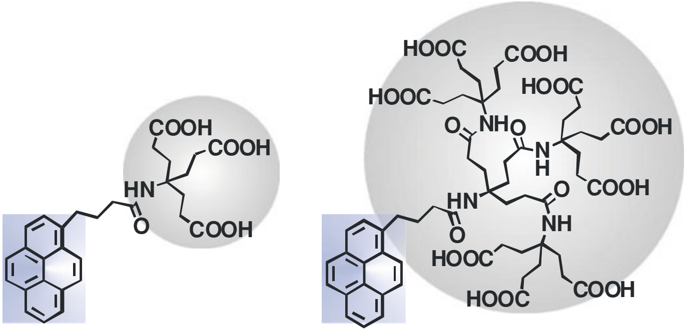

10 **11**

Scheme 3.2 Structures of the pyrene based surfactants **10** and **11**. The aromatic anchor is indicated by the rectangle, the solvophylic *Newkome*-type dendrimers by the *circles*, respectively

3.1.6 Dispersion by Pyrene Derivatives

Up to now, focus has been directed towards designed perylene based surfactants, as it has been evidenced that the PBI derivatives are excellent dispersion and solubilization additives for SWCNTs. For this purpose characterization protocols have been developed and evaluated to shed light into structure–property relationships of a variety of derivatives and to establish an appropriate adsorption hypothesis of the surfactants onto the SWCNT scaffold. However, so far no attention has been drawn towards the nature of the aromatic anchor group. In this regard it would be quite interesting to consider different π-systems, as the superior exfoliation efficiencies described above may not be a feature arising from perylene bisimide derivatives, but from π-surfactants in general.

In order to elucidate the importance of the anchor group, dispersion of HiPco, as well as CoMoCAT SWCNTs by two amphiphilic pyrene derivatives (pyr) **10** and **11** has been investigated (scheme 3.2) [96]. The pyrene derivatives are equipped with first or second generation *Newkome*-type dendrimers, respectively, in order to provide a pronounced water solubility [97].

In a typical dispersion experiment, the SWCNT raw material (0.1 g L^{-1}) was immersed in the buffered aqueous solution of **10** and **11** (0.5 g L^{-1}, pH = 7 or pH = 10), respectively. After sonication (20 min), the homogenous mixture was centrifuged (14 krpm, 30 min) in order to remove coarse aggregates and large SWCNT bundles. The optical absorption spectra (Fig. 3.52) of the supernatants reveal reasonably well resolved excitonic nanotube transitions being indicative for well dispersed SWCNTs at low surfactant concentrations similar to the perylene surfactants. Qualitatively, no striking differences are observed when comparing the pH = 7 (Fig. 3.52a) and the pH = 10 (Fig. 3.52b) dispersions except for the

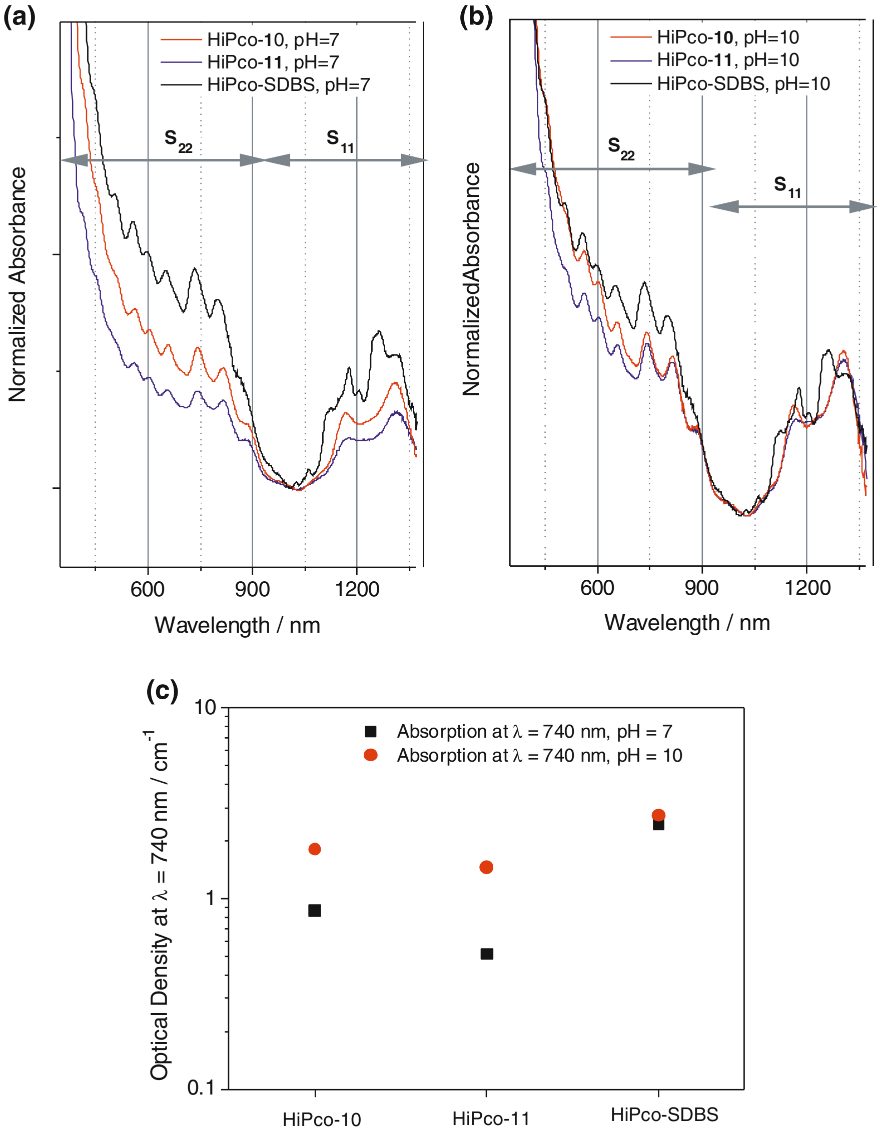

Fig. 3.52 Optical absorption spectra (normalized to the minimum) of HiPco SWNTs dispersed in buffered aqueous solutions of **10** and **11** (initial concentrations $[\mathrm{SWCNT}]_i = 0.1\ \mathrm{g\ L^{-1}}$ and $[\mathrm{pyr}]_i = 0.5\ \mathrm{g\ L^{-1}}$) compared to HiPco SWNTs dispersed in SDBS (1 wt%, $[\mathrm{SWCNT}]_i = 0.1\ \mathrm{g\ L^{-1}}$) at **a** pH = 7 and **b** pH = 10. The spectra of the supernatants (S) after centrifugation are displayed. **c** Absorbance at $\lambda = 740$ nm of HiPco SWCNTs dispersed in aqueous solutions of **10**, **11** and SDBS at pH = 7 and pH = 10, respectively. (Reproduced with permission from Wiley–VCH, reference 96)

Table 3.13 Calculated SWCNT concentrations in the supernatant of SWCNT-pyr after centrifugation with initial concentrations $[\text{SWCNT}]_i = 0.1$ g L^{-1} and $[\text{pyr}]_i = 0.5$ g L^{-1}. The concentration of SDBS is 10.0 g L^{-1}

		10	11	SDBS
[HiPco]/g L^{-1}	pH = 7	0.024 (24%)	0.014 (14%)	0.068
	pH = 10	0.046 (46%)	0.037 (37%)	0.069

reduced SWCNT resonant ratio in the pH = 7 dispersions pointing towards a less efficient solubilization at neutral pH.

The nanotube concentration in the supernatant (S) after centrifugation calculated from the extinction coefficients [2] and the optical density at 740 nm (represented in Fig. 3.52c) can be used as a measure for the dispersion efficiency of the surfactant. As summarized in Table 3.13, the dispersion efficiency of the pyrene surfactants is strongly enhanced at pH = 10—an observation that can be attributed to an increased exfoliation during the sonication induced unzippering of the nanotubes due to a higher charge density of the dendrimer head groups as already described for the perylene derivatives equipped with *Newkome*-type dendrimers (Sect. 3.1.1.1).

Significantly, the dispersion efficiency of **11** is reduced compared to **10** even though **11** is characterized by a higher intrinsic solubility due to the nine carboxylic acid functionalities opposed to the three COOH groups of **10**. Presumably, **11** can be less densely packed and organized on the nanotube scaffold due to the higher inter-pyrene Coulombic repulsion between adjacent pyrene head groups resulting in a reduced SWCNT dispersion efficiency in analogy to the scenario presented by the bolaamphiphilic perylene derivative **2** in comparison to **1**. In general, dispersion by the pyrene derivatives **10** and **11** is less efficient compared to the perylene derivatives (compare Table 3.1) under similar preparation conditions.

Nonetheless, the pyrene dispersions were furthermore subjected to fluorescence spectroscopy. In general, the nanotube emission intensity is strongly reduced compared to nanotubes dispersed in aqueous solutions of SDBS. After diluting the samples to the same optical density, the SWCNT emission appeared to be independent on the pyrene derivative and the pH strongly indicating that the nanotube emission pattern is dependent on the adsorption of the pyrene unit alone without contributions from the substituents or the buffer medium. Please note that this is in marked contrast to the situation extensively investigated and discussed for the perylene derivatives in Sects. 3.1.1 and 3.1.3.

Upon comparing the nanotube emission pattern of the pyrene dispersions with the dispersion in SDBS, a pronounced red-shift of the spectral features is discernable. Again, in contrast to the previously investigated perylene derivatives, this red-shift is more pronounced for larger diameter nanotubes (Fig. 3.53) compared to the smaller diameter nanotubes.

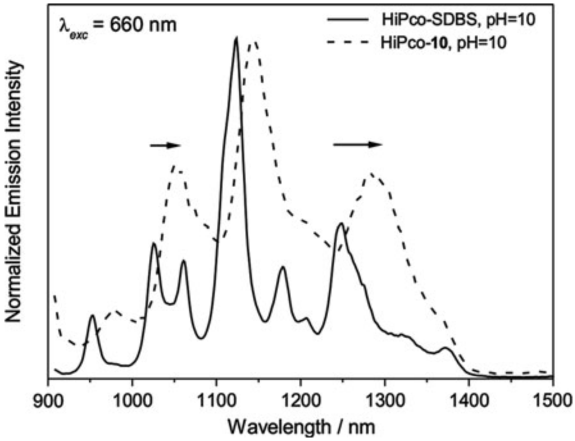

Fig. 3.53 nIR emission spectra normalized to the emission maximum of HiPco SWCNTs dispersed in aqueous solutions of **10** and SDBS ([SWNT] = 0.046 g L^{-1} and $[\mathbf{10}]_i = 0.5$ g L^{-1}, [SDBS] = 10 g L^{-1}) at $\lambda_{exc} = 660$ nm after degassing with nitrogen prior to the acquisition of the spectra. (Reproduced with permission from Wiley–VCH, reference 96)

This observation may be rationalized by the hypothesis that the SWCNT-pyr interaction is stronger for larger diameter nanotubes, as an enhanced interaction may lead to an increased alteration of the exciton binding energy. This is in marked contrast to the adsorption affinity of the perylene derivatives which exhibit a more pronounced interaction with smaller diameter SWCNTs. To further probe this impression, the diameter range of the SWCNTs has been expanded in the region of small diameters by using CoMoCAT SWCNTs which are characterized by a smaller and narrower diameter distribution (0.7–0.9 nm) compared to the HiPco material (0.8–1.4 nm), e.g. the average diameter is smaller by 30% in the CoMoCAT SWCNTs.

For the set of experiments described in the following focus has been laid on the derivative **10** at pH = 10, as it yields the highest dispersion efficiency within the SWCNT-pyrene systems investigated. After dispersing CoMoCAT (0.1 g L^{-1}) SWCNTs in **10** (0.5 g L^{-1}), it was found that the concentration of SWCNTs in the supernatant after centrifugation with identical parameters was 0.037 g L^{-1}, e.g. by 22% lower compared to the HiPco material (calculated from the optical density of 0.41 cm^{-1} at 652 nm and the extinction coefficient of CoMoCAT SWCNTs determined to be 1125 L g^{-1} m^{-1}). Furthermore, no transitions of very small diameter nanotubes in the region of 800–930 nm ((6, 4) and (9, 1) SWCNT) are discernable in CoMoCAT-**10** (Fig. 3.54a). However, such an indicated depletion may also be attributed to changes in the dielectric environment of the nanotube due to the adsorption of the pyrene derivatives. To ensure comparability with the pristine material dispersed in SDBS, **10** was replaced by the addition of SDBS to the CoMoCAT-**10** sample. Such a replacement can be mapped by fluorescence spectroscopy, as the original nanotube emission pattern is obtained after removal of the pyrene surfactant from the nanotube sidewall. The transitions of the (6, 4)

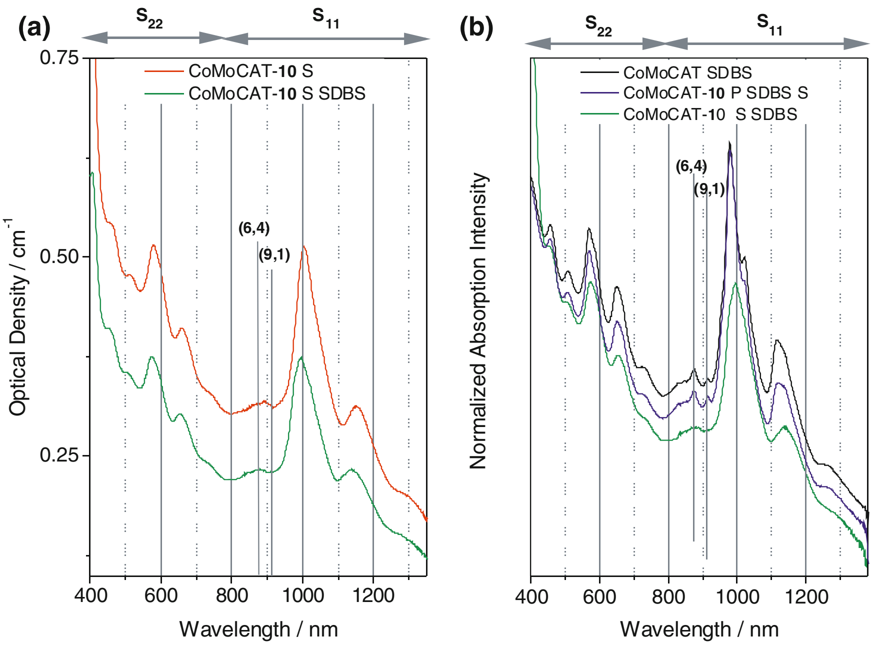

Fig. 3.54 **a** As recorded optical absorption spectrum of the supernatant after centrifugation of CoMoCAT SWCNTs dispersed in a buffered aqueous solution of **10** compared to the same dispersion after addition of 0.25 mL SDBS (10 g L^{-1}) solution to 0.75 mL of CoMoCAT-**10**. **b** UV/Vis/nIR absorption spectra (normalized to the minimum) of CoMoCAT SWCNTs dispersed in SDBS ([SDBS] = 10 g L^{-1}) compared to the SDBS redispersed supernatant and precipitate after predispersion with **10**—vertical offset for clarity. ([SWCNT] = 0.027 g L^{-1}, [**10**]$_i$ = 0.5 g L^{-1}, pH = 10). (Reproduced with permission from Wiley–VCH, reference 96)

and (9, 1)-nanotubes are not recovered after the addition of SDBS being indicative for depletion of the very small diameter nanotubes in the pyrene dispersed supernatant (S) (Fig. 3.54b). Both features are clearly present in the SDBS redispersed precipitate (P) of CoMoCAT-**10**.

In line with the absorption spectra, the fluorescence spectra at 580 nm excitation (Fig. 3.55) also point towards an increased interaction of **10** with larger diameter nanotubes leading to insufficient solubilization of the (6, 4)-SWCNT and thus loss of the (6, 4)-SWCNT emission.

Additional evidence can be obtained from the individualization degrees determined from statistical atomic force microscopic (AFM) analysis of the CoMoCAT-**10** and HiPco-**10** supernatants spin-casted on silicon wafers. In all cases, the height of minimum 250 SWCNT objects has been determined. Figure 3.56 depicts the histograms of the bundle size distributions of SWCNT-**10**. The exfoliation efficiency of **10** is determined to be 20–25% on the foundation of the statistical AFM analysis. Even though this is significantly smaller than the maximum exfoliation efficiencies yielded by the perylene derivatives (compare Fig. 3.9), the pyrene

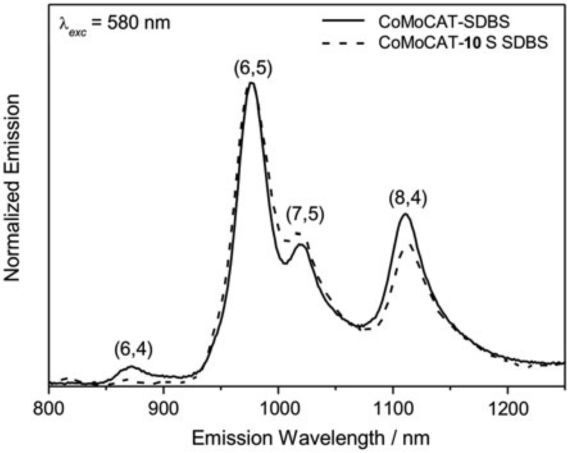

Fig. 3.55 Normalized emission spectra with $\lambda_{\mathrm{exc}} = 580$ nm of SWCNT-**10** and the same dispersion after replacement of **10** with SDBS; 0.25 mL SDBS (10 g L^{-1}) solution was added to 0.75 mL CoMoCAT-**10** with $[\mathbf{10}]_i = 0.5$ g L^{-1}). The dispersions were diluted prior to acquisition of the spectra to an optical density of 0.37 cm^{-1} at 580 nm corresponding to a nanotube concentration of 0.027 g L^{-1}. (Reproduced with permission from Wiley–VCH, reference 96)

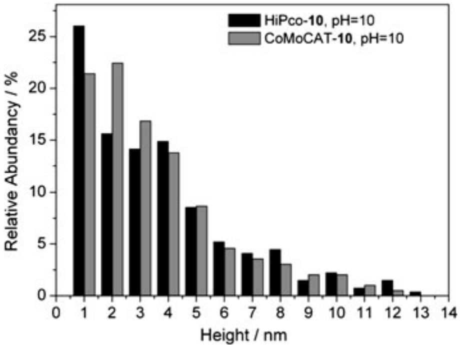

Fig. 3.56 Histograms of the bundle size distributions of HiPco and CoMoCAT nanotubes dispersed in a buffered aqueous solution of **10** ([HiPco] = 0.046 g L^{-1}, [CoMoCAT] = 0.037 g L^{-1} [**1**] = 0.5 g L^{-1}) derived from statistical AFM analysis after spin-casting the supernatant dispersions after mild centrifugation. (Reproduced with permission from Wiley–VCH, reference 96)

based π-surfactant **10** still outperforms SDBS (with individualization degrees of approximately 15% under equal experimental conditions). Since the exfoliation efficiency in case of HiPco SWCNT by **10** is higher compared to CoMoCAT SWCNTs, the more pronounced dispersion efficiency of larger diameter SWCNTs is further indicated by the AFM analysis.

In summary, the surfactant capability of pyrene based amphiphiles equipped with *Newkome*-type dendrimers has been demonstrated. The dispersion efficiency is highest for the first generation *Newkome* dendronized pyrene **10** in basic media (pH = 10). Dispersion and exfoliation efficiencies are reasonable, but significantly lower compared to the perylene derivatives. This further underlines the extraordinary potential of perylene bisimide based surfactants, presumably due to the rather strong charge transfer interaction between the anchor group and the SWCNT scaffold [89]. A more detailed investigation of the pyrene derivative dispersant **10** has pointed towards the preferential solubilization of larger diameter nanotubes, e.g. depletion of small diameter nanotubes in the CoMoCAT-**10** supernatant after mild centrifugation being in marked contrast to anionic perylene based surfactants which show enhanced adsorption towards smaller diameter SWCNTs. This observation indirectly confirms the adsorption hypothesis of the anionic perylene derivatives presented in Fig. 3.40.

Even though the selectivity in the SWCNT dispersability by **10** is not very pronounced, any progress towards selective SWCNT dispersion is bound to a great impact, as it may present the foundation for further tuning and tailoring the interactions of SWCNTs with π-surfactants. However, a long road is yet to be paved towards efficient and tailor-made selective nanotube dispersion so that the most promising SWCNT separation technique, namely density gradient ultracentrifugation, deserves some attention in the following.

3.2 SWCNT Sorting

3.2.1 Density Gradient Ultracentrifugation

3.2.1.1 Electronic Type Sorting

In order to adjust the parameters for a SWCNT separation by density gradient ultracentrifugation from the literature to the available set-up, electronic type sorting of laser ablation SWCNTs by the aid of commercially available surfactants such as SDS and SDC has been targeted. Comprehensive reviews about the underlying principles and an overview of the literature are presented in references [98], as well as in the introduction of this thesis (Chap. 1.3.2). In general, it is highly favorable to tune the buoyant densities of the SWCNTs in such a way that the desired SWCNTs have the lowest buoyant density and therefore travel to the topmost region.

Since it has been well documented in literature that electronic type sorting of SWCNTs is accomplished with mixtures of SC and SDS, these two surfactants have been chosen. In independent studies, different mixtures of both surfactants have been applied for the dispersion of SWCNTs prior to DGU. Hereby, mixtures of SC:SDS = 4:1 (by weight) [99, 100] yielded semiconducting SWCNTs in the top fraction, while mixtures of SC:SDS = 2:3 (also by weight) have been used for the spatial separation of the metallic species [101–105]. However, no example has been presented in literature where exactly the same SWCNTs have been subjected to DGU under equal experimental conditions, but with varying ratios of surfactant and cosurfactant so that no direct evidence for the influence of the surfactant ratio has been provided so far.

Exactly this question has been addressed by the experiments summarized in the following. For a detailed description of the DGU setup, please see the experimental section. Briefly, the SWCNT dispersions were prepared by sonicating 0.3 g L^{-1} laser ablation SWCNTs (LA) in the aqueous solutions of the respective mixtures of SC and SDS with total surfactant concentrations of 1.5 wt%. After mild pre-centrifugation (30 min, 15 krpm) iodixanol as density gradient medium was added to yield a iodixanol concentration of 10 wt%. This dispersion (1.3 mL) was layered on top of the gradient consisting of discrete layers with 60, 40 and 20 wt% iodixanol. The surfactant concentration has been kept constant throughout the centrifugation vials. The photographs after 16 h of centrifugation at 35 krpm are displayed in the left panels of Fig. 3.57. Visually colored bands are clearly discernable which appear red in the case of the SC:SDS = 2:3 surfactant mixture (Fig. 3.57a) and green in the case of the SC:SDS = 4:1 mixture (Fig. 3.57b).

Several fractions as indicated in Fig. 3.57 have been withdrawn and subjected to absorption spectroscopy. As revealed by the absorption spectra normalized to the minimum at 900 nm in Fig. 3.57a, the reddish fraction F1 with the surfactant mixture SC:SDS = 2:3 is strongly enriched in metallic species as concluded from the enhancement of the SWCNT transitions between 400 and 650 nm with respect to the transitions attributed to semiconducting nanotubes. The opposite trend is observed in Fig. 3.57b where a surfactant mixture of SC:SDS = 4:1 has been used throughout the experiment. These observations are in complete agreement with the literature and nicely demonstrate the wide applicability and flexibility of DGU based sorting. The greenish fraction F1 of the vial in Fig. 3.57b has furthermore been separated in two sub-fractions denoted as F1a and F1b. As indicated by the absorption spectra, diameter sorting is discernable within this fraction with the smaller diameter SWCNTs possessing lower buoyant densities (F1a).

A direct comparison of the metallic and semiconducting enriched fractions is presented in Fig. 3.57c and most clearly demonstrates the efficient sorting procedure with varying surfactant-cosurfactant ratios. Valuable information concerning the transitions in the regime of overlapping M_{11} and S_{22} transitions can also be extracted from the sorted fractions as demonstrated in Fig. 3.57e. Since the reddish fraction is enriched in metallic SWCNTs, while the greenish sub-fraction F1a is enriched in smaller diameter semiconducting SWCNTs, it is possible to precisely assign the SWCNT transitions between 550 and 700 nm to metallic or semiconducting species, respectively.

The DGU experiments summarized in Fig. 3.57 nicely underscore the information extracted from literature and furthermore demonstrate the effective transformation of the sorting technique to the available set-up. Additionally, the experiments raise a puzzling issue, as the sorting of laser ablation SWCNTs with a

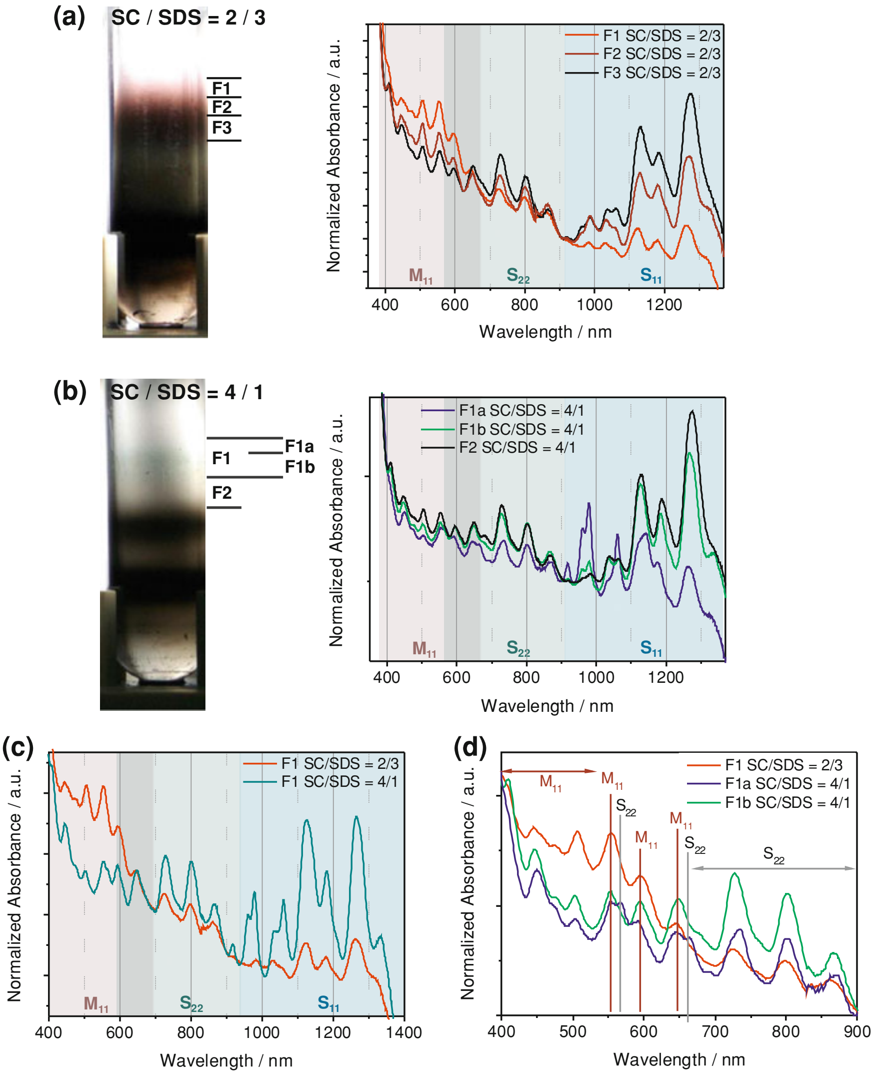

Fig. 3.57 Overview of the centrifugation vials after electronic type sorting DGU of laser ablation SWCNTs by mixtures of SC and SDS as surfactants. The absorption spectra of the respective fractions normalized to the local minimum at 900 nm are displayed on the *right* hand side. The regions of the respective SWCNT transitions are indicated by the colored shaded backgrounds. **a** Enrichment of metallic SWCNTs with a SC:SDS ratio of 2:3. **b** Enrichment of semiconducting SWCNTs with a SC:SDS ratio of 4:1. **c** Direct comparison of the absorption spectra of the two visually colored top fractions of vials a and b. **d** Magnified view of the region of overlapping M_{11} and S_{22} transitions and the accessible assignment to metallic and semiconducting SWCNTs

very similar diameter distribution compared to HiPco SWCNTs (0.8–1.4 nm) under standard experimental conditions in a linear density gradient has been achieved, even though separation of HiPco SWCNTs has shown to be problematic and only very recently been demonstrated [106].

Most interestingly, simply changing the SWCNT pristine material to HiPco SWCNTs in the set-up described above has not resulted in effective electronic-type sorting. This phenomenon is not easy to rationalize and strongly indicates that the problem in efficient sorting of HiPco SWCNTs is not based on the necessity of discriminating multiple species that differ only slightly in their buoyant density alone, as the same difficulties would have been expected for the laser ablation SWCNTs used in this study. This discrepancy can be rationalized by considering that the buoyant density of surfactant encapsulated SWCNTs is also altered in case of covalently functionalized SWCNTs as has been demonstrated by Strano and co-workers [107]. Since HiPco SWCNTs are structurally less perfect than laser ablation SWCNTs containing more defects or being of shorter length in average, it is reasonable that the buoyant densities are affected resulting in a convolution of the desired sorting scenario. However, at this stage, further investigations would be desirable to support this idea. Even though the alteration of the buoyant densities may result in undesired effects in the case of DGU on HiPco SWCNT, it can in principle be exploited to separate covalently functionalized from non-functionalized material as will be demonstrated in the following.

3.2.1.2 DGU Sorting According to Structural Integrity

In the following the efficient separation of covalently altered SWCNTs from their nonfunctionalized counterparts shall be outlined on the example of carboxylated SWCNTs [108]. The underlying covalent functionalization sequence first involves reduction of the pristine SWCNTs under Birch conditions. The negatively charged SWCNT intermediates are then carboxylated by CO_2 to yield the functionalized raw soot after aqueous work-up. This functionalization sequence holds great potential as it enables the direct sidewall carboxylation of SWCNTs (in contrast to oxidation based procedures where the functional entities are predominantly anchored at the ends) and thus opens the door towards a tremendous playground for further derivatization reactions. Furthermore, owing to the equilibrium based nature of this reductive functionalization procedure [109], the functionalization degrees can be fine-tuned and tailored by external stimuli such as pressure and time. To further complete the picture of this groundbreaking covalent derivatization, it is important to underline that, additional to the advantages already mentioned, it has been indicated that this type of sidewall functionalization preferentially attacks semiconducting SWCNTs.

However, despite the fact that semiconducting SWCNTs exhibit are more pronounced reactivity under carefully explored reaction conditions with tunable degrees of functionalization, a major obstacle is still presented in the clear and efficient separation of the functionalized from the non-functionalized material.

This not only hinges on the potential future applicability of this derivatization sequence with regard to scalable SWCNT sorting, but furthermore strongly complicates the characterization of the SWCNT mixture. A powerful methodology to overcome this problem is presented in density gradient ultracentrifugation, as it has been shown that covalently derivatized SWCNT possess significantly higher buoyant densities in aqueous surfactant solution compared to the non-functionalized counterparts [107]. In order to demonstrate the versatility of the DGU approach for the sorting of covalently functionalized SWCNTs and the benefits arising from this separation with regard to the precise characterization of the nanotubes, two samples with different degrees of carboxylation have been subjected to DGU.

The protocol established by Strano [107] has been slightly modified in order to separate the non-functionalized from the functionalized and the bundled material in one DGU step. The setup is summarized in Fig. 3.58a. The SWCNTs are dispersed in a 2 wt% aqueous solution of SDC by bath-type sonication (30 min) and mildly pre-centrifuged (15 krpm, 30 min). An iodixanol concentration of 32.5% was then established that allows for the injection between the 30 and the 40 wt% iodixanol layer. After 17.5 h ultracentrifugation at 40 krpm, three spatially clearly separated bands evolved that can be easily fractionated. The centrifugation vials of the as-received purified HiPco SWCNTs (AP) and two examples of carboxylated SWCNTs with medium functionalization degrees (MF) and high functionalization degrees (HF) in average are presented in Fig. 3.58b. As especially striking in case of the HF material, the topmost band containing the nanotubes that have not been covalently altered is visually colored. The red color indicates that metallic species are strongly enriched in fraction F1 pointing towards a selective functionalization sequence. Please also note that the SWCNT population in the bands undergoes an intense redistribution with a decreasing concentration of nanotubes in F1 with increasing degrees of covalent modification.

In order to (a) proof the successful sorting of non-functionalized and functionalized SWCNTs, (b) illustrate the selectivity of the covalent functionalization sequence and (c) provide a detail characterization of the carboxylated SWCNTs, the fraction F1–F3 of the three DGU experiments have been subjected to extensive characterization by absorption, emission and Raman spectroscopy, as well as AFM.

The results of the as-received material are summarized in Fig. 3.59. The absorption spectra normalized to the minimum provide the first evidence that the defect free SWCNT travel to the top of the centrifugation vial yielding clearly resolved peaks arising from the excitonic transitions in the nanotubes with high resonant ratios. The second fraction is also characterized by well resolved transitions, albeit with much lower resonant ratios indicating that the SWCNTs in F2 contain a significant amount of defects. The fraction of highest buoyant density only shows vanishing SWCNT transitions being red-shifted in comparison to fractions F1 and F2, as the SWCNTs in this fraction are bundled.

The AFM images of the respective fractions spin casted in Si/SiO$_2$ wafers reveal that the SWCNTs in fraction F1 are individualized and straight. Please note

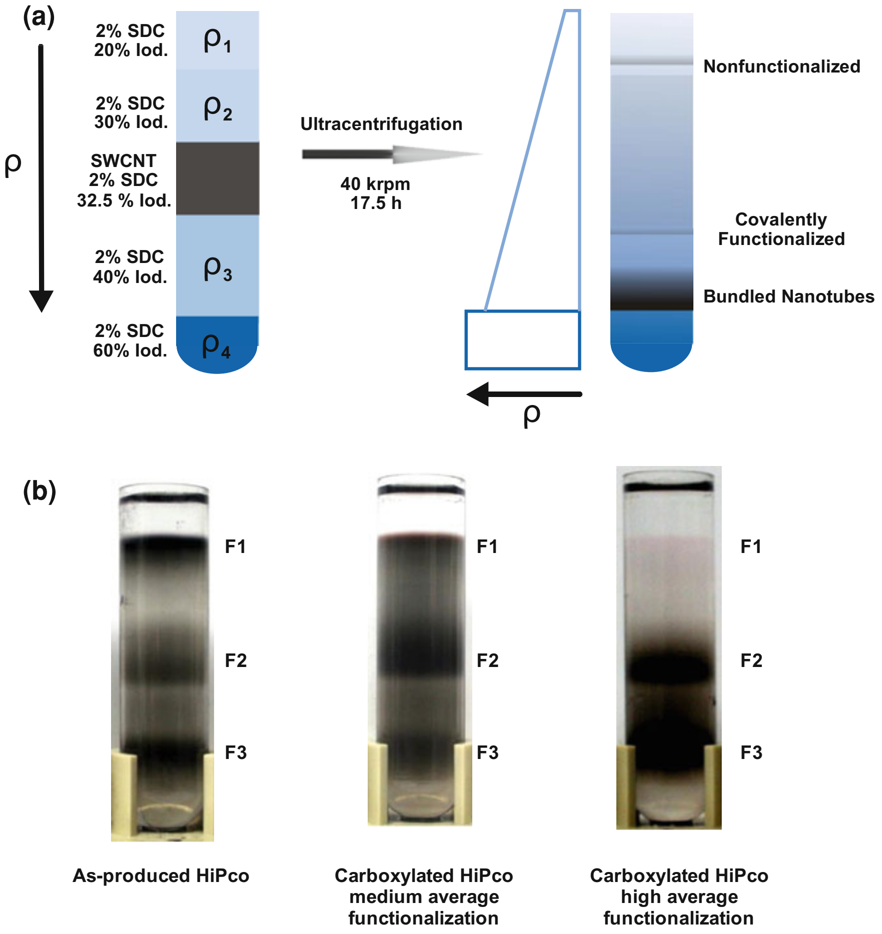

Fig. 3.58 **a** Schematic representation of the DGU setup for the separation of non-functionalized, covalently functionalized and bundled SWCNTs, **b** Examples of the centrifugation vials after DGU with as-received SWCNTs and carboxylated SWCNTs with medium and high functionalization degrees, respectively

that they are hardly discernable, as the diameter of the HiPco SWCNTs is 1 nm in average and the surface roughness of the wafers is 0.5 nm. The nanotubes in fraction F2 also appear as individualized species, but with kinks and inhomogeneities along their sidewall.

Unambiguous evidence for the successful sorting according to structural integrity is derived from Raman spectroscopy, as the Raman D/G ration are widely accepted as a measure of the sp^3 modifications of the nanotube network (see Sect. 1.4.3). In the samples after DGU, Raman spectroscopy is especially versatile, as contributions from amorphous material that may convolute the bulk spectra can be

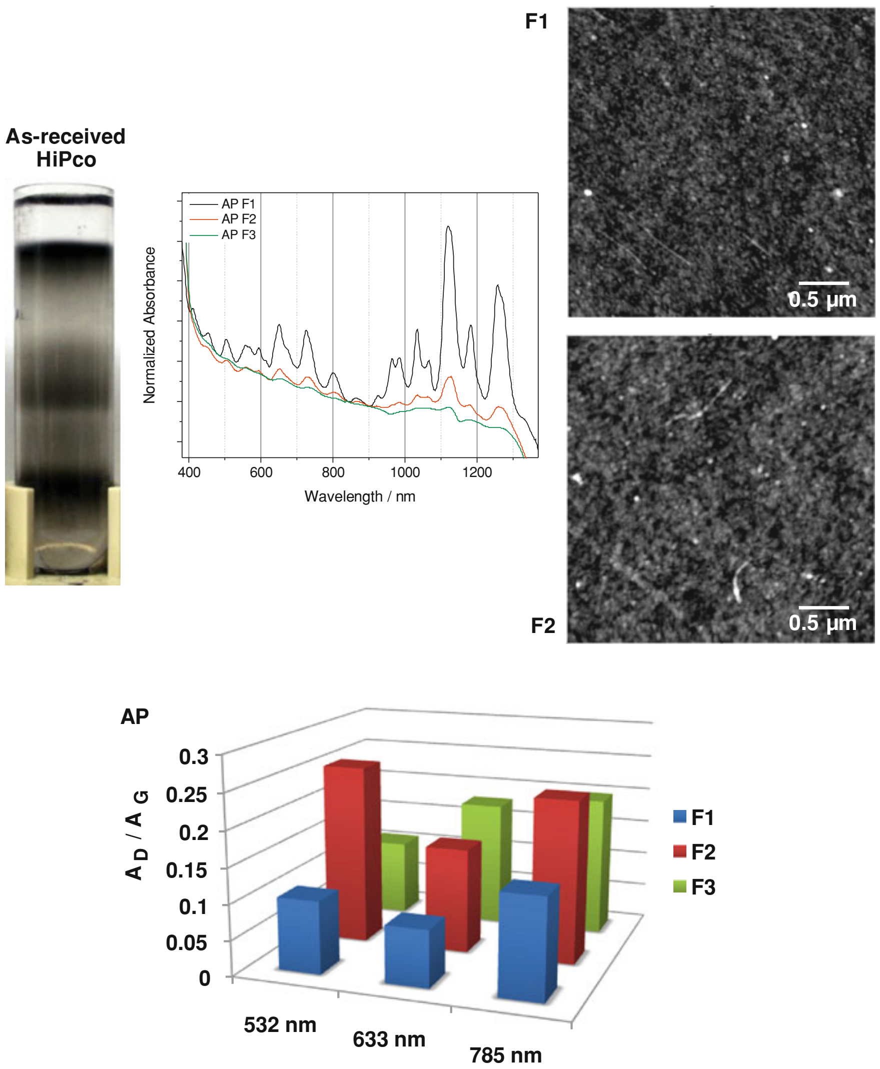

Fig. 3.59 Top panel: Centrifugation vial after DGU of as-received HiPco SWCNTs. The absorption spectra of the three fractions (normalized to the minimum at 900 nm) are displayed in the center of the image. The *top* and *bottom* images are representative atomic force micrographs of the respective fractions spin-casted on Si/SiO$_2$ wafers. Bottom panel: Raman A_D/A_G ratios of the three fractions recorded from the solid at three excitation wavelength, namely 532, 633 and 785 nm

excluded. In order to obtain representative spectra of the fractions, the solutions have been microfiltrated and subjected to Raman spectroscopy from the solid. The results of the A_D/A_G ratios for three different excitation wavelengths are displayed in the bottom panel of Fig. 3.59. The D-band with respect to the G-band of F2 is by a factor of 2 larger in average compared to F1 further supporting the conclusion that the structurally perfect SWCNTs have been separated from the defectous material. The Raman spectra of the bundled SWCNTs give rise to A_D/A_G ratios between F1 and F2.

The characterization of the as-received material after DGU sorting according to structural integrity nicely underlines the versatility of this separation and the accessible precise analysis. In this regard, it is interesting to note that this characterization routine may also be regarded as potential standard protocol for purity and integrity evaluation of as-received SWCNTs, as the multiple factors influencing the bulk characterization are limited in this case. Furthermore a qualitative impression on the amount of structurally perfect SWCNTs in a given sample is quickly obtained. As illustrated, the as-received HiPco SWCNTs already give rise to an intense band in fraction F2 so that it may be concluded that they contain a significant amount of defectous SWCNTs.

In the following, the characterization protocol has been applied to the covalently functionalized SWCNT samples. The overview on the material with medium average functionalization degree is provided in Fig. 3.60. As revealed by the absorption spectra, the non-functionalized material in F1 is comprised of large diameter semiconducting SWCNTs and metallic species, as the S_{22} transitions and S_{11} transitions attributed to small and medium diameter semiconducting nanotubes are clearly diminished (in the region of 620–900 nm and 900–1150 nm, respectively) compared to the reference material in Fig. 3.59. Accordingly, the chemical derivatization sequence has clearly addressed small and medium diameter SWCNTs preferentially. The absorption spectrum of the functionalized fraction F2 is characterized by the almost complete loss of the excitonic SWCNT transitions due to the comparatively high defect density (note that transitions in defectous F2 of the as-received material are not completely quenched).

In a bulk spectrum it would be hard to distinguish between bundled SWCNTs with also vanishing excitonic transitions, as can be concluded when comparing the spectrum of F2 to F3 in Fig. 3.60. However, the unique sorting power of DGU clearly rules out this potential data convolution. This is again supported by the AFM images where no bundled SWCNTs have been observed in F2. Representative images of F1 and F2 are presented in Fig. 3.60. They closely resemble the images of the as-received SWCNTs except for the fact that comparatively more pronounced inhomogeneities on the SWCNT sidewall appear in F2 of the MF carboxylated SWCNTs.

The Raman A_D/A_G ratios of the MF SWCNTs are summarized in the bottom panel of Fig. 3.60. In every case, the D-band is significantly increased in F2 compared to F1. The underlying selectivity of the covalent sidewall modification procedure is reflected by the significantly larger A_D/A_G ratios with 785 nm excitation where predominantly semiconducting SWCNTs are resonantly enhanced. The A_D/A_G at 785 nm is by a factor of 3 higher compared to A_D/A_G at 532 nm excitation where the majority of resonantly excited SWCNT exhibit metallic character. In this regard it is interesting to note that the A_D/A_G ratio of F2 of the MF SWCNTs at 532 nm is equal to that of F2 of the as-received reference

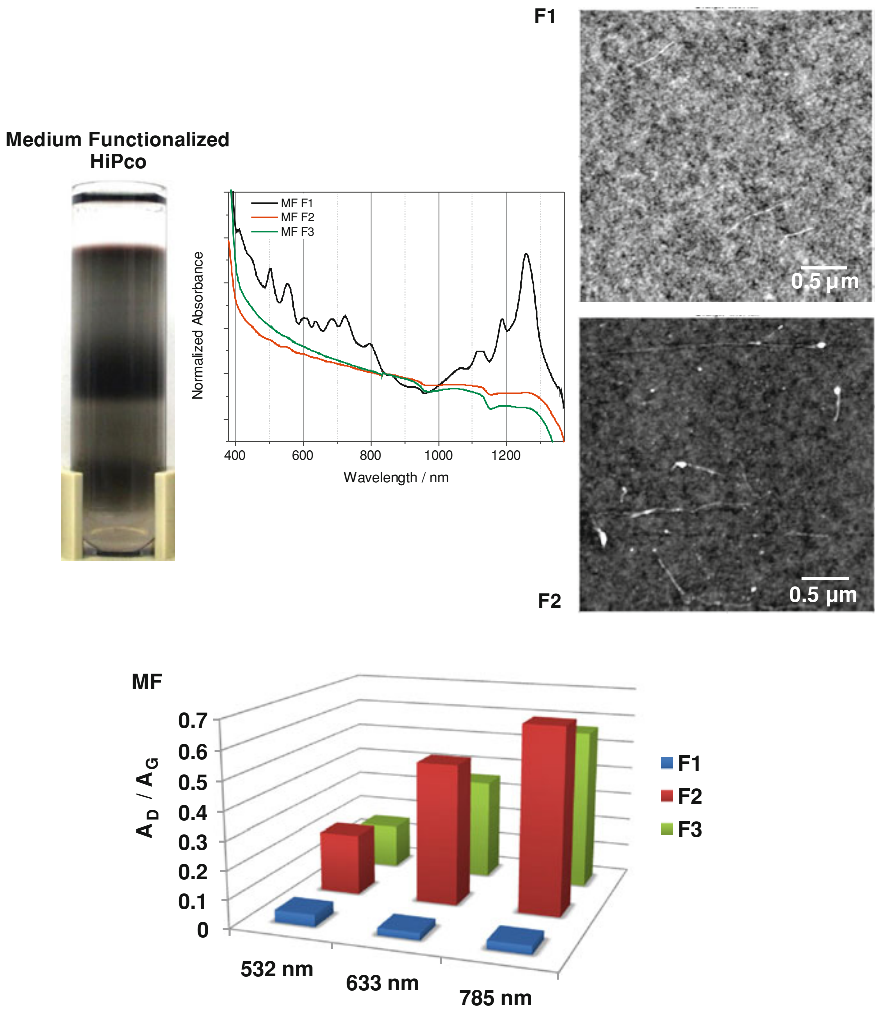

Fig. 3.60 Top panel: Centrifugation vial after DGU of medium functionalized HiPco SWCNTs. The absorption spectra of the three fractions (normalized to the minimum at 900 nm) are displayed in the *center* of the image. The *top* and *bottom* images are representative atomic force micrographs of the respective fractions spin-casted on Si/SiO_2 wafers. Bottom panel: Raman A_D/A_G ratios of the three fractions recorded from the solid at three excitation wavelength, namely 532, 633 and 785 nm. (Reproduced with permission from Wiley–VCH, reference 108)

within the experimental error (0.25 in the case of AP and 0.22 in the case of MF) indicating that no metallic SWCNTs have been attacked by the comparatively mild functionalization conditions.

To complete the characterization sequence, the highly functionalized nanotube material after DGU sorting according to structural integrity was analyzed

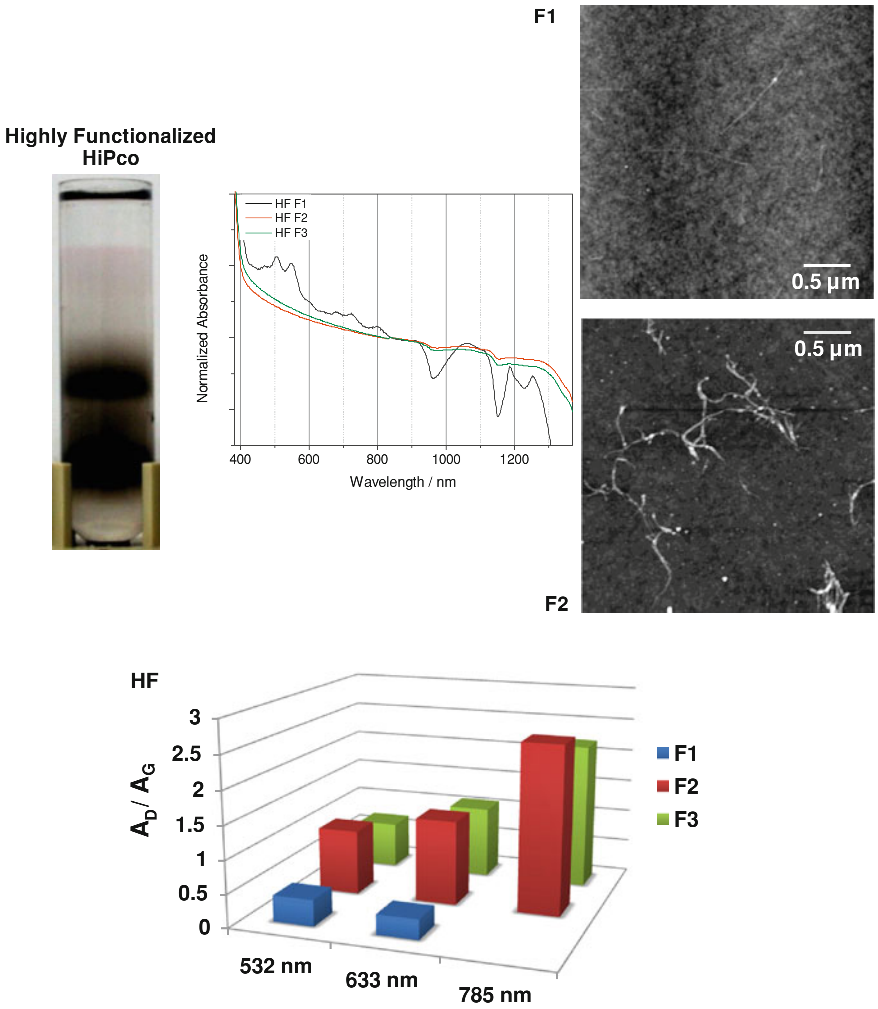

Fig. 3.61 Top panel: Centrifugation vial after DGU of highly functionalized HiPco SWCNTs. The absorption spectra of the three fractions normalized to the minimum at 900 nm are displayed in the *center* of the image. The *top* and *bottom* images are representative atomic force micrographs of the respective fractions spin-casted on Si/SiO_2 wafers. Bottom panel: Raman A_D/A_G ratios of the three fractions recorded from the solid at three excitation wavelength, namely 532, 633 and 785 nm. (Reproduced with permission from Wiley–VCH, reference 108)

(Fig. 3.61). The absorption spectrum of the non-functionalized F1 displays only two dominant bands at 505 and 550 nm giving rise to the intense red color of the metallic HiPco SWCNTs. The absorption spectrum of the strongly covalently modified SWCNTs in F2 is characterized by the complete loss of excitonic transitions and thus closely resembles the spectrum of the bundled nanotubes in F3.

However, the AFM images clearly demonstrate that the nanotubes in F2 are individualized, as all SWCNT objects exhibit heights below 2 nm. Nonetheless, their morphology is completely different compared to the medium functionalized HiPco SWCNTs presented in Fig. 3.60, as interwoven networks of nanotubes are observed. This intense crosslinking can be attributed to the formation of carboxylic acid dimers at high surface coverage along the nanotubes sidewall.

The extraordinarily high functionalization degrees of the SWCNTs in F2 of the HF material are also manifested in the Raman A_D/A_G ratios summarized in the bottom panel of Fig. 3.61 approaching 2.5 at an excitation wavelength of 785 nm meaning that the D-band becomes the dominant feature in the Raman spectrum. The selectivity of the underlying covalent functionalization sequence is again reflected when comparing the A_D/A_G ratios of F2 at different excitation wavelength. Again, the A_D/A_G ratio at 785 nm is by a factor of 2.5 higher compared to that at 532 nm where predominantly metallic nanotubes are excited.

The fact that the F1 containing the nonfunctionalized SWCNTs is comprised of metallic SWCNTs and the observation that the functionalization degrees of those metallic SWCNT species that have been functionalized are much lower compared to the semiconducting SWCNT further corroborates the very pronounced selectivity. In this regard, it is also interesting to note that no SWCNTs could be resonantly enhanced in F1 with an excitation wavelength of 785 nm.

Since the fractions F2 always contain an unknown contribution of defectous SWCNTs which are also present in the as-received HiPco SWCNTs, a detailed comparison of the F2 of different SWCNT samples needs to be—if at all—carried out with care, except for an evaluation of the Raman A_D/A_G ratios (Fig. 3.62a). The direct comparison of the functionalized fractions of the different materials clearly illustrates the differences in the structural integrity owing to the covalent functionalization sequence, as well as its underlying selectivity.

A comparison of F2 in absorption and emission spectroscopy is omitted due to the above mentioned uncertainty in material composition of the pristine material with respect to the presence of defectous SWCNTs. A comparison of F1, however, appears to be uncritical in any case. Therefore, a direct comparison of the absorption and emission spectra at 660 nm excitation of fractions F1 of the AP, MF and HF samples is provided in Fig. 3.62b, c, respectively.

The very pronounced selectivity towards preferred derivatization of semiconducting SWCNTs has already been extensively discussed and is again nicely reflected in the absorption spectra of the non-functionalized cross-section of SWCNTs of the as-received nanotubes compared to the MF and HF carboxylated samples (Fig. 3.62a). The fraction F1 after DGU shows an enhanced enrichment of metallic (or rather depletion of semiconducting) SWCNT species with increasing bulk functionalization degrees. This trend is further indicated by the nIR fluorescence intensities which drop by a factor of 40 in the MF sample and by a factor of 65 in the HF sample, respectively, at equal optical densities at 600 nm ($0.04\ \mathrm{cm}^{-1}$) and accordingly similar SWCNT concentrations.

From the values of the nIR emission intensities tabulated in Table 3.14 relative to the pristine material at equal SWCNT concentrations an enrichment factor of the

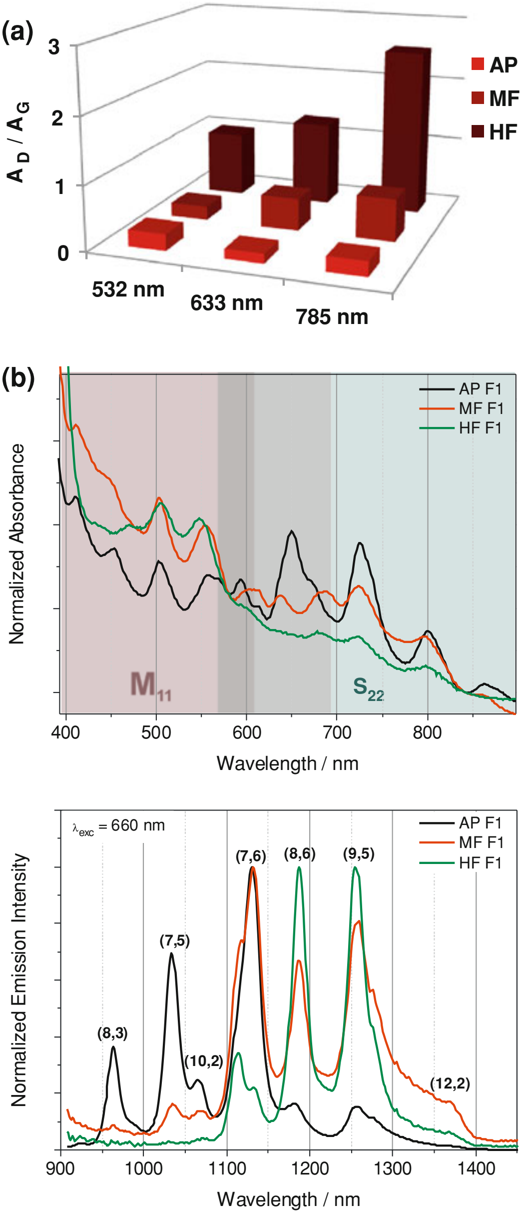

Fig. 3.62 **a** Direct comparison of the Raman A_D/A_G ratios of fractions F2 collected from AP SWCNTs, MF SWCNTs and HF SWCNTs recorded from the solid at three excitation wavelength, namely 532, 633 and 785 nm. **b** Optical absorption spectra (normalized to 830 nm) of F1 after DGU sorting according to structural integrity of as-received HiPco SWCNTs compared to HiPco SWCNT samples that have been moderately (MF) and strongly (HF) functionalized. **c** Emission spectra with an excitation wavelength of 660 nm normalized to the respective maximum of F1 after DGU sorting of AP, MF and HF SWCNT samples. The SWCNT (*n*, *m*) indices of the respective peaks are indicated. (Reproduced with permission from Wiley–VCH, reference 108)

metallic species in the nonfunctionalized fractions F1 can be estimated. In case of the HF-SWCNTs no semiconducting SWCNTs remain unfunctionalized with diameters smaller than 0.9 nm. The abundance of the (8, 6)-SWCNT with a diameter of 1 nm is also drastically reduced and constitutes 5.2% with respect to the

Table 3.14 Tabulated emission intensities of chosen SWCNT chiralities in the nonfunctionalized fraction after DGU sorting of AP-SWCNT, MF-SWCNT and HF-SWCNTs and the thus deduced relative abundancy of the (n, m) SWCNTs with respect to the pristine material

Sample	Emission position/nm	(n, m)	SWCNT diameter/nm	Emission intensity/ nW cm^{-1}	Relative abundance (%)
AP-SWCNT	1033	(7, 5)	0.83	2.7×10^{-9}	100
	1131	(7, 6)	0.89	3.9×10^{-9}	100
	1186	(8, 6)	0.97	6.3×10^{-10}	100
MF-SWCNT	1033	(7, 5)	0.83	1.1×10^{-11}	0.4
	1131	(7, 6)	0.89	6.9×10^{-11}	1.8
	1186	(8, 6)	0.97	4.7×10^{-11}	7.5
HF-SWCNTs	1033	(7, 5)	0.83	0	0
	1131	(7, 6)	0.89	7.2×10^{-12}	0.2
	1186	(8, 6)	0.97	3.3×10^{-11}	5.2

pristine material. Accordingly an enrichment factor of metallic SWCNTs in the nonfunctionalized fraction after DGU of HF-SWCNTs greater than 95% is estimated.

The electronic-type selectivity is furthermore accompanied with a preferred functionalization of smaller diameter SWCNTs opposed to the larger diameter counterparts. This phenomenon has already been well documented in literature and follows the theoretical prediction of increasing reactivity with increasing curvature and therefore decreasing diameter [110]. This increasing reactivity with decreasing diameter can best be followed in the normalized emission spectra (with an excitation wavelength of 660 nm), where an intense redistribution of the peaks attributed to the excitonic transitions of different (n, m)-SWCNTs occurs (Fig. 3.62b). Please note that no such changes have been apparent in the bulk spectra before DGU due to the low concentration of individualized non-functionalized semiconducting SWCNTs. In F1 of the MF carboxylated sample, the peaks attributed to the nanotubes with diameters smaller than 0.8 nm (for example the (8, 3) and (7, 5) SWCNTs) almost vanish, as they are obviously completely functionalized. In the HF sample that has been processed under harsher reaction conditions during the chemical functionalization, the traces of semiconducting SWCNTs that have not been functionalized possess diameters larger than 0.9 nm (for example the (8, 6) and (9, 5) chiralities).

In order to complete the picture of the detailed characterization, the Raman spectra of fractions F1 and F2 of the three samples are compared in Fig. 3.63 with an excitation wavelength of 633 nm. According to the *Kataura* plot, the RBM peaks below a Raman shift of 220 cm^{-1} can be attributed to metallic SWCNT species, while the region above 220 cm^{-1} arises from semiconducting SWCNTs. As clearly discernable in Fig. 3.63a, the metallic and large diameter semiconducting SWCNTs (larger than 1 nm in diameter) are enriched in F1 of the moderately functionalized sample in comparison to the as-received HiPco SWCNTs. In

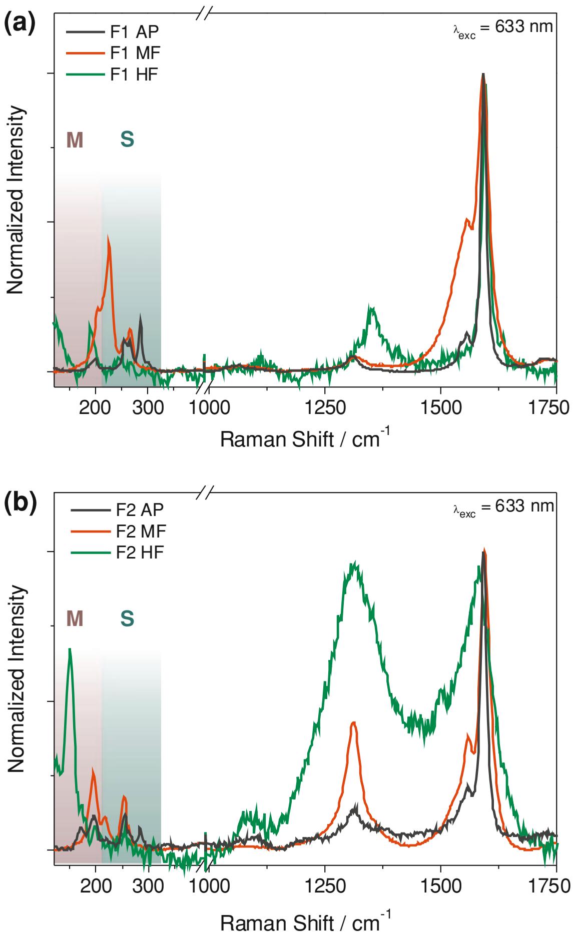

Fig. 3.63 Raman spectra with an excitation wavelength of 633 nm (normalized to the G-band) after DGU sorting according to structural integrity of as-received HiPco SWCNTs (AP) compared to HiPco SWCNT samples that have been moderately (MF) and strongly (HF) functionalized. The electronic structure of the SWCNTs yielding the respective peaks in the RBM region is indicated by the colored shaded background (*red*: metallic, *green*: semiconducting). **a** Fraction 1 containing the non-functionalized material of the bulk sample and **b** F2 containing the covalently functionalized SWCNTs

case of the highly functionalized SWCNTs, only one dominant RBM peak can be detected at this excitation wavelength presumably corresponding to the (9, 9)-SWCNT. Despite the fact that the material in fraction F1 of the HF has the same buoyant density as the F1 of the AP and MF sample and is therefore expected to be structurally perfect, a slightly increased D-band intensity arises. It is suggested that this is not an intrinsic problem of the DGU sorting, but rather of the fractionation (withdrawal of the bands from the vial) which always induced slight mixing of bands.

In case of the functionalized fractions F2 (Fig. 3.63b), the dramatic functionalization degrees that are accessible by this covalent functionalization protocol are documented by the very pronounced D-band in the HF samples that exceeds the G-band in intensity. In this regard it is important to note that the signal to noise ratio of this spectrum is strongly decreased, as the resonant conditions of the SWCNTs are strongly altered by the harsh alteration of the sp^2 carbon network. The RBM peaks also almost completely vanish in this case. Therefore, it is not surprising that no pronounced enrichment of (smaller diameter) semiconducting SWCNTs is discernable in the RBM region of the HF sample, as the strongly functionalized SWCNTs obviously lose their resonant conditions and are no longer completely captured by Raman spectroscopy. In order to fully understand the underlying physical phenomena, tip-enhanced Raman spectroscopy would be the perfect characterization tool, but unfortunately, it has been out of the scope of this thesis.

In conclusion, the versatility of the DGU sorting according to structural integrity of the SWCNTs has been demonstrated. For this purpose covalently derivatized SWCNTs equipped with carboxylic acid functionalities have been extensively characterized after their DGU separation into fractions of non-functionalized and structurally altered SWCNTs. Since the underlying covalent functionalization sequence is highly flexible and tunable, samples have been analyzed that have been subjected to moderate and harsh reaction conditions yielding different bulk functionalization degrees.

The DGU sorting enabled the precise analysis and characterization of the functionalized and non-functionalized SWCNTs in the bulk sample and thus provided deep insights. In general, it could be endeavored that such a characterization protocol should be established in order to assess quality and structural integrity of as-received SWCNTs. In case of the covalently modified SWCNTs the actual A_D/A_G ratios of the functionalized part of the sample could be determined without contributions from amorphous carbon impurities or non-functionalized SWCNT counterparts. Furthermore, atomic force microscopy revealed that the strongly altered SWCNTs tend to form interwoven networks of cross-linking SWCNTs presumably due to the formation of acid dimers. The chemical reaction sequence has been unambiguously shown to be selective towards the preferred functionalization of semiconducting SWCNT species (as could already been shown by independent techniques). The theoretically predicted diameter selectivity has been also observed experimentally by the nIR emission spectroscopic investigation of the non-functionalized fractions—an analysis that has not yielded reliable results from the bulk samples.

Last but not least, it is worth mentioning that the DGU described above in combination with the selective chemical derivatization constitutes an important tool for the efficient separation of SWCNTs, as the buoyant densities of the chemically altered and pristine SWCNTs are significantly different so that their fractionation in clearly spatially separated bands can be easily accomplished. With the aid of the scenario outlined above, the pristine, pure, individualized SWCNTs can be recovered together with the individualized functionalized semiconducting SWCNTs by a one step procedure and both materials could then be directly subjected to further processing if desired.

3.2.1.3 The Use of Perylene-Based Surfactants in DGU

Despite the efficient SWCNT sorting provided in Sects. 3.2.1.1 and 3.1.1.2, further progress is deemed necessary by considering the following aspects: (a) The success of the DGU sorting according to structural integrity completely depends on the appropriate covalent derivatization sequences. (b) Individualization rates of commercially available surfactants commonly applied in DGU are rather poor, at least when compared to the perylene based π-surfactants extensively described in Sect. 3.1. Accordingly, it may appear obvious to combine the outstanding exfoliation efficiencies of the perylene surfactants with the unique sorting capabilities of ultracentrifugation. One attempt which is based on a combined cosurfactant replacement DGU with HiPco and CoMoCAT SWCNTs dispersed by the amphiphilic perylene surfactant **3** will be outlined in the following [111].

Prior to the density differentiation, both HiPco and CoMoCAT SWCNTs have been dispersed in a buffered aqueous solution of **3** (0.1 wt%, pH = 7) by the aid of ultrasonication (30 min, 80 W, 45 kHz) to yield initial SWCNT concentrations of 0.5 g L^{-1}. The dispersions were centrifuged (15 000 rpm, 30 min) in order to remove coarse aggregates. For the DGU experiment, a step gradient containing the surfactant in 60, 40 and 20 wt% nycodenz, respectively, was prepared. The nanotubes dispersed in the aqueous surfactant solution containing 10 wt% nycodenz were layered on top of the gradient. The vials were then centrifuged in a Beckman Coulter ultracentrifuge equipped with a swinging bucket rotor (SW60Ti) for 18 h at 15,000 rpm. Figure 3.64 shows the result for CoMoCAT (Fig. 3.64a) and HiPco SWCNTs (Fig. 3.64b), respectively.

When nanotubes dispersed in **3** ([**3**] = 0.1 wt%) are centrifuged in a nycodenz gradient also containing **3**, no clear separation of the material in bands could be observed (trace II, Fig. 3.64). However, density differentiation occurred with the aid of SDS as cosurfactant. For this purpose, SDS (2 wt%) was added in the step gradient (except for the top layer containing the nanotubes), in addition to **3**. In the case of the CoMoCAT tubes, the formation of four bands was observed, while five bands could be identified for the HiPco material (trace III, Fig. 4.65). It is important to note that no band formation could be observed for SDS alone under the same centrifugation conditions (trace I, Fig. 3.64).

The clearest band formation for both HiPco and CoMoCAT SWCNTs (trace IV, Fig. 3.64) was obtained when nanotubes dispersed in a buffered aqueous solution of perylene **3** were added on top of a step gradient containing 2 wt% of SDS (without perylene in the step gradient). Presumably, this procedure not only resulted in nanotube band formation, but also in replacement of the perylene units from the sidewall of the nanotube by SDS during the movement of the nanotubes through the gradient, as SDS is present in large molar excess compared to **3**. It shall be mentioned that the diffusion of perylene throughout the centrifuge vial is very slow as indicated by the dark red colour attributed to free bulk perylene in the top one third of the centrifuge tube which is not spread all over the vial (trace IV, Fig. 3.64).

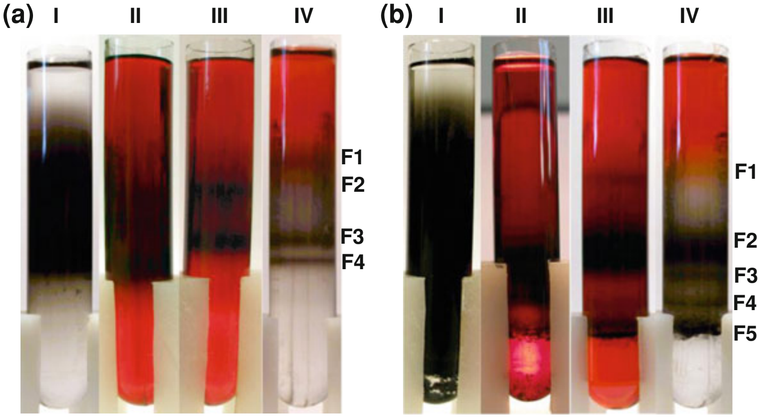

Fig. 3.64 Centrifuge vials after DGU (18 h, 15 krpm) in a nycodenz gradient **a** CoMoCAT SWCNTs, **b** HiPco SWCNTs; from *left* to *right*: *1* SWCNTs dispersed in SDS in a gradient containing SDS ([SDS] = 2 wt%); *2* SWCNTs dispersed in **3** with [**3**] = 0.1 wt% throughout the centrifuge tube; *3* SWCNTs dispersed in **3** with [**3**] = 0.1 wt% and [SDS] = 2 wt% throughout the centrifuge tube; *4* SWCNTs dispersed in **3** [**3**] = 0.1 wt% in a gradient containing SDS ([SDS] = 2 wt%). (Reproduced with permission from the Royal Society of Chemistry, reference 111)

In order to analyze the nanotube fractions, UV/Vis/nIR absorption spectroscopy was carried out after isolating the clearly separated bands of the right centrifugation vials in Fig. 3.64. It shall be mentioned that the detection range was limited to 600–1400 nm due to the strong absorption of the perylene core between 500 and 550 nm.

Figure 3.65a reveals that, on the one hand, fractions 3–4 (F3–4) of the CoMoCAT material contain a large amount of SWCNTs bundles, as the resonant ratio is significantly lower compared to the other fractions. On the other hand, F1 and F2 both show a significantly high degree of individualized tubes as can be concluded from the higher resonant ratios compared to F3–4. An evaluation of the enrichment and depletion of certain (n, m)-SWCNT species is challenging, however, as the nanotubes are dispersed in aqueous media containing different relative amounts of surfactants, e.g. F1 contains free bulk perylene, while free perylene **3** is absent in F2. Thus, the dielectric environment of the nanotube is different for F1 and F2 resulting in changes in the absorption pattern, e.g. adsorption of the perylene unit results in a red-shift of the SWCNT transitions for F1.

To increase comparability, a solution of SDS was added to SWCNTs dispersed in a buffered aqueous solution of **3** ([**3**] = 0.1 wt%) in order to simulate the replacement of perylene by SDS during DGU. The peak position was shown to be the same as for F1 mirroring the same chemical environment for both systems. Fraction F2 exhibits similar optical absorption as pristine CoMoCAT SWCNTs dispersed in a solution of SDS (2 wt%) further underlining the differing chemical surrounding of the nanotubes in F1 and F2, respectively.

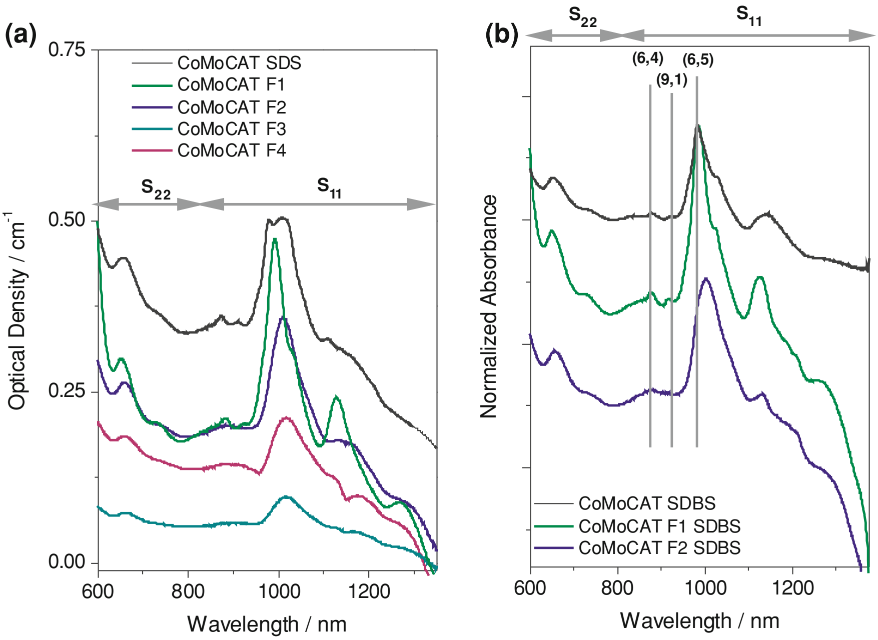

Fig. 3.65 **a** As recorded UV/Vis/nIR absorption spectra of the CoMoCAT fractions F1–4 as indicated in Fig. 3.64 compared to pristine SWCNTs dispersed in a solution of SDS ([SDS] = 2 wt%), **b** UV/Vis/nIR absorption spectrum (normalized to the minimum at 795 nm) of CoMoCAT-fraction F1–2 after addition of SDBS ([SDBS] ≈ 5 wt%) compared to the pristine material dispersed in SDBS ([SDBS] = 1 wt%) – vertical offset for clarity. (Reproduced with permission from the Royal Society of Chemistry, reference 111)

In order to evaluate differences in the fractionated nanotube material, furthermore, the anionic surfactant SDBS was added to the fractions in a high excess compared to **3** and SDS ([SDBS] = 5 wt%), as it has been shown that a solution of SDBS is capable of replacing **3** from the nanotube sidewall. Moreover, introducing SDBS on the nanotube sidewall is advantageous with regard to two aspects: (1) the formation of well resolved absorption and emission feature of the nanotube is ensured, (2) comparison to literature is possible as SDBS is commonly used. As shown by Fig. 3.65, DGU of CoMoCAT SWCNTs with the aid of **3** leads to an enrichment of the (6, 4) and (9, 1)-SWCNTs in the region of the S_{11}-transitions in F1, while fraction F2 is depleted of the (6, 5), (6, 4) and (9, 1) SWCNTs (Fig. 3.65b).

A similar behavior is observed for the HiPco material, although the differences in the absorption spectra are more striking (Fig. 3.66). In the case of the HiPco tubes, F3–5 appear rather bundled as can be concluded from the low resonant ratio as indicated by Fig. 3.66a. Again, F1 appears comparable in the structure of the absorption to the pristine material dispersed in **3** ([**3**] = 0.1 wt%) after addition of SDS, while absorption of F2 resembles HiPco tubes dispersed in SDS.

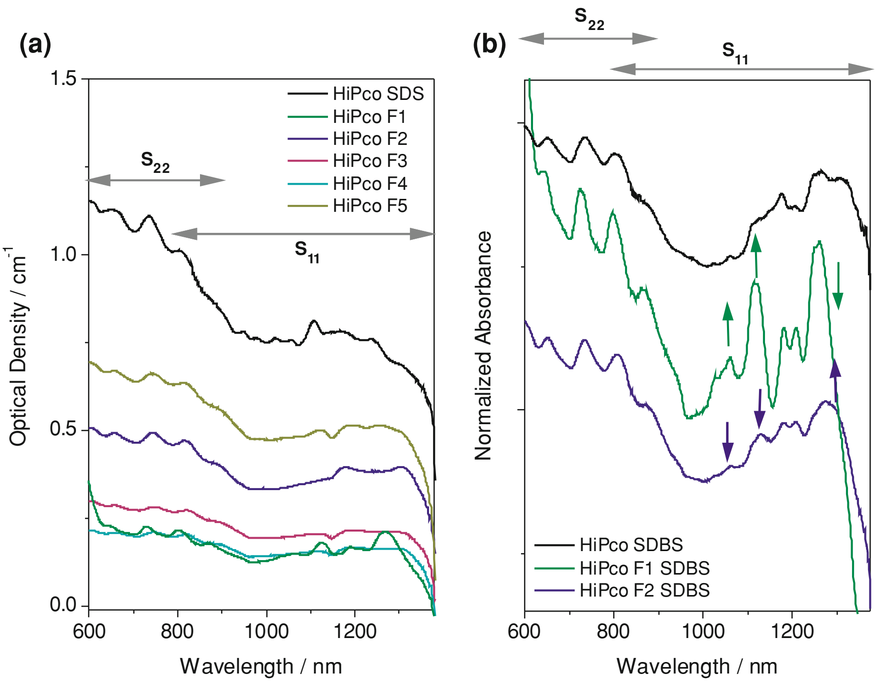

Fig. 3.66 **a** As recorded UV/Vis/nIR absorption spectra of the HiPco fractions F1–5 as indicated in Fig. 3.64 compared to pristine SWCNTs dispersed in a solution of SDS ([SDS] = 2 wt%), **b** UV/Vis/nIR absorption spectrum (normalized to the minimum at 1000 nm) of HiPco-fraction F1–2 after addition of SDBS ([SDBS] $\approx$ 5 wt%) compared to the pristine material dispersed in SDBS ([SDBS] = 1 wt%) – vertical offset for clarity. (Reproduced with permission from the Royal Society of Chemistry, reference 111)

After addition of SDBS, the S_{11}-transitions of the smaller diameter nanotubes (from 975–1175) are more dominant compared to the pristine material, as represented by the green arrows pointing upwards in Fig. 3.65b. Additionally, the spectral features in the region from 1175 to 1250 nm are significantly decreased indicating depletion of larger diameter tubes in F1. This is consistent with the observation that F2 is enriched in larger diameter tubes (blue arrows in Fig. 3.66b), while being depleted in smaller diameter tubes, as would be expected from DGU with a uniform surfactant coating where density differentiation is related only to the diameter as outlined by Hersam et al. [112]. However, presumably, density differentiation is more complex in our case due to an underlying replacement.

Even though the enrichment quality of the DGU approach summarized above may not appear groundbreaking, it is important to note that it has been one of the first reports on fractioning as-received HiPco SWCNTs by DGU without covalent alteration of the nanotubes, as DGU with HiPco SWCNTs has not shown to be problematic under the conditions of successful sorting with CoMoCAT or laser ablation material as already mentioned in Sect. 3.2.1.1.

The sorting mechanism is believed to be a combination of density gradient fractionation and replacement of the π-surfactant which preferentially occurs on larger diameter SWCNTs due to the enhanced adsorption affinity of the anionic perylene surfactants on smaller diameter SWCNTs (see Sect. 3.1.3). However, the question arises whether the addition of a density gradient medium in unambiguous when a selective interaction can be exploited as in the case of the anionic perylene based surfactants. Since the sorting has been successful at rather low centrifugation speeds, it appears that the process has been stopped before the equilibrium has been reached, e.g. before all the SWCNTs have travelled to their respective isopycnic points. If this was the case, the addition of a gradient medium would not be mandatory for the success of the experiment as will be analyzed in the following.

3.2.2 Cosurfactant-Replacement-Sedimentation Centrifugation

In the following, a novel SWCNT sorting procedure will be described and evaluated based on band sedimentation ultracentrifugation. The experimental setup is displayed in Fig. 3.67. Since it has been shown that diameter fractioning of SWCNTs occurs in a replacement DGU (3.2.1.3) by exploiting the selective interaction of the designed anionic perylene based surfactants, a modification of the scenario is proposed. For this purpose, the SWCNT-Per dispersion in aqueous media is layered on top of a so-called race layer containing the cosurfactants SDBS dissolved in D_2O.

During ultracentrifugation the SWCNT-surfactant complexes sediment in response to the centrifugal force. Eventually, the SWCNTs with an enhanced affinity to the perylene based surfactant will be hold back in the perylene layer. Especially at the interface to the SDBS containing race layer, the perylene concentration is expected to be increased, as the perylene molecules that have been replaced by SDBS from the SWCNTs passing into the race layer will accumulate at the interface which in turn decelerates the sedimentation of the preferred SWCNT species.

In principle, the deceleration of the SWCNTs with an enhanced affinity to the perylene derivative is then reflected in the relative spatial distributions of the SWCNT species in the centrifuge vial. In comparison to DGU, this cosurfactant-replacement band sedimentation ultracentrifugation (BSU)—if successful- is expected to outperform the already established DGU technique, as it requires much shorter centrifugation times (only a few hours), as no equilibrium needs to be established. Furthermore, the high exfoliation efficiencies of the π-surfactants can be exploited and the preparation of the experiment is rather uncomplicated. The greatest advantage lies in the fact that no gradient medium is required that is expensive and cannot easily be removed from the sorted SWCNTs after DGU.

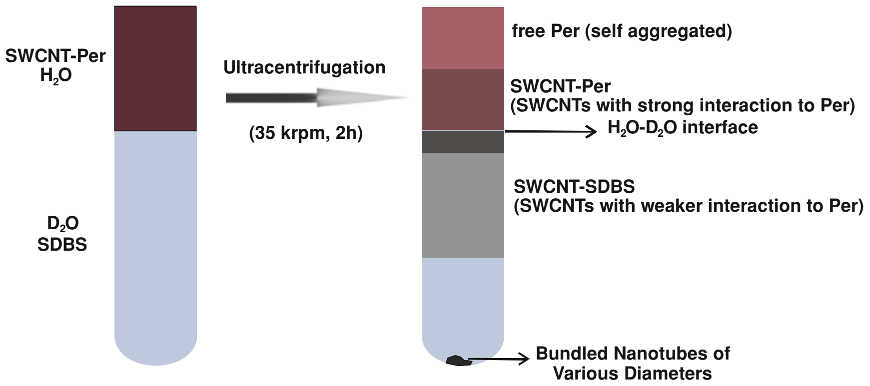

Fig. 3.67 Experimental setup of the cosurfactant replacement band sedimentation ultracentrifugation (BSU) experiment

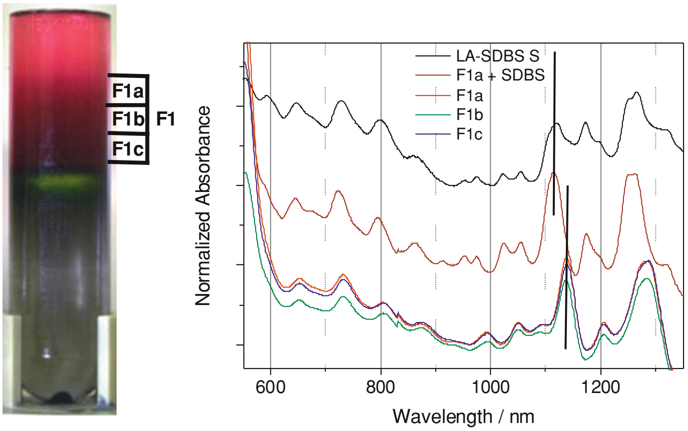

Fig. 3.68 Left: centrifugation vial after cosurfactant replacement BSU of laser ablation SWCNTs dispersed in a buffered aqueous solution of perylene **3** ($[\mathrm{LA}]_\mathrm{i} = 0.1\ \mathrm{g\ L^{-1}}$, $[\mathbf{3}]_\mathrm{i} = 0.15\ \mathrm{g\ L^{-1}}$) layered on top of a SDBS (1 wt%)-D_2O race layer. Right: Absorption spectra normalized to 900 nm of fractions F1a–F1c as indicated beside the photograph in comparison to laser ablation SWCNTs dispersed in a 1 wt% aqueous solution of SDBS and F1a after replacement of perylene surfactant from the sidewall of the SWCNTs by SDBS

An example of a centrifugation vial after cosurfactant replacement BSU is presented in Fig. 3.68. Prior to the ultracentrifugation experiments, laser ablation SWCNTs have been dispersed ($[\mathrm{LA}]_\mathrm{i} = 0.1\ \mathrm{g\ L^{-1}}$) in a buffered aqueous solution ($\mathrm{pH} = 7$) of the amphiphilic perylene derivative **3** ($[\mathbf{3}]_\mathrm{i} = 0.15\ \mathrm{g\ L^{-1}}$) by bath-type sonication (30 min). 1 mL of the dispersion after mild pre-centrifugation (15 krpm, 30 min) has been layered on top of 4 mL of 1 wt% SDBS in D_2O. After ultracentrifugation at 35 krpm (2 h), the SWCNTs have spread throughout the vial. The diffusion of the free perylene into the SDBS layer is much slower than the sedimentation of the SWCNTs and does not lead to significant redistribution of surfactant concentrations in the vial. The H_2O/D_2O interface is easily discernable in this experiment, as the mixed aggregates of **3** and SDBS formed at the interface (see Sect. 3.1.5) are characterized by strongly increased fluorescence intensity as indicated by the orange color.

Prior to comparing fractions at different positions in the vial, it needs to be ensured that the dielectric environment of the nanotube is equal in every fraction. In the fraction F1a–1c, the perylene surfactant is bound to the nanotube scaffold inducing red-shifted and broadened SWCNT transitions (compare Sect. 3.1.1) in the absorption spectra (Fig. 3.68 right). In order to ensure comparability with the SWCNT fractions of the race layer where perylene has been replaced by SDBS, solid SDBS has been added to all perylene fractions (to establish a concentration of 1 wt%). As revealed by the absorption spectra in Fig. 3.68, the characteristic SWCNT transitions appear at the same spectral positions as the reference sample that has been dispersed in a 1 wt% SDBS solution. Since the fractions F1a, F1b and F1c are virtually identical in their absorption, they have been fused for the following characterization to F1.

The cosurfactant replacement BSU has been carried out with laser ablation (Fig. 3.69a), CoMoCAT (Fig. 3.69b) and HiPco (Fig. 3.69c) SWCNTs in order to evaluate the applicability to SWCNTs with different (*n*, *m*) compositions. In every case, the SWCNTs were spread throughout the vial after 2 h of ultracentrifugation at 35 krpm. The fractions as indicated beside the photographs of the vials in Fig. 3.69 have been subjected to absorption spectroscopy. In the cases of fractions F1 and F2, solid SDBS has been added prior to acquisition of the spectra to establish a SDBS concentration if 1 wt% in order to ensure the comparability with the higher fractions.

As clearly discernable for the laser ablation SWCNTs (Fig. 3.69a), fractions F1 and F2 are enriched in smaller diameter SWCNTs (as indicated by the orange arrows pointing upward) giving rise to S_{11} transitions below 1100 nm in comparison to the reference material LA-SDBS (black trace). In contrast, these SWCNT species are depleted in the higher fractions (indicated by the grey arrows pointing downward) F3 and F4. The transitions at lower energy (above 1150 nm) appear additionally more pronounced pointing towards an enrichment of larger diameter SWCNTs in the higher fractions. These investigations strongly suggest that the cosurfactant replacement BSU is indeed a possible SWCNT sorting technique.

This is further supported by the absorption spectra of the CoMoCAT and the HiPco fractions presented in Fig. 3.69b, c, respectively. Qualitatively the same trend is observed, e.g. enrichment of smaller diameter SWCNTs in the lower fractions F1 and F2 and enrichment of larger diameter SWCNTs in the higher fractions.

It needs to be emphasized that the quality of the enrichment and depletion is rather low compared to DGU sorting. Nonetheless, the preliminary results are promising and provide the proof of principle of this novel separation approach.

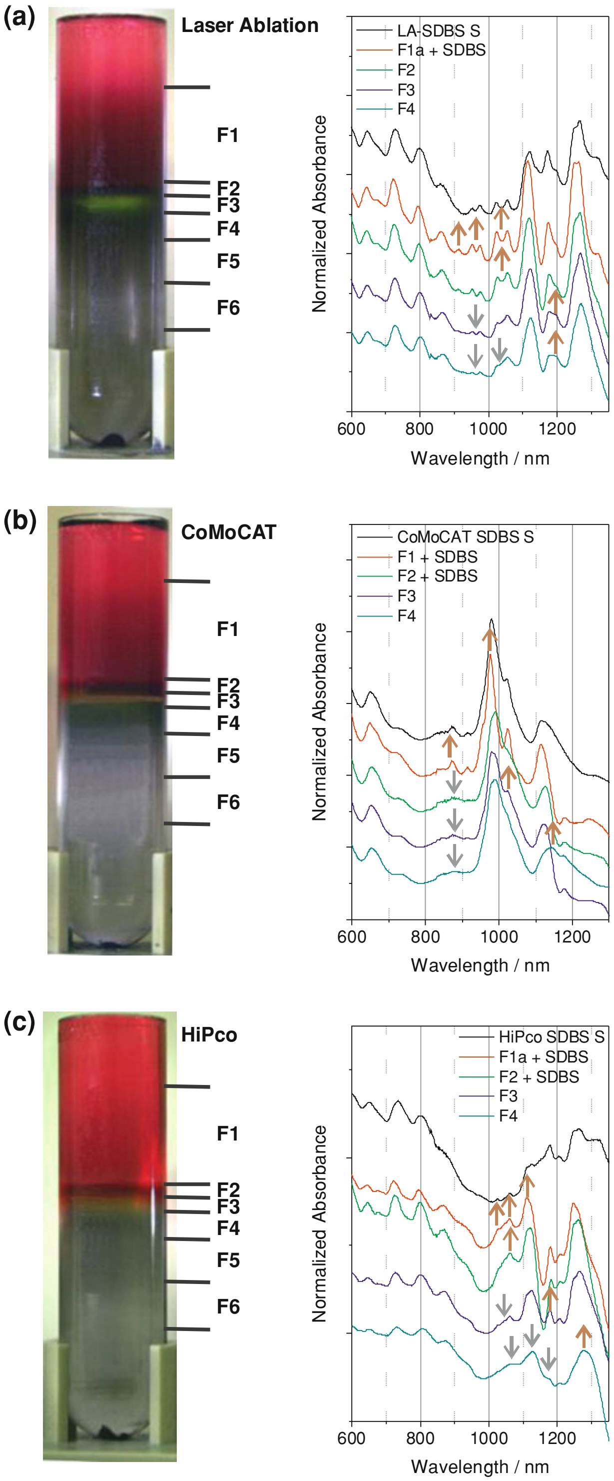
(a)
Laser Ablation
F1
F2
F3
F4
F5
F6
LA-SDBS S
F1a + SDBS
F2
F3
F4
Normalized Absorbance
600
800
1000
1200
Wavelength / nm
(b)
CoMoCAT
F1
F2
F3
F4
F5
F6
CoMoCAT SDBS S
F1 + SDBS
F2 + SDBS
F3
F4
Normalized Absorbance
600
800
1000
1200
Wavelength / nm
(c)
HiPco
F1
F2
F3
F4
F5
F6
HiPco SDBS S
F1a + SDBS
F2 + SDBS
F3
F4
Normalized Absorbance
600
800
1000
1200
Wavelength / nm

◀ **Fig. 3.69** Left: centrifugation vials after BSU of SWCNTs dispersed in a buffered aqueous solution of perylene **3** ($[\mathrm{SWCNT}]_i = 0.1\ \mathrm{g\ L^{-1}}$, $[\mathbf{3}]_i = 0.15\ \mathrm{g\ L^{-1}}$) layered on top of a SDBS (1 wt%)-D_2O race layer. Right: Absorption spectra normalized to the respective minima of fractions F1–F4 as indicated beside the photograph in comparison to SWCNTs dispersed in a 1 wt% aqueous solution of SDBS. In case of the F1 and F2, SDBS has been added in order to replace the perylene derivative from the SWCNT scaffold as indicated in the figure legends. Fractions F5 and F6 contained significant amount of bundles and have been excluded from detailed analysis. **a** Laser ablation SWCNTs, **b** CoMoCAT SWCNTs and **c** HiPco SWCNTs

Future work should be concerned with the optimization of the centrifugation conditions such as concentration of the surfactants, centrifugation speed and time. Another problem that arises is the fractionation of the material after the centrifugation, as no clear spatially separated bands arise.

Furthermore, a major obstacle is constituted by the pronounced polydispersity in SWCNT lengths, as sedimentation coefficients are strongly dependent on the molecular weight of the particles and in the case of SWCNTs therefore the length of the nanotubes. Accordingly, in order to improve sorting efficiencies by cosurfactant replacement band sedimentation ultracentrifugation, the length sorting problem of SWCNTs needs to be solved first.

3.2.3 SWCNT Length Sorting by Band Sedimentation

In order to address the problem of polydispersity of the SWCNTs with regard to length, a novel length sorting approach has been followed that relies on the different sedimentation velocities. For this purpose, a similar setup as for the cosurfactant replacement band sedimentation has been used as schematically illustrated in Fig. 3.70. SWCNTs dispersed in aqueous surfactant solution (independent on the surfactant) are layered on top of a surfactant-D_2O race layer. The SWCNTs are expected to spread in the race layer according to their sedimentation velocities.

This methodology resembles that of Fagan and co-workers [113, 114] but with the significant difference that no density gradient medium is required so that the SWCNTs after length sorting can be directly applied to further experiments. A great advantage of this length sorting scenario is presented in the high flexibility, as it can in principle be applied to any aqueous dispersion (of SWCNTs, graphene or any other colloid). Additionally, it constitutes a low-cost protocol that can easily be set up in short time spans.

Similarly to column chromatography in organic chemistry, the success of the separation depends on the thickness of the starting band containing the sample. Accordingly, a rather small volume (0.3 ml) of a concentrated dispersion of HiPco SWCNTs in an aqueous solution of 1 wt% SDBS has been layered on top of 4.7 mL of the race layer (initial concentrations of HiPco SWCNTs were $0.5\ \mathrm{g\ L^{-1}}$ prior to mild pre-centrifugation). A mixture of H_2O and D_2O (3:2 by volume)

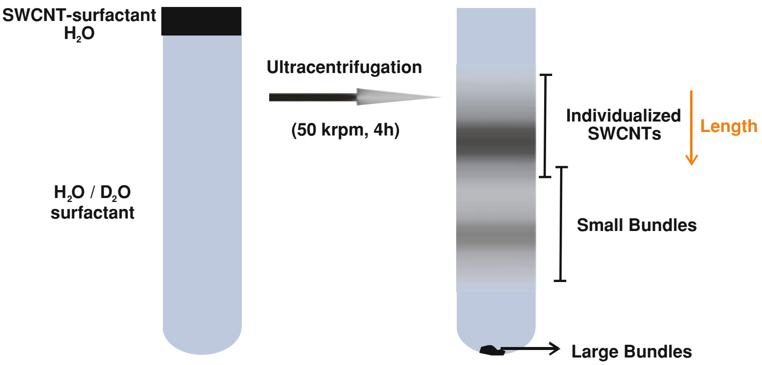

Fig. 3.70 Experimental setup for the length sorting of SWCNTs by band sedimentation ultracentrifugation

instead of pure D_2O has been chosen in order to reduced the density of the race layer and therefore accelerate the sedimentation.

A representative centrifugation vial is presented in Fig. 3.71. Fractions have been withdrawn as indicated beside the photograph and the solutions have been subjected to absorption spectroscopy. The resonant ratio of longer SWCNTs is larger compared to shorter counterparts [115]. Fractions containing bundled SWCNTs yield red-shifted transitions and reduced oscillator strengths. Accordingly, suitable fractions for further analysis containing only vanishing traces of SWCNT bundles can be chosen on the foundation of absorption spectroscopy. In this case, fraction F4 and F6 have been subjected to statistical AFM analysis. For this purpose the fractions have been spin-casted on SiO_2 wafers and the length of minimum 200 SWCNTs has been determined on the foundation of the atomic force micrographs.

The result of the analysis is presented in Fig. 3.71 along with representative AFM images of F4 and F6. The optical impression arising from the AFM images that indicates a successful length sorting is unambiguously supported by the results from the statistical analysis summarized in the bottom panel of Fig. 3.71. F4 as one of the topmost fractions containing SWCNTs is mainly comprised of nanotubes with lengths shorter than 250 nm. These species are drastically reduced in F6 where the nanotubes exhibit lengths centered around 450 nm. No bundled SWCNTs have been detected in both fractions so that the length analysis appears reliable.

The microscopic characterization provides the proof of principle of the length separation of SWCNTs by a simple band centrifugation experiment, where SWCNTs spread in a race layer according to their sedimentation velocities which is a function of their molecular weight. Thus, bundled SWCNTs are found in higher fractions (in this case greater than F7), while the lower fractions contain individual SWCNTs with differing lengths. In order to minimize the overlapping regime of individual SWCNTs and small bundles further experiments are necessary to optimize the centrifugation and dispersion conditions.

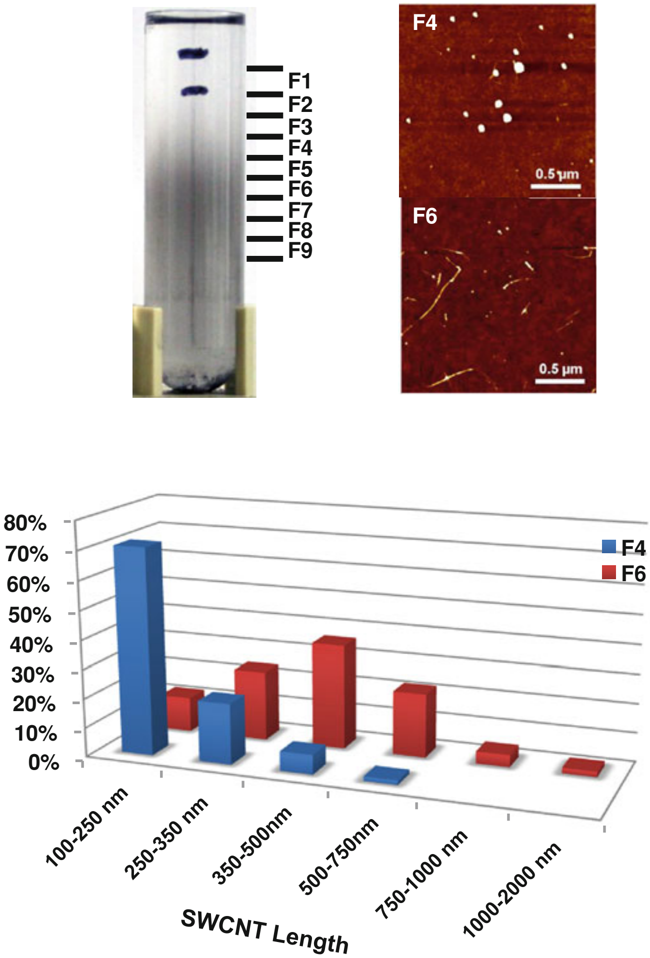

Fig. 3.71 Top: Centrifugation vial after band sedimentation of HiPco-SWCNTs dispersed in 1 wt% SDBS layered on top of a H_2O–D_2O race layer also containing 1 wt% SDBS and representative AFM images of F4 and F6 as indicated beside the photographs. Bottom: Histograms of the SWCNT length distributions in F4 and F6 determined from statistical AFM analysis

Another interesting aspect of band sedimentation ultracentrifugation shall also be briefly mentioned in this context even though it has not yet been evaluated experimentally. For some applications, a readily available technique to remove excess surfactant is desired. This could also be achieved concomitantly with length sorting (and separation of individual from bundled SWCNTs) by band sedimentation, if a race layer without dispersant is used. However, the surfactant cannot be prevented from desorbing from the nanotube scaffold upon passing through the race layer. Thus, the flexibility would be limited to dispersants that exhibit a strong

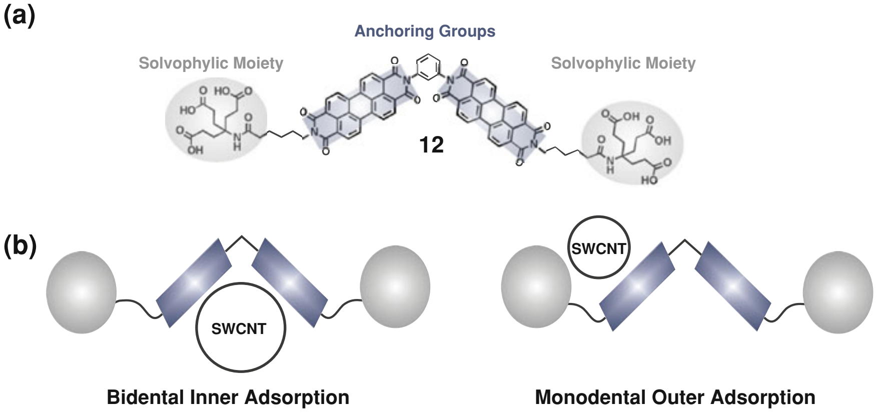

Fig. 3.72 **a** Structure of the perylene based nanotweezer **12** equipped with first generation *Newkome*-type dendrimers as solvophylic moieties. **b** Schematic illustration of perylene-SWCNT interaction in the desired bidental inner adsorption pattern (*left*) and the monodental outer adsorption pattern (*right*). (Reproduced with permission from Wiley–VCH, reference 116)

interaction with the SWCNT backbone and which are not removed upon dilution such as polymers, and possibly π-surfactants.

In summary, band sedimentation ultracentrifugation of SWCNT dispersions presents a powerful, flexible, low-cost, scalable approach towards the sorting of SWCNTs according to selective interactions in a cosurfactant replacement setup (Sect. 3.2.2) or according to sedimentation velocities and directly related to that SWCNT lengths. The preliminary results are highly promising and are expected to pave the road towards establishing this technique as novel SWCNT separation methodology.

3.2.4 Selective Dispersion by a Perylene-Based Nanotweezer

Even though centrifugation based SWCNT separation approaches, as described above, are highly versatile, the ideal separation scenario would nonetheless involve a selective dispersion of the desired SWCNT species from as-produced bulk SWCNT materials without the need for nanotube purification or complicated processing. This concept has been addressed by the investigation of SWCNT dispersion by the novel perylene-based nanotweezer **12** (Fig. 3.72) [116].

The nanotweezer **12** is equipped with two perylene bisimide moieties as SWCNT anchor groups and a first generation *Newkome*-type dendrimer as solvophylic moiety on each perylene branch (Fig. 3.72a). Thus, two different adsorption mechanisms may be hypothesized as summarized in Fig. 3.72b. The desired bidental inner adsorption of the SWCNTs presumably exhibiting selective interactions according to the diameter of the nanotube. However, the sorting

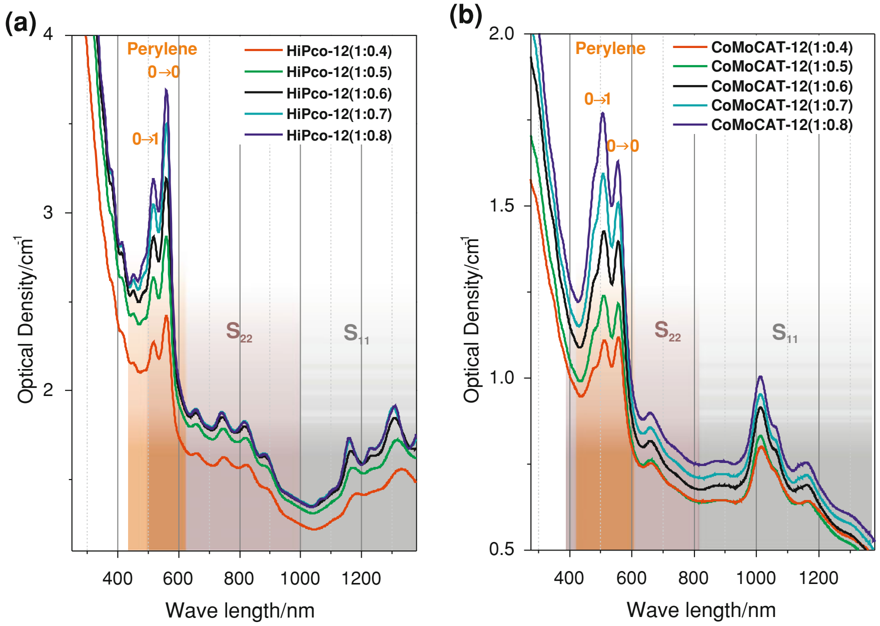

Fig. 3.73 As recorded optical absorption spectra of **a** HiPco SWCNTs and **b** CoMoCAT SWCNTs dispersed in buffered aqueous solutions ($pH = 10$) of **12** with different ratios of SWCNT to **12** as indicated in the figure legend. A stock solution of **12** ($2\ g\ L^{-1}$) was added to SWCNTs with an initial concentration $[SWCNT]_i$ of $0.05\ g\ L^{-1}$ and sonicated for 5 min after each addition of **12** in a bath type sonicator. (Reproduced with permission from Wiley–VCH, reference 116)

efficiency can be convoluted by the possibility of the monodental SWCNT adsorption on the exterior perylene surface (Fig. 3.72b).

Thus, it is crucial to determine the minimum ratio of **12** in relation to SWCNT sufficient for stably dispersing and individualizing the nanotubes, as an excess of **12** would result in the non-desired monodental adsorption. For this purpose, a stock solution of **12** ($2\ g\ L^{-1}$) was subsequently added to SWCNTs ($0.05\ g\ L^{-1}$) in buffered aqueous media (borate buffer, $pH = 10$) and sonicated for 5 min in a bath type sonicator. After each addition step UV/Vis/nIR absorption characteristics of the respective HiPco and CoMoCAT dispersions were determined with different ratios of SWCNT:**12** (Fig. 3.73).

The 0→1 (at 500 nm) and 0→0 (at 550 nm) bands of the perylene unit are indicated by the orange color, whereas the semiconducting S_{11} and S_{22} nanotube transitions are marked by the grey and red shaded background, respectively. Absorption spectroscopy is of uttermost importance for the characterization of perylene dye solutions, as the ratio of the 0→0 transition in relation to the 0→1 transition is directly related to the degree of perylene aggregation (see Sect. 3.1). The unbound perylene tweezer **12** is highly self-aggregated in buffered aqueous solution with $A^{0\rightarrow 0}/A^{0\rightarrow 1} \leq 0.5$.

Table 3.15 Dispersion efficiencies of **12** for HiPco and CoMoCAT SWCNTs with different ratios of SWCNT:**12**. The dispersion efficiency has been calculated from the ratio of the optical density at 740 (HiPco) and 660 nm (CoMoCAT), respectively, before and after centrifugation. The nanotube concentration in the supernatant solution c_s (SWCNT) has been calculated from the dispersion efficiencies and the initial SWCNT concentration (0.05 g L^{-1})

Ratio SWCNT:12	Optical density in the Supernatant		Dispersion efficiency		c_S (SWCNT)	
	HiPco (740 nm) (cm^{-1})	CoMoCAT (660 nm) (cm^{-1})	HiPco (%)	CoMoCAT (%)	HiPco (g L^{-1})	CoMoCAT (g L^{-1})
1:0.4	0.40	0.23	25	31	0.013	0.015
1:0.6	1.05	0.36	57	43	0.029	0.021
1:0.8	1.36	0.39	72	43	0.036	0.021

This observation is further corroborated by the solubilization efficiencies of **12** which can be determined from the absorbance of the SWCNT dispersions before and after centrifugation. The optical densities in the supernatant solutions, the dispersion efficiencies and the thus calculated actual SWCNT concentration in the supernatant for different ratios of SWCNT:**12** are summarized in Table 3.15.

As summarized in Table 3.15, the ratio of SWCNT to **12** has a dramatic impact on the dispersion efficiency of the HiPco SWCNTs being in line with the observation that only a diminishing amount of free bulk perylene is present at a SWCNT:**12** ratio of 1:0.8. In contrast to HiPco SWCNTs, where the dispersion efficiency increases almost linearly with increasing concentrations of the surfactant, no such effect is observed for the smaller diameter CoMoCAT SWCNTs. The fact that CoMoCAT SWCNTs are only poorly solubilised by **12** compared to the HiPco SWCNTs in combination with the observation that a higher portion of free bulk perylene can be detected in the CoMoCAT dispersions, points towards a much weaker interaction of **12** with SWCNTs of smaller diameters.

In order to strengthen this hypothesis, it has furthermore been investigated whether the HiPco-**12** dispersions are enriched in larger diameter SWCNTs, or depleted in smaller diameter SWCNTs, respectively. Since the interaction of the perylene moiety by π-π-stacking and charge transfer strongly alters the optical properties of the SWCNTs (Sects. 3.1.1 and 3.1.3) it is crucial to remove the π-surfactant in order to ensure comparability with a reference system such as SWCNTs dispersed in an aqueous solution of sodium dodecyl benzene sulfonate (HiPco-SDBS). Since it has been demonstrated that designed perylene bisimide (Sects. 3.1.3 and 3.2.2) and pyrene surfactants (Sect. 3.1.6) can be conveniently replaced by SDBS, an aqueous solution of SDBS was added to the SWCNT-**12** supernatant dispersions (SWCNT-**12** S). As exemplarily depicted in Fig. 3.74a removal of **12** by SDBS is evidenced by the redistribution of the perylene transitions in HiPco-**12** S SDBS in comparison to HiPco-**12** S, re-establishing the perylene signature of the free self-aggregated perylene **12**. Concomitantly, the absorption pattern of the SWCNTs is changed and closely resembles that of the reference material HiPco-SDBS. A magnified view presented in Fig. 3.74b reveals

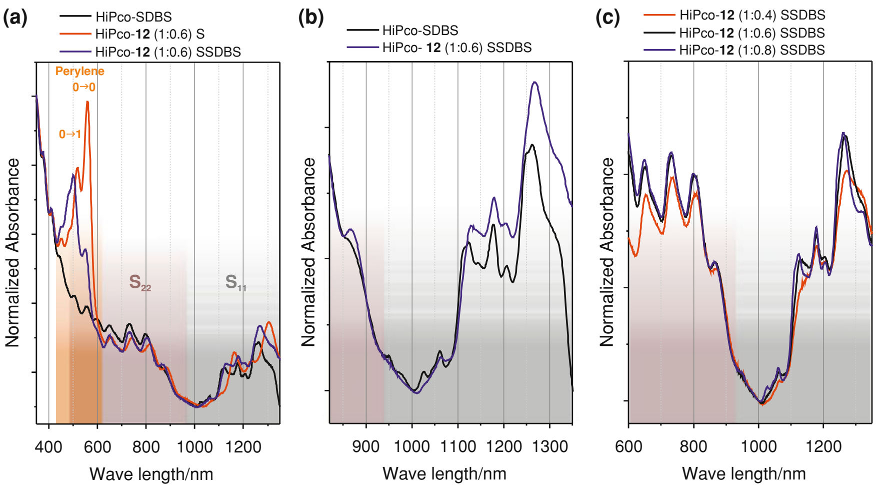

Fig. 3.74 Optical absorption spectra of HiPco SWCNTs ($[\text{SWCNT}]_I = 0.05$ g L^{-1}) dispersed in buffered aqueous solutions (pH = 10) of **12** normalized to the local minimum at 1000 nm. **a** Absorption of the supernatant (S) after centrifugation of HiPco-**12** with a SWCNT:**12** ratio of 1:0.6 by weight compared to HiPco-SDBS and the respective HiPco-**12** supernatant solution after addition of SDBS (S SDBS). As concluded from the perylene and SWCNT transitions, the π-surfactant has been replaced by SDBS. **b** Direct comparison of the SWCNT S_{11} transitions of HiPco-**12** after addition of SDBS and HiPco-SDBS. **c** Absorption spectra of HiPco-**12** S SDBS with different ratios of SWCNT to **12**. (Reproduced with permission from Wiley–VCH, reference 116)

that the dispersion HiPco-**12** S SDBS is depleted in small diameter SWCNTs with optical S_{11} transitions at 1000–1150 nm. Significantly, the depletion of small diameter SWCNTs is more pronounced for lower ratios of HiPco:**12** (Fig. 3.74c), as the outer monodental adsorption of **12** onto the SWCNT scaffold strongly convolutes the enrichment. Thus, with an increasing concentration of **12** no diameter discrimination in the dispersion of SWCNTs occurs.

Please note that no enrichment or depletion is discernable in the case of CoMoCAT SWCNTs, as dispersion of the small diameter nanotubes is not based on the bidental tweezer-type interaction (for details see Ref. [116]).

The successful replacement of **12** from the nanotube sidewall after the addition of SDBS is also derived from the emission of the perylene moieties. The as recorded emission spectra with an excitation wavelength of 500 nm for HiPco-**12** S and CoMoCAT-**12** S with a SWCNT:**12** ratio of 1:0.6 before and after addition of SDBS are depicted in Fig. 3.75. In the case of the HiPco SWCNTs (Fig. 3.75a), the fluorescence of the perylene unit is strongly decreased upon interaction with the SWCNT scaffold. After removal of **12** from the nanotube sidewall, the fluorescence of free perylene is recovered. Interestingly, the perylene emission pattern in HiPco-**12** S is significantly altered. Since the same components at virtually identical concentrations are present in SWCNT-**12** S and SWCNT-**12** S SDBS,

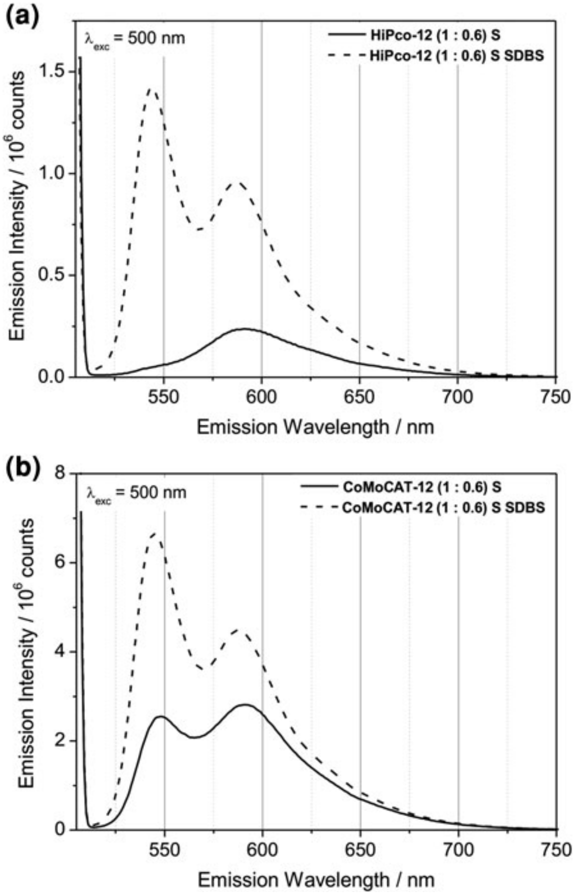

Fig. 3.75 Emission spectra ($\lambda_{exc} = 500$ nm, perylene transitions) of SWCNT-**12** S and SWCNT-**12** S SDBS (supernatant after centrifugation before and after addition of SDBS, respectively). **a** HiPco SWCNTs and **b** CoMoCAT SWCNTs. (Reproduced with permission from Wiley–VCH, reference 116)

innerfilter effects, e.g. absorption of the emitted photons by neighboring molecules can be ruled out as source of data convolution so that the residual perylene emission of SWCNT-**12** S most probably arises from the adsorbed tweezer molecules. The same trend is observed for CoMoCAT-**12** S (Fig. 3.75b). However, as already concluded from the absorption spectra, non-adsorbed, e.g. free perylene moieties in CoMoCAT-**1** S render the effect less pronounced.

The depletion of small diameter SWCNTs in the supernatant of HiPco-**12** is furthermore evidenced by nIR emission spectroscopy (Fig. 3.76). The normalized SWCNT fluorescence spectra of HiPco-**12** S with different ratios of SWCNT:**12** at an excitation wavelength of 660 nm are displayed in Fig. 3.76a. The alteration of the nanotube optical properties upon adsorption of **12** in comparison to the reference HiPco-SDBS is documented by the red-shifted emission and an intense redistribution of the emission pattern. In general, the emission peaks corresponding to the nanotubes with diameters larger than 0.85 nm (emission wavelengths greater than 1100 nm) are still well resolved, whereas the transitions of the smaller diameter SWCNTs widely diminish. However, upon replacement of **12** from the SWCNT sidewall by the addition of SDBS, these transitions are partly recovered (Fig. 3.76b). In complete agreement with the absorption spectra, the HiPco-**12** S SDBS dispersions are depleted in nanotubes with diameters smaller than 0.8 nm in comparison to the reference sample HiPco-SDBS, especially at lower concentrations of **12**. Again, no enrichment or depletion has been observed for CoMoCAT SWCNTs.

On the foundation of these findings it is proposed that nanotubes with diameters larger than 0.8 nm are trapped inside the tweezer cavity, while smaller nanotubes are partly solubilized by the interaction with only one perylene branch of **12**. On the one hand this leads to a decreased dispersion efficiency for smaller diameter nanotubes. On the other hand it results in a less homogenous coverage of the SWCNT sidewall resulting in a loss of their nIR emission features in the presence of **12** due to the possible contact with H_2O and O_2 [20, 32, 33].

Further support of this conclusion is derived from molecular dynamics simulations (Spartan'04; Molecular Mechanics MMFF) of the energy minimized tweezer molecule **12** in the absence of nanotubes and in the presence of a (6, 5)-SWCNT (diameter 0.74 nm) and a (10, 5)-SCWNT (diameter 1.03 nm), respectively. The images of the respective structures are displayed in Fig. 3.77.

As qualitatively indicated by Fig. 3.77b, the (6, 5)-SWCNT with a diameter of 0.74 nm is too small to completely fill out the inner cavity of the tweezer molecule. Especially the front view reveals that one perylene branch is in close interaction with the SWCNT scaffold, while the other branch protrudes away from the SWCNT surface so that interaction is rendered less efficient compared to larger diameter nanotubes. In contrast, the (10, 5)-SWCNT with a diameter of 1.03 nm (Fig. 3.77c), perfectly matches the shape of the tweezer molecule with both perylene branches being in contact with the aromatic nanotube surface. This results in a preferred interaction of **12** with SWCNTs with diameters greater than 0.8 nm, as experimentally revealed.

Furthermore, it is proposed that the dendritic solvophylic moieties are also oriented towards the SWCNT surface, as nanotube p-type doping by the perylene moieties occurs [89]. Thus, the negatively charged dendrimers are attracted by the positively polarized SWCNT scaffold leading to the possibility of a highly homogenous coverage of the nanotubes (see Sect. 3.1.3). The SWCNT surface is therefore shielded from the aqueous environment resulting in the detection of SWCNT nIR emission despite the adsorption of the aromatic perylene moieties.

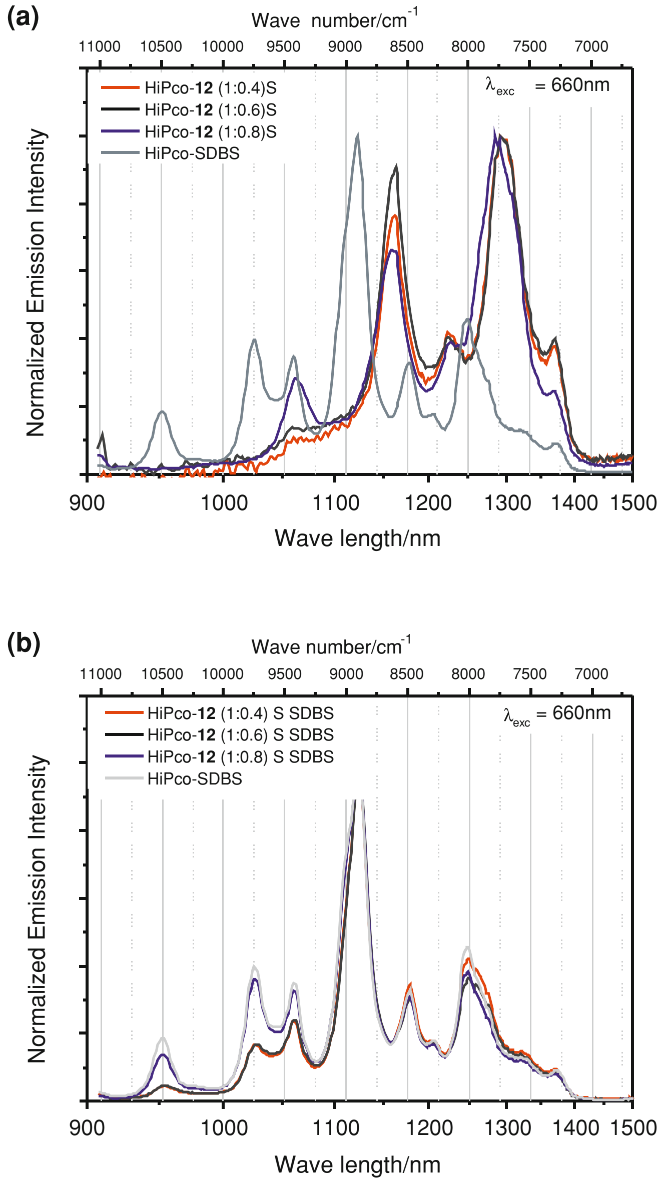

Fig. 3.76 **a** nIR emission spectra ($\lambda_{exc} = 660$ nm, nanotube transitions) of HiPco-**12** S (supernatant after centrifugation) with different ratios of SWCNT:**12** normalized to the maximum. **b** nIR emission spectra ($\lambda_{exc} = 660$ nm) of HiPco-**12** S SDBS (supernatant after centrifugation and replacement of **12** with SDBS) with different ratios of SWCNT:**12** normalized to the maximum. (Reproduced with permission from Wiley–VCH, reference 116)

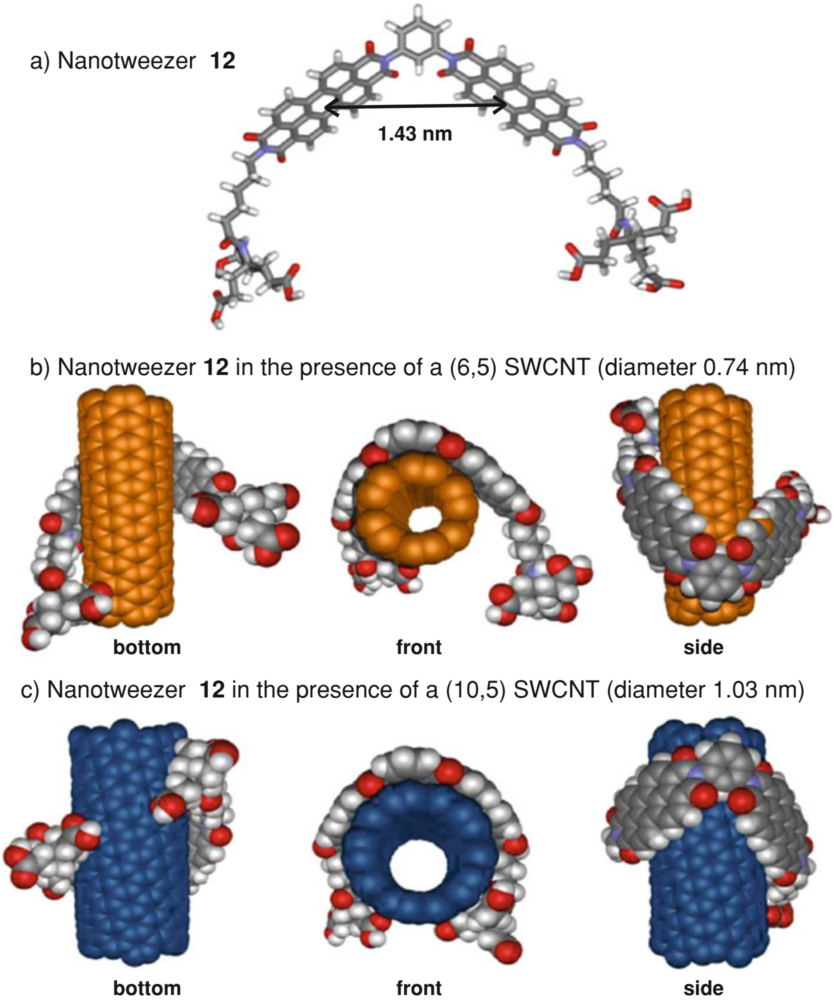

Fig. 3.77 **a** Energy minimized structures of the nanotweezer **12** in the absence of SWCNTs. **b** Interaction of **12** with a fragment (2.5 nm) of a (6, 5) SWCNT. **c** Interaction of **12** with a fragment (2.5 nm) of a (10, 5) SWCNT. (Reproduced with permission from Wiley–VCH, reference 116)

In conclusion, the nanotweezer **12** is capable of dispersing up to 70% of as-produced HiPco SWCNTs with an enhanced interaction towards larger diameter SWCNTs. As revealed by absorption and emission (perylene UV/Vis and SWCNT nIR) spectroscopy, SWCNTs with diameters larger than 0.8 nm are preferentially solubilized resulting in a depletion of smaller diameter SWCNTs in the supernatant dispersions after mild centrifugation. These results are highly promising, as the extraordinary surfactant capabilities of water soluble perylene bisimide derivatives can be combined with diameter recognition by tweezer shaped molecules. However, a monodental adsorption of the SWCNTs with only one perylene branch in the tweezer molecules decreases the effectiveness of selective dispersion so that future work should be directed towards tweezer-type molecules, where the outer adsorption region is shielded by bulky substituents on the bridging moiety.

3.3 Facilitating SWCNT Characterization by Optical Microscopy

The previous chapters of this thesis have been concerned with dispersion, solubilization and separation of SWCNTs based on noncovalent interactions. The fundamental understanding of the underlying interactions has evolved to a prerequisite in order to improve and tune dispersability. For this purpose a variety of analytical techniques have been used and characterization sequences probed and developed. Despite the progress towards the precise characterization of SWCNTs that have been interwoven with the study of novel perylene bismide dispersants throughout Sect. 3.1 and centrifugation sorted SWCNTs in Sect. 3.2, some drawbacks for the analysis of derivatized SWCNTs remains. One is presented in the certainly time consuming characterization sequences, especially striking for example in the case of statistical AFM analysis. Another obstacle is presented in the lack of the direct correlation of the different microscopic and spectroscopic techniques. Thus, the development of a more precise, less time-consuming and low-cost characterization protocol that provides the foundation for correlative microscopy and spectroscopy would be highly desirable.

Significant progress towards reaching this goal is provided by optical microscopy on SWCNTs as will be outlined in the following [117]. The work has been inspired by recent investigations on graphene, where optical microscopy has become an essential tool [118–120], as it allows for the visualization of the nanoscaled objects by simple and readily available means. As a consequence, a variety of microscopic and spectroscopic techniques on individual graphene flakes can easily be applied on one and the same defined object. Moreover, the microfabrication of graphene devices is considerably facilitated by light microscopic inspection of the corresponding graphene nano-objects. Light microscopy in this case relies on an interference contrast arising from deposited graphene flakes onto opaque bi-layered or multi-layered substrates [118]. In a more detailed investigation, it has been demonstrated that Si/SiO_2 substrates with a 300 nm oxide layer are most suitable for the visual detection of objects below the diffraction limitation of optical microscopy [121].

The question arises whether such a highly versatile characterization tool can also be applied to the visualization of single walled carbon nanotubes (SWCNTs) which are below the optical detection limit of $\lambda/2$ in two dimensions. As will be described in the following, SWCNT spin-casted from dispersion on Si/SiO_2

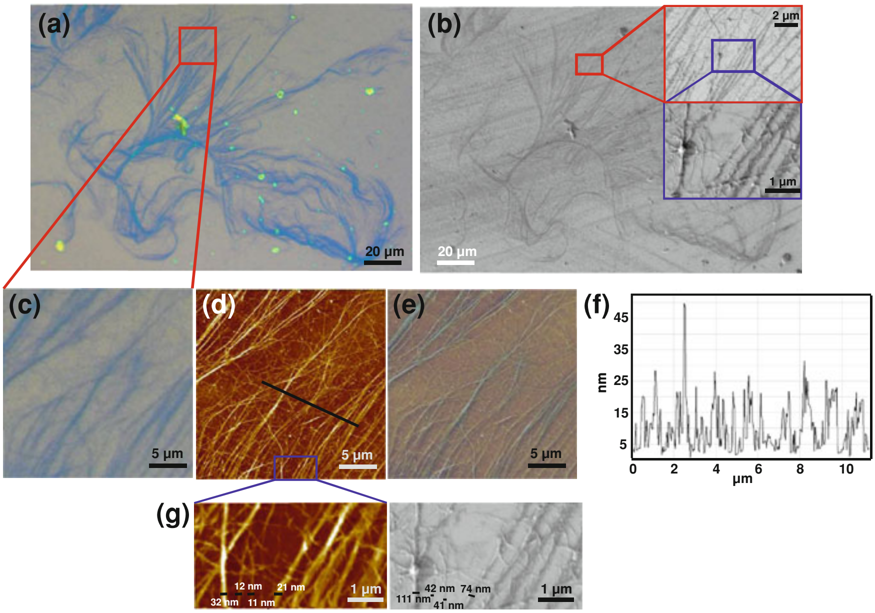

Fig. 3.78 Optical micrographs of HiPco-SDBS spin-casted onto a Si/SiO$_2$ substrate (SiO$_2$ thickness 300 nm). **a** Bright field image, **b** SEM image with different magnifications of the respective areas, **c** enlarged bright field image displaying the same spot as **d** atomic force microscopic image; **e** overlay of bright field image and AFM image; **f** height profile along the black line in **d**; **g** direct comparison of AFM and SEM images from the area indicated by the *blue shaded* background in Fig. 3.78d. (Reproduced with permission from Wiley–VCH, reference 117)

substrates with an oxide layer thickness of 300 nm can indeed by visualized by optical bright and dark field microscopy.

Nanotube samples were prepared by dispersing HiPco SWCNTs in an aqueous solution of SDBS (1 wt%) by sonication (30 min, bath-type). The resulting dispersion was mildly centrifuged (15 krpm, 30 min) in order to remove coarse aggregates and insoluble material, followed by spin-casting the supernatant on Si/SiO$_2$ wafers (SiO$_2$ layer thickness of 300 nm). This distinct layer thickness has been chosen, as it is most suitable for the characterization of graphene [118–120], which can be considered as two-dimensional structural analogue of carbon nanotubes.

Figure 3.78 displays the optical micrograph in bright field mode with normal incident white light illumination. A mat of tubular aggregates appears which can also precisely be investigated by scanning electron microscopy (SEM, Fig. 3.78b). The SEM overview image with a magnification of 600 represents an exact overlay of the respective optical bright field image in Fig. 3.78a. Higher magnification SEM images are shown as inset in Fig. 3.78b. Furthermore, the area marked by the red square in Fig. 3.78a has been recovered by the aid of the optical camera of an atomic force microscope and subjected to AFM tapping mode imaging. The structure and morphology strongly suggests that the objects under consideration are bundles of SWCNTs (Fig. 3.78d). Height analysis reveals that the objects are nano-scaled, e.g. 5–45 nm in height. Figure 3.78f exemplarily depicts the height profile corresponding to the black line in Fig. 3.78d. The optical visualization is highly versatile, as the visual inspection can be used for the retrieval of the sample area under investigation. Thus, a direct comparison of AFM and SEM on the very same sample spot, as exemplarily depicted by Fig. 3.78g, is accessible. The height of four SWCNT bundles is indicated in the AFM image, while the width of the same objects is marked in the SEM image. Most importantly, the width measured in the SEM image is overestimated by a factor of 3–4 opposed to the AFM heights. This underlines that the quantification of the bundles size distribution as a measure for the quality of the dispersion should not be targeted with SEM.

The question arises, whether the bi-layered Si/SiO$_2$ substrate is essential for the optical visualization. In this regard it is important to note that no contrast from SWCNTs, or SWCNT bundles spin-casted on Si wafers or glass substrate could be monitored in the bright field imaging mode. In an attempt to nonetheless visualize the nanotubes by microscopy, deposited SWCNTs (onto the bi-layered substrate and glass, respectively) have been coated with the fluorescent perylene dye **13** (the protected analogue of the surfactant **2**) by drop-casting a solution of **13** in toluene onto the substrates.

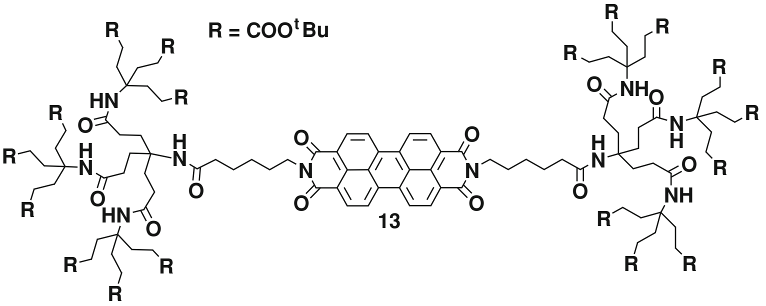

13

As depicted in Fig. 3.79a, the fluorescence of **13** is quenched in the presence of on observed on the bi-layered substrate (Fig. 3.79a—left) appear blacknanotubes so that the areas yielding a blue contrast under bright field illuminati in the fluorescence microscopic image (Fig. 3.79a—right). Similar aggregates are visualized by fluorescence microscopy when the nanotubes are deposited and coated on the glass substrate (Fig. 3.79b—right). However, no related objects are observed in the bright field image (Fig. 3.79b—left). This unambiguously underlines the importance of the bi-layered Si/SiO$_2$ substrate for the visual detection of nanotubes by optical microscopy.

In the following, the designed water-soluble aromatic surfactant **2** (which is structurally related to the perylene dye **13**) has been used as dispersant in order to elucidate whether the visual detection can be applied to nanotube samples with a

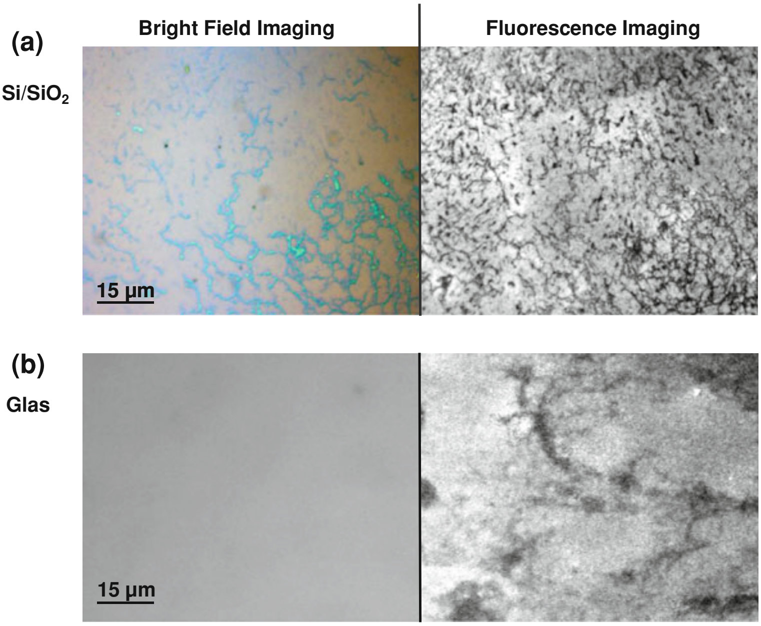

Fig. 3.79 Optical micrographs of HiPco-SDBS spin-casted onto **a** a Si/SiO$_2$ substrate (SiO$_2$ thickness 300 nm) and **b** a glass substrate. The substrates were coated with the perylene dye **13** by drop casting a solution of **13** in toluene prior to optical microscopy. The micrographs under bright field illumination are depicted in the left panel, while the fluorescence microscopic images of the same area are shown in the right panel. For acquisition of the fluorescence microscopic images a 545 nm cut-off filter was used in excitation and a 570 nm long-pass filter for the emission. Please note that the focus for acquisition of the bright field and respective fluorescence microscopy images has not been changed. The objects in case of the glass substrate, however, appear slightly blurred which can be traced back to difficulties in focusing due to the absence of contrast in bright field illumination. (Reproduced with permission from Wiley–VCH, reference 117)

different morphology and distributions of individual and bundled nanotubes. A dispersion of HiPco-**2** S in borate buffer (pH = 10) has been used. For the thorough characterization of the dispersion please see Sect. 3.1. Sample preparation again involved sonication, centrifugation and spin-casting on Si/SiO$_2$ substrates as already outlined.

Compared to HiPco-SDBS, no such well defined bundles are observed for HiPco-**2** (Fig. 3.80), as dispersion by the perylene π-surfactant is characterized by higher degrees of nanotube exfoliation leading to smaller nanotube aggregates than in the case of SDBS as dispersant. However, objects with a deep blue contrast also appear marked by the red circles in Fig. 3.80. In order to prove that the contrast arises from SWCNTs, a detailed Raman spectroscopic investigation has been carried out.

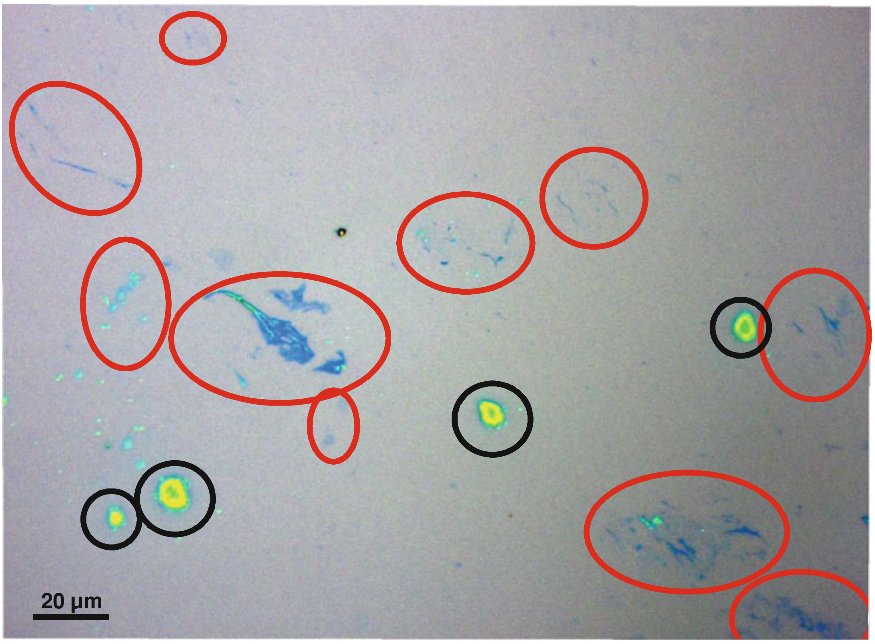

Fig. 3.80 Optical bright field micrographs of HiPco SWCNTs dispAs outlined in the introduction, Raman spectroscopy is a powerful tool in SWCNT characterization, as the characteristic radial breathing modes (RBMs) of the SWCNTs, which correlate to the diameter of the nanotubes allow drawing conclusions on the diameter distribution and composition of the material [122]. Furthermore, it is highly important for the determination of the degree of functionalization of covalently modified nanotubes based on the D/G ratio [122]. However, Raman spectroscopy has so far lacked structural information of the SWCNT aggregates. Thus, the interpretation of the Raman spectra has been challenging, as alterations of the optical nanotube transitions by bundling or functionalization give rise to redistributions in the relative RBM intensities at one excitation wavelength [123–125]. These might be easily misinterpreted as changes in the diameter composition of the SWCNTs and/or selective functionalization. An optical visualization that allows for a correlation of spectroscopic and microscopic information would thus be highly desirable

The results from the Raman spectroscopic investigation ($\lambda_{\text{exc}} = 532$ nm) on HiPco-**2** are summarized in Fig. 3.81. Figure 3.81b depicts the area of the nanotube G-band centered at 1586 cm^{-1} extracted from the Raman spectra which have been recorded by line-wise acquisition of individual spectra in 0.5 µm steps. The area investigated corresponds to the optical micrograph in Fig. 3.81a. Exemplarily, the Raman spectra of the spots marked as 1, 2, 3 and 4 are displayed in Figs. 3.81d–g. The Raman spectrum clearly identifies the deposits under investigation as SWCNTs with the RBMs (150–300 cm^{-1}), the D-band (1330 cm^{-1}) and the G-band (1586 cm^{-1}) being clearly discernable. The excitation wavelength of 532 nm has been chosen, as the resonant Raman signals attributed to the perylene moiety of the surfactant at 1304 and 1376 cm^{-1} are recorded simultaneously with the SWCNTs

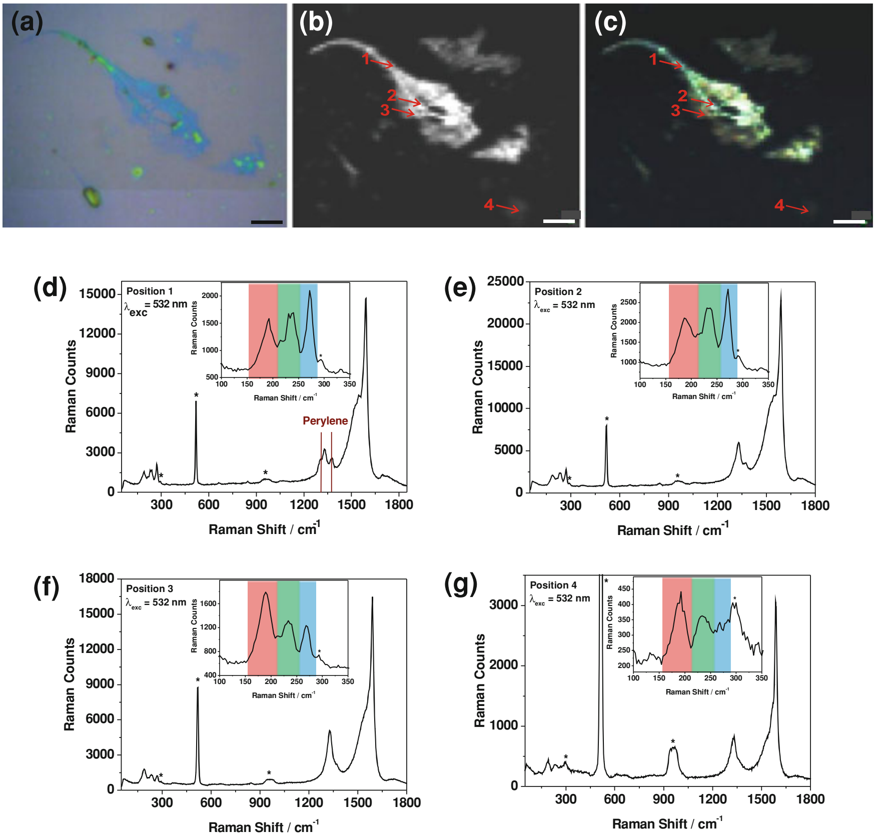

Fig. 3.81 **a** Optical microscopy image of HiPco-**2** deposited on a Si/SiO_2 substrate with a 300 nm layer thickness (scale bar 5 μm). The setup enables optical detection of thin-layer deposits through interference contrast and scanning with the Raman microscope. **b** Raman amplitude of the G peak (*black*—low count rate to *white*—high count rate) measured every 0.5 μm, indicating the presence of nanotubes. **c** Map of the RBM region measured every 0.5 μm. The colors arise from the overlay of three domains colored in *red* (155–207 cm^{-1}), *green* (216–253 cm^{-1}) and *blue* (256–287 cm^{-1}), respectively. **d**–**g** Raman spectra corresponding to the positions indicated by the *red arrows* in the Raman maps of Figs. 3.81b, c recorded with an excitation wavelength of 532 nm. (Reproduced with permission from Wiley–VCH, reference 117)

(also see Sect. 3.1.3.2), as most clearly identified in the Raman spectrum in Fig. 3.81d. The variations in the ratio of the peaks attributed to the perylene to the signals arising from the nanotubes reflect that the nanotube surface is inhomogenously covered by the perylene surfactant as analyzed in detail in Sect. 3.1.

The structure and morphology of the SWCNT bundle (Fig. 3.81a) is nicely reflected by the Raman map in Fig. 3.81b, as the intensity of the Raman signal correlates with the number of nanotubes being resonantly enhanced, resulting in variations of the integrated G-band intensity. A map of the RBM amplitudes has

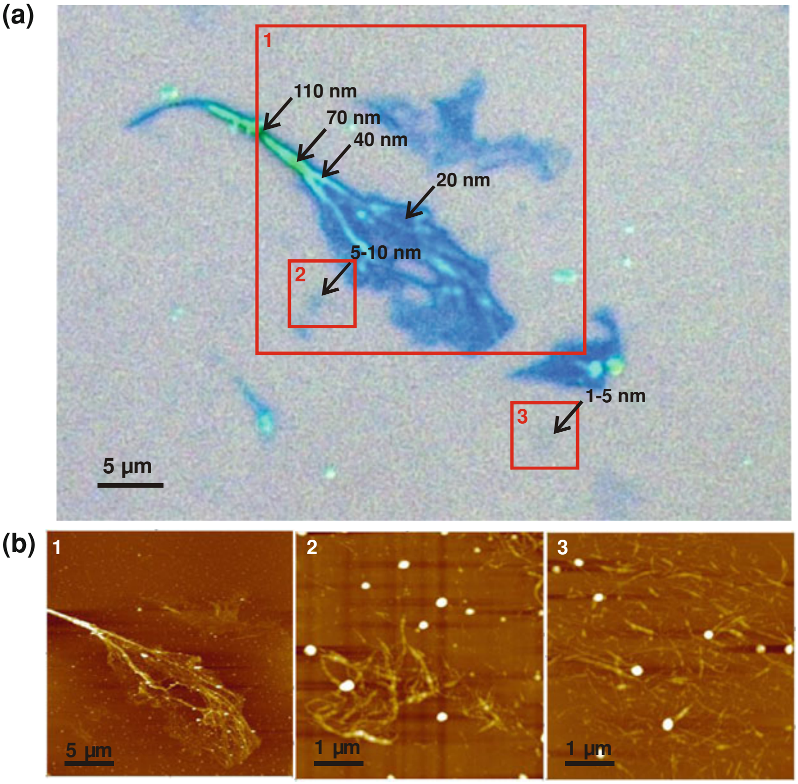

Fig. 3.82 **a** Optical bright field micrograph of HiPco-**2** spin-casted onto a Si/SiO$_2$ substrate (SiO$_2$ thickness 300 nm), **b** AFM tapping mode images corresponding to the areas marked by the *red squares*. (Reproduced with permission from Wiley–VCH, reference 117)

also been included in Fig. 3.81c in order to underline the versatility of the Raman investigations on the deposited nanotubes. For this purpose the RBM region was divided in three domains ranging from 155–207 cm^{-1} (large diameters), 216–253 cm^{-1} (medium diameters) and 256–287 cm^{-1} (small diameters) corresponding to the red, green and blue color code, respectively. Thus, differences in the relative distributions of the nanotubes in the bundle can conveniently be followed, e.g. a blue pixel such as at position 2 in Fig. 3.81c corresponds to a higher relative concentration of smaller diameter nanotubes, while a red pixel such as at position 3 arises from an increased relative concentration of larger diameter SWCNTs.

Additionally, the question has been addressed whether the colors in the optical micrograph ranging from deep blue over cyan to green can be correlated with the height of the nano-scaled objects. Therefore, exactly the same SWCNT bundle of the Raman spectroscopic investigation has been recovered by the aid of the optical microscope of the AFM and subjected to AFM imaging, as exemplarily depicted

Fig. 3.83 **a** Optical bright field micrograph of HiPco-**2** spin-casted onto a Si/SiO$_2$ substrate (SiO$_2$ thickness 300 nm), **b** corresponding *dark* field image. (Reproduced with permission from Wiley–VCH, reference 117)

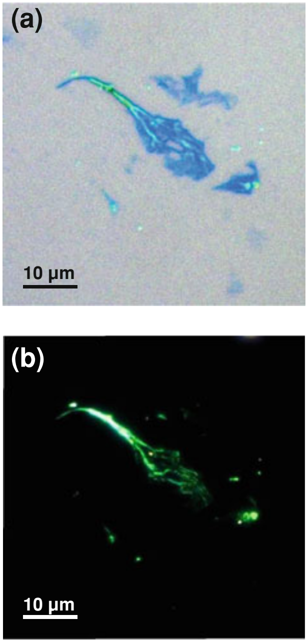

for HiPco-**2** in Fig. 3.82. The height profiles of the images displayed in Fig. 3.82b reveal that very well dispersed nanotubes with a height of 1–5 nm (position 3) can hardly be visualized optically. Regions, where nanotube bundles with a height of 5–10 nm (position 2) are deposited, give rise to a deep blue contrast. In analogy, the height at different spots at area 1 has been determined leading to the conclusion that the color of the interference contrast can be roughly correlated to the morphology of the SWCNTs with increasing heights from blue over cyan to green.

Finally, it has been investigated whether the dark field imaging mode of the optical microscope is also suitable for the optical visualization of SWCNTs. Figure 3.83 depicts the bright field image of HiPco-**2** (Fig. 3.83a), which has been extensively investigated above, in relation to the corresponding dark field image (Fig. 3.83b). Obviously, only strongly aggregated, e.g. bundled nanotubes with a height larger than approximately 30 nm can be precisely mapped in the dark field imaging mode. Thus the use of dark field imaging is limited, as the contrast intrinsically arises from objects capable of scattering the incident light.

In summary, the optical visualization of SWCNTs deposited onto Si/SiO$_2$ substrates provides simple and efficient access to a low-cost in-depth characterization of SWCNT dispersions, as it enables the direct correlation of microscopic (SEM and AFM) and spectroscopic (Raman) information. The importance of using a bi-layered substrate has been underlined by the aid of fluorescence microcopy on dye-coated SWCNTs deposited onto a Si/SiO$_2$ and glass substrate, respectively. The fluorescence quenching of the fluorescent dye by the underlying nanotubes can conveniently be followed by fluorescence microscopy on any substrate. Only in the case of the bi-layered substrate, however, the same objects as in bright field imaging mode are detected. By the aid of this novel optical visualization, multiple SWCNT characterization techniques can now be applied to exactly the same region on the substrate. Thus, for example, a direct comparison of SEM and AFM has been provided. The color of the interference contrast ranging from deep blue over cyan to green of the SWCNTs spin-casted onto the opaque bi-layered substrate roughly correlates to the height of the SWCNT bundles. The Raman investigation outlines the versatility of the optical detection, as differences in the morphology and the local composition of the SWCNT bundles are reflected by variations in the Raman G-band intensity, as well as relative changes in the RBM distributions, respectively.

It is important to point out that this strikingly simple observation is expected to drive nanotube characterization forward significantly, especially with regard to covalently functionalized nanotube samples, where the degree of functionalization could now be probed locally by the Raman D/G ratios. Additionally, the optical visualization greatly facilitates AFM measurements, as areas of interest can be retrieved within minutes under any conventional microscope. One can also imagine to systematically investigate the fluorescence quenching ability of nanotubes with different fluorescent dyes by the aid of fluorescence microscopy. Owing to the visual bright field detection, the same area of deposited SWCNTs could be characterized in detail by Raman and AFM analysis and then coated by the dye of interest and subjected to fluorescence microscopy.

References

1. C. Backes, C.D. Schmidt, F. Hauke, C. Boettcher, A. Hirsch, J. Am. Chem. Soc. **131**, 2172–2184 (2009)
2. C. Backes, C.D. Schmidt, K. Rosenlehner, J.N. Coleman, F. Hauke, A. Hirsch, Adv. Mater. **22**, 788–802 (2010)
3. C.D. Schmidt, C. Bottcher, A. Hirsch, Eur. J. Org. Chem. 5497–5505 (2007)
4. Y. Tomonari, H. Murakami, N. Nakashima, Chem. Eur. J. **12**, 4027–4034 (2006)
5. H. Paloniemi, T. Aeaeritalo, T. Laiho, H. Liuke, N. Kocharova, K. Haapakka, F. Terzi, R. Seeber, J. Lukkari, J. Phys. Chem. B **109**, 8634–8642 (2005)
6. J. Chen, C.P. Collier, J. Phys. Chem. B **109**, 7605–7609 (2005)
7. A. Mateo-Alonso, C. Ehli, K.H. Chen, D.M. Guldi, M. Prato, J. Phys. Chem. A **111**, 12669–12673 (2007)
8. V. Zorbas, A.L. Smith, H. Xie, A. Ortiz-Acevedo, A.B. Dalton, G.R. Dieckmann, R.K. Draper, R.H. Baughman, I.H. Musselman, J. Am. Chem. Soc. **127**, 12323–12328 (2005)
9. S.-Y. Ju, J. Doll, I. Sharma, F. Papadimitrakopoulos, Nat. Nanotechnol. **3**, 356–362 (2008)
10. A. Nish, J.-Y. Hwang, J. Doig, R.J. Nicholas, Nat. Nanotechnol. **2**, 640–646 (2007)
11. F. Chen, B. Wang, Y. Chen, L.-J. Li, Nano Lett. **7**, 3013–3017 (2007)
12. J.-Y. Hwang, A. Nish, J. Doig, S. Douven, C.-W. Chen, L.-C. Chen, R.J. Nicholas, J. Am. Chem. Soc. **130**, 3543–3553 (2008)
13. O. Matarredona, H. Rhoads, Z. Li, J.H. Harwell, L. Balzano, D.E. Resasco, J. Phys. Chem. B **107**, 13357–13367 (2003)
14. Y. Tan, D.E. Resasco, J. Phys. Chem. B **109**, 14454–14460 (2005)

15. S. Utsumi, M. Kanamaru, H. Honda, H. Kanoh, H. Tanaka, T. Ohkubo, H. Sakai, M. Abe, K. Kaneko, J. Colloid Interface Sci. **308**, 276–284 (2007)
16. M.F. Islam, E. Rojas, D.M. Bergey, A.T. Johnson, A.G. Yodh, Nano Lett. **3**, 269–273 (2003)
17. W. Wenseleers, I.I. Vlasov, E. Goovaerts, E.D. Obraztsova, A.S. Lobach, A. Bouwen, Adv. Funct. Mater. **14**, 1105–1112 (2004)
18. B.R. Priya, H.J. Byrne, J. Phys. Chem. C **112**, 332–337 (2008)
19. T. Okazaki, T. Saito, K. Matsuura, S. Ohshima, M. Yumura, S. Iijima, Nano Lett. **5**, 2618–2623 (2005)
20. T.J. McDonald, C. Engtrakul, M. Jones, G. Rumbles, M.J. Heben, J. Phys. Chem. B **110**, 25339–25346 (2006)
21. M. Brettreich, Dissertation, Friedrich-Alexander Universität Erlangen-Nürnberg (Germany) 44ff, 2000
22. B. Zhao, M.E. Itkis, S. Niyogi, H. Hu, J. Zhang, R.C. Haddon, J. Phys. Chem. B **108**, 8136–8141 (2004)
23. H. Cathcart, S. Quinn, V. Nicolosi, J.M. Kelly, W.J. Blau, J.N. Coleman, J. Phys. Chem. C **111**, 66–74 (2007)
24. M.S. Arnold, M.O. Guler, M.C. Hersam, S.I. Stupp, Langmuir **21**, 4705–4709 (2005)
25. A.D.Q. Li, W. Wang, L.-Q. Wang, Chem. Eur. J. **9**, 4594–4601 (2003)
26. W.E. Ford, J. Photochem. **37**, 189–204 (1987)
27. W. Wang, J.J. Han, L.-Q. Wang, L.-S. Li, W.J. Shaw, A.D.Q. Li, Nano Lett. **3**, 455–458 (2003)
28. C. Ehli, C. Oelsner, D.M. Guldi, A. Mateo-Alonso, M. Prato, C.D. Schmidt, C. Backes, F. Hauke, A. Hirsch, Nat. Chem. (2009). doi:10.1038/NCHEM.214
29. S.D. Bergin, V. Nicolosi, H. Cathcart, M. Lotya, D. Rickard, Z. Sun, W.J. Blau, J.N. Coleman, J. Phys. Chem. C **112**, 972–977 (2008)
30. M.J. O'Connell, S.M. Bachilo, C.B. Huffman, V.C. Moore, M.S. Strano, E.H. Haroz, K.L. Rialon, P.J. Boul, W.H. Noon, C. Kittrell, J. Ma, R.H. Hauge, R.B. Weisman, R.E. Smalley, Science **297**, 593–596 (2002)
31. S.M. Bachilo, M.S. Strano, C. Kittrell, R.H. Hauge, R.E. Smalley, R.B. Weisman, Science **298**, 2361–2366 (2002)
32. H. Cathcart, V. Nicolosi, J.M. Hughes, W.J. Blau, J.M. Kelly, S.J. Quinn, J.N. Coleman, J. Am. Chem. Soc. **130**, 12734–12744 (2008)
33. J.J. Brege, C. Gallaway, A.R. Barron, J. Phys. Chem. C **111**, 17812–17820 (2007)
34. R. Marquis, C. Greco, I. Sadokierska, S. Lebedkin, M.M. Kappes, T. Michel, L. Alvarez, J.-L. Sauvajol, S. Meunier, C. Mioskowski, Nano Lett. **8**, 1830–1835 (2008)
35. V. Nicolosi, H. Cathcart, A.R. Dalton, D. Aherne, G.R. Dieckmann, J.N. Coleman, Biomacromolecules **9**, 598–602 (2008)
36. S. Giordani, S.D. Bergin, V. Nicolosi, S. Lebedkin, M.M. Kappes, W.J. Blau, J.N. Coleman, J. Phys. Chem. B **110**, 15708–15718 (2006)
37. B. White, S. Banerjee, S. O'Brien, N.J. Turro, I.P. Herman, J. Phys. Chem. C **111**, 13684–13690 (2007)
38. Z. Sun, V. Nicolosi, D. Rickard, S.D. Bergin, D. Aherne, J.N. Coleman, J. Phys. Chem. C **112**, 10692–10699 (2008)
39. D.C.H. Cheng, E. Gulari, J. Colloid Interface Sci. **90**, 410–423 (1982)
40. J.F. Cardenas, A. Gromov, Nanotechnology **20**, 465703/465701–465703/465708 (2009)
41. L.S. Witus, J.-D.R. Rocha, V.M. Yuwono, S.E. Paramonov, R.B. Weisman, J.D. Hartgerink, J. Mater. Chem. **17**, 1909–1915 (2007)
42. V.C. Moore, M.S. Strano, E.H. Haroz, R.H. Hauge, R.E. Smalley, J. Schmidt, Y. Talmon, Nano Lett. **3**, 1379–1382 (2003)
43. N. Grossiord, O. Regev, J. Loos, J. Meuldijk, C.E. Koning, Anal. Chem. **77**, 5135–5139 (2005)
44. Y. Dror, W. Pyckhout-Hintzen, Y. Cohen, Macromolecules **38**, 7828–7836 (2005)

45. R. Bandyopadhyaya, E. Nativ-Roth, O. Regev, R. Yerushalmi-Rozen, Nano Lett. **2**, 25–28 (2002)
46. M.S. Strano, V.C. Moore, M.K. Miller, M.J. Allen, E.H. Haroz, C. Kittrell, R.H. Hauge, R.E. Smalley, J. Nanosci. Nanotechnol. **3**, 81–86 (2003)
47. D.A. Tsyboulski, E.L. Bakota, L.S. Witus, J.-D.R. Rocha, J.D. Hartgerink, R.B. Weisman, J. Am. Chem. Soc. **130**, 17134–17140 (2008)
48. S.-Y. Ju, W.P. Kopcha, F. Papadimitrakopoulos, Science **323**, 1319–1323 (2009)
49. R. Garcia, J. Tamayo, A. San Paulo, Surf. Interface Anal. **27**, 312–316 (1999)
50. J.P. Cleveland, B. Anczykowski, A.E. Schmid, V.B. Elings, Appl. Phys. Lett. **72**, 2613–2615 (1998)
51. O.P. Behrend, L. Odoni, J.L. Loubet, N.A. Burnham, Appl. Phys. Lett. **75**, 2551–2553 (1999)
52. G. Bar, Y. Thomann, M.H. Whangbo, Langmuir **14**, 1219–1226 (1998)
53. S.N. Magonov, V. Elings, V.S. Papkov, Polymer **38**, 297–307 (1997)
54. R. Garcia, R. Perez, Surf. Sci. Rep. **47**, 197–301 (2002)
55. B. Gigliotti, B. Sakizzie, D.S. Bethune, R.M. Shelby, J.N. Cha, Nano Lett. **6**, 159–164 (2006)
56. M. Zheng, A. Jagota, M.S. Strano, A.P. Santos, P. Barone, S.G. Chou, B.A. Diner, M.S. Dresselhaus, R.S. McLean, G.B. Onoa, G.G. Samsonidze, E.D. Semke, M. Usrey, D.J. Walls, Science **302**, 1545–1548 (2003)
57. P.P.T.I.T. Okpalugo, H. Murphy, J. McLaughlin, N.M.D. Brown, Carbon 2005, 43, 153–161
58. R. Graupner, J. Abraham, D. Wunderlich, A. Vencelova, P. Lauffer, J. Roehrl, M. Hundhausen, L. Ley, A. Hirsch, J. Am. Chem. Soc. **128**, 6683–6689 (2006)
59. Z. Syrgiannis, F. Hauke, J.R. Hundhausen, R. Graupner, Y. Elemes, A. Hirsch, Eur. J. Org. Chem. 2008, 2544–2550
60. J. Tarabek, L. Kavan, L. Dunsch, M. Kalbac, J. Phys. Chem. C **112**, 13856–13861 (2008)
61. S. Hüfner, *Photoelectron Spectroscopy* (Springer, Berlin, 1995)
62. R. Graupner, J. Abraham, A. Vencelova, T. Seyller, F. Hennrich, M.M. Kappes, A. Hirsch, L. Ley, Phys. Chem. Chem. Phys. **5**, 5472–5476 (2003)
63. A. Krüger, *Neue Kohlenstoffmaterialien* (Teubner, Wiesbaden, 2007)
64. M.S. Dresselhaus, G. Dresselhaus, P.C. Eklund, *Science of Fullerenes and Carbon Nanotubes* (Academic, New York, 1996)
65. P.C. Eklund, J.M. Holden, R.A. Jishi, Carbon **33**, 959–972 (1995)
66. U.J. Kim, X.M. Liu, C.A. Furtado, G. Chen, R. Saito, J. Jiang, M.S. Dresselhaus, P.C. Eklund, Phys. Rev. Lett. **95**, 157402/157401–157402/157404 (2005)
67. C. Branca, F. Frusteri, V. Magazu, A. Mangione, J. Phys. Chem. B **108**, 3469–3473 (2004)
68. U. Kuhlmann, H. Jantoljak, N. Pfander, P. Bernier, C. Journet, C. Thomsen, Chem. Phys. Lett. **294**, 237–240 (1998)
69. U. Kuhlmann, H. Jantoljak, N. Pfander, C. Journet, P. Bernier, C. Thomsen, Synth. Met. **103**, 2506–2507 (1999)
70. K. Rosenlehner, B. Schade, C. Boettcher, C.M. Jaeger, T. Clark, F.W. Heinemann, A. Hirsch, Chem. Eur. J. **16**, 9544–9554 (2010)
71. C. Backes, T. Schunk, F. Hauke, A. Hirsch, J. Mater. Chem. **21**, 3554–3557 (2011)
72. J.-H. Lee, S.-M. Yoon, K.K. Kim, I.-S. Cha, Y.J. Park, J.-Y. Choi, Y.H. Lee, U. Paik, J. Phys. Chem. C **112**, 15267–15273 (2008)
73. Y. Fujita, S. Bandow, S. Iijima, Chem. Phys. Lett. **413**, 410–414 (2005)
74. E. Karabudak, C. Backes, F. Hauke, C.D. Schmidt, H. Cölfen, A. Hirsch, W. Wohlleben, Chem. Phys. Chem. **11**, 3224–3227 (2010)
75. N. Nair, W.-J. Kim, R.D. Braatz, M.S. Strano, Langmuir **24**, 1790–1795 (2008)
76. M.S. Arnold, J. Suntivich, S.I. Stupp, M.C. Hersam, ACS Nano **2**, 2291–2300 (2008)
77. W. Maechtle, L. Boerger, *Analytical Ultracentrifugation of Polymers and Nanoparticles* (Springer, Berlin, 2006)
78. H. Coelfen, Anal. Ultracentrifugation 2005, 501–583
79. W. Maechtle, Makromol. Chem. **185**, 1025–1039 (1984)

80. H.G. Mueller, F. Herrmann, Prog. Colloid Polym. Sci. **99**, 114–119 (1995)
81. P.H. Brown, P. Schuck, Comput. Phys. Commun. **178**, 105–120 (2008)
82. C. Backes, E. Karabudak, C.D. Schmidt, F. Hauke, A. Hirsch, W. Wohlleben, Chem. Eur. J. **16**, 13176–13184 (2010)
83. P. Schuck, in SEDFIT, version 10.09b (Ed.: N. I. o. Health), 2007
84. P. Schuck, Biophys. J. **78**, 1606–1619 (2000)
85. N.R. Tummala, A. Striolo, Phys. Rev. E Stat. Nonlinear Soft Matter Phys. **80**, 021408/021401–021408/021410 (2009)
86. E.E. Lees, M.J. Gunzburg, T.-L. Nguyen, G.J. Howlett, J. Rothacker, E.C. Nice, A.H.A. Clayton, P. Mulvaney, Nano Lett. **8**, 2883–2890 (2008)
87. N. Nakashima, Y. Tomonari, H. Murakami, Chem. Lett. 2002, 638–639
88. J. Zhao, J.P. Lu, J. Han, C.-K. Yang, Appl. Phys. Lett. **82**, 3746–3748 (2003)
89. C. Ehli, C. Oelsner, D.M. Guldi, A. Mateo-Alonso, M. Prato, C. Schmidt, C. Backes, F. Hauke, A. Hirsch, Nat. Chem. **1**, 243–249 (2009)
90. M.J. O'Connell, E.E. Eibergen, S.K. Doorn, Nat. Mater. **4**, 412–418 (2005)
91. C. Backes, C.D. Schmidt, J.N. Coleman, W. Wohlleben, F. Hauke, A. Hirsch, Chem. Eur. J. **16**, 13185–13192 (2010)
92. N.V. Kozhemyakina, J.M. Englert, G. Yang, E. Spiecker, C.D. Schmidt, F. Hauke, A. Hirsch, Adv. Mater. 5483–5487 (2010)
93. P.C. Schulz, M.A. Morini, R.M. Minardi, J.E. Puig, Colloid Polym. Sci. **273**, 959–966 (1995)
94. S.K. Hait, P.R. Majhi, A. Blume, S.P. Moulik, J. Phys. Chem. B **107**, 3650–3658 (2003)
95. M.L. Corrin, W.D. Harkins, J. Chem. Phys. **14**, 641 (1946)
96. C. Backes, U. Mundloch, A. Ebel, F. Hauke, A. Hirsch, Chem. Eur. J. **16**, 3314–3317 (2010)
97. A. Ebel, W. Donaubauer, F. Hampel, A. Hirsch, Eur. J. Org. Chem. 3488–3494 (2007)
98. C. Backes, A. Hirsch, in *Chemistry of Nanocarbons,* 2010 eds. by T. Akasaka, F. Wudl, S. Nagase, Wiley, p. 528
99. M.S. Arnold, A.A. Green, J.F. Hulvat, S.I. Stupp, M.C. Hersam, Nat. Nanotechnol. **1**, 60–65 (2006)
100. C.W. Lee, C.-H. Weng, L. Wei, Y. Chen, M.B. Chan-Park, C.-H. Tsai, K.-C. Leou, C.H.P. Poa, J. Wang, L.-J. Li, J. Phys. Chem. C **112**, 12089–12091 (2008)
101. A.A. Green, M.C. Hersam, Nano Lett. **8**, 1417–1422 (2008)
102. Y. Sato, K. Yanagi, Y. Miyata, K. Suenaga, H. Kataura, S. Iijima, Nano Lett. **8**, 3151–3154 (2008)
103. Y. Miyata, K. Yanagi, Y. Maniwa, H. Kataura, J. Phys. Chem. C **112**, 13187–13191 (2008)
104. Y. Miyata, K. Yanagi, Y. Maniwa, H. Kataura, Phys. Stat. Sol. (b) **245**, 2233–2238 (2008)
105. Y. Miyata, K. Yanagi, Y. Maniwa, H. Kataura, J. Phys. Chem. C **112**, 3591–3596 (2008)
106. S. Ghosh, S.M. Bachilo, R.B. Weisman, Nat. Nanotechnol. **5**, 443–450 (2010)
107. W.-J. Kim, N. Nair, C.Y. Lee, M.S. Strano, J. Phys. Chem. C **112**, 7326–7331 (2008)
108. B. Gebhardt, F. Hof, C. Backes, M. Müller, T. Plocke, C. Thomsen, F. Hauke, A. Hirsch, J. Am. Chem. Soc. (2011). doi: 10.1021/ja206818n
109. Z. Syrgiannis, B. Gebhardt, C. Dotzer, F. Hauke, R. Graupner, A. Hirsch, Angew. Chem. Int. Ed. **49**, 3322–3325, S3322/3321–S3322/3329 (2010)
110. D.M. Guldi, N. Martín, Carbon Nanotubes and Related Structures: Synthesis, Characterization, Functionalization, and Applications. Wiley-VCH 2010
111. C. Backes, C.D. Schmidt, F. Hauke, A. Hirsch, Chem. Commun. **19**, 2643–2645 (2009)
112. M.C. Hersam, Nat. Nanotechnol. **3**, 387–394 (2008)
113. J.A. Fagan, M.L. Becker, J. Chun, E.K. Hobbie, Adv. Mater. **20**, 1609–1613 (2008)
114. J.A. Fagan, M.L. Becker, J. Chun, P. Nie, B.J. Bauer, J.R. Simpson, A. Hight-Walker, E.K. Hobbie, Langmuir **24**, 13880–13889 (2008)
115. J.A. Fagan, J.R. Simpson, B.J. Bauer, S.H. De Paoli Lacerda, M.L. Becker, J. Chun, K.B. Migler, A.R. Hight Walker, E.K. Hobbie, J. Am. Chem. Soc. **129**, 10607–10612 (2007)
116. C. Backes, C.D. Schmidt, F. Hauke, A. Hirsch, Chem. Asian J. **6**, 438–444 (2011)
117. C. Backes, J. Englert, N. Bernhard, F. Hauke, A. Hirsch, Small **6**, 1968–1973 (2010)

118. K.S. Novoselov, A.K. Geim, S.V. Morozov, D. Jiang, Y. Zhang, S.V. Dubonos, I.V. Grigorieva, A.A. Firsov, Science **306**, 666–669 (2004)
119. D.S.L. Abergel, A. Russell, V.I. Fal'ko, Appl. Phys. Lett. **91**, 063125 (2007)
120. X. Wang, M. Zhao, D.D. Nolte, Appl. Phys. Lett. **95**, 081102 (2009)
121. P. Blake, E.W. Hill, A.H. Castro Neto, K.S. Novoselov, D. Jiang, R. Yang, T.J. Booth, A.K. Geim, Appl. Phys. Lett. **91**, 063124/063121–063124/063123 (2007)
122. R. Graupner, J. Raman Spectrosc. **38**, 673–683 (2007)
123. M.J.O'Connell, S. Sivaram, S.K. Doorn, Phys. Rev. *B*. **69**, 235415/235411–235415/235415 (2004)
124. A.M. Rao, J. Chen, E. Richter, U. Schlecht, P.C. Eklund, R.C. Haddon, U.D. Venkateswaran, Y.K. Kwon, D. Tomanek, Phys. Rev. Lett. **86**, 3895–3898 (2001)
125. D.A. Heller, P.W. Barone, J.P. Swanson, R.M. Mayrhofer, M.S. Strano, J. Phys. Chem. B **108**, 6905–6909 (2004)

Chapter 4
Conclusion

The work presented here served the purpose to gain fundamental insights in noncovalent functionalization of single-walled carbon nanotubes. The focus was directed towards establishing structure–property relationships of adsorbates and nanotubes in aqueous solution in order to understand nanotube dispersion and exfoliation, especially by designed surfactants. Up to now, despite the extraordinary progresses in the development of nanotube sorting techniques [1], the efficiency of nanotube separation as a foundation for their increased processability has been restricted by the limited exfoliation efficiencies of commercially available detergents. This is exactly the point where this work hooked in and enabled to pave the way to improved sorting.

Within this thesis, it was demonstrated for the first time that amphiphilic perylene bisimide derivatives (PBIs) are excellent candidates for dispersing nanotubes in aqueous media especially with regard to the exfoliation efficiencies as determined by statistical atomic force microscopy (AFM) [2, 3]. I was thus able to extent the small library of anchor groups to the SWCNT scaffold by an electron deficient aromatic system. The novel π-surfactants are equipped with first and second generation *Newkome*-type dendrimers terminated with carboxylic acid functionalities as hydrophilic moieties. The convergent synthesis [4] enabled the construction of different surfactants bearing similar structural motives which can be classified as being bolaamphiphilic or amphiphilic (Scheme 3.1). Therefore, an in-depth investigation of the adsorption behavior and supramolecular arrangement became possible and a structure–property relationship could be established for the first time.

In order to evaluate the role of the substituents in the periphery of the aromatic anchor, the dispersion and exfoliation efficiencies of the SWCNTS by the aid of the surfactants was investigated (Sects. 3.1.1.1 and 3.1.1.3) [3]. Interestingly, the amphiphilic perylene derivative **6** with the rather small first generation dendrimer head group does not adsorb on the SWCNT scaffold by its perylene core as determined from the spectroscopic signatures of the perylene dye, as well as the carbon nanotubes. Since the nanotube features strongly resemble those of an aqueous dispersion in SDBS, it can be concluded that the perylene dispersant **6** adsorbs by the branched alkyl chain and thus prefers a micellar arrangement attributed to the

C. Backes, *Noncovalent Functionalization of Carbon Nanotubes*, Springer Theses,
DOI: 10.1007/978-3-642-27582-1_4,

increased micelle stability due to the smaller head group bearing a maximum of three charges combined with the amphiphilicity generated by the nonpolar tail. It is important to note that the dispersion efficiency of the perylene derivative **6** is by a factor of approximately two lower compared to the derivatives **1** or **3** (Table 3.1). This points towards the importance of considering the supramolecular structure of the perylene derivatives in aqueous solution in more detail, as the self-aggregation behavior obviously impacts the adsorption to the nanotube backbone and, directly related to that, the dispersion efficiency.

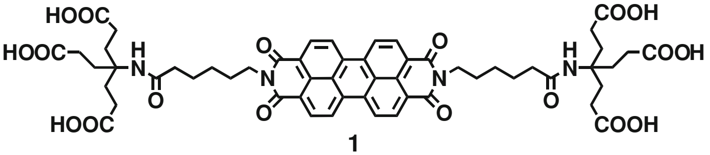

1

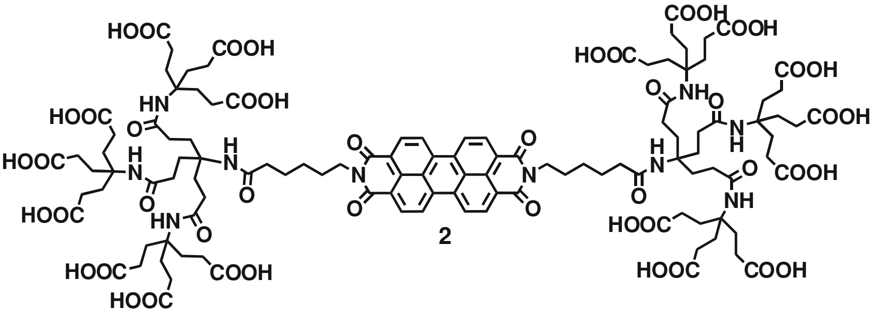

2

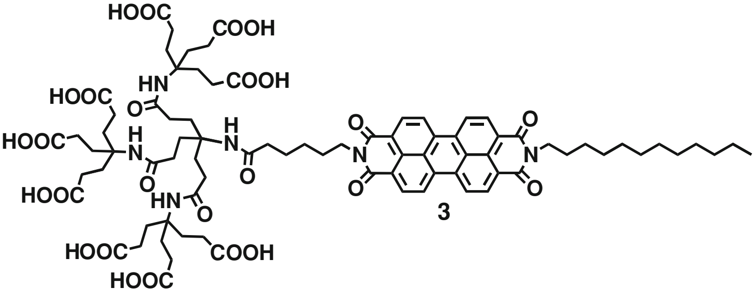

3

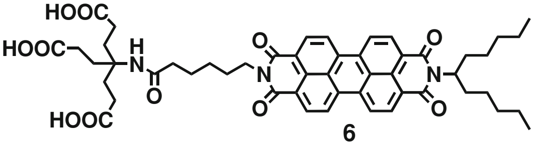

6

The importance of environmental effects is furthermore reflected by the dependency of SWCNT dispersion efficiencies on the pH of the buffered aqueous surrounding [3]. In case of all anionic perylene surfactants under investigation (including the derivative **6** which prefers a micellar arrangement), nanotube dispersion and individualization was increased by approximately a factor of two in the pH = 10 buffer solution. In a first approximation this can be attributed to a higher effective charge density on the surfactant head group and therefore an increased repulsion between adjacent SWCNTs in a bundle during the sonication induced unzippering.

The dispersion efficiencies of the perylene bisimide derivatives **1** and **3** in the borate buffer at pH = 10 in the concentration range investigated are similar to those of SDBS, albeit with a surfactant concentration that is lower by a factor of 100. Most significantly, exfoliation capabilities of the bolaamphiphilic perylene derivative **1** and the amphiphilic perylene derivative **3** are outstanding approaching 76% (at pH = 10). This is by a factor of five higher than the commonly used detergent SDBS. Since nanotube individualization is the key factor for any separation scenario, improving the exfoliation will also ultimately have the potential to enhance sorting yields.

Another critical point that was addressed for the first time within this thesis was the effect of the cationic counterion in the periphery of the anionic perylene surfactants (Sect. 3.1.1.4) [5]. In line with the amphiphilic carboxylates [6] without aromatic core, a pronounced sodium effect impacts the aggregation behavior of the anionic perylene dyes due to a counterion affinity that increases in the order $K^+ < Li^+ < Na^+$. Going one step further, it was demonstrated that the counterion plays a significant role in SWCNT dispersion due to the impact on the supramolecular structure of the surfactant dye. This enabled to enhance the dispersion efficiency in the presence of the appropriate counterion reaching 88% with the perylene surfactant **1** in non-buffered aqueous media with K^+ as counterion at pH = 11.

A similar improvement in nanotube dispersability was achieved by the addition of perylene tetra carboxylic acid dianhydride (PTCDA) as intercalant (Sect. 3.1.2.1) [7]. Due to the rather bulky substituents in the periphery, the designed surfactants may be partly hindered from slipping between adjacent SWCNTs in a bundle during the sonication induced exfoliation. Despite the lack of solubility of PTCDA in aqueous solution a pronounced effect could be observed upon its addition to the SWCNT-surfactant mixture. Boundary sedimentation experiments in buffered aqueous media (pH = 10) in analytical ultracentrifugation with a universal spectrometer enabled to visualize the different components of the complex dispersion. Based on these findings in combination with steady state absorption spectroscopy, it is suggested that PTCDA is intermittently adsorbed onto the SWCNT surface during sonication where it can propagate along the nanotube surface thus improving SWCNT exfoliation and dispersability. Concomitantly, the dianhydride is exposed to the basic environment resulting in a hydrolysis to the corresponding diacid and desorption from the SWCNT surface. Under carefully chosen conditions, dispersion efficiencies by the amphiphilic perylene derivative **3** reached 88%.

In further experiments concentrating on the bolaamphiphilic perylene derivatives **1** and **2**, as well as on the amphiphile **3**, I was able to provide experimental evidence for the correlation of the dispersion and exfoliation with the packing

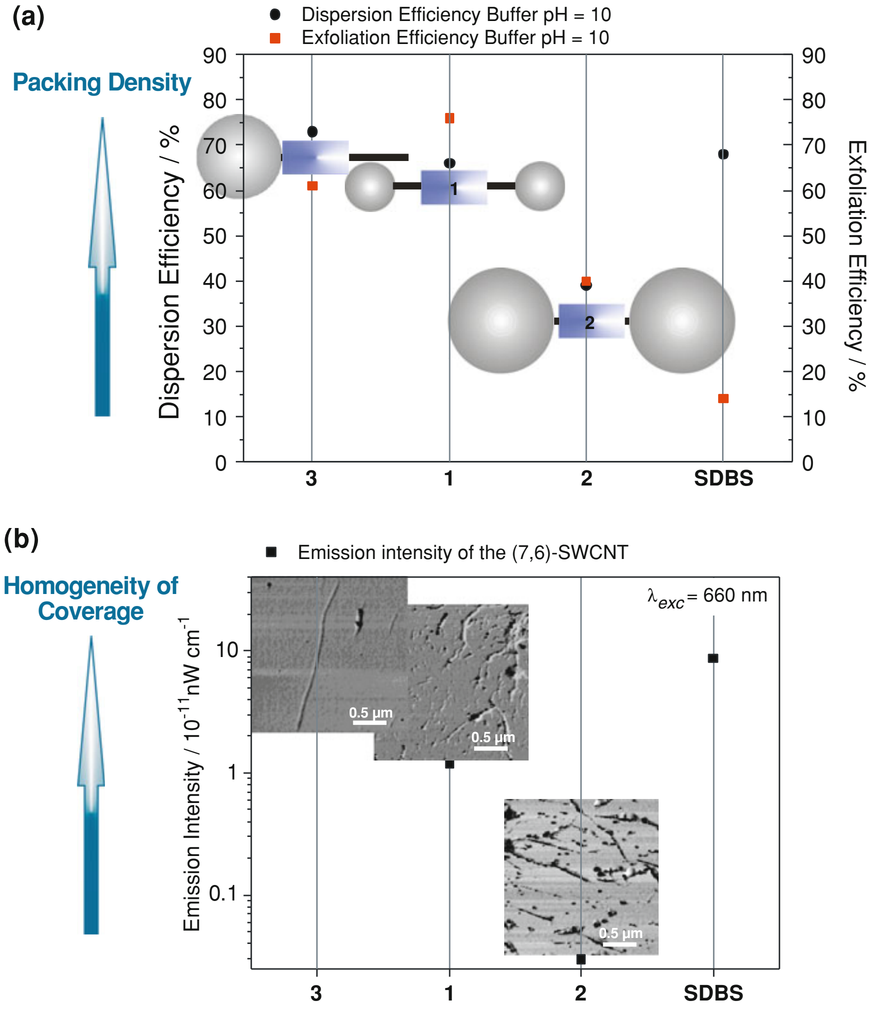

Fig. 4.1 **a** The dispersion and exfoliation efficiencies of the designed perylene based surfactants 1, **2** and **3** can be correlated to their packing density on the SWCNT scaffold. **b** SWCNT fluorescence intensity is dominated by the homogeneity of the surfactant coverage which is illustrated by AFM phase images

density of the surfactant on the nanotube scaffold (Sects. 3.1.1.3 and 3.1.2.2). The adsorption behavior of the designed perylene based surfactants was investigated by their hydrodynamic characterization via analytical ultracentrifugation (Sect. 3.1.2.2) [8]. The results were completely in line with the investigations by zeta potential, absorption spectroscopy, IR spectroscopy, XPS (Sect. 3.1.1.3), as well as replacement titrations (Sect. 3.1.3.2) [9]. As summarized in Fig. 4.1a, the packing density on the nanotube surface directly correlates with the dispersion and exfoliation capabilities.

Based on these observations, it is proposed that the amphiphilic PBI adsorbs on the nanotube surface in such a way that the solvophylic head and the lipophylic tail alternate to allow maximum loading (Fig. 3.32). As imaged by atomic force microscopy the nanotubes are accordingly more homogenously covered by PBI **3** compared to the bolaamphiphiles (Fig. 3.12). As summarized in Fig. 4.1b, the homogeneity of the SWCNT coverage directly impacts the fluorescence quantum yields of the carbon allotrope (Sect. 3.1.1.2) presumably due to the reduced contact with water and oxygen. In perfect agreement, the nanotube fluorescence intensity is highest in the case of the SWCNT-**3** dispersion in comparison to the other designed perylene π-surfactants, albeit being lower than the SDBS reference due to the charge transfer and π–π-stacking interaction contribution.

An appealing comparison to further demonstrate the extraordinary surfactant capabilities of functional PBIs arises from the possibility to investigate structurally related amphiphiles with pyrene as anchor group (Sect. 3.1.6) [10]. In this context, SWCNT dispersion and exfoliation by the aid of pyrene **10** and **11** being derivatized with first and second generation *Newkome*-type dendrimers, respectively, was analyzed. In line with the perylene based surfactants, the bulky second generation *Newkome*-type dendrimer is not necessarily favorable for the adsorption on the nanotube scaffold exhibiting lower surfactant capabilities. Accordingly, the dispersion efficiencies are significantly lower for the larger amphiphile **11** compared to the smaller derivative **10**. In analogy to the PBIs, dispersion in the buffer medium at pH = 10 outperforms efficiency in the pH = 7 buffer.

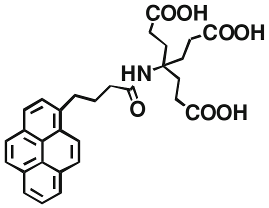

10

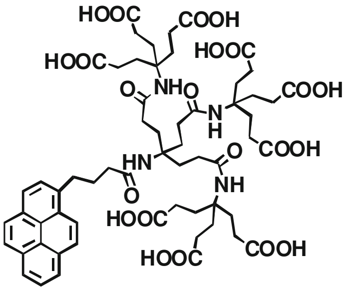

11

A significant aspect that should be mentioned is the much lower surfactant capability for the pyrene dispersants compared to the structurally related PBIs manifested in a maximum dispersion efficiency of 46% with an individualization rate of 26% (pH = 10, pyrene **10**) under equal processing conditions (nanotube material, initial nanotube concentration, sonication power and time, centrifugation condition). This is again underscoring the importance of the electron deficient perylene bisimide core that bears great potential to outperform pyrene derivatives that have been widely applied as nanotube anchor systems [11].

The difference between the pyrene and perylene bisimide unit and the impact on SWCNT-surfactant interactions is furthermore reflected in different affinities towards smaller and larger diameter SWCNTs, respectively. While pyrene exhibits a more pronounced affinity towards SWCNTs with larger diameters (Sect. 3.1.6), the anionic PBIs follow the opposite trend (Sect. 3.1.3). From electronic grounds, the enhanced adsorption affinity and higher packing density of the PBIs on SWCNTs with smaller diameter (larger band gap) that has been demonstrated by three independent techniques (zeta potential, analytical ultracentrifugation and replacement titrations followed by SWCNT absorption and emission spectroscopy) is a puzzling issue. Upon considering the charge transfer interaction from the nanotube to the PBI unit, one may predict a stronger interaction with smaller band gap nanotubes (larger diameter). The experimental observations were rationalized by the following adsorption hypothesis (Fig. 3.40): [9] The *p*-type doping induced by adsorption of the perylene core imparts a positive charge on the nanotube scaffold which results in a *Coulombic* attraction of the anionic solvophylic moieties. Since the *p*-type doping should be more pronounced in the case of larger diameter SWCNTs [12], the nanotubes possess a higher positive charge density leading to a pronounced attraction of the dendritic substituents. This in turn reduces the packing density on larger diameter nanotubes (despite a stronger core-nanotube interaction), or in other words an enhanced packing density on smaller diameter nanotubes where the solvophylic moieties presumably point into solution.

In an attempt to strengthen this adsorption hypothesis, the cationic perylene derivative **9** was investigated (Sect. 3.1.4).

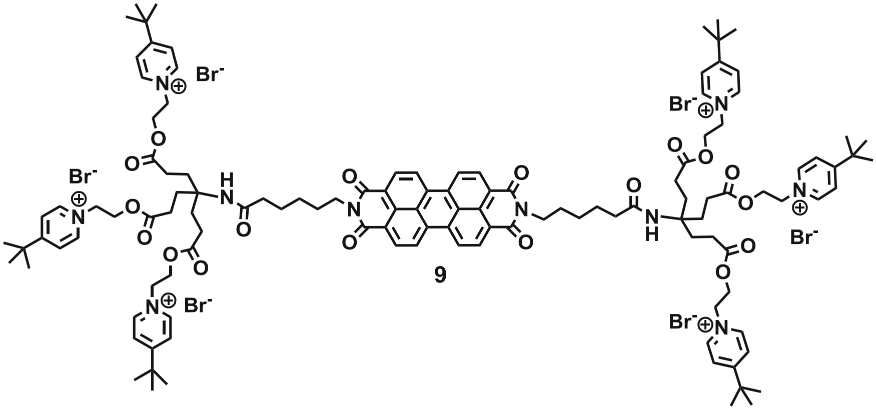

9

The analysis of the dispersion efficiencies and adsorption behavior was problematic due to the instability of the ester functionalities in aqueous media. Furthermore, a replacement from the nanotube sidewall by DTAB (as cationic analogue of SDBS) could not be precisely followed presumably due to the formation of mixed supramolecular architectures of the cationic perylene derivative with the cationic detergent DTAB (Sect. 3.1.5). However, if at all, an enhanced interaction with larger diameter nanotubes was observed.

A closer inspection of the supramolecular structures formed by the perylene bisimide surfactants **1**, **3** and **9** with a variety of cosurfactants such as SDBS, SDS, SDC, SC and DTAB (Sect. 3.1.5) revealed that a strong interaction of oppositely charged systems (for example **1**-DTAB or **9**-SDBS) takes place in any case as evidenced by absorption and emission spectroscopy. In addition, the amphiphilic perylene derivative **3** in contrast to the bolaamphiphile **1** is interacting with anionic amphiphiles (SDBS and SDS) despite the like head charges. In this regard, it appeared interesting that the cationic detergent DTAB is also affecting the assembly of the cationic bolaamphiphilic perylene derivative **9** above the critical micelle concentration of DTAB. The study of the PBI-cosurfactant structures does not only provide a deeper understanding for the highly versatile replacement titrations on the nanotube scaffold, but can furthermore by exploited to tune the emission quantum yields of the PBI fluorophores by the clever choice of additives in aqueous solution.

Since the PBI surfactants are characterized by outstanding exfoliation efficiencies in combination with the differentiation in the adsorption behavior according to nanotube diameter, they constitute promising candidates for efficient nanotube sorting. In the second part of this thesis, the development of alternative SWCNT sorting routes based on ultracentrifugation (Sects. 3.2.1–3.2.3), as well as selective dispersion (Sect. 3.2.4) was therefore targeted. Density gradient ultracentrifugation was successfully applied for SWCNT sorting according to structural integrity (Sect. 3.2.1.2) [13], e.g. covalently functionalized material was separated from the non-functionalized counterparts enabling the in-depth characterization of the functional adducts.

Furthermore, the concept of cosurfactant replacement DGU was introduced (Sect. 3.2.1.3) which resulted in fractionation of HiPco and CoMoCAT SWCNTs according to diameter [14]. In the following it was evaluated whether the success of the cosurfactant replacement DGU is dependent on the presence of a gradient medium by setting up a cosurfactant replacement band sedimentation experiment (Sect. 3.2.2). The proof of principle of diameter sorting of the SWCNTs was provided owing to the underlying enhanced affinity of the anionic PBIs with smaller diameter nanotubes. However, enrichment was not very pronounced due to the convolution by varying SWCNT lengths and directly related to that sedimentation velocities. As a consequence, a novel length sorting approach by band sedimentation ultracentrifugation was successfully developed (Sect. 3.2.3).

In addition, the extraordinary surfactant capabilities of perylene bisimide derivatives were combined with the encouraging results of selective nanotube dispersion by tweezer shaped molecules (Sect. 3.2.4) [15]. To this end selective dispersion of SWCNTs with diameters larger than 0.8 nm was demonstrated by the designed nanotweezer **12**.

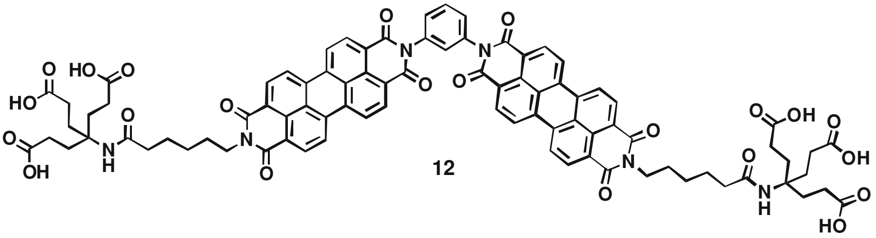

12

Finally, it is important to note that a number of characterization routines allowing the precise analysis of the nanotube-surfactant complexes have been developed within this thesis providing an understanding for the underlying interactions and establishing structure–property relationships. A cornerstone towards the improved SWCNT characterization could be laid by the optical visualization of the 1D nano-scaled SWCNTs in bright field microscopy (Sect. 3.3) [16]. To this end it was demonstrated that nanotubes, despite being below the diffraction limit of $\lambda/2$ in two dimensions, could be optically detected when deposited on Si/SiO_2 wafers with an oxide layer thickness of 300 nm. This visualization is extremely versatile, as it facilitates atomic force microscopic investigations significantly and furthermore it enables the correlation of morphology (AFM) with Raman spectroscopy. Thus, this low-cost methodology was finally able to bridge the gap between microscopic and spectroscopic characterization.

In conclusion, the results summarized in this thesis can be regarded as pieces in the jigsaw puzzle towards understanding noncovalent SWCNT functionalization in water, as a deeper understanding of the interactions of SWCNTs with highly potent designed surfactants was generated that enabled the development of novel SWCNT sorting scenarios (or modifications of already established scenarios). Furthermore, methodologies for the precise analysis and characterization of SWCNTs were established which are widely applicable.

References

1. M.C. Hersam, Nat. Nanotechnol. **3**, 387–394 (2008)
2. C. Backes, C.D. Schmidt, F.F. Hauke, C. Boettcher, A. Hirsch, J. Am. Chem. Soc. **131**, 2172–2184 (2009)
3. C. Backes, C.D. Schmidt, K. Rosenlehner, J.N. Coleman, F.F. Hauke, A. Hirsch, Adv. Mater. **22**, 788–802 (2010)
4. C. D. Schmidt, C. Bottcher, A. Hirsch, Eur. J. Org. Chem, pp. 5497–5505 (2007)
5. C. Backes, T. Schunk, F.F. Hauke, A. Hirsch, J. Mater. Chem. **21**, 3554–3557 (2011)
6. K. Rosenlehner, B. Schade, C. Boettcher, C.M. Jaeger, T. Clark, F.F.W. Heinemann, A. Hirsch, Chem. Eur. J. **16**, 9544–9554 (2010)
7. E. Karabudak, C. Backes, F.F. Hauke, C.D. Schmidt, H. Cölfen, A. Hirsch, W. Wohlleben, ChemPhysChem **11**, 3224–3227 (2010)

8. C. Backes, E. Karabudak, C.D. Schmidt, F.F. Hauke, A. Hirsch, W. Wohlleben, Chem. Eur. J. **16**, 13176–13184 (2010)
9. C. Backes, C.D. Schmidt, J.N. Coleman, W. Wohlleben, F.F. Hauke, A. Hirsch, Chem. Eur. J. **16**, 13185–13192 (2010)
10. C. Backes, U. Mundloch, A. Ebel, F.F. Hauke, A. Hirsch, Chem. Eur. J. **16**, 3314–3317 (2010)
11. T. Fujigaya, N. Nakashima, Polym. J. **40**, 577–589 (2008)
12. M.J. O'Connell, E.E. Eibergen, S.S.K. Doorn, Nat. Mater. **4**, 412–418 (2005)
13. B. Gebhardt, F. F. Hof, C. Backes, M. Müller, T. Plocke, C. Thomsen, F. Hauke, A. Hirsch, J. Am. Chem. Soc. (2011). Published online, doi: 10.1021/ja206818n
14. C. Backes, C.D. Schmidt, F.F. Hauke, A. Hirsch, Chem. Commun. **19**, 2643–2645 (2009)
15. C. Backes, C.D. Schmidt, F.F. Hauke, A. Hirsch, Chem. Asian J. **6**, 438–444 (2011)
16. C. Backes, J. Englert, N. Bernhard, F.F. Hauke, A. Hirsch, Small **6**, 1968–1973 (2010)

Chapter 5
Experimental Details

5.1 Materials and Methods

5.1.1 *Materials*

The purified HiPco SWCNTs (Batch P0343, residual weight 5 %) were purchased from Unidym Inc. (U.S.). In case of the covalently functionalized SWCNTs, the batch P0261 has been the used for further processing. Laser ablation SWCNTs (batch R0448) were obtained from Carbon Nanotechnology Inc. (U.S.). The purified CoMoCAT SWCNTs (batch SG65-0012, residual weight 20%) were purchased from Southwest Nanotechnology Inc. (U.S.). All SWCNT materials were used as received without further purification.

All other chemicals were purchased from Thermo Fisher, Sigma Aldrich or Merck and applied without further treatment. The dispersants **1**–**7**,[1, 2] as well as **12** [3] were synthesized by Cordula Schmidt, **8** was synthesized by Karin Rosenlehner [2], **9** by Torsten Schunk and **10**, as well as **11** by Alexander Ebel [4] (all of them members of the group of Prof. Hirsch, Chair of Organic Chemistry II, University Erlangen-Nuremberg).

5.1.2 *Methods*

5.1.2.1 Absorption Spectroscopy

Absorption spectra were recorded with a Shimadzu UVPC3100 or a Perkin Elmer Lambda 1050 in transmission with 0.2, 0.4 or 1 cm path length in quarzglass suprasil (Hellma) cuvettes. The pathlength of the cuvette was chosen in such a way that the maximum absorption intensity in the region of interest did not exceed 1.5 a.u. In the case of the aqueous detergent solution, the background of H_2O was subtracted.

C. Backes, *Noncovalent Functionalization of Carbon Nanotubes*, Springer Theses,
DOI: 10.1007/978-3-642-27582-1_5, © Springer-Verlag Berlin Heidelberg 2012

5.1.2.2 Fluorescence Spectroscopy

The SWCNT nIR emission was most commonly recorded with a Nanospectralyzer NS1 from Applied Nanofluorescence with laser excitations of 660 and 785 nm. Integration times were commonly 300 ms and 50 spectra were averaged.

In cases where a 3D nIR emission contour plot was desired, a Fluorolog-3 from Horiba Scientific was used equipped with a nitrogen cooled Symphony InGaAs diode array detector with a 600 grooves mm^{-1} grating in excitation and a 180 grooves mm^{-1} grating in emission. Typical integration times were 15 s with slit width of 10 nm (in excitation and emission). UV/Vis emission was recorded with a photomultiplier tube detector with 1,200 grooves mm^{-1} in emission.

5.1.2.3 Raman Spectroscopy

Raman spectra were recorded on a Horiba Scientific Labram Aramis confocal Raman microscope equipped with an automated XYZ-table using 0.80 NA objectives and laser excitations of 532, 633 and 785 nm, respectively.

5.1.2.4 IR Spectroscopy

IR spectra were obtained in transmission with KBr as matrix on a Tensor27 (Bruker). The SWCNTs were pre-grind with pistil and mortar prior to homogenously distributing 0.3 wt% of functionalized SWCNTs (and 0.1 wt in the case of the as-received material) homogenously with KBr by ball milling. Pellet were fabricated by pressing the KBr under vacuum at 10 bar for 10 min. Commonly, 1,000 scans with a resolution of 4 cm^{-1} have been recorded.

5.1.2.5 Optical Microscopy

The optical microscopic images were acquired with a Zeiss Axio Imager M1 m with white light illumination (100 W halogen lamp, HAL100) using bright and dark-field imaging modes and 0.80 NA objectives. For the fluorescence microscopic images a filter043 with BP545 nm/25 nm in excitation, FT570 nm as beam splitter and BP605 nm/70 nm in emission has been used (filter43) upon illumination with a metal halogen lamp (HXP120). In all cases, a Zeiss AxioCam MRc5 has been used for recording the images.

5.1.2.6 Atomic Force Microscopy

AFM tapping mode images were recorded on a Solver Pro scanning probe microscope (NT-MDT) equipped with a Sony Exwave HAD camera optical zoom (6.5).

5.1.2.7 Scanning Electron Microscopy

SEM images were recorded by Nicolas Bernhard on a field emission SEM (Hitachi S-4800). The CNT-coated Si/SiO_2-wafer was fixed on an aluminium specimen-stub using a conductive carbon adhesive (N650 Planocarbon). The specimen-stub was then heated to 80 °C for 15 min to allow for a complete solvent evaporation. Imaging was performed at acceleration voltages of 1.0 kV. The focal length was varied between 7.3 (overview) and 7.5 mm (higher magnification).

5.1.2.8 Zeta Potential Measurements

Zeta potential measurements were carried out on a Malvern Zetasizer Nano system with irradiation from a 633 nm He–Ne laser. The samples were injected in folded capillary cells, and the electrophoretic mobility (μ) was measured using a combination of electrophoresis and laser Doppler velocimetry techniques. The electrophoretic mobility relates the drift velocity of a colloid (v) to the applied electric field (E); $v = \mu E$. All measurements were conducted at 25 °C.

The zeta potential ζ is related to the measured electrophoretic mobility μ according to the *Smoluchowski* approximation (Eq. 1.4).

5.1.2.9 X-ray Photoelectron Spectroscopy

XPS spectra were recorded on a Surface Science Instruments, type M-Probe, using a monochromized Al K_α small spot X-ray gun ($\hbar\omega = 1{,}486.6$ eV). Binding energy calibration was carried out by setting the binding energy of the Au 4f 7/2 core level energy at 84.00 eV. The XPS measurements were carried out by Dr. Ralf Graupner at the Department of Physics, Chair of Technical Physics, University Erlangen-Nuremberg.

5.1.2.10 Preparative Ultracentrifugation

For preparative ultracentrifugation, a Beckman Coulter Optimamax XP tabletop ultracentrifuge was used with a swinging bucket rotor (MLS-50) in the cases of band centrifugation and DGU or a fixed angle rotor (TLA 100.3).

5.1.2.11 Analytical Ultracentrifugation

Experimentally, an XLA (Beckman–Coulter) analytical ultracentrifuge was used to directly measure the redistribution of SWCNTs in a centrifugal force field. This instrument enabled the characterization of the sedimentation and diffusion of SWCNTs in situ at an angular velocity of 40 krpm. Dispersed SWCNTs and reference aqueous solutions (water and deuterated water, respectively) were loaded into two-hole Epon cells equipped with quartz windows (d = 1.2 cm). These cells were housed in a four-cell rotor (Ti-60, Beckman–Coulter), which was kept at a constant temperature of 25 °C. The optical density of the SWCNT solutions at 550 nm (unless otherwise noted) was measured as a function of time and position to track the redistribution of the SWNTs. Experiments were typically continued for 1–2 h until predominantly all the SWNTs had sedimented to the bottom of the cells. Alternatively an analytical ultracentrifuge with a multi-wavelength detector was used that was recently developed by BASF SE and MPI Golm, described elsewhere [5]. In short, a vacuum-compatible UV/vis spectrometer (Ocean-Optics) is placed inside the rotor chamber with suitable mechanotronics for radial scanning. The white-light source flashes synchronized with the rotation, such that the full absorption spectrum is recorded for each radial position at each time scan. The design and the operating software (written in LabVIEW) are open source as part of the Open-AUC work group [6].

5.2 Preparation of the SWCNT Dispersions

The SWCNT dispersions were in principle prepared by immersing the nanotubes in aqueous solutions of the surfactant. After sonication (30 min in a bath type sonicator with an ultrasonic input of 300 W) the homogenous dispersions were centrifuged at 15 krpm for 30 min in a Sigma 4K15 centrifuge at 15 °C (unless otherwise noted). The top 80% of the supernatant were carefully decanted and subjected to further analysis. The exact concentrations of nanotubes and dispersant, as well as the pH values (buffered or non-buffered) are noted in the respective paragraphs of the results and discussion section.

The absorption and zeta potential measurements were directly conducted from the supernatant solutions. In case of nIR emission spectroscopy, the dispersions were diluted with H_2O (in the case of the π-surfactants) or surfactant solution (in case of classical detergents) to the same optical density, commonly below 0.4 cm^{-1} at 740 nm. For the analytical ultracentrifugation experiments, the supernatant dispersions were diluted (if necessary) with the corresponding surfactant solution to yield optical densities of approximately 1 cm^{-1} at 740 nm.

For analysis of the SWCNT samples by optical microscopy and AFM, approximately 5–10 drops of the dispersion were spin-casted with 100 rps on Si/SiO_2 wafers (300 nm oxide layer thickness), washed with 10 mL of water and 10 mL of isopropanol and dried on air.

Raman spectra were recorded from the solid either directly from the Si/SiO_2 wafers, or in case of the bulk spectra, after microfiltration (regenerated cellulose, 0.2 μm pore size) of the dispersions and washing with minimum 50 mL of water (buckypaper). XPS was also measured from the buckypaper. For IR spectroscopy, the dispersions were microfiltrated, the SWCNT material removed from the filter and dried at 70 °C under vacuum prior to grinding and pellet fabrication.

5.3 Determination of the SWCNT Absorption Coefficients

For the determination of the SWCNT absorption coefficients, 1 mg of as-received SWCNTs were dispersed in 10 mL of 1 wt% aqueous SDBS solution (in buffered media at pH = 7 and 10, respectively) by sonication (30 min in a bath type sonicator). The absorption spectra were immediately measured after sonication in order to minimize sedimentation of the coarse aggregates (please note that scattering and bundling convolute the data acquisition, but cannot be avoided). The dispersions were then subsequently diluted 1:1 with aqueous surfactant solution. The SWCNT absorption coefficients can be derived from the slope of the plot of the optical density at characteristic wavelengths *versus* the nanotube concentrations (see Fig. 5.1).

The absorption cross sections of HiPco SWCNTs were determine in buffered solutions at pH = 7 and 10, respectively at 735 nm. Commonly the S_{22}-transition at 660 nm is chosen as wavelength for the determination of the absorption cross section of HiPco SWCNTs. However, this particular wavelength was not perfectly suitable in the context of this thesis as the major focus was directed towards perylene bisimide dispersants which have a nonzero absorption cross section at 660 nm. The slopes a of the linear relationship presented in Fig. 5.1a were determined to be 0.0276 and 0.0252 yielding SWCNT absorption coefficients z of 36 L g^{-1} cm^{-1} (=432 L mol^{-1} cm^{-1}) and 39 L g^{-1} cm^{-1} (468 L mol^{-1} cm^{-1}) in buffered media at pH = 7 and 10, respectively.

The absorption coefficient of the as-received CoMoCAT SWCNTs is significantly lower than for the HiPco nanotubes with 11 L g^{-1} cm^{-1} (=132 L mol^{-1} cm^{-1}) in nonbuffered SDBS solution as determined from the linear relationship presented in Fig. 5.1b.

5.4 Density Gradient Ultracentrifugation

5.4.1 Electronic Type Sorting

Density gradients were formed from aqueous solutions of the non-ionic density gradient iodixanol (purchased as Optiprep 60 wt% in water, 1.32 g cm^{-3}). The linear density gradients were created directly in the centrifuge vial (Beckman Polyclear, 5 mL volume) by layering and subsequent diffusion of four discrete layers with decreasing iodixanol concentration from bottom to top. The nanotubes were inserted in the top layer for both enrichment experiments of metallic and semiconducting species, respectively. In any case the bottom layer (0.7 mL) consisted of 60 wt% iodixanol, the second layer (1 mL) of 40 wt% iodixanol, the third layer of 20 wt% iodixanol (1 mL) and the top layer containing the dispersed nanotubes of 10 wt% (1.3 mL).

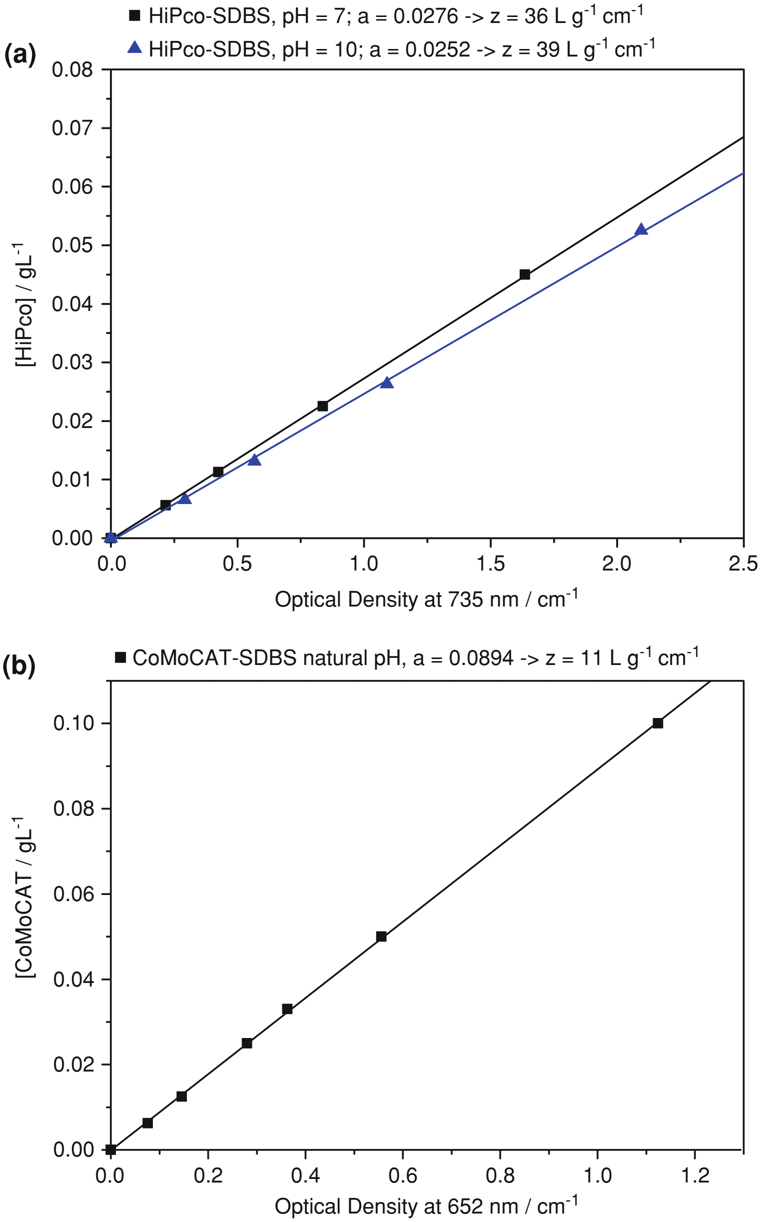

Fig. 5.1 Plots of nanotube concentrations *versus* optical density at characteristic positions in the absorption spectra (735 nm in the case of HiPco and 652 nm for CoMoCAT SWCNTs). The absorption coefficient z of (**a**) HiPco SWCNTs and (**b**) CoMoCAT SWCNTs can be derived from the slope a of the linear plots

In the case of the enrichment of the metallic SWCNTs a surfactant ratio of SC : SDS = 2 : 3 with a total surfactant concentration of 1.5 wt% was used throughout the centrifugation vial, whereas a ratio of SC : SDS = 4 : 1 with a total surfactant concentration of 2 wt% was applied in the case where semiconducting SWCNTs were targeted.

For the preparation of the top layer 0.5 g L^{-1} SWCNTs (laser ablation R0448) were dispersed in the respective surfactant solutions by sonication (30 min in a bath type sonicator). After mild pre-centrifugation(15 krpm for 30 min in a Sigma 4K15 centrifuge at 15 °C), the appropriate amount of iodixanol was added to the supernatant dispersions to yield concentrations of 10 wt%. The mixture was then directly used as top layer in the gradient.

The ultracentrifugation experiment was carried out in a swinging bucket rotor (MLS-50) at 35 krpm for 16 h.

5.4.2 Sorting According to Structural Integrity

Density gradients were formed from aqueous solutions of the non-ionic density gradient iodixanol (purchased as Optiprep 60 wt% in water, 1.32 g cm^{-3}). The linear density gradients were created directly in the centrifuge vial (Beckman Polyclear, 5 mL volume) by layering and subsequent diffusion of five discrete layers with decreasing iodixanol concentration from bottom to top of 60 wt% (0.7 mL), 40 wt% (1.5 mL), 32.5 wt% (1 mL; layer containing SWCNTs). 30 wt% (1 mL) and 20 wt% (0.8 mL), respectively. SDC was used as surfactant for the stabilization of the nanotubes with a concentration of 2 wt% throughout the centrifugation vial.

For the preparation of the layer containing the nanotube material 0.5 g L^{-1} SWCNTs were dispersed in 2 wt% SDC solutions by sonication (30 min in a bath type sonicator). After mild pre-centrifugation (15 krpm for 30 min in a Sigma 4K15 centrifuge at 15 °C), the appropriate amount of iodixanol was added to the supernatant dispersions to yield concentrations of 32.5 wt%. The mixture was then directly used as layer in the gradient.

The ultracentrifugation experiment was carried out in a swinging bucket rotor (MLS-50) at 40 krpm for 17.5 h. The non-functionalized SWCNT material travelled upward during the centrifugation, while the bundles sedimented to the very bottom.

5.4.3 Sedimentation Replacement DGU

Density gradients were formed from aqueous solutions of the non-ionic density gradient nycodenz (purchased as solid). The density gradients were created directly in the centrifuge vial by layering and subsequent diffusion of four discrete layers with decreasing nycodenz concentration from bottom to top of 60, 40, 20 and 10 wt% (1 mL), respectively. The nanotubes were contained in the top layer with 10 wt% nycodenz.

For the preparation of the top layer 0.5 g L^{-1} SWCNTs (HiPco and CoMoCAT) were dispersed in a buffered aqueous solution of **3** (10 g L^{-1}, pH = 7) by sonication (30 min in a bath type sonicator). After mild pre-centrifugation, the appropriate amount of nycodenz was added to the supernatant dispersions to yield concentrations of 10 wt%. The mixture was then directly used as top layer in the gradient.

To all non-nanotube layers, SDS was added as a cosurfactant at a concentration of 2 wt% throughout the gradient in order to induce the replacement of the perylene dispersant from the nanotube sidewall.

Ultracentrifugation was performed in a swinging bucket rotor (Beckman Coulter SW60Ti) at 15 krpm for 16 h.

References

1. C.D. Schmidt, C. Bottcher, A. Hirsch, Eur. J. Org. Chem. 5497–5505 (2007)
2. C. Backes, C.D. Schmidt, K. Rosenlehner, J.N. Coleman, F. Hauke, A. Hirsch, Adv. Mater. **22**, 788–802 (2010)
3. C. Backes, C.D. Schmidt, F. Hauke, A. Hirsch, Chem. Asian J. **6**, 438–444 (2011)
4. A. Ebel, W. Donaubauer, F. Hampel, A. Hirsch, Eur. J. Org. Chem. 3488–3494 (2007)
5. H.M. Strauss, E. Karabudak, S. Bhattacharyya, A. Kretzschmar, W. Wohlleben, H. Coelfen, Colloid Polym. Sci. **286**, 121–128 (2008)
6. H. Cölfen, T. Laue, W. Wohlleben, K. Schilling, E. Karabudak, B. Langhorst, E. Brookes, B. Dubbs, D. Zollars, M. Rocco, B. Demeler, Eur. Biophys. J. Biophys. Lett. **39**, 347–359 (2010)

Curriculum Vitae

Personal Data

Name: Claudia Backes
Date of Birth: 04.04.1982
Place of Birth: Nuremberg
Marital Status: unmarried
Nationality: German

Education

1988–1992	Pestalozzi Elementary School Oberasbach
1992–2002	Dietrich-Bonhoeffer-Gymnasium Oberasbach

Abitur

- Stay abroad in 1999–2000 in Ontario/Canada; Attendance at the Central Algoma Secondary School
- Courses of final examination: Mathematics (main), Chemistry (main), English, Religion
- Award for the best leaving certificate of the city Oberasbach (average 1.5)

Higher Education

2002–2008 Friedrich-Alexander-University Erlangen

Study Course: Molecular (Nano) Science

- Bachelor qualification 2005;

Bachelor Thesis in the group of Prof. Dr. Hirsch (Organic Chemistry) with the topic "*Synthesis, Synthesis Optimization and Characterization of a Multifunctional Fullerene Bingel Addend.*"

C. Backes, *Noncovalent Functionalization of Carbon Nanotubes*, Springer Theses,
DOI: 10.1007/978-3-642-27582-1, © Springer-Verlag Berlin Heidelberg 2012

- Modules during Master level:

Nano Science, Molecular Syntheses, Physical Chemistry

- November 2006–August 2007: Master Thesis

Cooperation between the group of Prof Dr. Hirsch (Organic Chemistry) and the group of Prof Dr. Kisch (Inorganic Chemistry) with the topic: "*Visible Light Photocatalysis of* TiO_2 *Modified by Single-Walled Carbon Nanotubes.*"

Degree: Master of Science

- Grade point average: 1.5
- Grade in Master Thesis: 1.0

11/2007–04/2011 Friedrich-Alexander-University Erlangen

- Titel: "*Fundamental Aspects of the Noncovalent Functionalization of Single-Walled Carbon Nanotubes in Water.*"
- At the Institute of Advanced Materials and Processes (ZMP) under the guidance of Prof. Andreas Hirsch (Chair of Organic Chemistry II)
- Day of oral examination: June 9th 2011

Employment Career

08/2005–09/2005 Friedrich-Alexander-University Erlangen

- Student Assistant at the Chair of Physical Chemistry II (Prof. Guldi)

11/2007–04/2011 Friedrich-Alexander-University Erlangen

Research Assistant

- At the Institute of Advanced Materials and Processes (ZMP)
- Organizational duties: Responsible for safety, hazardous waste disposal, wastewater, ordering chemicals and equipment, maintenance of chemical laboratories
- Scientific duties: Responsible for atomic force microscope, fluorescence spectrometers, absorption spectrometer, ultracentrifuge, dynamic light scattering and zeta potential (Zetasizer)

07/2008 BASF SE Ludwigshafen

- Internship (density gradient ultracentrifugation)

02/2009 Trinity College Dublin, Ireland

- Internship (general analytics, Zeta Potential)
- *Two joint publications* (*Adv. Mater*, *Chem. Eur. J.*)

05/2009 BASF SE Ludwigshafen

- Internship (analytical ulracentrifugation)
- *Three joint publications* (2 *Chem. Eur. J.*, *ChemPhysChem*)

Since 05/2011 Friedrich-Alexander-University Erlangen

Scientific Coordinator in the Cluster of Excellence Engineering of Advanced Materials (EAM)

- Coordination of the DFG renewal proposal within the framework of the excellence initiative and its evaluation
- Deputy chief executive of the cluster of excellence

Language Skills

- German (native)
- English (language proficient)
- French (fluent)

Publications

Articles in Peer-Reviewed Journals

1. Gebhardt, G., Hof F., Backes C., Müller, M., Plocke, T., Thomsen. C., Hauke, F., Hirsch, A. Selective Reductive Sidewall Carboxylation of Semiconducting Single-Walled Carbon Nanotubes. *Journal of the American Chemical Society* **133**, 19459–19473 (2011).
2. Backes, C., Bosch, S., Mundloch, U., Hauke, F. & Hirsch, A. Density Gradient Ultracentrifugation on Carbon Nanotubes According to Structural Integrity as a Foundation for an Absolute Purity Evaluation. *ChemPhysChem* **12**, 2576–2580 (2011).
3. Backes, C., Hauke, F. & Hirsch, A. The Potential of Perylene Bisimide Derivatives for the Solubilization of Carbon Nanotubes and Graphene. *Advanced Materials* **23**, 2588–2601 (2011). (feature article, review)
4. Gebhardt, B., Syrgiannis, Z., Backes, C., Graupner, R., Hauke, F. & Hirsch, A. Carbon Nanotube Sidewall Functionalization with Carbonyl Compounds-Modified Birch Conditions vs the Organometallic Reduction Approach. *Journal of the American Chemical Society* **133**, 7985–7995 (2011).
5. Backes, C., Schunk, T., Hauke, F. & Hirsch, A. Counterion effect on the aggregation of anionic perylene dyes and the influence on carbon nanotube dispersion efficiencies. *Journal of Materials Chemistry* **21**, 3554 (2011).
6. Backes, C., Schmidt, C. D., Hauke, F. & Hirsch, A. Perylene-Based Nanotweezers: Enrichment of Larger-Diameter Single-Walled Carbon Nanotubes. *Chemistry—An Asian Journal* **6**, 438–444 (2011).
7. Backes, C., Englert, J. M., Bernhard, N., Hauke, F. & Hirsch, A. Optical Visualization of Carbon Nanotubes-a Unifying Linkage between Microscopic and Spectroscopic Characterization Techniques. *Small* **6**, 1968–1973 (2010). (feature article, highlighted by Nanowerk Platform)

8. Karabudak, E., Backes, C., Hauke, F., Schmidt, C. D., Cölfen, H., Hirsch, A. & Wohlleben, W. A Universal Ultracentrifuge Spectrometer Visualizes CNT-Intercalant-Surfactant Complexes. *ChemPhysChem* **11**, 3224–3227 (2010).
9. Backes, C., Mundloch, U., Schmidt, C. D., Coleman, J. N., Wohlleben, W., Hauke, F. & Hirsch, A. Enhanced Adsorption Affinity of Anionic Perylene-Based Surfactants towards Smaller-Diameter SWCNTs. *Chemistry—A European Journal* **16**, 13185–13192 (2010).
10. Backes, C., Karabudak, E., Schmidt, C. D., Hauke, F., Hirsch, A. & Wohlleben, W. Determination of the Surfactant Density on SWCNTs by Analytical Ultracentrifugation. *Chemistry—A European Journal* **16**, 13176–13184 (2010).
11. Backes, C., Mundloch, U., Ebel, A., Hauke, F. & Hirsch, A. Dispersion of HiPco® and CoMoCAT® Single-Walled Nanotubes (SWNTs) by Water Soluble Pyrene Derivatives-Depletion of Small Diameter SWNTs. *Chemistry—A European Journal* **16**, 3314–3317 (2010). (feature article)
12. Backes, C., Schmidt, C. D., Rosenlehner, K., Hauke, F., Coleman, J. N. & Hirsch, A. Nanotube Surfactant Design: The Versatility of Water-Soluble Perylene Bisimides. *Advanced Materials* **22**, 788–802 (2010).
13. Ehli, C., Oelsner, C., Guldi, D. M., Mateo-Alonso, A., Prato, M., Schmidt, C. D., Backes, C., Hauke, F. & Hirsch, A. Manipulating single-wall carbon nanotubes by chemical doping and charge transfer with perylene dyes. *Nature Chemistry* **1**, 243–249 (2009).
14. Backes, C., Hauke, F., Schmidt, C. D. & Hirsch, A. Fractioning HiPco and CoMoCAT SWCNTs via density gradient ultracentrifugation by the aid of a novel perylene bisimide derivative surfactant. *Chemical Communications*, 2643 (2009). (feature article)
15. Backes, C., Schmidt, C. D., Hauke, F., Böttcher, C. & Hirsch, A. High Population of Individualized SWCNTs through the Adsorption of Water-Soluble Perylenes. *Journal of the American Chemical Society* **131**, 2172–2184 (2009).

Book Chapter and Book

Backes, C., "Noncovalent Functionalization of Carbon Nanotubes- Fundamental Aspects of Dispersion and Separation in Water" published within Springer Theses, Springer Berlin Heidelberg, **2012**. (book)

Backes, C., Hirsch, A., "Noncovalent Functionalization of Carbon Nanotubes" in *Chemistry of Nanocarbons* (Eds.: T. Akasaka, F. Wudl, S. Nagase), John Wiley & Sons, **2010**, p. 528ff. (book chapter)

Book Review

Hirsch, A., Backes, C. Carbon Nanotube Science. Synthesis, Properties and Applications. By Peter J. F. Harris. *Angewandte Chemie, International Edition* **49**, 1722–1723 (2010).

Conference Contributions (International Concerences)

1. Backes, C., Hirsch, A, *IWEPN*, Kirchberg, Austria **2012**. (Invited Talk)
2. Backes, C., Hirsch, A. “Functionalization of Synthetic Carbon Allotropes—The Chemist’s Toolkit for Dispersion and Tailoring Surface Properties.” Nanotough Dissemination Seminar, Lyngby, Denmark **2011**. (Talk)
3. Backes, C. “Absorption Spectroscopy on Single-Walled Carbon Nanotubes—A Highly Versatile Characterization Tool.” Colloquium Optical Spectroscopy, Berlin **2011**. (Invited Talk)
4. Backes, C., Hauke, F., Hirsch A. “On the Way to Sorted Carbon Nanotubes Based on Tailor Made Surfactants.” Euchems, Nuremberg **2010**. (Poster Presentation)
5. Backes, C., Schmidt, C. D., Hauke, F., Hirsch, A. “Solubilization and Density Gradient Fractioning of SWNTs by a Novel three Component Surfactant.” *IWEPN*, Kirchberg, Austria **2009**. (Poster Presentation)

Additional Evidence of Qualification

- Review activities for *Chem. Commun., J. Mater. Chem.*, *Green Chemistry*, *Materials*
- Co-supervision of five Bachelor Theses
- Lectures on behalf of Prof. Hirsch (single sessions in supramolecular chemistry and functional π-systems)